

RESOLVING THE FORMATION OF PROTOGALAXIES

A DISSERTATION

SUBMITTED TO THE DEPARTMENT OF PHYSICS
AND THE COMMITTEE ON GRADUATE STUDIES
OF STANFORD UNIVERSITY

IN PARTIAL FULFILLMENT OF THE REQUIREMENTS
FOR THE DEGREE OF
DOCTOR OF PHILOSOPHY

John H. Wise

June 2007

© Copyright by John H. Wise 2019
All Rights Reserved

I certify that I have read this dissertation and that, in my opinion, it is fully adequate in scope and quality as a dissertation for the degree of Doctor of Philosophy.

(Tom Abel) Principal Adviser

I certify that I have read this dissertation and that, in my opinion, it is fully adequate in scope and quality as a dissertation for the degree of Doctor of Philosophy.

(Roger D. Blandford)

I certify that I have read this dissertation and that, in my opinion, it is fully adequate in scope and quality as a dissertation for the degree of Doctor of Philosophy.

(Robert V. Wagoner)

Approved for the University Committee on Graduate Studies.

Abstract

Cosmic structure originated from minute density perturbations in an almost homogeneous universe. The first stars are believed to be very massive and luminous, providing the first ionizing radiation and heavy elements to the universe and forming 100 million years after the Big Bang. The impact from primordial stellar radiation is far reaching and affects subsequent star and galaxy formation. In this thesis, we present results from adaptive mesh refinement calculations of the formation of the first galaxies. We gradually introduce important physical processes, such as molecular hydrogen cooling and stellar feedback, to base models that only consider atomic hydrogen and helium cooling. In these base models, we find that gas in dark matter halos with masses $\sim 10^8 M_\odot$ centrally collapse before multiple fragmentation occurs in a global disc. We then investigate the importance of molecular hydrogen cooling in early structure formation in the presence of a soft ultraviolet radiation background. We find that molecular hydrogen plays an important role in star formation in halos well below a virial temperature of 10,000 K even in the most extreme assumptions of negative radiative feedback. We also present results from the first radiation hydrodynamics calculations of early dwarf galaxy formation. We develop a novel technique, adaptive ray tracing, to accurately transport radiation from primordial stars. We find primordial stellar feedback alters the landscape of early galaxy formation in that its angular momentum is increased and baryon fractions are decreased. We also describe the metal enrichment of the intergalactic medium and early dwarf galaxies. Finally we explore cosmological reionization by these massive, metal-free stars and its effects on star formation in early galaxies.

Preface

The purpose of this preface is to provide a synopsis of the original methods and applications developed by the candidate for the work presented in this thesis. I also describe the most important conclusions of the thesis that have not been demonstrated yet by numerical simulations.

The first luminous objects are believed to have a profound impact on its surroundings and future star and galaxy formation. There have been numerous numerical studies concerning (i) primordial star formation, (ii) primordial stellar feedback, and (iii) early galaxy formation. However, nobody has been successful in accurately simulating the evolution of ionized and heated regions around the first stars until the epoch of galaxy formation. In this thesis, I connect these three topics together. We approach this problem methodically through an extensive suite of adaptive mesh refinement simulations that focus on the formation of some of the earliest galaxies in the universe while including important physical processes, such as molecular hydrogen cooling and radiation transport.

Chapter 2, “The Number of Supernovae from Primordial Stars in the Universe”, describes results from a semi-analytic model of star formation and feedback that was developed by the candidate. Although such models are widespread in the literature, our approach includes a time-dependent and self-consistent approach to include negative feedback. It considers a soft ultraviolet radiation background that is generated by ongoing star formation, which in turn suppresses future star formation by requiring a larger dark matter halo mass to form primordial stars. The critical halo mass is generally set to be constant in many semi-analytic models that focus on primordial star formation and reionization. This aspect sets our approach apart from other

studies. This chapter was published in the *The Astrophysical Journal*, 2005, Volume 629, 615.

Chapter 3, “The Virialization of Baryons in Protogalaxies”, shows that baryons experience an analog of violent relaxation that happens in the virialization of collisionless dark matter. Some groups assume that pre-galactic gas clouds rotate like solid bodies that collapse into galactic discs. This assumption dates back to Crampin & Hoyle (1964), who showed that the rotation curves of spiral galaxies could be explained by a uniform rotating spheroid. We show that virialization stirs turbulence to become supersonic. In other words, turbulent velocities dominate the rotational ones. The properties of a turbulent collapse differ greatly from a solid body rotator and should affect calculations that rely on these idealized initial conditions. This chapter has been submitted to *The Astrophysical Journal* for publication.

Chapter 4, “Central Gas Collapse of a Atomic Hydrogen Cooling Halo”, applies theories of rotational bar-like instabilities to the context of a collapsing cosmological halo. The instabilities are secular in that turbulent viscosity amplifies perturbations created when rotational energies are large enough. We were the first to demonstrate that these instabilities occur in the gaseous collapse of turbulent clouds in numerical simulations. I interpreted and confirmed that our data exhibited such an instability. These bars transport angular momentum outward so that only the gas with the lowest specific angular momentum falls to the center. This partially alleviates the difficulties imposed by angular momentum conservation during a gaseous collapse to a dense central core if one considers the initial gas cloud as a solid-body rotator. This scenario is also applicable to star formation in galactic molecular clouds.

Chapter 5, “Suppression of H₂ Cooling in the UVB”, strengthens the importance of molecular hydrogen cooling in dark matter halos with masses well below the ones associated with galaxy formation. We show that molecular hydrogen cooling cannot be neglected when studying structure formation in the early universe.

Chapter 6, “The Nature of Early Dwarf Galaxies”, and Chapter 7, “How Massive Metal-Free Stars Start Cosmological Reionization”, focus on the radiative feedback from primordial stars and its impact on early galaxy formation and the beginning of cosmological reionization. We have developed a novel technique, adaptive ray tracing

(Abel & Wandelt 2002), to accurately compute radiation transport from point sources. Tom Abel originally integrated this method into a single-processor version of the AMR code *enzo*. The radiative transfer is coupled with the hydrodynamics, energy, and chemistry solvers in *enzo*. I then created and tested routines to automatically create primordial star particles, whose luminosities and lifetimes are determined from primordial stellar models, in overdensities that will form such as shown by Abel et al. (2002) and Yoshida et al. (2006b). The star particles are treated as point sources of radiation in our adaptive ray tracing scheme.

More importantly, I developed a massively parallel version of the adaptive ray tracing method that is functional on distributed and shared memory machines. The code is dynamically load-balanced so it runs efficiently on many processors and minimizes inter-processor communication of the “photon packages”. It is necessary to optimize this method because approximately 10^6 photons are traced through $\sim 10^7$ grid cells per timestep per point source. Currently the radiation transport consumes the same amount of computing time as the hydrodynamics solver and increases the run time by approximately 50%. This additional time is a small cost to pay compared to the benefits of the accurate depiction of radiative feedback in our simulations. This code is one of two cosmology radiation hydrodynamics codes that is parallelized and optimized for radiative feedback studies with enough resolution to resolve Pop III hosting halos. This is the first time that a radiation hydrodynamics code has self-consistently followed the formation of tens of primordial stars and their associated H II regions to the formation of an early dwarf galaxy.

We first demonstrated our code in the article “The H II Region of a Primordial Star” that was authored by Tom Abel, John Wise, and Greg Bryan in *The Astrophysical Journal: Letters*, 2007, Volume 659, L87. Before the publication of our results, I thoroughly tested the radiative transfer against analytical models of H II regions that propagate through, e.g., a uniform medium or a radially decreasing density profile. I further tested the star formation and feedback algorithm with cosmological initial conditions. For this publication, I conducted the simulation and analysis in its entirety.

Additionally, I am involved in a collaboration with Ralf Kähler, developing a

photo-realistic volume renderer on graphics hardware for astrophysical applications. I created an accurate colormap generator that is based on the blackbody spectrum of the temperature of the rendered gas, which is then convolved with telescopic filters. This method is generalized so that any type of intrinsic spectrum, e.g. $H\alpha$, [O III], can be passed through an arbitrary set of filters. This effectively mimics an actual “observation” of our simulation data. It provides a good physical basis and standard for imaging numerical datasets instead of using an arbitrary colormap. Data can be easily compared between groups with this method. This work was published in the refereed article, “GPU-Assisted Raycasting of Cosmological Adaptive Mesh Refinement Simulations” by Ralf Kähler, John Wise, Tom Abel, and Hans-Christian Hege in the *Proceedings of Volume Graphics 2006*, in which I authored the sections that describe the astrophysical basis and possible applications of our method.

Acknowledgements

First and foremost, I would like to thank my adviser, Tom Abel, for his guidance throughout my graduate career. His enthusiasm for astrophysics is contagious, and I have profited from the positive environment that he creates. The research that composes this thesis would not have been possible without him. I thank my thesis committee, Roger Blandford, Bradley Efron, Robert Wagoner, and Risa Wechsler, for their constructive criticism and involvement in this thesis.

This thesis has also benefited from many useful discussions with my collaborators and scientific peers. I thank Marcelo Alvarez, Greg Bryan, Renyue Cen, Andrés Escala, Ralf Kähler, Richard Klein, Michael Kuhlen, Paul Kunz, Michael Norman, Brian O’Shea, Jeremiah Ostriker, Ralph Pudritz, Darren Reed, Martin Rees, Tom Theuns, Peng Wang, and Naoki Yoshida. The simulations in this thesis were executed mainly on the computers at SLAC for which I appreciate the continuous support from the Scientific Computing and Computing Services (SCCS) group and Stuart Marshall. Furthermore, I could not have made it through these six years without some entertainment outside the office. In my first three years in graduate school at the Pennsylvania State University, I want to thank in particular Simos Konstantinidis, Bret Lehmer, Suvrath Mahadevan, Avi Mandell, Miroslav Mičić, Nikola Milutinović, Kenneth Moody, Dave Morris, Manodeep Sinha, Michael Sipior, Britton Smith, Junfeng Wang, and the whole international crew. At Stanford, the people I thank are Teddy Cheung, Fabio Iocco, Ji-hoon Kim, Kevin Schlaufman, Matthew Turk, and Fen Zhao. I have also been lucky to live close to fantastic mountain roads in both Central PA and the Bay Area on which I have enjoyed “spirited” driving in my rotary sports cars.

I would like to thank my parents for supporting me in whatever I please to do and encouraging me to always to try my best and to never give up. Even though they can't read this, the attention and compassion that my two cats, Jeremy and Sampson, give me after everyday helped me make it through graduate school. Most importantly, I thank Emily Alicea-Muñoz for being with me and loving me for the last few years and for making me smile and laugh in even the toughest moments and hopefully many more to come.

Contents

Abstract	iv
Preface	v
Acknowledgements	ix
1 Introduction	1
1.1 The Foundation of Galaxy Formation Theories	1
1.2 Galaxy Formation prior to Dark Matter Cosmogonies	3
1.2.1 Growth and Dampening of Perturbations	5
1.2.2 Tidal Torque Theory	10
1.3 Galaxy Formation with Cold Dark Matter	11
1.3.1 Observational Motivation and Evidence	12
1.3.2 Hierarchical Structure Formation	14
1.3.3 Biased Galaxy Formation	16
1.3.4 Semi-Analytic Models	17
1.4 Molecular Hydrogen Cooling	18
1.5 Computational Techniques	20
1.5.1 Gravity Solvers	21
1.5.2 Hydrodynamics Solvers	23
1.5.3 Additional Physical Models	25
1.5.4 Applications	27
1.6 Thesis Overview	28

2	Number of Primordial Supernovae	30
2.1	Introduction	31
2.2	The Method	33
2.2.1	Minihalo Star Formation	34
2.2.2	Star Formation in Protogalaxies	35
2.2.3	Clumping Factor	39
2.2.4	The Evolution of UV Background and Halo Densities	41
2.3	Results	44
2.3.1	Optical Depth to Electron Scattering	44
2.3.2	Primordial Supernovae Rates	47
2.3.3	Magnitudes and Observability	49
2.4	Discussion	52
2.5	Summary	56
3	Baryonic Virialization	58
3.1	Introduction	59
3.2	The Simulations	62
3.3	Virial Analysis	65
3.3.1	Local Analysis	67
3.3.2	Variations in the Virial Shock	74
3.3.3	Virial Heating and Turbulence	76
3.4	Velocity Distributions	77
3.4.1	Halo and Filament Contrasts	80
3.4.2	Turbulence	80
3.5	Discussion	84
3.5.1	Pop III Feedback	86
3.6	Summary	87
4	Central Gas Collapse	88
4.1	Motivation & Previous Work	89
4.2	Simulation Techniques	92
4.3	Results	96

4.3.1	Halo Collapse	96
4.3.2	Turbulence	102
4.3.3	Spin Parameter Evolution	105
4.3.4	Global Disk	107
4.3.5	Instability of Maclaurin Spheroids	107
4.3.6	Rotational Instabilities	110
4.3.7	Rotational Properties	111
4.4	Discussion	115
4.4.1	Secular Instabilities	115
4.4.2	The Fate of the Central Object	116
4.4.3	The Role of Low Angular Momentum Gas	117
4.4.4	Applicability	118
4.5	Conclusions	120
5	Suppression of H₂ Cooling in the UVB	122
5.1	Motivation	123
5.2	Simulations and Assumptions	126
5.2.1	Virial Temperature	128
5.3	Results	128
5.3.1	Halo Properties	130
5.3.2	Comparison to Previous Studies	133
5.4	Discussion	134
5.4.1	The Nature of the UVB	134
5.4.2	H ₂ Cooling within a UVB	136
5.4.3	Impact on Semi-analytic Models	137
5.5	Summary	139
6	The Nature of Early Dwarf Galaxies	141
6.1	Motivation	142
6.2	Radiation Hydrodynamical Simulations	145
6.2.1	Simulation Setup	146
6.2.2	Star Formation Recipe	147

6.2.3	Radiative Transfer	149
6.3	Results	150
6.3.1	Number of Star Forming Halos	151
6.3.2	Global Nature of Objects	152
6.3.3	ISM Phases	156
6.3.4	Metallicity	157
6.3.5	Metal-enriched Star Formation History	162
6.4	Discussion	163
6.5	Summary	166
7	The Beginning of Reionization	168
7.1	Motivation	169
7.2	Radiation Hydrodynamical Simulations	171
7.3	Star Formation	174
7.3.1	Star Formation Rate	175
7.3.2	Star Forming Halo Masses	177
7.3.3	Star Formation Environments	180
7.4	Starting Cosmological Reionization	182
7.4.1	UV Emissivity	185
7.4.2	Effective Number of Ionizations per UV Photon	186
7.4.3	Clumping Factor Evolution	188
7.4.4	Kinetic Energy Feedback	190
7.4.5	Thermal Energy	193
7.5	Discussion	196
7.5.1	Comparison to Previous Models	197
7.5.2	Potential Caveats and Future Directions	202
7.6	Summary	204
8	Conclusions and Future Work	207
8.1	Supernovae from Primordial Stars	208
8.2	Galaxy Formation without Molecular Hydrogen	209
8.3	Importance of Molecular Hydrogen	210

8.4	Primordial Stellar Feedback and the First Galaxies	211
8.5	Starting Cosmological Reionization	212
8.6	Future Work	213
	Bibliography	216

List of Tables

2.1	Ionizing luminosities for metal-poor IMFs	37
2.2	Gaussian fits to M_{\min} for the main models	46
3.1	Simulation Parameters	64
3.2	Halo Properties	70
4.1	Simulation Parameters	94
4.2	Halos of interest	95
5.1	Simulation Properties	127
6.1	Simulation Parameters	146
6.2	Global halo properties with star formation	151
7.1	Simulation Parameters	172
7.2	Selected Star Forming Halo Parameters	180

List of Figures

1.1	Density Perturbation Evolution	8
1.2	Variance of Density Fluctuations	9
1.3	Cooling Function for Metal-free Gas	15
2.1	Clumping Factor	39
2.2	Sawtooth Spectrum in the Lyman-Werner band	43
2.3	Primordial SNe rates	45
2.4	Evolution of ionized filling factors	48
2.5	Earliest epoch of negative feedback	49
2.6	Primordial SNe Luminosities	50
2.7	Primordial SNe Observability	51
3.1	Radial profiles of energies in the virial theorem	68
3.2	Density and Enclosed Gas Mass Profiles	69
3.3	Entropy and Density Projections	75
3.4	Velocity Distributions	79
3.5	Velocity Convergence	82
3.6	Vorticity	83
4.1	Overview of density structures in a collapsing halo	97
4.2	Bonner-Ebert mass	98
4.3	Electron fraction and temperature of a collapsing halo	99
4.4	Radial profiles at large scales	100
4.5	Radial profiles at small scales	101

4.6	Infall times	103
4.7	Turbulent Mach Numbers	104
4.8	Evolution of the spin parameter	106
4.9	Secular instability timescale	109
4.10	Rotational instability parameter	110
4.11	Radial profiles of rotational quantities at large scale	112
4.12	Radial profiles of rotational quantities at small scale	113
5.1	Dwarf Galaxy Progenitor Abundances	124
5.2	Density and Temperature Projections	129
5.3	Collapsing Halo Properties	131
5.4	Temperature and Electron Fraction Radial Profiles	132
5.5	H ₂ Formation Conditions with an Ultraviolet Background	138
6.1	Density and Temperature Projections of Simulation A	153
6.2	Density and Temperature Projections of Simulation B	154
6.3	Dwarf Galaxy Radial Profiles	156
6.4	Density–Temperature Phase Diagrams	158
6.5	Phase Diagram after a Supernova	159
6.6	Phase Diagram with Metallicity	160
6.7	Phase Diagram with Metallicity after a Supernova	161
6.8	Star Formation History with Supernovae	162
7.1	Cumulative star formation rate	175
7.2	Star formation rate	176
7.3	Star formation history versus halo mass	178
7.4	Radial profiles of star forming regions	179
7.5	Density and temperature profiles of simulation A	183
7.6	Density and temperature profiles of simulation B	184
7.7	Volume-averaged emissivity and ionization fractions	185
7.8	Effective ionizations per UV photon	187
7.9	Clumping factor evolution	188

7.10 Ionized clumping factor evolution	190
7.11 Maximum halo mass for baryon expulsion	193
7.12 Volume-averaged temperature	194
7.13 Mass-averaged temperature	196
7.14 Jeans filtering mass and averaged temperature in ionized regions . . .	197
7.15 Anisotropic H IIregion	201

Chapter 1

Introduction

“When judging a physical theory, I ask myself whether I would have made the Universe in that way had I been God”

— Albert Einstein

Pulchritudo splendor veritatis. (Beauty is the splendor of truth.)

It is human nature to be inquisitive of nature, which is the basis of science in general. Countless people have asked the long-standing question, *what is the origin of our world?* Philosophers dating back to ancient times have pondered this exact question in detail. As evidence grew that the universe is not geocentric, the scope of this stimulating question then grew to the origin of the Milky Way, which is ultimately influenced by the nature of the universe. This progression to the largest scales leads us to the topic of cosmology, the study of the universe in its entirety.

1.1 The Foundation of Galaxy Formation Theories

Galaxy formation plays an important role in any cosmological theory that must explain the observed dynamics and structures in the local and distant universe. We begin with a historical overview¹ of cosmological, in particular galaxy formation,

¹The majority of the references in this overview originate from Jones (1976).

theories because it is beneficial to understand how the succession of scientific advancements influences future scientists, which clarifies its current status.

There were two main documented views of cosmology in ancient Greece. Even two thousand and three hundred years later, the following philosophies have modern counterparts. The Epicurean view entailed the universe beginning chaotic from which order arose by some means, which parallels with the cosmic turbulence theory of galaxy formation. Aristotle pictured the universe as initially uniform and orderly, and departures from this state increase with time. This philosophy is strikingly similar to the gravitational instability theory of galaxy formation.

Perhaps the birth of the study of galaxies is the discovery of spiral structures in nebulae by Lord Rosse (1850a,b). At the time, all nebulae were believed to exist within the galaxy, so this instigated further work on the origins of the solar system. Alexander (1852) realized that this observation was evidence for Laplace's nebulae hypothesis (1799) that envisaged the Sun forming from a hot, tenuous gas cloud that is nearly spherical and rotating like a solid body (see Aitken, 1906, for a review). Self-gravity causes a gravitational contraction that continues until the system is rotationally supported at its surface. He postulated that an equatorial ring was left behind at this stage, and the collapse continues. This repeats as necessary to create several rings that are not in dynamical equilibrium, and individual rings then aggregate into planets. Alexander also suggested that the initial angular momentum may differentiate "elliptical nebulae" and "spiral nebulae"; unfortunately, this did not spark any further investigations.

The next spurring moment in the history of galaxy formation models was the publication of the first photographs of galaxies (Roberts, 1889; Keeler, 1900) that incited many theories about the formation of the observed structures (e.g. Chamberlain, 1901; Jeans, 1902; Sutherland, 1911). The nebulae hypothesis was the main underlying of these works. This is where Jeans formulated the conditions necessary for a cloud to gravitationally overcome pressure forces, i.e. the Jeans length. Here he invoked his theory to suggest that the gas cloud fragments into planets.

The last foundation established for galaxy formation was the actual discovery by Hubble of the extragalactic nature of these spiral nebulae (Hubble, 1925a,b,c). Now

previous theories had to be reformulated to length scales five orders of magnitude larger and applied to billions of stars instead of one. Jeans (1918, 1928) now applied his theory of gravitational collapse to cosmological scales, theorizing that galaxies formed from gravitational instabilities in an initially uniform universe. This is the main foundation for the gravitational instability picture of galaxy formation that has dominated modern cosmology theories. Hubble (1929) then discovered that more distant galaxies were receding faster than closer ones – indicative of an expanding universe. Although Jeans did not consider this scenario in his later works, Gamow & Teller (1939), who envisioned the universe as an enormous primeval gas cloud, generalized the collapse problem to an expanding universe, where material fragmented into galaxies that is the basis of modern galaxy formation theories.

1.2 Galaxy Formation prior to Dark Matter Cosmogonies

The gravitational instability picture of galaxy formation was established by Jeans (1918, 1928), in which galaxies grow from initial density perturbations in the early universe. This line of research has dominated the field for the last sixty years.

To illustrate Jeans’ theory, consider an isolated, uniform gas cloud within a gravitational potential. The potential can be either be generated by the gas itself or some other concentric system (e.g. a dark matter halo). Jeans postulated for the system to collapse, its gravitational forces must overcome pressure forces. For this condition to be valid, we use the virial theorem of the system, neglecting any bulk motions or magnetic fields,

$$\begin{aligned} \langle E \rangle_{\text{grav}} &> -2\langle E \rangle_{\text{kin}} \\ \frac{3}{5} \frac{GM^2}{R} &> 3NkT \end{aligned} \tag{1.1}$$

where G and k are the gravitational and Boltzmann’s constant, respectively. Here M , R , $N = M/\mu m_{\text{H}}$, and T are the mass, radius, total particle number, and temperature

of the system, where m_{H} and μ is the mass of a hydrogen atom and mean molecular weight in units of m_{H} , respectively. After some simple algebra and putting the mass in terms of radius and density ρ , we arrive at the length scale,

$$L_J = \sqrt{\frac{15kT}{4\pi G\mu m_{\text{H}}\rho}}, \quad (1.2)$$

the Jeans' length, that a system becomes unstable to collapse. Similarly the Jeans' mass

$$M_J = \frac{4\pi}{3}\rho L_J^3 \propto T^{3/2}\rho^{-1/2} \quad (1.3)$$

is the critical mass of a system that gravitationally collapses. For collisionless dark matter, the temperature can be replaced by a term proportional to the velocity dispersion squared, v^2 .

Before further focusing on this preferred theory, we note that there was the parallel effort of cosmic turbulence that attempted to explain galaxy formation from an initial turbulent medium. It was applied to the formation of the solar system, galactic dynamics, and galaxy formation (von Weizsäcker, 1943, 1948; Heisenberg & von Weizsäcker, 1948). However, there were some concerns expressed by Gamow (1952) and Bonnor (1956) about the necessity of ab initio turbulence. The cosmic turbulence theory model dropped out of favor in the 1950's for the gravitational instability theory but had a brief resurgence a decade later by the Ozernoi group (e.g. Ozernoi & Chernin, 1968a,b; Ozernoi & Chibisov, 1971) after the discovery of the cosmic microwave background (CMB).

Now we focus back on the gravitational instability theory. There lies a difficulty in this theory in that there is no exact solution to this cosmological problem if there are no special symmetries. Nevertheless at early times in the universe, the growth of structure can be computed using linear perturbation theory that evolves the initial density fluctuations until they reach overdensities, $\delta \equiv \rho/\bar{\rho}$, approach unity, which we explore next.

1.2.1 Growth and Dampening of Perturbations

The growth of adiabatic perturbations in an expanding universe was first calculated by Lifschitz (1946). Two decades later, the CMB was discovered and measured to be ~ 3.5 K (Penzias & Wilson, 1965). This background was predicted in the seminal papers of Gamow (1946) and Alpher, Bethe, & Gamow (1948), which outlined a cosmogony starting with a hot Big Bang. After this discovery, galaxy formation models and the associated growth of perturbations were formulated in this new cosmological model (Peebles, 1965, being the first of many).

The growth of structure can be understood by three scales. Firstly, the horizon length scale ($R_H = ct$) determines the amount of matter

$$M_H = \frac{1}{6} \pi \rho(ct)^3 \quad (1.4)$$

that is causally connected. Secondly, the Jeans length scale (eq. 1.2) determines the scales that can gravitationally collapse. Lastly at $l \ll L_J$, perturbations are subjected to dissipative forces, such as Thomson drag forces and viscosity, and act as acoustic modes.

Ignoring any inhomogeneities on small scales, Einstein's general relativistic equations can describe the dynamics of an isotropic and homogeneous universe, using the Robertson-Walker metric,

$$ds^2 = dt^2 - a^2(t) \left[\frac{dr^2}{1 - kr^2} + r^2(d\theta^2 + \sin^2 \theta d\phi^2) \right], \quad (1.5)$$

where $a = (1 + z)^{-1}$ is the scale factor that describes the expansion of the universe, k describes the curvature of the universe, and z is the redshift. Appropriate choices for k are 0, -1 , and $+1$ for a flat, open, and closed universes. The solution to Einstein's equations with this metric is the Friedmann equation

$$\frac{k}{a_0^2} = \frac{8\pi G}{3} \rho_0 - H_0^2, \quad (1.6)$$

where the "0" subscripts denotes the present-day values, and $H = \dot{a}/a$ is the Hubble

constant. We can now apply this to the growth of structure.

Before recombination and at sufficiently early times, an adiabatic perturbation will be larger than the horizon scale. The growth rate in this regime can be calculated by comparing a perturbed spherical region to the background universe. In this exercise, the background is a spatially flat Friedmann universe, i.e. $k = 0$, with a density ρ_a . The perturbation can be treated like a closed $k = 1$ universe because the metric of a $k = 1$ universe and a 3-sphere embedded in an abstract 4-dimensional Euclidean space are exactly equal. Its density ρ_b is perturbed with a small and positive displacement $\delta\rho$ from ρ_a . From equation (1.6), we have

$$H_a^2 = \frac{8\pi G}{3}\rho_a; \quad H_b^2 + \frac{1}{a_b^2} = \frac{8\pi G}{3}\rho_b. \quad (1.7)$$

To calculate the growth of the perturbation $\delta\rho$, we compare the perturbation to its background when the expansion rates are equal, $H_a = H_b$ at a given time. This results in the relation

$$\left(\frac{\rho_b - \rho_a}{\rho_a}\right) = \frac{\delta\rho}{\rho_a} = \frac{3}{8\pi G\rho_a a_b^2} \quad (1.8)$$

We want the evolution of $\delta\rho$ in terms of a . We therefore state the density of the universe in terms of the scale factor. In a radiation dominated universe, $\rho \propto a^{-4}$, and in a matter dominated universe, $\rho \propto a^{-3}$. Combining these proportionalities with equation (1.8), we obtain

$$\frac{\delta\rho}{\rho} \propto \begin{cases} a^2 & (\text{radiation dominated}) \\ a & (\text{matter dominated}) \end{cases}. \quad (1.9)$$

Once the density perturbation enters the horizon scale, it can be suppressed by two processes. The first suppresses it by pressure support that was discussed previously. The system is pressure supported when $t_{\text{pressure}} > t_{\text{dyn}}$ or equivalently

$$\frac{L_J}{c_s} < \sqrt{\frac{1}{G\rho_{\text{dom}}}}. \quad (1.10)$$

Here the “dom” subscript denotes the dominant mass-energy component of the universe at a given scale factor, and c_s is the sound speed. If matter is non-relativistic, the velocity v decays as a^{-1} because of the redshifting of momentum; otherwise it is constant. The second process suppresses the growth when the expansion timescale, $t_{\text{exp}} \sim (G\rho_{\text{dom}})^{-1/2}$, is less than the collapse timescale, which is particularly true in the radiation dominated phase.

Now we consider the case when a perturbation enters the horizon scale when the background is relativistic and radiation dominated. The Jeans length is first affected by the momentum redshifting when matter is relativistic, and afterwards it follows the growth in a radiation dominated universe, $\rho \propto a^{-4}$. When it enters the matter dominated phase, $\rho \propto a^{-3}$. Putting this all together, we have

$$L_J \propto \frac{v}{\rho_{\text{dom}}^{1/2}} \propto \begin{cases} a^2 & \text{(relativistic)} \\ a & \text{(radiation dominated)} \\ a^{1/2} & \text{(matter dominated)} \end{cases} . \quad (1.11)$$

Analogously the Jeans mass scales as

$$M_J \propto \rho_{\text{DM}} L_J^3 \propto \begin{cases} a^2 & \text{(relativistic)} \\ \text{constant} & \text{(radiation dominated)} \\ a^{-3/2} & \text{(matter dominated)} \end{cases} . \quad (1.12)$$

Figure 1.1 shows the evolution of M_J and M_H .

Baryons behave similarly to dark matter with the major exception of a significant drop in L_J at recombination at $z \sim 1100$ when the temperature drops to 3000 K in approximately 20% of the Hubble time. After recombination, baryons are regulated by gas pressure instead of photon pressure. This causes the pressure to drop by a factor $n_\gamma/n_b \sim 10^9$, and the Jeans length decreases by a similar factor.

Density perturbations come in two major types: adiabatic and isothermal. The former type retain a particular entropy and behave like sound waves with equal photon and baryon fluctuations. These perturbations do not grow before recombination. Additionally they are damped below a mass scale $\sim 10^{12} M_\odot$ because of Thomson

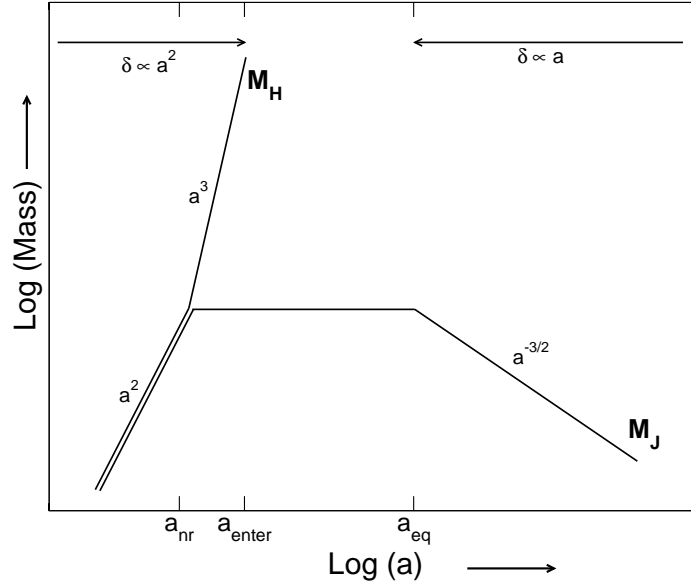


Fig. 1.1.— The evolution of a density perturbation in the early universe. The scale factors a_{nr} , a_{enter} , and a_{eq} denote when matter becomes non-relativistic, enters the horizon, and decouples from radiation. This figure has been adapted from figure 4.1 in Padmanabhan (1993).

drag forces, i.e. photon viscosity (Silk, 1974). The latter type are density fluctuations immersed in a photon bath and do not conserve entropy. They cannot grow in amplitude before recombination because they are coupled with radiation. After recombination, the Jeans mass is $\sim 10^5 M_{\odot}$ in a Einstein-deSitter (EdS) universe. Both types of fluctuations result in a smaller mass scales becoming non-linear earlier, which is represented by the baryon fluctuation spectrum

$$\left(\frac{\delta\rho}{\rho}\right)_{\text{baryon}} \propto M^{-1/3-n/6}. \quad (1.13)$$

But as stated before, mass scales below $10^{12} M_{\odot}$ are suppressed in adiabatic fluctuations.

The physical picture painted by these two types of baryon fluctuations differ

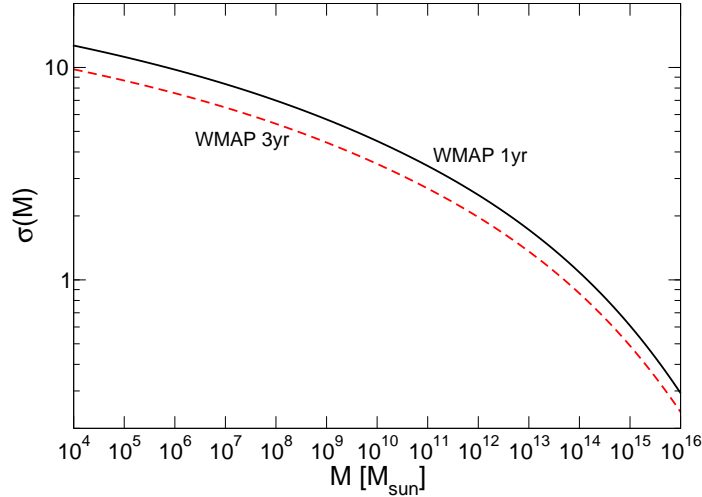


Fig. 1.2.— The variance of density fluctuations as a function of smoothing mass for first (*black solid*) and third (*red dashed*) year results from WMAP.

greatly in nature. Adiabatic ones create a scenario of top-down structure formation, in which objects that are large as galaxy clusters form first then fragment to form galaxies through Jeans instabilities in “pancake” overdensities (Doroshkevich et al., 1974). Isothermal fluctuations produce a bottom-up scenario of structure formation, where smaller objects form first and combine to form larger entities (Peebles, 1974). An analysis of the covariance function of galaxies provides evidence for the latter scenario because there is no preferred mass scale (Totsuji & Kihara, 1969; Peebles, 1974). Conversely, one would expect a strong feature at $\sim 10^{12} M_{\odot}$ for a $\Omega = 1$ universe if structure had formed top-down. Furthermore, the three-point correlation function of galaxies indicates that they are hierarchically clustered (Peebles & Groth, 1975).

Density perturbations may exist on all scales and follow a random Gaussian distribution; therefore it is useful to consider the statistics of a smoothed density field. The power spectrum of perturbations $P(k)$ that is extrapolated to $z = 0$ is smoothed with a top-hat filter, whose Fourier transform is

$$\tilde{W}(x) = \frac{3(\sin x - x \cos x)}{x^3}. \quad (1.14)$$

The resulting variance of the fluctuations at $z = 0$ is

$$\sigma^2(R) = \frac{1}{2\pi^2} \int_0^\infty dk k^2 P(k) \tilde{W}^2(kR). \quad (1.15)$$

This is usually normalized to the variance of fluctuations σ_8 in a sphere with a radius $8 h^{-1}$ Mpc that is derived from galaxy clusters and the CMB. Figure 1.2 shows $\sigma(M)$ for cosmological parameters determined from the first and third year CMB data of the Wilkinson Microwave Anisotropy Probe (WMAP; Spergel et al., 2003, 2006). In linear perturbation theory, a top-hat collapses to a point when the overdensity $\delta_c = 1.686$ (Peebles, 1993) that can be extrapolated to redshift z by $\delta_{\text{crit}}(z) = \delta_c/D(z)$, where $D(z)$ is the growth factor for linear perturbations. It is customary to express the rarity of a collapse with $\delta_{\text{crit}}(z)$ in units of $\sigma(M)$, i.e. a 3σ fluctuation being more rare than a typical 1σ one.

1.2.2 Tidal Torque Theory

A previously outstanding problem in structure formation was the acquisition of angular momentum that results in the universal rotation in spiral galaxies. How did it arise from an expanding, almost uniform, universe in a way that angular momentum is conserved? Kelvin’s circulation theorem states that an irrotational system must remain irrotational in the absence of dissipative forces, which is true when structure is growing linearly. During the collapse of protogalactic gas clouds, there are certainly dissipative forces and thus Kelvin’s theorem is inapplicable. This is also true in relaxing stellar systems (i.e. violent relaxation; Lynden-Bell, 1967).

Angular momentum must exist before galaxies formed. One might conclude that there was an original vorticity field in the universe, but Hoyle (1949) and Peebles (1969) independently suggested that tidal torques from neighboring conglomerations induced galactic spins. Within the gravitational instability theory, tidal torques have its greatest influence on protogalactic clouds when they decouple from the Hubble flow (“turn-around”). When the overdensity turns around, the radius is largest and $\delta\rho/\rho = 1$. The tidal torques do not violate angular momentum conservation as the two systems gain orbital energy that is equal and opposite of the induced spins. We

note, however, that both early analytic and numerical work by Peebles (1969, 1971) and Efstathiou & Jones (1979) showed that there is a deficiency of a factor of 5 in the predicted amount of angular momentum in the Milky Way when compared with the observation of Innanen (1966).

Peebles (1969) predicted that the spin parameter,

$$\lambda \equiv \frac{|L|\sqrt{|E|}}{GM^{5/2}}, \quad (1.16)$$

which measures the net rotation of a halo, has a cosmological average of ~ 0.08 . He verified this through numerical simulations of a cosmologically expanding system. Here L , E , and M are the angular momentum, energy, and mass of the object. During the clustering of systems, most of the angular momentum is acquired during its early assembly. Linear perturbation theory predicts that this angular momentum scales as $a^{5/2} \propto t^{5/3}$. Efstathiou & Jones (1979) confirmed the results of Peebles with higher resolution n -body simulations and also concluded that galactic discs must have dissipated a large amount of energy during the collapse from a large initial radius. More recent n -body simulations and analytical works (e.g. Barnes & Efstathiou, 1987; Steinmetz & Bartelmann, 1995) have constrained $\langle \lambda \rangle \approx 0.04$, and later it was found to have a log-normal distribution

$$p(\lambda)d\lambda = \frac{1}{\sigma_\lambda\sqrt{2\pi}} \exp\left[-\frac{\ln^2(\lambda/\lambda_0)}{2\sigma_\lambda}\right] \frac{d\lambda}{\lambda}, \quad (1.17)$$

where $\lambda_0 = 0.042 \pm 0.006$ and $\sigma_\lambda = 0.5 \pm 0.04$ (e.g. Bullock et al., 2001) in a CDM universe that has become the currently favored model. We discuss the nature of galaxy formation in such a universe next.

1.3 Galaxy Formation with Cold Dark Matter

By the 1980's, there was growing evidence that the universe was dominated by cold dark matter (CDM) that hierarchically assembles cosmic structure. CDM is collisionless and has a thermal velocity smaller than peculiar velocities and the Hubble flow

(see Blumenthal et al., 1984). The best candidate for CDM are weakly-interacting massive particles (WIMPs)², whose radiation from annihilation may be detected by the *Gamma-ray Large-Area Space Telescope* (GLAST; Gehrels & Michelson, 1999).

Previously popular theories of dark matter include hot DM that is composed of light neutrinos ($m \sim 30$ eV) and warm DM that is composed of more massive ($m \sim 1$ keV) neutrinos.

1.3.1 Observational Motivation and Evidence

The ultimate goal of galaxy formation theories is to explain the origin and properties of all galaxies. It is thus necessary to connect and test theories with observations. Jones (1976) gives a list of five broad characteristics of galaxies that can be tested against, which is still relevant 30 years later.

1. The masses of galaxies, galactic internal dynamics, interacting galaxies, dynamics of groups, aggregation of galaxy clusters, galaxy luminosity function.
2. The angular momenta and binding energies of galaxies
3. The origin of different morphologies of galaxies
4. The clustering of galaxies
5. An explanation of how young galaxies, if not all galaxies, form early in the universe.

Dark Matter

Zwicky (1933) observed that the galaxies in the Coma cluster were moving faster than the velocity dispersion of a system, $\sigma^2 = GM/R$, with a mass of the observed material. This prompted the “missing mass” problem in galaxy clusters. Further evidence accumulated when the rotation velocity of M31 was observed to be constant with radius out to 24 kpc (Rubin & Ford, 1970). Observations established that there

²For a recent review of detection techniques, see Wai (2007)

was a dark component to the universe, whereas its mass and nature can be constrained by comparing observations with galaxy formation models.

Mass scales below 10^{11} and 10^{15} solar masses are suppressed in warm and hot DM cosmologies, respectively, because the neutrinos freely stream from the perturbation when it enters the horizon. To explain the multitude of galaxies below these scales, structure must have formed “top-down” as in the case of adiabatic perturbations. Hot DM models predict that galaxy clusters form first at $z \sim 2$ with smaller objects fragmenting from them, conflicting with the ages of globular clusters, stellar ages in galaxies, and dwarf galaxies. Warm DM models are slightly more successful in this respect but still cannot account for the properties and abundances of dwarf galaxies. In contrast, the “bottom-up” structure formation model of CDM explains the properties of galaxies and galaxy clusters over a mass range from 10^7 to $10^{15} M_{\odot}$.

Galaxies

Hubble (1926) first categorized the morphologies of galaxies into elliptical, spiral, S0, and irregular types. He also realized that the surface brightness of elliptical galaxies is approximated well by a decreasing function, $I(r) = I_0/(1 + r/r_0)^2$, where r_0 is a scale length. de Vaucouleurs (1959) provided another good fit with an exponentially decreasing function that is proportional to $\exp(r^{1/4})$. However, these fits deviated in the centers of galaxies, and the surface brightness was dynamically modeled by King (1966), who considered a Maxwellian velocity distribution of the stars and a tidal cutoff radius. Combining all of the previous works, Faber & Jackson (1976) then showed that the luminosity of elliptical galaxies $L \propto \sigma^4$, now referred to as the Faber-Jackson relation. A similar relation for spiral and S0 galaxies was established by Tully & Fisher (1977), $L \propto V_c^4$, where V_c is the rotational velocity of the disk.

However, there are peculiar outliers in galaxy catalogs that do not fit with any of the above categorizations. There are approximately 10 galaxies out of ~ 4000 NGC galaxies that are undergoing mergers or close encounters. Toomre & Toomre (1972) proposed that there had been a total of ~ 500 collisions in the NGC sample throughout the history of the universe, based on their numerical simulations of spiral galaxy mergers that resulted in an elliptical object. From this, they suggested that

this could explain the ~ 400 ellipticals in the catalog. In the next section, we will discuss hierarchical clustering that induces these mergers.

We can also use the abundances and clustering of galaxies to refine and develop galaxy formation models. For the former, the abundances of galaxies can be characterized with a luminosity function in the form,

$$\Phi(L)dL = \Phi_* \left(\frac{L}{L_*}\right)^\alpha \exp\left(-\frac{L}{L_*}\right) \frac{dL}{L_*}, \quad (1.18)$$

where L is the luminosity of the galaxy, $L_* \approx 4 \times 10^{10} L_\odot$, $\alpha \approx -1$, and Φ_* is the number of galaxies per Mpc^{-3} at the characteristic luminosity (Schechter, 1976). This predicts that low-luminosity galaxies are extremely abundant with an exponential cutoff at high luminosities. This was first formulated for galaxies in rich clusters, but later it has been confirmed to apply to all galaxies (e.g. Moore et al., 1993; Benson et al., 2003). The clustering of galaxies are explained by hierarchical assembly that is the next topic in the introduction.

1.3.2 Hierarchical Structure Formation

Structure in a CDM cosmogony forms hierarchically, and this was first proposed, albeit not in a CDM context, by Peebles (1965). Smaller objects collapse first and merge with other objects to form larger cosmological halos, and matter organizes in a self-similar nature that grows with the scale factor. White & Rees (1978) were the first to consider galaxies forming within a hierarchical clustering of “heavy halos”, where the baryons are not the dominate source of gravity. During the initial collapse of the protogalactic cloud, baryons are shock-heated to the virial temperature,

$$T_{\text{vir}} = \frac{\mu m_h V_c^2}{2k}, \quad (1.19)$$

where

$$V_c = \sqrt{\frac{GM}{r_{200}}} \quad \text{and} \quad r_{200} = \left[\frac{GM}{100\Omega_{\text{CDM}}(z)H^2(z)} \right]^{1/3}, \quad (1.20)$$

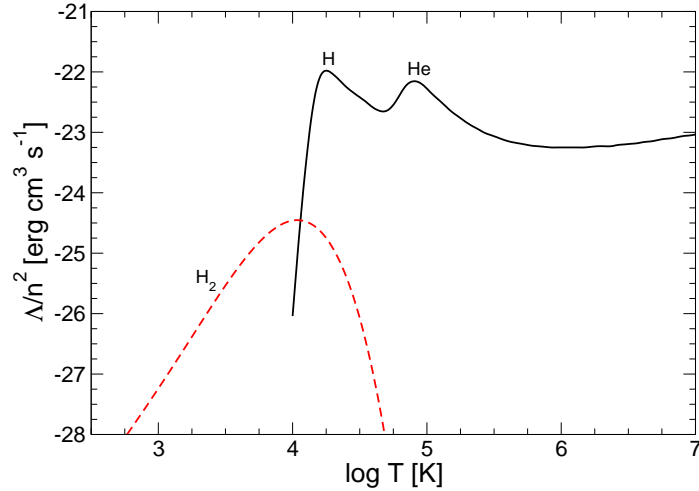


Fig. 1.3.— The cooling function for atomic line cooling of metal-free gas (*black solid*) and cooling from H_2 formation in the gas phase (*red dashed*). The humps in the atomic cooling function at $10^{4.3}$ K and 10^5 K are created by excitations of hydrogen and helium, respectively. The cooling rates are taken from Sutherland & Dopita (1993) and Galli & Palla (1998) for the atomic and molecular cases, respectively.

are the circular velocity of the halo and r_{200} is the radius enclosing an average DM overdensity of 200. Here Ω_{CDM} is the mass-energy fraction of CDM in units of the critical density $\rho_c = 3H_0^2/8\pi G$. The first galaxies to form have $T_{\text{vir}} > 10^4$ K because the cooling function of pristine atomic gas sharply rises by several orders of magnitude. At this temperature, the number of free electrons able to excite hydrogen greatly increases, and these excitations cool the gas (Spitzer, 1978). We plot the cooling function for pristine, metal-free gas in Figure 1.3. Only when the gas can cool efficiently ($t_{\text{dyn}} > t_{\text{cool}}$), the gas is able to radiate its energy away and rapidly collapse on a free-fall time (Rees & Ostriker, 1977). Based on the same timescale argument, objects above $10^{13} M_\odot$ have virial temperatures 4×10^6 K, where the gas cannot cool within a Hubble time. This can explain the sharp cutoff in the galaxy luminosity function above $10^{13} M_\odot$. Additionally this explains the hot, X-ray emitting gas in galaxy clusters.

White & Rees (1978) also proposed that galaxies forming by hierarchical assembly will likely have an imprint on present-day galaxies. As halos merge together, they

suggested that the outer layers of low-mass halos are stripped during the virialization of the parent halo on a timescale greater than a dynamical time t_{dyn} . Since low-mass galaxies merge together to form Milky Way type galaxies, the luminous cores of low-mass galaxies may survive to the present-day and exist in identifiable stellar systems. Additionally, some fraction of dwarf galaxies may have formed in the early universe (see Mateo, 1998). Numerical calculations and cosmological simulations show that CDM models with hierarchical clustering can account for the abundances and characteristics of both galaxies and clusters (e.g. Peebles, 1982; Springel et al., 2005). However, one must consider feedback effects in low-mass galaxies to correctly describe galaxies across the mass spectrum.

1.3.3 Biased Galaxy Formation

Dark matter constitutes more than 80% of matter in the universe (Spergel et al., 2006) and dominates the gravitational potential field of large-scale structure and individual halos. It is important to quantify how galaxies and baryons trace these potential wells. There is a “bias” in galaxies in that galactic properties depend on the formation environment (Dekel & Rees, 1987). Higher σ objects collapse earlier and form in a different environment than lower σ peaks of the same mass. Since $\bar{\rho}(z) \propto (1+z)^3$, the timescales of the cooling and dynamical processes differ at higher redshift as they scale with ρ^{-1} and $\rho^{-1/2}$, respectively. Additionally for $z > 10$, Compton cooling can be dominant in ionized regions, in which the cooling time $t_C \propto f_e^{-1}(1+z)^{-4}$, where f_e is the electron fraction.

There is also bias in the suppression of galaxy formation from stellar feedback and intergalactic medium (IGM) heating. As low-mass galaxies ($M \sim 10^8 M_\odot$) are more susceptible to stellar feedback and outflow, the ultraviolet (UV) heating of the IGM from stellar sources may inhibit gravitational collapse and star formation in such galaxies. Earlier forming galaxies are affected less than their lower- σ counterparts since the UV radiation background, which affects cooling rates and can photo-evaporate small gas clouds, steadily grows with time. The clustering of halos also biases galaxy formation, which is very relevant for the first stars and galaxies.

This creates biasing in most feedback processes in these first structures because there could be more nearby stars. This could lead to the observed differences in the galaxy-environment correlation (Dekel & Rees, 1987).

1.3.4 Semi-Analytic Models

Semi-analytic galaxy formation models (e.g. Somerville & Primack, 1999; Benson et al., 2000; Cole et al., 2000) are an alternative to studying galaxy formation with explicit numerical cosmological simulations. The philosophy of their methods originated from the works of White & Rees (1978), White & Frenk (1991), Cole (1991), and Lacey & Silk (1991). They use simplistic models of baryon physics and star formation that are set in a dark matter merger tree that is usually produced by extended Press-Schechter formalism (Press & Schechter, 1974; Bond et al., 1991; Lacey & Cole, 1993). Density profiles and spins of dark matter halos in the merger tree are accurately represented statistically by results of numerical simulations (Navarro et al., 1997; Bullock et al., 2001). Some of the simplifications are however justified as some processes, in particular star formation and feedback, are not well understood. Furthermore, most of the free parameters are tuned to match observations and analytics, which allows the application of this method to other poorly understood galaxy populations.

One main ingredient in semi-analytic models is disc formation. Motivated by the observation that the Milky Way formed from a gaseous collapse (Eggen et al., 1962) and tidal torque theory (Hoyle, 1949; Peebles, 1969), Fall & Efstathiou (1980) investigated the properties of disc formation in the collapse of a slowly rotating cloud within a “heavy halo”, i.e. dark matter dominated. The system rotates like a solid-body, i.e. $v \propto r$, in that all of the small-scale kinetic motions have been dissipated into heat, which is represented by the spin parameter λ (eq. 1.16). The resulting disc model agrees remarkably well with observations, in particular the exponentially decreasing surface density. These models were improved by Mo et al. (1998), who embed the collapsing gas cloud in a more accurate dark matter density profile (Navarro et al., 1997). Furthermore, they only allow discs to form if they are dynamical stable against bar

formation (see Christodoulou et al., 1995, and references therein) that results in an excellent match with the Tully-Fisher relation. Many modern semi-analytic models use the formalism of Mo et al. (1998) for disc formation.

Semi-analytic models of galaxy formation have been broadly successful in reproducing a large range of galaxy properties and their evolution. They have successfully reproduced (i) the local field galaxy luminosity function (Kauffmann et al., 1993), (ii) the slope and scatter of the Tully-Fisher relation and the formation of most stars at $z < 1$ (Cole et al., 1994), (iii) the counts and redshift distribution of faint galaxies (Kauffmann et al., 1994), (iv) a sharp decline in elliptical galaxies at high redshift (Kauffmann et al., 1996), and (v) the strong clustering of Lyman break galaxies at $z = 3$ (Wechsler et al., 2001).

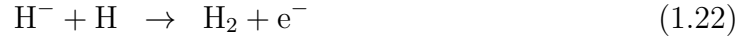
Despite their many accomplishments in galaxy formation, current implementations may lose accuracy in the early universe when star and galaxy formation differed greatly from the properties observed at $z < 6$. In the early universe, the first stars form from metal-free gas, which affects the collapse dynamics of the parent gas cloud and results in a large stellar mass. Thus some of the smallest galaxies may be greatly affected by radiative feedback that originate from these stars. We focus on metal-free Population III (Pop III) star formation in the next section.

1.4 Molecular Hydrogen Cooling in the Early Universe

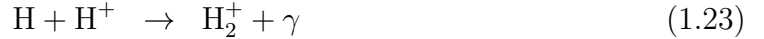
Big bang nucleosynthesis mainly produces hydrogen and helium with only trace amounts of deuterium and lithium (Alpher, Bethe, & Gamow, 1948; Wagoner et al., 1967). The first stars in the universe must have been devoid of heavy elements. However, there is a metallicity floor of 10^{-4} of solar metallicity in Galactic halo stars, residing in the outskirts of the Galaxy (Beers & Christlieb, 2005). This prompts the following questions: *Where are the first stars? What are their properties?* To answer these questions, we describe the collapse and cooling of their parent gas clouds.

Galactic star forming regions condense through molecular hydrogen (H_2) cooling

that mainly occurs on dust grains composed of carbon, silicon, oxygen, iron, and several other elements. This cannot be the case in metal-free, pristine gas. At low metallicities and temperatures above 1000 K, H_2 formation can occur in the gas-phase by two processes (McDowell, 1961):



or less efficiently



Saslaw & Zipoy (1967) were the first to realize that H_2 formation in the gas-phase was important in star formation in the early universe. They used the latter reactions to determine that H_2 cooling dominates the collapse of a pre-galactic cloud above number densities n of 10^4 cm^{-3} . These high density regions can cool to $\sim 300 \text{ K}$ and continue to collapse. Peebles & Dicke (1968) suggested that globular clusters were the first bound objects in the universe with masses $\sim 5 \times 10^5 M_\odot$. In their calculations, they first compute the properties of these objects from linear perturbation theory and then follow the initial contraction of the cloud, including H_2 cooling (eq. 1.21, 1.22). They find that molecular hydrogen cooling is indeed efficient enough to drive a free-fall collapse, in which only a small fraction of the total gas mass forms stars due to the inside-out nature of the collapse. The determination of the properties of Pop III stars ultimately relies on the mass scale on which the structure fragments. Gravitationally induced fragmentation can occur when

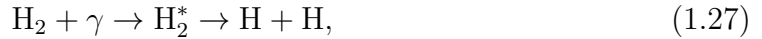
$$\Gamma_{\text{frag}} = 1 + \frac{(d \ln T / dt)}{(d \ln \rho / dt)} < 4/3, \quad (1.25)$$

and thermal instabilities produce fragmentation when

$$\rho \left(\frac{\partial L}{\partial \rho} \right)_T - T \left(\frac{\partial L}{\partial T} \right)_\rho + L(\rho, T) > 0, \quad (1.26)$$

where L is the radiative cooling rate. Yoneyama (1972) followed the evolutionary track of a collapsing primordial gas cloud and found that the central regions fragmented into $60 M_\odot$ clumps (for cloud mass $M = 10^6 M_\odot$), in which he suggested that the first stars were massive.

Molecular hydrogen is photo-dissociated by photons in the Lyman-Werner (LW) band, 11.26 – 13.6 eV (Field et al., 1966; Stecher & Williams, 1967), through the two-step Solomon process,



where H_2^* is an electronically or vibrationally excited state that decays into the continuum state, dissociating the molecule. In this energy band, the universe is optically thin with the exception of Lyman resonances, i.e. $\text{Ly}\alpha$, $\text{Ly}\beta$, etc, resulting in non-local suppression of H_2 formation by a soft UV radiation background. Most Pop III stars will have to contend with such a background. The critical halo mass for a cool, dense core to form increases with the LW radiation background intensity (Machacek et al., 2001) that is the main basis for the results of Chapter 2. We leave the details of stellar and associated supernovae (SNe) properties to the chapter introductions.

1.5 Computational Techniques

The astrophysical community have benefited from numerical cosmology simulations that have matured over the last two decades. They have improved our understanding of the nature of many astrophysical systems. Modern simulation techniques have advanced through both ingenious software algorithms and the continual increase in computing power.

The first gravitational n -body simulation intriguingly was not performed on a

digital computer but by photocells and light bulbs, where the inverse-square law of radiation emulated a gravitational field, to study the interaction of two colliding galaxies (Holmberg, 1941). After the advent of digital computers, the first n -body simulations that computed the dynamics of up to 100 particles were performed in the early 1960's (von Hoerner, 1960, 1963; Aarseth, 1963). A decade later, the first true cosmological simulations of structure formation were carried out to confirm an analytic framework that predicted the abundances of bound objects in the universe (Press & Schechter, 1974). Several advances in cosmology allowed the tremendous growth in activity in the following decade, such as (i) plausible dark models (e.g. CDM, hot DM), (ii) cosmic inflation (Guth, 1981) provided an explanation for the generation of primordial density fluctuations and a scale-invariant Harrison-Zel'dovich spectrum (Harrison, 1970; Zel'dovich, 1972), (iii) evolution of fluctuations during recombination (Peebles & Yu, 1970), and (iv) applications of random Gaussian fields and linear perturbation theory to density fluctuations.

CDM became the favored cosmological model starting in the 1980's (e.g. Peebles, 1982; Blumenthal et al., 1984), and cosmological simulations could readily test this cosmogony and compare it with observations and expectations. In the following years, baryonic physics were added to the calculations, providing access to additional astrophysical problems. First we focus on the techniques to evolve gravity in these simulations. We then detail some hydrodynamics solvers in the succeeding section.

1.5.1 Gravity Solvers

Particle trajectories are evolved in time by solving Newton's laws written in comoving coordinates:

$$\frac{d\mathbf{x}}{dt} = \frac{1}{a}\mathbf{v}, \quad \frac{d\mathbf{v}}{dt} + H\mathbf{v} = \mathbf{g}, \quad \nabla \cdot \mathbf{g} = -4\pi G a[\rho(\mathbf{x}, t) - \bar{\rho}(t)], \quad (1.28)$$

where \mathbf{g} is the gravitational potential field Peebles (1993). The time integration is usually calculated with a second-order accurate leapfrog method (Efstathiou et al., 1985), which is more than adequate for cosmological applications. In practice, it is beneficial to use the time variable $s = \int a^{-2} dt$ instead of proper time because the

equation of motion (second equation in eq. [1.28]) simplifies to $d^2\mathbf{x}/ds^2 = a\mathbf{g}$. This allows the use of a symplectic integrator, i.e. phase space volume preserving (see Quinn et al., 1997). For large numbers of particles, the direct summation of gravitational forces for all particle pairs is prohibitive for cosmological simulations. Several clever methods have thus been formulated to overcome this dilemma, which we describe below.

- **Barnes-Hut Tree Algorithm**— This method recursively divides the volume into cells that contain one or more particles (Appel, 1985; Barnes & Hut, 1986). The cells must be smaller than some solid angle, usually $\delta x/r < 1$, where δx and r are the cell size and distance. It is fully spatially adaptive. A low-order multipole expansion of these cells are used to calculate the gravitational field instead of direct summation. Its biggest advantage is speed, which scales as $O(N \log N)$, where N is the number of particles. However, its main shortcoming is the large memory footprint of $\sim 25N$ words (Hernquist, 1987). This method is publicly available and fully parallelized by many groups (e.g. Hillis & Barnes, 1987; Makino & Hut, 1989; Dubinski, 1996).
- **Particle-Mesh (PM) Algorithm**³— The density field is mapped to a Cartesian grid. The main mapping techniques used are (i) Nearest Grid Point that only considers particles inside the cell, (ii) Cloud-in-Cell that uses multi-linear interpolation to the surrounding eight cells, and (iii) Triangular Shaped Cloud that considers the nearest 27 cells in a higher-order interpolation scheme. Fast Fourier Transforms allow the efficient computation of the Poisson equation, which scales as $O(N_g \log N_g)$, where N_g is the number of grid points. After the gravitational field has been calculated, the forces are interpolated back to the particles, using the same scheme to perform the first interpolation to reduce error propagation. The advantage in this method is its speed and light memory consumption, but the force resolution is poor for particle separations under ~ 5 grid cells.

³For a review of PM and P³M, see Hockney & Eastwood (1988).

- **P³M and Adaptive P³M**— This algorithm (Efstathiou & Eastwood, 1981) combines the advantages of PM and direct summation methods. At long distances, gravitational forces are calculated with the PM method, but contributions from nearby particles are calculated by direct summation. The particle pair summations limit the speed in strong overdensities, but this can be overcome by using the tree algorithm at short distances (Xu, 1995). However, Couchman (1991) devised a more elegant solution to adaptively place subgrids (adaptive P³M) that have isolated boundary conditions in overdensities. Then the PM method solves the Poisson equation in these subgrids. In the finest subgrids, pair summation is only computed when the separation is less than a few cell widths, dramatically increasing the speed and accuracy of the calculation.
- **Multi-resolution Mesh Methods**— Some improved methods use the ideas of adaptive P³M in which the resolution of the calculation increases with overdensities. These include (i) adaptive mesh refinement of the density field (e.g. Jessop et al., 1994; Kravtsov et al., 1997), (ii) splitting of particles in overdensities (Splinter, 1996), and (iii) a moving mesh that deforms to sample overdensities at higher resolutions (Gnedin, 1995; Pen, 1995).

1.5.2 Hydrodynamics Solvers

Almost twenty percent of matter in the universe is baryonic, some of which radiatively cools and condenses to form stars and galaxies. The hydrodynamics of cosmological structures have been studied since Doroshkevich et al. (1978) studied the one-dimensional collapse of sheet-like structures (Zel’dovich pancakes). The difficulty of baryonic physics arises from the non-linearity and discontinuities in strong shocks. The solution of the fluid equations in an expanding universe is aided by rewriting them in comoving coordinates: the continuity equation,

$$\frac{\partial}{\partial t} \left(\frac{\rho_b}{\bar{\rho}_b} \right) + \frac{1}{a} \nabla \cdot \mathbf{v}_b = 0, \quad (1.29)$$

the momentum equation,

$$\frac{\partial \mathbf{v}_b}{\partial t} + \frac{1}{a} \mathbf{v}_b \cdot \nabla \mathbf{v}_b + H \mathbf{v}_b = -\frac{1}{a \rho_b} \nabla p + \mathbf{g}, \quad (1.30)$$

and the energy equation,

$$\frac{\partial u}{\partial t} + \frac{1}{a} \mathbf{v}_b \cdot \nabla u = -\frac{p}{a \rho_b} \nabla \cdot \mathbf{v}_b + \frac{1}{\rho_b} (\Gamma - \Lambda). \quad (1.31)$$

Here ρ_b , $\bar{\rho}_b$, \mathbf{v}_b , u , p , Γ , and Λ are the gas density, mean gas density, peculiar velocity, specific energy, pressure, and heating and cooling rates per unit volume, respectively. For a perfect gas, the specific energy $u = p/[(\gamma - 1)\rho_b]$, where γ is the adiabatic index. There have been three major approaches that we discuss next in solving these fluid equations.

- **Smoothed Particle Hydrodynamics (SPH)**— This Lagrangian method (Lucy, 1977; Gingold & Monaghan, 1977; Evrard, 1988) describes fluid parcels with particles that have gas properties, such as density, temperature, and chemical abundances. These quantities are calculated by smoothing over usually 20–30 of the nearest neighboring particles with a kernel. For example, the density at a particular position \mathbf{x} is

$$\rho_b(\mathbf{x}) = \sum_{i=1}^N m_i W(\mathbf{x} - \mathbf{x}_i, h), \quad (1.32)$$

where W and h are the smoothing kernel and smoothing length. The kernel W is usually a spline with some cutoff radius proportional to h . Then a modified set of fluid equations using the kernel are solved. SPH benefits from the advances in collisionless particle algorithms because of its particle nature. It is inherently spatially adaptive but suffers from poor resolution in underdense regions.

- **Eulerian Grid Algorithms**— Grid algorithms with finite differencing have been utilized to solve the fluid equations since the 1960's (see Ritchmyer & Morton, 1967, for an early review), who also established that additional terms (e.g. heating and cooling rates, gravity, cosmological expansion, etc.) could be

solved by operator splitting. In order to capture strong shocks, robust schemes must be used, which have been extensively tested in the computational fluid dynamics community (e.g. Sod, 1985; LeVeque, 1992). There are two main approaches for shock captures: the total-variational diminishing method (TVD) and the piecewise-parabolic method (PPM). TVD uses an approximation to the Riemann solution, is second-order accurate outside of shocks, and can resolve shocks in two grids cells (Ryu et al., 1993). PPM is a third-order accurate Godunov solution for the Riemann problem, which is solved using a quadratic interpolation of the densities that minimizes post-shock oscillations (Colella & Woodward, 1984; Woodward & Colella, 1984).

- **Adaptive Mesh Refinement (AMR)**— Eulerian methods can capture shocks well but cannot follow high density regions well since it is constrained to a fixed grid. This drawback can be bypassed, however, by using AMR that dynamically places higher resolution grids in regions of interest (e.g. high densities, shocks, etc.). AMR has been successfully implemented in several cosmology codes (e.g. Anninos et al., 1994; Bryan & Norman, 1997; Kravtsov et al., 1997) to date and has demonstrated that it can evolve systems over 12 orders of magnitude in length (Bryan et al., 2001).

1.5.3 Additional Physical Models

The accurate treatment of gas dynamics involves not only gravity and hydrodynamics but also additional physics such as heating and cooling, chemical reactions, and radiation transport. Cen et al. (1990) was the first to include radiative cooling in the form of a cooling function that considered equilibrium between recombinations and collisional ionization. Considering radiative cooling permits the simulation to follow the condensation of galaxies in virialized objects. However, the assumption of equilibrium chemistry breaks down behind shocks and in dense cooling regions. Here one must solve a rate equation network for non-equilibrium chemistry (Cen, 1992; Haehnelt et al., 1996). These methods have also been successful in following the formation of the first objects with non-equilibrium solvers that include molecular

hydrogen cooling (Haiman et al., 1996; Abel et al., 1997; Anninos et al., 1997; Gnedin & Ostriker, 1997).

Heating rates in cosmology emerge from stellar radiation, supernova explosions, and active galactic nuclei (AGN). These processes are usually included by a phenomenological method that represents stars or galaxies as collisionless particles that return thermal energy (and in some cases, metals) to the hydrodynamical grid or SPH particles (Cen & Ostriker, 1992).

Gas heating from stellar radiation can be represented better if one considers radiative transfer, an essential ingredient to most astrophysical scenarios. However, its solution is most difficult since it is a function of seven variables: position, frequency, direction, and time. This has not deterred the community from appropriate solutions, in which we note three effective methods.

- A spatially homogeneous and isotropic radiation field in the computational volume can be used to study the effects of a radiation background. Additionally, one can focus on the energy dependence of this background on structure formation (Cen, 1992). This approach has also been extended to include an approximation to local absorption (Gnedin & Ostriker, 1997).
- Variable Eddington factors, the ratio of radiation stress to energy density, provides accurate solutions for radiation transport in both optically thin and thick regimes (Ducloux et al., 1992; Stone et al., 1992; Gnedin & Abel, 2001).
- Ray tracing from point sources of radiation accurately tracks ionization fronts and regions through the computational volume (e.g. Abel et al., 1999; Abel & Wandelt, 2002; Mellema et al., 2006). However, to obtain well-sampled radiation fields at large distances, one must trace an obscene amount of rays originating from the source. Adaptive ray tracing avoids this problem by tracing only hundreds of rays from the source and splitting them as they propagate farther from the source (Abel & Wandelt, 2002; Abel et al., 2007).

1.5.4 Applications

The first true application of cosmological simulations tested various cosmology models and parameters, i.e. CDM, HDM, Ω , H_0 . They proved useful in refining the CDM model and ruling out the HDM model. In addition to that application, there have been other significant applications to astrophysics. We highlight four of them here.

1. Galaxy clusters are the most recently virialized objects and provide a good problem for simulations (see Frenk et al., 1999), which have refined the relationships between mass, luminosity, and velocity dispersions. Furthermore, comparing the substructure, morphologies, and radial profiles of clusters found in simulations to observations can constrain cosmological parameters.
2. They have constrained the nature of quasar absorption and Ly α forest lines. Absorption in these lines occurs in a few different cases: well-defined clouds, filamentary and sheet-like structures, and velocity caustics. Cosmological simulations can accurately account for the column density distribution of Ly α lines (Zhang et al., 1997; Bryan & Norman, 1999).
3. A universal density profile of DM halos has been discovered using cosmological simulations (Navarro et al., 1997). The density $\rho(r) \propto [(r/r_s)(1 + r/r_s)^2]^{-1}$, where r_s is a scale radius, in all DM halos regardless of their formation redshift and mass, initial power spectrum, and cosmological parameters.
4. Cosmological simulations have verified that structure forms in a self-similar way that evolves as $a(t)^\alpha$, where $\alpha = 2/(3 + n)$ and n is the spectral index of the density fluctuation power spectrum.
5. Additionally, they have fine-tuned the Press-Schechter mass function (Jenkins et al., 2001) and verified the nature of galaxy clustering (Kravtsov et al., 2004; Weinberg et al., 2004) and the non-linear power spectrum of dark matter (Wechsler et al., 2006). Simulations have also investigated and confirmed the predicted halo merging rates and halo accretion histories from extended Press-Schechter formalism (Wechsler et al., 2002).

Clearly numerical simulations can be used as a powerful astrophysical tool. They will be the basis for this thesis, which we outline in the next section.

1.6 Thesis Overview

Recent developments have shown that the first luminous objects in the universe are metal-free massive ($M \sim 100M_{\odot}$) stars that form in dark matter halos with masses $\sim 10^6 M_{\odot}$ (Abel et al., 2002; Bromm et al., 2002; Yoshida et al., 2006b). These stars form at redshifts between 10 and 50. Closer to the present-day, galaxy formation models are well established and have made several successful interpretations about the nature of galaxy formation in the universe after reionization ($z < 6$). This thesis aspires to bridge the gap between theories of the first stars and galaxy formation. Hence its focus is the formation of the first galaxies in the universe, shortly after the birth of Pop III stars.

Before delving into extensive numerical investigations, it is beneficial to determine whether Pop III stars play a significant role in the early universe through a semi-analytic model of reionization that utilizes Press-Schechter formalism and results of numerical simulations that study the negative feedback in the first bound objects. This is the subject of Chapter 2.

Galaxy formation involves many physical processes outlined in §1.5.3. In order to isolate the importance of each process, we gradually introduce new physics into our simulations. All of the simulations in this thesis have the same initial conditions but consider different physical models. Chapter 3 shows the simplest models to which we compare all later simulations to assess the relevance of the added process. Here we study the baryonic virialization of cosmological objects through an analysis of the virial theorem of such objects, in particular the generation of turbulence. Here we see supersonic turbulence when radiative cooling is efficient. This can have applications to galaxy formation models and galactic molecular clouds that are supersonically turbulent.

We next describe the collapse of halos with masses $\sim 10^8 M_{\odot}$, undergoing atomic hydrogen cooling in Chapter 4. These objects are usually considered as the first

galaxies and sources of radiation in galaxy formation models. We investigate this case to study the nature of the first galaxy under this assumption. We find that it centrally collapses before fragmentation occurs in a global disk. This may, however, never occur in nature because we neglect H_2 formation and cooling and stellar feedback from Pop III stars. Nevertheless, it is a great testbed for theories of turbulent collapses that are ubiquitous in the universe.

In Chapter 5, we consider H_2 formation and cooling in the calculations. We extend the work of Machacek et al. (2001), who investigated the negative feedback of a Lyman-Werner background in H_2 formation in the early universe. We add the models with no residual electrons from recombination, an essential part to H_2 formation in the gas-phase, from recombination. We find that collisional ionization in halos aids H_2 formation and the collapse (Shapiro & Kang, 1987). These collapsing halos are three times less massive than previously thought, which translates into early galaxies being an order of magnitude more abundant. We conclude that H_2 plays an essential role in early galaxy formation and cannot be neglected.

Finally we include radiative transfer, a vital component to simulations of early structure formation. This is the first time an accurate radiation transport scheme has been applied to galaxy formation at any epoch. We use adaptive ray tracing to compute the radiation transport from Pop III stars. In one simulation, we include the effects of pair-instability SNe from Pop III stars from which we track the propagation of the first metals in the universe. In Chapter 6, we study the global properties of early dwarf galaxies, including the metallicities of such galaxies and the IGM. The baryon fractions of such galaxies are reduced up to a factor of three, and the angular momentum is increased by a factor of two when considering the effects of stellar feedback from Pop III on early galaxy formation. Chapter 7 then focuses on star formation rates at redshifts greater than 15, the properties of star formation regions, and the start of cosmological reionization.

We state the main conclusions of this thesis in Chapter 8.

Chapter 2

The Number of Supernovae from Primordial Stars in the Universe

Cosmological structure assembles hierarchically. If one follows this logic, Milky Way type galaxies must have formed from the mergers of thousands of smaller entities over the history of the universe. This leads to the following questions: *What are the smallest and first objects with luminous counterparts that eventually compose most of the present-day structure? What are their properties? Are they observable?*

These questions have aroused much interest in the formation of the first objects. It has been established by both analytical work and numerical simulations that the first stars form in dark matter halos with masses $\sim 10^6 M_\odot$. The gas in these objects condense by molecular hydrogen cooling and form a single, central massive star. Observations of primordial stars are currently out of reach even by the most powerful telescopes. In this chapter, we investigate the feasibility of future observations of supernovae from primordial stars, in particular their magnitudes and rates on the sky. This work involves semi-analytic models of structure formation, which are less computationally intensive than explicit three-dimensional numerical simulations. This allows for a parameter-space study before proceeding to three-dimensional computations of the formation of the first stars and its feedback on galaxy formation.

This chapter was published in the *The Astrophysical Journal*, 2005, Volume 629, 615. This paper is co-authored by Tom Abel, who guided me in the development of

the semi-analytic code and the interpretation of its results.

2.1 Introduction

The properties of pre-reionization luminous objects are integral to our comprehension of the process of reionization and their effect on subsequent structure formation. Observations of distant ($z = 6.28, 6.4$) quasars depict the relics of reionization with their accompanying Gunn-Peterson troughs (Becker et al., 2002; Fan et al., 2002). Furthermore, Lyman alpha forest carbon abundances of $\sim 10^{-2} Z_{\odot}$ and $10^{-3.7} Z_{\odot}$ observed at redshifts 3 and 5, respectively, indicate that numerous early supernovae (SNe) enriched the intergalactic medium (IGM) (Songaila & Cowie, 1996; Songaila, 2001). These early generations of stars are at least partly responsible for ionizing the Universe. A fraction of these stars lie in protogalaxies, but the other fraction of early stars are metal-free, form through molecular hydrogen cooling, and are very massive ($M \sim 100M_{\odot}$) (Abel et al., 2000, 2002). In Λ CDM cosmologies, these stars form at $10 \lesssim z \lesssim 50$. The Wilkinson Microwave Anisotropy Probe (WMAP) data further constrains the epoch of reionization from the measurement of the optical depth due to electron scattering, $\tau_{es} = 0.17 \pm 0.04$ (68% confidence), which corresponds to a reionization redshift of 17 ± 5 when assuming instantaneous reionization (Kogut et al., 2003). However in this paper, we shall show this epoch is gradual and its effect on primordial star formation.

In hierarchical models of structure formation, small objects merge to form more massive structures. Eventually, a fraction of halos are massive ($\sim 5 \times 10^5 M_{\odot}$ at $z \sim 20$) enough to host cooling gas (Couchman & Rees, 1986; Tegmark et al., 1997; Abel et al., 1998; Fuller & Couchman, 2001). These halos do not cool through atomic line cooling since $T_{vir} < 10^4$; however, primordial gas contains a trace of H_2 . Free electrons allow H_2 to form, which acts as an effective coolant at several hundred degrees through rotational and vibrational transitions. H_2 is easily photo-dissociated by photons in the Lyman-Werner (LW) band, 11.26–13.6eV (Field et al., 1966; Stecher & Williams, 1967), thus H_2 can be destroyed by distant sources in a neutral Universe. Primordial stars produce copious amounts of UV photons in the LW band,

destroying the most effective cooling process at $z \sim 20$. This negative feedback from the UV background significantly inhibits the primordial star formation rate in the early Universe by requiring a larger potential well for gas to condense. Many groups have explored the effects of a UV background on cooling and collapsing gas. Firstly, Dekel & Rees (1987) discovered that H_2 can be dissociated from large distances. Then more quantitatively, Haiman et al. (1997) questioned how collapsing, homogeneous, spherical clouds are affected by a UV background. In more detail, Haiman et al. (2000) determined whether a gas cloud collapsed by comparing the cooling time with the current lifetime of the cloud, which was calculated in the presence of solving the spherically symmetric radiative transfer equation along with time-dependent H_2 cooling functions. However, these studies only considered spherically symmetric cases while realistically these halos are overdensities within filaments. To combat this problem, Machacek et al. (2001) employed a three-dimensional Eulerian adaptive mesh refinement (AMR) simulation to determine quantitative effects of a UV background on gas condensation.

We consider lower mass stars to form in more massive halos that may fragment via atomic line cooling as well as the metal lines from the heavy elements expelled by earlier generations of stars. We use the prescription outlined in Haiman & Loeb (1997) (hereafter HL97) to model the metal abundances and ionizing photon rates of these stars.

With infrared space observatories, such as the Spitzer Space Telescope, Primordial Explorer (PRIME; Zheng et al., 2003), and James Webb Space Telescope (JWST), sufficient sensitivity is available to detect the SNe from primordial stars. Although SNe remnants are bright for short periods of time, they may be the best chance to directly observe primordial stars due to their large intrinsic luminosities. If these events are recorded, many properties, such as mass, luminosity, metallicity, and redshift, of the progenitors can be calculated using metal-free or ultra metal-poor SNe models, which can validate or falsify simulations of the first stars (Abel et al., 2002). To evolve our calculation through redshift, we need to retain information about the UV background and number densities of primordial stars, which can extend to determining such quantities as volume-averaged metallicity and ionized fraction of the

Universe. Our model is constrained with (a) the WMAP optical depth measurement, (b) primordial star formation and suppression in high resolution hydrodynamical simulations, and (c) local observations of dwarf galaxies that constrain high redshift protogalaxies properties.

We organize the paper as follows. In §2.2, we report the semi-empirical method behind our calculations, which incorporates effects from negative feedback and an ionized fraction and is constrained from the WMAP result and local dwarf galaxy observations. In §2.3, we present the number density of primordial SNe in the sky. We also explore the feasibility of observing these SNe by calculating their magnitudes and comparing them with the sensitivities of infrared space observatories. Then in §2.4, we discuss possible future observations and numerical simulations that could further constrain our model. Finally, §2.5 summarizes our results and the implications of the first observations of SNe from primordial stars.

2.2 The Method

We use several theories and results from simulations of structure formation and metal-free stars. We use a Λ CDM cosmology with $\Omega_\Lambda = 0.70$, $\Omega_{\text{CDM}} = 0.26$, $\Omega_b = 0.04$, $h = 0.7$, $\sigma_8 = 0.9$, and $n = 1$. Ω_Λ , Ω_{CDM} , and Ω_b are the fractions of mass-energy contained in vacuum energy, cold dark matter, and baryons, respectively. h is the Hubble parameter in units of $100 \text{ km s}^{-1} \text{ Mpc}^{-1}$. $n = 1$ indicates that we use a scale-free power spectrum, and σ_8 is the variance of random mass fluctuations in a sphere of radius $8h^{-1} \text{ Mpc}$. We use a CDM power spectrum defined in Bardeen et al. (1986), which depends on σ_8 and h .

The remaining parameters are the primordial stellar mass and the factors f_{esc} and f_\star , which dictate the production and escape of ionizing photons. f_{esc} is the photon escape fraction, and f_\star is the star formation efficiency.

To evolve the ionization and star formation behaviors of the Universe, we must determine the density of dark matter halos that host early stars. In $T_{\text{vir}} < 10^4 \text{ K}$ halos (henceforth “minihalos”), H_2 cooling is the primary mechanism that provides means of condensation into cold, dense objects. However in $T_{\text{vir}} > 10^4 \text{ K}$, which

corresponds to $M_{vir} > 10^8 M_{\odot} [(1+z)/10]^{-3/2}$, halos, hydrogen atomic line cooling allows the baryons to fragment and cool into stars.

2.2.1 Minihalo Star Formation

The first quantity we need to begin our calculation is the minimum halo mass that forms a cold, dense gas core due to H_2 cooling. Radiation in the LW band photo-dissociates H_2 , which inhibits star formation in minihalos. This negative feedback from a UV background does not necessarily prohibit the formation of primordial stars in minihalos, but only increases the critical halo mass in which condensation occurs, and delays the star formation. From their simulations of pre-galactic structure formation, Machacek et al. (2001) determined the minimum mass of halo that hosts a massive primordial star is

$$\frac{M_{min}}{M_{\odot}} = \exp\left(\frac{f_{cd}}{0.06}\right) \left(1.25 \times 10^5 + 8.7 \times 10^5 F_{LW,-21}^{0.47}\right), \quad (2.1)$$

where M_{min} is the minimum halo mass that contains a cold, dense gas core; f_{cd} is the fraction of gas that is cold and dense; F_{LW} is the flux within the LW band in units of $10^{-21} \text{ erg s}^{-1} \text{ cm}^{-2} \text{ Hz}^{-1}$. For our calculation, we consider $f_{cd} = 0.02$, which is a conservative estimate in which we have an adequate source of star forming gas. With our chosen f_{cd} and no UV background, a $1.74 \times 10^5 M_{\odot}$ halo will form a cold, dense core, which will continue to form a primordial star. In a typical UV background of $J = 10^{-21} \text{ erg s}^{-1} \text{ cm}^{-2} \text{ Hz}^{-1} \text{ sr}^{-1}$, the minimum mass is $4.16 \times 10^6 M_{\odot}$. Additionally, minihalos can only form a star within neutral regions of the Universe since they are easily photo-ionized (Haiman et al., 2001; Oh & Haiman, 2003), and H I is a necessary ingredient for producing H_2 .

Numerical simulations (e.g. Abel et al., 2002; Bromm et al., 2002) illustrated that fragmentation within the inner molecular cloud does not occur and a single massive ($M \sim 100 M_{\odot}$) star forms in the central regions. These stars produce hard spectra and tremendous amounts of ionizing photons. For example, the ionizing photon to stellar baryon ratio $n_{\gamma} \sim 91300, 56700, \text{ and } 5173$ for H, He, He^+ in a $200 M_{\odot}$ star

(Schaerer, 2002). We calculate the ionizing photon flux by considering

$$\left(\frac{dN_\gamma}{dt}\right)_{mini} = \bar{Q} T_{life} \frac{d\rho_{mini}}{dz} \frac{dz}{dt}, \quad (2.2)$$

where N_γ is the total number of ionizing photons in the Universe; \bar{Q} is the time-averaged photon flux; T_{life} is the stellar lifetime; and ρ_{mini} is the comoving number density of minihalos that we determine from an ellipsoidal variant of Press-Schechter (PS) formalism (Press & Schechter, 1974; Sheth & Tormen, 2002).

The primordial initial mass function (IMF) is unknown, therefore, we assume a fixed primordial stellar mass for each calculation. We run the model for primordial stellar masses, M_{fs} , of 100, 200, and 500 M_\odot and use the time-averaged emissivities from metal-free stellar models with no mass loss (Schaerer, 2002). In our models, the minihalo is quickly ionized and all photons escape into the IGM (Whalen et al., 2004). Furthermore, we use a blackbody spectrum at 10^5 K to approximate the spectrum of the primordial star since surface temperatures are virtually independent of mass at $M \gtrsim 80M_\odot$.

2.2.2 Star Formation in Protogalaxies

In $T_{vir} > 10^4$ K halos, baryons can cool efficiently through atomic line cooling, thus fragmenting and forming stars. As described in HL97, we parametrize the properties of these stars by a couple of factors.

Star formation efficiency

High redshift galaxies appear to have similar properties as local dwarf galaxies. We can constrain the star formation efficiency f_\star by letting local observations guide us. In these galaxies, f_\star ranges from 0.02 to 0.08 (Taylor et al., 1999; Walter et al., 2001). Using the orthodox Schmidt star formation law in local dwarf galaxies, Gnedin (2000) estimated f_\star to be 0.04 if it were constant over the first 3 Gyr but can also be as low as 0.022. It should be noted that f_\star can be higher if star formation ceased after a shorter initial burst.

Analyses of metallicities in local dwarf galaxies reveal their prior star formation. Both Type Ia and Type II SNe contribute iron to the IGM, but Type II SNe provide most of the α -process elements (e.g. C, N, O, Mg) to the IGM. Type II SNe occur on timescales $< 3 \times 10^7$ yr while Type Ia are delayed by 3×10^7 yr to a Hubble time (Matteucci & Recchi, 2001). Therefore, we expect an overabundance of α -process elements with respect to iron just after the initial starburst. $[\alpha/\text{Fe}]$ versus $[\text{Fe}/\text{H}]$ ¹ plots help us inspect the evolution of the ISM/IGM metallicity. If the prior star formation is inefficient (i.e. spirals and irregulars), $[\alpha/\text{Fe}]$ is only shortly overabundant, which is characterized by a short plateau versus $[\text{Fe}/\text{H}]$. On the other hand, if the star formation is fast and occurs early in the lifetime of the galaxy, $[\alpha/\text{Fe}]$ remains in the plateau longer due to the quick production of metals by Type II SNe (see Figure 1 in Matteucci, 2002). Also, Venn et al. (2003) discovered no apparent plateau in $[\alpha/\text{Fe}]$ versus $[\text{Fe}/\text{H}]$ comparisons in dwarf spheroidal and irregular galaxies. They conclude that star formation must have been on timescales longer than Type Ia SNe enrichment, which hints at a low and continuous star formation rates in these protogalaxies when compared to recent star formation.

These low star formation efficiencies are further supported by the galaxies contained in the Sloan Digital Sky Survey (SDSS; York et al., 2000). Star formation efficiencies within low mass galaxies ($M < 3 \times 10^{10} M_{\odot}$) decline as $M^{2/3}$ (Kauffmann et al., 2003). At high redshift and before reionization, most of the protogalaxies tend to be $\text{few} \times 10^7 M_{\odot}$, which is comparable to many local dwarf galaxies (Mateo, 1998). It should also be noted that no star formation history is alike within individual Local Group galaxies, but it is worthwhile to adopt a global star formation efficiency and observe the consequences on reionization and primordial star formation. With the stated constraints, we set $f_{\star} = 0.04$ in our main model in concordance with the Schmidt Law (Gnedin, 2000) and stellar abundances (Venn et al., 2003).

¹We use the conventional notation, $[\text{X}/\text{H}] \equiv \log(\text{X}/\text{H}) - \log(\text{X}_{\odot}/\text{H}_{\odot})$

Table 2.1: Ionizing photon production per stellar baryon and luminosities for metal-poor IMFs

Z	$n_{\gamma, H}$	$n_{\gamma, He}$	n_{γ, He^+}	$\log \mathcal{L}$ [erg s ⁻¹ M _⊙ ⁻¹]
10 ⁻⁷	20102	8504	8	36.20
10 ⁻⁵	15670	5768	0.2	36.16
0.0004	13369	3900	0	36.28 ^a

Stellar luminosities

We consider multiple IMFs for star formation within protogalaxies. Our main model uses a Salpeter IMF with a slope $\alpha = -2.35$, metallicity $Z = 10^{-7}$, 10^{-5} , and 0.0004, and $(M_{low}, M_{up}) = (1, 100)M_{\odot}$. We take the continuous starburst spectrum evolution from these particular IMFs that were calculated with Starburst99 (Schaerer, 2003; Leitherer et al., 1999). To estimate the ionizing photon per stellar baryon ratio, n_{γ} , and luminosities of the IMF at a particular metallicity, we interpolate in \log_{10} space between the two adjacent IMFs. When $Z < 10^{-7}$, we consider the $Z = 10^{-7}$ IMF. The properties of these IMFs are listed in Table 1. Note that more metal-rich starbursts result in a softer spectrum and less ionizing photons in which $n_{\gamma, H}$ decreases almost by a factor of 2.

In the $Z = 0.0004$ IMF, we retain the luminosity from the $Z = 10^{-5}$ and set $n_{\gamma, He^+} = 0$. We choose to do so because of the theoretical uncertainty of hot Wolf-Rayet (WR) stars and their presence (for a review, see Schaerer, 2000). In Schaerer (2003), the luminosity and spectral hardness increases due to the presence of WR stars at higher metallicities. However, Smith et al. (2002) calculate WR spectra that are significantly softer.

^aSee text for a discussion on values.

Ionizing photon escape fraction

Radiation emitted by these stars have a probability f_{esc} to escape from the protogalaxy and ionize the IGM. The protogalaxy ISM density and composition plays the biggest role in determining this factor. Heckman et al. (2001) showed that local and distant starburst galaxies, including the gravitationally lensed galaxy MS 1512-cB58 ($z = 2.7$), have $f_{esc} \lesssim 0.06$. This result agrees with previous analyses of the f_{esc} in the Lyman continuum (Leitherer et al., 1995; Hurwitz et al., 1997). However, Lyman break galaxies may have $f_{esc} \gtrsim 0.2$ (Steidel et al., 2001). In conjunction with $f_{\star} = 0.04$ and $M_{f_s} = [100, 200, 500]M_{\odot}$, the choice of $f_{esc} = [0.050, 0.033, 0.028]$, respectively, in our calculation results in the same optical depth from WMAP, $\tau_{es} = 0.17$, thus we use these values in the main models. Wood & Loeb (2000) and Ricotti & Shull (2000) have argued that the escape fraction may be very small due to the much higher densities at high redshift. However, the shallow potential wells and their small size make them susceptible to photo-evaporation and effects of radiation pressure (Haehnelt, 1995). Other uncertainties such as dust content, metallicity, and whether the ISM density scales as $(1+z)^3$ blur our intuition about the escape of ionizing radiation. Therefore, we allow f_{esc} to vary from 0.001–0.25 since it is unclear whether high-redshift, low-mass protogalaxies allow photons to escape due to self-photoevaporation or absorb the photons due to a higher proper gas density when compared to starburst galaxies.

Ionizing Photon Rates

These factors are multiplicative in the amount of radiation that is available from protogalaxies to ionize the IGM. The rate of photons emitted that can ionize species X is

$$\left(\frac{dN_{\gamma}}{dt}\right)_{proto} = \rho_0 \frac{f_{esc} f_{\star} n_{\gamma,X}}{\mu m_p} \frac{d\psi_{proto}}{dz} \frac{dz}{dt}, \quad (2.3)$$

where μ is the mean molecular weight; $\rho_0 = \Omega_b(3H_0^2/8\pi G)$; m_p is the mass of a proton; ψ_{proto} is the mass fraction contained in protogalaxies that is calculated by PS formalism. We restrict the product of f_{esc} and f_{\star} to be in a range from 10^{-4} – 10^{-2} since the resulting reionization histories fall within the measured τ_{es} error bars. The reionization epoch greatly depends on the factors f_{esc} and f_{\star} . In order to explore

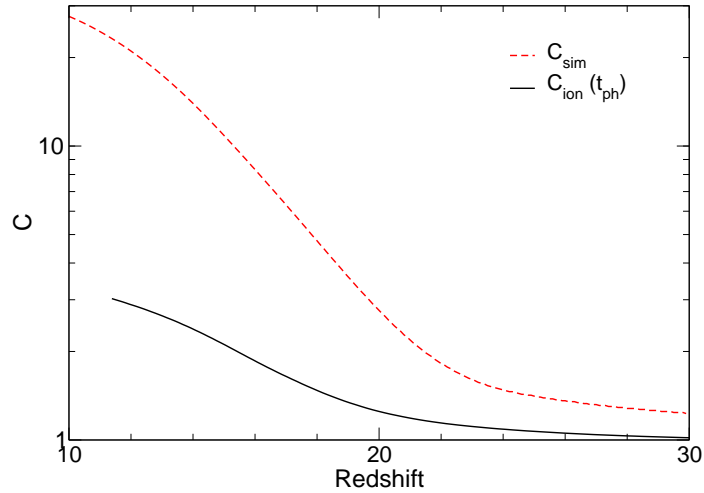


Fig. 2.1.— The dashed line is the gas clumping factor as calculated in our adiabatic hydrodynamical AMR simulation. Using equation (2.5), we estimate the clumping factor in the ionized region to be solid line.

the consequences of different values of τ_{es} and their resulting SNe rates, we vary the factors f_{esc} and f_{\star} .

2.2.3 Clumping Factor

Overdense regions experience an increased recombination rate. Overdensities are characterized by the gas clumping factor $C = \langle n_H^2 \rangle / \langle n_H \rangle^2$, and the recombination rate is increased by this factor. To calculate this parameter in our model, we utilize the same cosmological Eulerian AMR code *enzo* (Bryan & Norman, 1999) as in Machacek et al. (2001) in a 256^3 simulation with a comoving box side of 500kpc, eight levels of refinement, and the previously specified cosmological parameters. The top grid has a total (gas) mass resolution of 1013 (135) M_{\odot} , which is smaller than the cosmological Jeans mass,

$$M_J \approx 10^4 \left(\frac{\Omega_M h^2}{0.15} \right)^{-1/2} \left(\frac{\Omega_b h^2}{0.02} \right)^{-3/5} \left(\frac{1+z}{11} \right)^{3/2} M_{\odot}. \quad (2.4)$$

Thus, we account for all collapsed halos in our clumping factor calculation. The simulation is purely adiabatic with no background radiation or atomic/molecular cooling. We show the clumping factor in our simulation, C_{sim} , in Figure 2.1. Cooling only affects localized regions of star formation and does not contribute greatly in the boosting of C . However, ionizing radiation causes photoevaporation of halos, which decreases C in the process (Haiman et al., 2001). We correct for this process by considering all minihalos with $M_J < M < M_{min}$ are photo-evaporated in the ionized regions of the Universe. For simplicity, we assume the IGM has a clumping factor of unity although underdense regions in the IGM correspond to $C_{IGM} \lesssim 1$. We concentrate on the gas clumping factor in the ionizing regions since the goal is to calculate the increase in recombination rates. Consider an ionized region whose volume filling fraction F_H is increasing. The evolution of the gas clumping factor is

$$\dot{C} = C_{sim}\dot{F}_H - \frac{C-1}{t_{ph}}. \quad (2.5)$$

The first term accounts for the expansion that will incorporate unaffected, clumpy material into the region, and the second term represents the photoevaporation of overdensities. Any overdensities in the ionized region will be photo-evaporated by a background UV flux in approximately a sound crossing time of the halo,

$$t_{ph} \approx \beta \frac{R_{vir}}{10 \text{ km s}^{-1}}, \quad (2.6)$$

where β is a normalization factor that accounts for the differences in halo densities at various redshifts and masses, and R_{vir} is the mean virial radius of a halo with $M_J < M < M_{min}$ (Haiman et al., 2001). Since β remains within $\sim 15\%$ of unity for minihalos, we infer $\beta = 1$.

The effect from photoevaporation is illustrated in Figure 2.1. Overdensities that are engulfed by ionized regions cannot sufficiently increase the gas clumping factor to overcome the photoevaporation that occurs, and C remains within the range 1–3 for the entire calculation in our main model. This equation is weakly sensitive to t_{ph} since varying t_{ph} by a factor of 6 alters C only by a factor of 2. In a later paper, we

shall computationally address the effect of radiation on the clumping factor.

2.2.4 The Evolution of UV Background and Halo Densities

We initialize the following method at $z = 75$ with no UV background, evolve the UV background at the questioned redshift, and repeat the described procedure until cosmological hydrogen reionization occurs.

Given a minimum mass of a star-forming halo, we can exploit PS formalism to calculate number densities of these halos. For minihalos, we calculate their number densities for halos with masses above M_{min} (eq. 2.1) and virial temperatures below 10^4 K. Likewise, the protogalaxy mass fraction is calculated by considering all halos more massive than a corresponding $T_{vir} = 10^4$ K.

We choose a variant of PS formalism, which is an ellipsoidal collapse model that is fit to numerical simulations (Sheth & Tormen, 1999; Sheth et al., 2001; Sheth & Tormen, 2002). This model is concisely summarized in Mo & White (2002). In minihalos, it is reasonable to assume one star forms per halo since $E_{bind} \lesssim E_{SNe}$, where E_{bind} and E_{SNe} are the binding energy of the host halo and kinetic energy of the primordial SNe, respectively. The gas is totally disrupted in the halo and requires ~ 100 Myr, which is approximately the Hubble time at cosmological reionization, to re-collapse (Abel, Bryan, & Norman 2002, unpublished). Therefore,

$$\frac{d\rho_\star}{dz} = \frac{d\rho_{mini}}{dt} \frac{dt}{dz}, \quad (2.7)$$

where ρ_\star is the comoving density of primordial stars.

We evolve the spectrum from early stars to investigate how the UV background behaves, particularly in the LW band, with the cosmological radiative transfer equation,

$$\left(\frac{\partial}{\partial t} - \nu H \frac{\partial}{\partial \nu} \right) J = -3HJ - c\kappa J + \frac{c}{4\pi}\epsilon, \quad (2.8)$$

where $H = H(z) = 100hE(z)$ is the Hubble parameter, and $E(z) = \sqrt{\Omega_\Lambda + \Omega_m(1+z)^3}$. $J = J(\nu, z)$ is specific intensity in units of $\text{erg s}^{-1} \text{cm}^{-2} \text{Hz}^{-1} \text{sr}^{-1}$. κ is the continuum absorption coefficient per unit length, and $\epsilon = \epsilon(\nu)$ is the proper volume-averaged

emissivity in units of $\text{erg s}^{-1} \text{cm}^{-3} \text{Hz}^{-1}$ (Peebles, 1993). We define the luminosity of the objects as

$$L(\nu) = \begin{cases} 4\pi R^2 B_\nu(T = 10^5 K) & (\text{mini}) \\ f_{O\star} f_\star \mathcal{L} \frac{B_\nu(T=23000K)}{B_\nu(\nu=2.7kT/h_p; T=23000K)} & (\text{proto}) \end{cases},$$

where B_ν is a blackbody spectrum, and \mathcal{L} is listed in Table 1. R is the radius of the primordial star (Schaerer, 2002). $f_{O\star}$ is the fraction of O stars in the starburst (Schaerer, 2003). k and h_p are Boltzmann's constant and Planck's constant, respectively. For the protogalaxies, $T \sim 23000\text{K}$ because the spectrum in the LW band will be dominated by OB stars, and we weight the luminosity by this blackbody spectrum. Emissivity will be nearly zero above 13.6eV in the neutral Universe due to hydrogen and helium absorption.

Photons from primordial stars and protogalaxies between 13.6eV and several keV ionize the surrounding neutral medium. Using the intrinsic $\geq 13.6\text{eV}$ ionizing photon rates from primordial stars (eq. 2.2) and protogalaxies (eq. 2.3), we calculate a volume-averaged neutral fraction. The change of ionized hydrogen comoving density due to photo-dissociation and recombination is

$$\frac{dn_{HII}}{dt} = -\frac{dN_\gamma}{dt} + C k_{rec} (1+z)^3 n_H^2 \left(1 - \frac{n_{HII}}{n_H}\right)^2, \quad (2.9)$$

where n_{HII} and $n_H = 0.76\rho_0/m_p$ are the ionized and total hydrogen comoving density; dN_γ/dt is the rate of ionizing photons from primordial stars and protogalaxies; C is the clumping factor; and $k_{rec} = 2.6 \times 10^{-13} \text{s}^{-1} \text{cm}^{-3}$ is the case B recombination rate of hydrogen at $T \approx 10^4$.

In the case for once-ionized helium, k_{rec} is approximately equal to the hydrogen case, but since the helium number density is less than hydrogen, less recombinations occur. Naïvely, this will result in a higher He^+ fraction than H^+ due to the hardness of the primordial radiation. Realistically when the ionizing photons reach the ionization front, they will ionize either helium or hydrogen since hydrogen still has a finite photo-ionization cross-section above 23.6eV. We consider the He^+ regions to be equal to the H^+ regions. Then we add $N_{\gamma, He}$ to $N_{\gamma, H}$ to compensate for this effect. We perform a

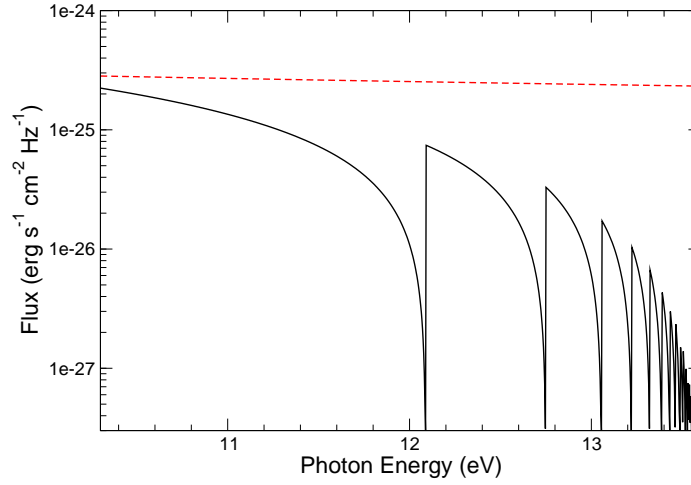


Fig. 2.2.— The red dashed line is an example unprocessed spectrum of a continuous source of radiation. After being absorbed and re-emitted by Lyman-series transitions, it transforms into the “sawtooth” spectrum (*black solid line*). This particular spectrum is for $z_{on} = 30$ and $z_{obs} = 20$.

similar analysis on doubly ionized helium in which $k_{rec, He^+} = 1.5 \times 10^{-12} \text{ s}^{-1} \text{ cm}^{-3}$, but we evaluate equation (2.9) directly with N_{γ, He^+} . The absorption coefficient in equation (2.8) is ignored since we take into account the Lyman series line absorption by the following procedure. Photons with $11.26\text{eV} < E < 13.6\text{eV}$ escape into the IGM, which will photo-dissociate H_2 . To calculate the flux within the LW band, we must consider the processing of photons by the Lyman series transitions (Haiman et al., 1997). Before reionization, these transitions absorb all photons at their respective energies. These absorbers can be visualized as optically thick “screens” in redshift space, for which the photon must have been emitted after the farther wall in redshift. This process creates a sawtooth spectrum with minimums at redshift screens, which is illustrated in Figure 2.2. For instance, an observer at $z = 20$ observes photons at 12.5eV ; it must have been emitted by the $\text{Ly}\gamma$ line at 12.75eV at $z = 20.4$. The fraction of photons that escape from these walls during an integration step is

$$f = \frac{1 - [(1+z)/(1+z_{screen})]^{1.5+\alpha}}{1 - [(1+z)/(1+z+\Delta z)]^{1.5+\alpha}}, \quad (2.10)$$

where $\alpha = -1.8$ is the slope of a power-law spectrum ($F_\nu \propto \nu^{-\alpha}$) and

$$z_{screen} = \frac{\nu}{\nu_{Lyi}}(1 + z_{obs}) - 1. \quad (2.11)$$

ν_{Lyi} is the nearest, blueward Lyman transition to ν . Inherently, z_{screen} must be between z and $z + \Delta z$.

Considering the processes described above, we finally evolve the UV background with the volume averaged emissivity,

$$\epsilon_{mini}(\nu) = \rho_{mini} \times L(\nu) \times \left(1 - \frac{n_{HII}}{n_H}\right), \quad (2.12)$$

$$\epsilon_{proto}(\nu) = \nu^{-1} \rho_0 \frac{d\psi_{proto}}{dt} \times L(\nu, f_\star), \quad (2.13)$$

$$\epsilon(\nu) = (1 + z)^3 [\epsilon_{mini}(\nu) + \epsilon_{proto}(\nu)] \times f(\nu). \quad (2.14)$$

2.3 Results

In this Section, we present the results of our calculation of the evolution of SNe rates and the UV background. We also present the variance of optical depth to electron scattering and SNe rates with different primordial and protogalaxy star formation scenarios. In Figure 2.3, we plot minimum halo masses that host primordial stars, densities of those halos, SNe rates, and the UV background in the LW band for the main models.

2.3.1 Optical Depth to Electron Scattering

Optical depth due to electron scattering,

$$\tau_{es}(z) = \int_0^z \bar{n}_e \sigma_{THC} \left(\frac{dt}{dz}\right) dz, \quad (2.15)$$

where n_e and σ_{TH} are the proper electron density and Thomson cross-section, respectively, is a good observational test to determine the neutral fraction of the Universe

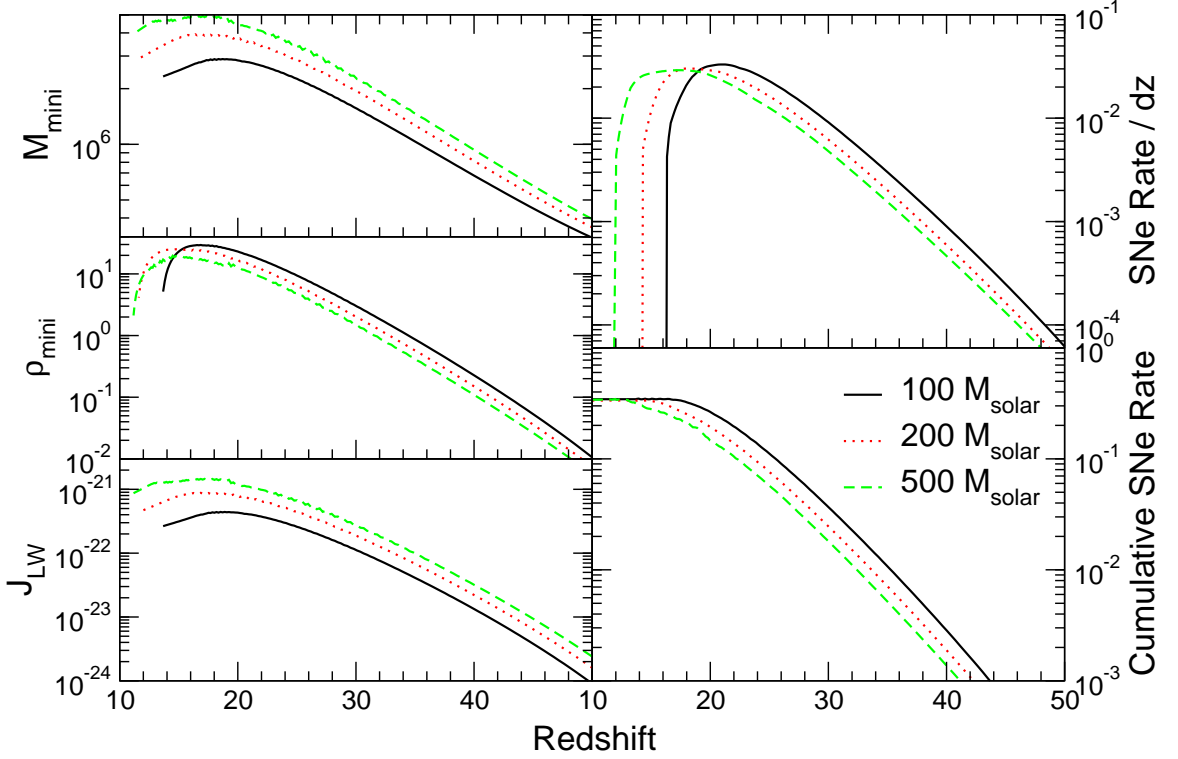


Fig. 2.3.— (*Clockwise from upper right*) Primordial SNe rates ($\text{yr}^{-1} \text{deg}^{-2}$) per unit redshift; Cumulative primordial SNe rate ($\text{yr}^{-1} \text{deg}^{-2}$); Specific intensity ($\text{erg s}^{-1} \text{cm}^{-2} \text{Hz}^{-1} \text{sr}^{-1}$) in the LW band; Comoving density (Mpc^{-3}) of halos above the critical star formation mass in neutral regions; Critical halo mass (M_{\odot}) for primordial star formation. The solid, dotted, and dashed lines correspond to calculations run with a fixed primordial stellar mass of 100, 200, and 500 M_{\odot} , respectively.

before reionization. The WMAP satellite measured $\tau_{es} = 0.17 \pm 0.04$ at 68% confidence.

To accurately calculate n_e , we must consider all ionizations of primordial gas, which includes H^+ , He^+ , and He^{++} . Therefore, the proper electron density is

$$n_e = (1+z)^3 (n_{\text{H}} F_{\text{H}^+} + n_{\text{He}} F_{\text{He}^+} + 2n_{\text{He}} F_{\text{He}^{++}}), \quad (2.16)$$

where F_{H^+} , F_{He^+} , and $F_{\text{He}^{++}}$ are the ionized volume fraction of H^+ , He^+ , and He^{++} , respectively. The effect of more luminous primordial stars is evident in Figure 2.4 as

they ionize the Universe faster at high redshifts. To match the WMAP result, less ionizing photons are required from protogalaxies if the primordial IMF is skewed toward higher masses. Although these models have the same total τ_{es} , cosmological reionization occurs at $z = 13.7, 11.6, 11.2$ for $M_{FS} = 100, 200, \text{ and } 500M_{\odot}$, respectively. However, these reionization redshifts are not consistent with observed Gunn-Peterson troughs in $z \sim 6$ quasars (Becker et al., 2002; Fan et al., 2002) and the high IGM temperatures at $z \sim 4$ inferred from Ly α clouds (Hui & Haiman, 2003). Perhaps portions of the Universe recombine after complete reionization, which will match the most distant quasar observations (Cen, 2003b). If this were true, the first reionization epoch has to be faster and earlier to compensate for this partial recombination and to match the WMAP result. This would lower our SNe rates slightly since primordial star formation will be further suppressed by the quicker reionization.

The ionizing history of the Universe is directly related to the number of ionizing photons that are produced and escape into the IGM. If we fix $\tau_{es} = 0.17$, we constrain f_{\star} and f_{esc} to a power law

$$f_{esc} = B f_{\star}^{-a}, \quad (2.17)$$

where $B = [0.00307, 0.00239, 0.00217]$ and $a = [0.906, 0.839, 0.806]$ for primordial stellar masses 100, 200, and $500M_{\odot}$, respectively. The flattening of the power law with increasing M_{FS} indicates the increasing ionizing contribution from primordial stars.

Table 2.2: Gaussian fits to M_{\min} for the main models

M_{\odot}	A	z_0	σ	C
100	1.67 ± 0.01	10.0 ± 0.2	21.9 ± 0.1	5.19 ± 0.01
250	1.71 ± 0.00	10.5 ± 0.0	23.3 ± 0.0	5.16 ± 0.00
500	1.72 ± 0.01	11.3 ± 0.2	23.5 ± 0.1	5.15 ± 0.00

Note. — Coefficients are for the function $\log(M) = A \times \exp[-(z-z_0)^2/(2\sigma^2)] + C$.

2.3.2 Primordial Supernovae Rates

The natural unit in our computation is comoving density, yet a more useful unit is observed SNe yr⁻¹ deg⁻². First we assume these SNe are bright for 1 yr and then correct for time dilation. We consider the equation

$$\frac{d^2 N}{dt dz} = \frac{dV_c}{dz} \frac{d\rho_\star}{dt} (1+z)^{-1}, \quad (2.18)$$

where the $(1+z)^{-1}$ converts the proper SNe rate into the observer time frame, and

$$\frac{dV_c}{dz} = D_H \frac{(1+z)^2 D_A^2}{E(z)} \Omega \quad (2.19)$$

is the comoving volume element. Ω (deg² = 3.046 × 10⁻⁴ sr) is the solid angle of sky that we want to sample. $D_H = c/H_0$ is the Hubble distance. $D_A = D_M/(1+z)$ is the angular diameter distance, and $D_M = D_H \int_0^z E^{-1}(z') dz'$ is the comoving distance (Peebles, 1993). The above equations are only valid for a flat Λ CDM universe.

Since we only allow primordial stars to form in neutral regions, SNe rates from these stars are highly dependent on the f_{esc} and f_\star , but less sensitive to the stellar primordial mass, M_{fs} . In our main models, the SNe rate varies little with primordial stellar mass and is 0.34 yr⁻¹ deg⁻². Even if we vary f_\star in a range 0.01–0.1 and fix τ_{es} , primordial SNe rates do not vary more than 10% from the main models when constrained by WMAP. As f_{esc} increases, the SNe rates decrease due to a higher ionized volume filling factor. The effect of a higher f_\star squelches SNe rates by two processes, a higher ionized filling factor and higher UV background, which restricts primordial stars to form in more massive halos.

The primordial SNe rate peaks at $z \sim 14$ –20, earlier epochs for larger primordial stellar masses, and falls sharply afterwards due to the ensuing cosmological reionization. Primordial star formation ceases after $z \sim 12$ –16. The combination of an increasing UV background, reionizing Universe, and disruption of minihalos from primordial SNe suppresses all primordial star formation. For each main model, we fit a Gaussian curve to the minimum mass of a minihalo that can host a primordial star, and the parameters are listed in Table 2.2 and are valid for $z > z_0$.

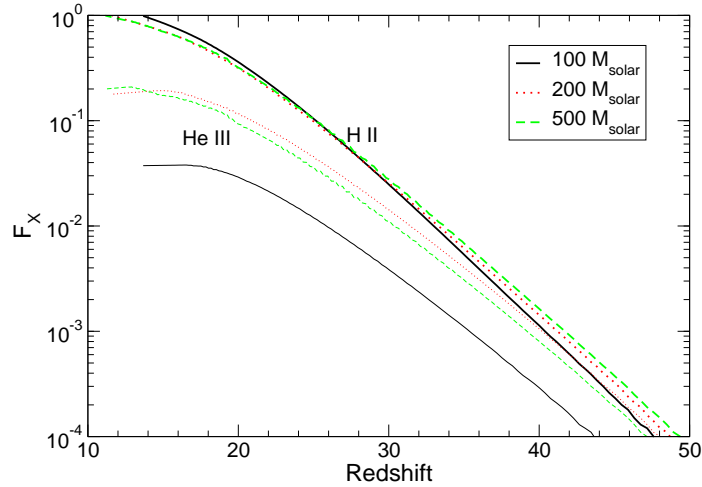


Fig. 2.4.— Evolution of filling factors of ionized hydrogen (top) and doubly ionized helium (bottom). The legend is the same as Figure 2.3.

It is fascinating that some rare primordial SNe occur at $z \gtrsim 40$. As an exercise, we estimate the earliest epoch of minihalo star formation in the visible Universe with PS formalism and by considering it takes ~ 9.33 Myr for a halo to form a protostellar core (Abel et al., 2002). With PS formalism, the “first” epoch equals where the minihalo density is the inverse of the comoving volume inside $z = 1000$ (10523 Gpc^3). Then we include an additional 9.33 Myr for the ensuing star formation. The halo masses of 1.74×10^5 and $10^6 M_\odot$ correspond to formation times of $z \sim 71$ and 64, respectively. Another interesting event to calculate is when the SNe rate equals one per sky per year, which occurs at $z \sim 51$ when considering the collapse and star formation timescales. This epoch is in agreement with the Miralda-Escudé (2003) estimate of $z \simeq 48$.

Furthermore using the proper minihalo density, we calculate the average light travel time between sources, which indicates when negative H_2 feedback first affects star formation. Star formation occurs ~ 9.33 Myr after halo formation, so radiation escapes into the IGM at a time $t_{\text{rad}} = t_{\text{H}}(z_{\text{form}}) + 9.33 \text{ Myr}$, where z_{form} is the halo formation redshift. These sources have a mean proper separation of $d = \rho_\star^{-1/3} / (1+z)$; therefore the time where radiation influences other halos is $t_{\text{rad}} + d/c$. The

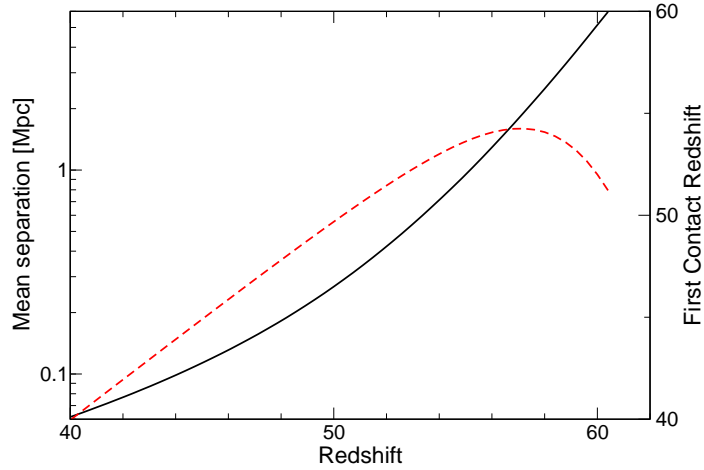


Fig. 2.5.— The *solid* line is the mean proper separation between minihalos. The *dashed* line is the redshift where minihalos first receive radiation from neighboring sources forming at the same epoch.

minimum of this time, corresponding to $z = 54$, is where radiation reaches other halos for the first time. We illustrate the mean proper separation and epoch of first radiation effects in Figure 2.5.

2.3.3 Magnitudes and Observability

The magnitudes of primordial SNe are as important as their occurrence rates to catch these events unfolding in the distant universe. We exploit the ^{56}Ni output from metal-free SNe models to calculate luminosities $L(t)$ from the two-step decay of ^{56}Ni to ^{56}Fe (Heger & Woosley, 2002). We consider the emission spectrum to be a blackbody spectrum with a time-dependent temperature,

$$T(t) = \left[\frac{L(t)M}{8\pi\sigma Et^2} \right]^{1/4} (1+z), \quad (2.20)$$

where M and E are the stellar mass and kinetic energy of the SNe, respectively, calculated using free expansion arguments. The temperature and luminosity of a 175, 200, and $250M_{\odot}$ primordial star SNe are depicted in Figure 2.6. For comparison, we

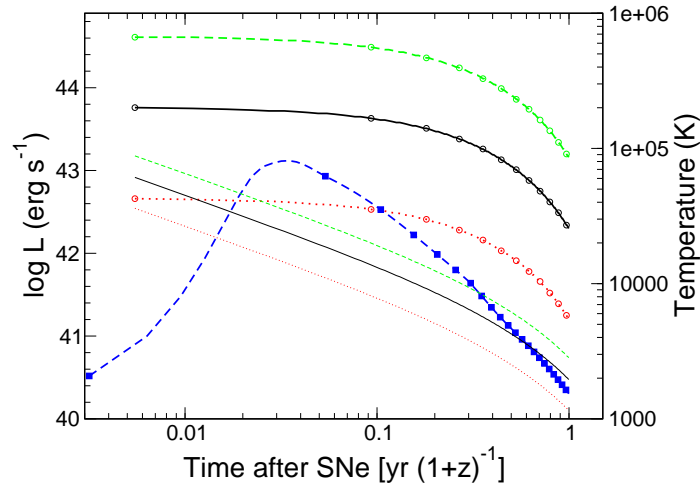


Fig. 2.6.— Using the decay of ^{56}Ni and Equation (2.20), we calculate the luminosity of primordial SNe and their effective temperature. Heavy (*top*) lines with circles are luminosities and light (*bottom*) lines are temperature. The blue dashed line with filled squares is a Type Ia luminosity evolution for comparison (Woosley & Weaver, 1986). The lines from top to bottom (*dotted*, *solid*, *dashed*) are for stellar masses 175, 200, and $250 M_{\odot}$.

plot the typical light curve for a Type Ia SN. Kinetic energy is taken from the SNe models (Heger & Woosley, 2002). We consider the SNe remnant to be in free expansion for the first year because radiation from the primordial star should expel most of surrounding medium to create a low density, highly ionized region of approximately 100 pc in size for a $120 M_{\odot}$ primordial star (Whalen et al., 2004).

In the upper range ($M > 200 M_{\odot}$) of pair-instability SNe, these events produce 1– $57 M_{\odot}$ of ^{56}Ni (Heger & Woosley, 2002), which will produce tremendous luminosities when compared to typical Type II SNe outputs of only 0.1– $0.4 M_{\odot}$ (Woosley & Weaver, 1986). However, uncertainty in the primordial IMF places doubt on the frequency of primordial star SNe with high ^{56}Ni yields. Using conventional Type II SNe parameters of $L \simeq 3 \times 10^{42} \text{ erg s}^{-1}$, $T = 25000\text{K}$ ($2 \text{ days} \lesssim t \lesssim 7 \text{ days}$), and $T = 7000\text{K}$ ($7 \text{ days} \lesssim t \lesssim 2 \text{ months}$) that are tuned by observed light curves, Miralda-Escudé & Rees (1997) determine apparent magnitudes that are 1–3 mag lower than our values, which are brighter due to the greater nickel production of pair-instability

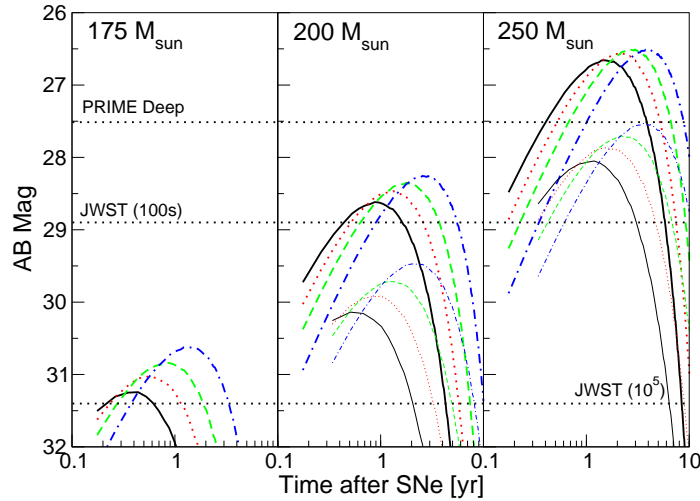


Fig. 2.7.— (*Left to right*) Magnitudes for $M_{FS} = 175, 200, 250 M_{\odot}$. The dashed horizontal lines indicate limiting magnitudes of space infrared observatories. The heavy (*top*) and light (*bottom*) lines are SNe at $z = 15$ and 30 , respectively. The magnitudes for the $175 M_{\odot}$ and $z = 15$ case is not shown since it is too dim. The solid, dotted, dashed, and dash-dotted lines are for Spitzer wavebands centered at $(3.56, 4.51, 5.69, 7.96) \mu\text{m}$. *Note:* The detection limits of Spitzer and PRIME Medium are not shown since they are too high at 24.5 and 25.6 , respectively.

SNe models. Their model should apply to the pair-instability SNe with little ^{56}Ni ejecta. Furthermore, our temperatures are higher due to the greater amount of ^{56}Ni decay in pair-instability SNe.

In typical Type II light curves, radioactive decay does not significantly contribute to the luminosity in the plateau stage (Popov, 1993). In primordial SNe, the ^{56}Ni decay may overwhelm the typical sources of energy within the expanding fireball and create a totally different light curve. We stress that our light curve is a very rough estimate of the processes occurring within a primordial SNe.

In Figure 2.7, we compare maximum AB magnitudes of low- and high-mass pair-instability SNe at various redshifts and sensitivities of space infrared observatories. We consider the sensitivities of SIRTf at $3.5\mu\text{m}$, PRIME medium and deep surveys, and JWST with exposure times of 100s and 10^5s . Our simple estimate leads to very high predicted luminosities, and more detailed numerical models of these explosions

are clearly desirable.

2.4 Discussion

Other factors could alter the feasibility of observing primordial SNe. For instance, $\sim 2\%$ of primordial stars might die in collapsar gamma-ray bursts (GRBs) (Heger et al., 2002). Lamb (1999) also provides a ratio of GRBs to Type Ib/c SNe rates that is $\sim 3 \times 10^{-5} (\theta_b / 10^{-2})^{-1}$, where θ_b is the beaming angle. However, this estimate is for a normal Salpeter IMF, and as mentioned before, the primordial star IMF could be skewed toward high masses, which would increase the probability of a GRB. Zero- and low-metallicity massive stars outside the pair-instability mass range die as GRBs or jet-driven SNe, which are similar to GRBs but not as energetic and spectrally hard. If we consider a proportionality constant, f_{GRB} , and beaming angle, we estimate that the all-sky primordial GRB rate,

$$R_{GRB} = 2.8 \left(\frac{\theta_b}{0.01} \right) \left(\frac{f_{GRB}}{0.02} \right) \text{ GRBs yr}^{-1}. \quad (2.21)$$

In $M \lesssim 140M_\odot$ stars, a collapsar results when it forms a proto-neutron star, cannot launch a supernova shock, and directly collapses to form a black hole in ~ 1 s (Woosley, 1993; MacFadyen & Woosley, 1999). In $M \gtrsim 260M_\odot$ stars, it does not create a proto-neutron star and directly collapses into a massive black hole (Fryer et al., 2001). Afterwards, these black holes can accrete gas and produce X-rays that can further ionize the Universe (Ricotti & Ostriker, 2004b). A few of these X-ray sources could be detected in the Chandra deep field (Ricotti et al., 2005; Alexander et al., 2003). In most GRB models (for an overview, see Mészáros, 2002), the radiation is beamed to small opening angles due to relativistic effects, which would render a fraction of GRBs to be unobservable in our perspective. Finally, gravitational lensing will significantly decrease the apparent magnitudes for selected primordial SNe for very small survey areas. However, the overall magnitude distribution is slightly dimmed by gravitational lensing (Marri & Ferrara, 1998; Marri et al., 2000).

Deviations in the amplitudes of fluctuations, σ_8 , and a running spectral model

(Liddle & Lyth, 1992, 1993) also affect primordial SNe rates. We ran a set of models with $\sigma_8 = 0.8$, and predictably, the rates decreased by a factor of ~ 2.5 due to lesser powers at small mass scales. When we match $\tau = 0.17$, rates range from 0.12 to $0.2 \text{ yr}^{-1} \text{ deg}^{-2}$ with the rates peaking earlier at $z \sim 20$, but now the redshift peaks are nearly independent of redshift with only $\delta z \approx 1$ separating the 100 and $500 M_\odot$ models. If we keep the protogalaxy parameters from the main models, rates do not change; however, the rates peak later than our main models by $\delta z \approx 4$, and τ lowers to 0.14. According to inflationary models, the spectral index of fluctuations should be slowly varying with scale. While analyzing WMAP data, Peiris et al. (2003) determined that the fluctuation amplitude is significantly lower at small scales. With lesser powers at small scales, primordial SNe rates decrease such as the case of a lower σ_8 . In principle, studying primordial SNe occurrences with respect to redshift could furnish direct constraints on the power spectrum at these small scales.

We have demonstrated our model's dependence on the free parameters, f_{esc} , f_* , and M_{fs} . We now suggest several observational and numerical methods in order to constrain our models. To constrain early star formation history of dwarf irregulars with the $[\alpha/\text{Fe}]$ versus $[\text{Fe}/\text{H}]$ comparison, metal analyses of stars with $[\text{Fe}/\text{H}] < -1.5$ are needed to determine early star formation rates of particular systems (see Figure 1.5 in Venn et al., 2003). Dwarf spheroidals exhibit greater variance in star formation histories from system to system, but a similar study will increase our knowledge of high redshift star formation in these small galaxies to further constrain f_* at high redshifts. To improve on these studies, the advances in multi-object spectrographs (e.g. VIMOS², FLAMES³, and GMOS⁴) enable the gathering of many stellar spectra in one exposure. This will greatly increase the stellar population data of dwarf galaxies.

Since some massive stars die as a long-duration GRB, these events can convey information from the death of Pop III stars. The propagation of the initial burst and afterglow provide information about the total energy, gas density in the vicinity, and the Lorentz factor of the beam. The host galaxy ISM properties will help constrain

²<http://www.eso.org/instruments/vimos/>

³<http://www.eso.org/instruments/flames/>

⁴<http://www.gemini.edu/sciops/instruments/gmos/gmosIndex.html>

the f_{esc} in high redshift galaxies. As in the case of GRB 030329 (Stanek et al., 2003), the power-law spectra of the afterglow can be subtracted to obtain a residual that resembles a typical SN spectrum, which may be used to roughly determine the mass of the progenitor. Observing the afterglow is necessary to determine its redshift. The prospect of observing prompt afterglows will be accomplished easier with *Swift*⁵, which can possibly detect GRB afterglows to $z = 16$ and 33 in the K and M bands, respectively (Gou et al., 2004). Furthermore, $\gtrsim 50\%$ of GRBs occur earlier than $z = 5$, and 15% of those high redshift GRBs are detectable by *Swift* (Bromm & Loeb, 2002). The comparison to nearby SNe can provide crucial information about the high redshift ISM. Finally, it is a possibility to explore the intervening absorption with the fast-pointing and multi-wavelength observations of *Swift* (Vreeswijk et al., 2003; Loeb, 2003; Barkana & Loeb, 2004). This IGM absorption would constrain the reionization history of the Universe better, which may change the primordial SNe rates, but more specifically the rate per unit redshift, which would roughly conform to the filling factor evolution.

The radiation from protogalaxies and primordial stars will not only ionize the Universe but also contribute to the near-infrared background (NIRB). Calculations have shown that primordial stars can provide a significant fraction of radiation to the NIRB (Santos et al., 2002; Salvaterra & Ferrara, 2003); however, the paradigm of early reionization set by WMAP was not considered at the time. f_* of protogalaxies and densities of primordial stars can be further constrained if future studies of the NIRB consider the large emissivities of zero- and low-metallicity sources at $z \gtrsim 15$.

Other outlooks include detecting high redshift radio sources and searching for 21cm absorption and emission (Hogan & Rees, 1979; Scott & Rees, 1990; Iliev et al., 2003; Furlanetto et al., 2004). By looking for 21cm signatures, observations would be directly probing the neutral regions of the Universe since the Gunn-Peterson trough saturates only at a neutral filling factor of $\sim 10^{-5}$. Lastly, additional searches for high redshift starbursts (e.g. Ellis et al., 2001; Pello et al., 2004) in lensed fields will furnish an understanding of the characteristics of these objects and help tighten our models of early “normal” and primordial star formation.

⁵<http://swift.gsfc.nasa.gov/>

Metal-free stars with masses between $\sim 140\text{--}260M_{\odot}$ result in a SNe that is visible and eject heavy elements into the IGM. When a star is within this range, the stellar core has sufficient entropy after helium burning to create positron/electron pairs. These pairs convert the gas energy into mass while not greatly contributing to pressure. This creates a major instability, where the star contracts rapidly until oxygen and silicon implosive burning occurs. Then the star totally disrupts itself by these nuclear explosions and leaves no remnant (Barkat et al., 1967; Bond et al., 1984). Stars between $\sim 100\text{--}140M_{\odot}$ experience this instability. It is not violent enough to disrupt the star, but pulsations and mass loss occur until equilibrium is reached and the hydrogen envelope is ejected (Bond et al., 1984; Heger & Woosley, 2002).

Metal production from primordial stars cannot account for the volume filling factor of metals as seen in Ly α clouds in current models (Norman et al., 2004). To further test this work, we determine a volume-averaged metallicity of $[\text{Fe}/\text{H}] \lesssim -4.1$ using our SNe densities and the metal production of pair-instability SNe (Heger & Woosley, 2002). Therefore, ubiquitous star formation in protogalaxies most likely polluted the sparse regions of the Universe. Combining the primordial and protogalaxy metal output, simulations with proper metal transport should agree with the abundances observed in Ly α clouds. Such simulations that takes into account both of these metal sources and matches the results of Songaila & Cowie (1996) and Songaila (2001) is needed to constrain star formation before reionization.

Numerical simulations are also needed to investigate radiative transfer from a protogalaxy stellar population. This scenario will contain more complexities than a single primordial star in a spherical halo as in Whalen et al. (2004). With a protogalactic simulation with the Jeans length resolved, star formation and feedback, and radiative transfer, it will be possible to study the evolution of the ISM in a protogalaxy, which will produce insight and better constraints on the photon escape fraction, f_{esc} , in the Lyman continuum at high redshifts. Ricotti et al. (2002a,b) thoroughly study radiative transfer around protogalaxies; however, f_{esc} is still a parameter when it should be determined from the radiative transfer results in the simulations. Ideally, the analytical ideas about ionizing the Universe in Madau (1995); Haardt & Madau (1996); Madau et al. (1999) should be realized in such simulations but in the context

of the current paradigm of a high redshift reionization as indicated by WMAP. Also we may hope by using numerical radiative transfer techniques for line and continuum radiation in three dimensions to push the simulations of Abel et al. (2002) to follow the entire accretion phase of the first stars. This would lead to stronger constraints on the masses of the very first stars.

2.5 Summary

The WMAP measurement of optical depth to electron scattering places a constraint of early cosmological reionization of the universe, which we show to be mainly from star formation in protogalaxies. This general result is in agreement with other studies of reionization after WMAP (e.g. Cen, 2003a; Somerville & Livio, 2003; Ciardi et al., 2003; Ricotti & Ostriker, 2004a; Sokasian et al., 2004).

- The radiation from protogalaxies squelches primordial star formation, and ~ 0.34 *primordial SNe deg⁻² yr⁻¹* are expected. SNe rates can vary from 0.1 to >1.5 deg⁻² yr⁻¹ depending on the choice of primordial stellar mass and protogalaxy parameters while still constrained by the WMAP result. The peak of SNe rate occurs *earlier* with *increasing primordial stellar masses*. These results are upper limits since the rate of visible primordial SNe depends on the IMF because only a fraction will lie in the pair instability SNe mass range. The other massive primordial stars might result in jet-driven SNe or long duration GRBs.
- Stellar metal abundances and star formation in local dwarf galaxies aid in estimating protogalaxy characteristics. We choose $f_{\star} = 0.04$ and $f_{esc} = 0.050$ in our $100 M_{\odot}$ model. In protogalaxies, the star formation efficiency is slightly lower than local values, but the photon escape fraction is within local observed fractions.
- Primordial stars enrich the IGM to a maximum volume-averaged $[\text{Fe}/\text{H}] \simeq -4.1$ if the IMF is skewed toward the pair-instability upper mass range. A proper IMF will lessen this volume-averaged metallicity since only a fraction of stars will exist in this mass range.

- The entire error bar of the WMAP measurement of optical depth to electrons can be explained by a higher/lower f_* and f_{esc} . Protogalaxies can ionize the IGM easily since low metallicity starburst models produce 20–80% more ionizing photons than previously used ($Z = 0.001$) IMFs. Massive primordial stars provide $\sim 10\%$ of the necessary photons to achieve reionization. No exotic processes or objects are necessary.
- Only the upper mass range of pair instability SNe will be observable with JWST since the low mass counterparts do not produce enough ^{56}Ni to be very luminous.

Although the IMF of primordial stars is unknown, simulations have hinted that a fraction of metal-free stars may exist in the pair-instability mass range. When observational rates, light curves, and spectra are obtained from future surveys, these data would provide very stringent constraints on the underlying CDM theory as well as our understanding of primordial star formation.

Chapter 3

The Virialization of Baryons in Protogalaxies

Galaxy formation entails a complex interplay of many processes, e.g. star formation, hydrodynamics, central black holes, hierarchical merging, and non-local radiative feedback. The philosophy of the rest of this thesis aims to isolate the effects of each relevant process in galaxy formation. In this light, we start with a set of control simulations that use a simple model of galaxy formation. We consider the hydrodynamics and gas chemistry of early galaxy formation. These calculations provide a basis for comparison against more complicated simulations that include primordial star formation and feedback. Nevertheless even in the absence of star formation and feedback, the gas dynamics of a hierarchically assembling and virializing object proves to be a rich subject, which we detail in this chapter.

This chapter has been submitted to *The Astrophysical Journal* for publication. This paper is co-authored by Tom Abel, who suggested many of the analysis techniques and their physical interpretations.

3.1 Introduction

The process of virialization is clearly fundamental to all scales of galaxy formation. Lynden-Bell (1967) demonstrated that violent relaxation occurs during the virialization of a dissipationless system, but does the equivalent occur for the baryonic matter? If it does, how it achieves virial equilibrium should be inherently different because of hydrodynamical effects and radiative cooling. Additionally, this would create a Maxwellian velocity distribution for the baryons as well. Turbulent velocities would exceed rotational ones. This would be at odds with the standard galaxy formation theories, which generally assume smooth rotating gaseous distributions (e.g. Crampin & Hoyle, 1964; Fall & Efstathiou, 1980; Mo et al., 1998). The first occurrence of widespread star formation can be regarded as the commencement of galaxy formation, and its feedback on its host will affect all subsequent star formation. It is crucial to model the initial stage of galaxy formation accurately. Differences in initial configurations of a collapsing halo may manifest itself in different types of central luminous objects, whether it be a stellar disk (Fall & Efstathiou, 1980; Mo et al., 1998), a starburst (see §4 in Kennicutt, 1998, for a review), or a massive black hole (Bromm & Loeb, 2003; Volonteri et al., 2005; Spaans & Silk, 2006; Begelman et al., 2006). These differences may result from varying merger histories and the ensuing virial heating or turbulence generation of the new cosmological halo.

For galaxy clusters, cosmological virialization has been studied extensively (Norman & Bryan, 1999; Nagai & Kravtsov, 2003a; Nagai et al., 2003b; Schuecker et al., 2004; Dolag et al., 2005). It is customary to connect the velocity dispersion to a temperature through the virial theorem for a collisionless system, where the potential energy equals twice the kinetic energy. However X-ray observations and such cosmological simulations of galaxy clusters have indicated that turbulent energies are comparable to thermal energies. Central turbulent pressure decreases the density, but the temperature is largely unchanged. This leads to an increased entropy and a flatter entropy radial profile (Dolag et al., 2005) that is in better agreement with X-ray observations (e.g. Ponman et al., 1999). Simulations of merger dynamics suggest that turbulence is mostly generated in Kelvin-Helmholtz instabilities between bulk

flows and virialized gas during minor mergers (e.g. Ricker & Sarazin, 2001; Takizawa, 2005). Alternatively turbulence can be generated by conduction (Kim & Narayan, 2003; Dolag et al., 2004) or acoustic transport of energy (Norman & Bryan, 1999; Cen, 2005).

In standard galaxy formation models (Rees & Ostriker, 1977; Silk, 1977; White & Rees, 1978; Blumenthal et al., 1984; White & Frenk, 1991; Mo et al., 1998), gas shock-heats to the virial temperature as it falls into DM halos. These models succeed with considerable accuracy in matching various observables, such as star formation histories, galaxy luminosity functions, and the Tully-Fisher relationship (White & Frenk, 1991; Lacey & Silk, 1991; Cole et al., 1994, 2000). Galaxy formation models depend on the virial temperature, most notably through the cooling function that controls star formation rates and their associated feedback mechanisms. Atomic hydrogen and helium radiative cooling is efficient in halos with masses between 10^8 and $10^{12}M_{\odot}$ as cooling times can be less than the dynamical time of the system, a condition that galaxy clusters do not satisfy. This strong cooling suggests that in galaxies thermal energy may be less important for virialization than turbulent kinetic energy. Motivated by the results of galaxy cluster turbulence, we investigate this potentially important role of turbulence and radiative cooling in galaxy formation, using a series of high resolution numerical simulations of protogalactic halos in this work.

We consider kinetic energy and pressure forces in our virial analysis of protogalactic halos (cf. Shapiro et al., 1999; Iliev & Shapiro, 2001). This allows us to investigate the equilibrium throughout the entire halo and determine the importance of each energy component in the virial theorem. Kinetic energy can be decomposed into radial and azimuthal motions along with turbulence, which affects the collapse of gas clouds primarily in three ways. First as seen in galactic molecular clouds, turbulence plays an integral part in current theories of star formation as the density enhancements provide a favorable environment for star formation (Larson, 1979, 1981; Myers, 1999; Goldman, 2000). Second if the turbulence is supersonic, gas dissipates kinetic energy through radiative cooling, which aids the gaseous collapse (Rees & Ostriker, 1977). Conversely turbulent pressure adds an additional force for the

collapsing object to overcome and can delay the collapse into a luminous object. Last, turbulence provides an excellent channel for angular momentum transport as the halo settles into rotational equilibrium to satisfy Rayleigh’s inviscid rotational stability argument (Rayleigh, 1920; Chandrasekhar, 1961) in which the specific angular momentum must increase with radius. Cosmological hydrodynamic simulations have just begun to investigate angular momentum transport within turbulent collapsing objects, and turbulence seems to play a large role in segregating low (high) angular momentum gas to small (large) radii (Norman & Bryan, 1999; Abel et al., 2002; Yoshida et al., 2006b).

We study idealized cases of structure formation where stellar feedback is ignored because it provides a convenient problem to focus on the interplay between cosmological merging, hydrodynamics, and cooling physics during the assembly of early halos. Some of the discussed physical principles should, however, be applicable to galaxies of all masses. These simulations provide the simplest scenario to which we can incrementally consider further additional physics, such as H_2 and HD cooling physics (Saslaw & Zipoy, 1967; Palla et al., 1983; Flower et al., 2000), primordial stellar feedback (Whalen et al., 2004; Kitayama et al., 2004; Alvarez et al., 2006; Yoshida et al., 2006a; Abel et al., 2007), metal enrichment from primordial stars (Heger & Woosley, 2002; Tumlinson, 2006), AGN feedback (Springel et al., 2005; Kuhlen & Madau, 2005), and “normal” metal-enriched star formation (see Larson, 2003, for a review).

We present a suite of adaptive mesh refinement simulations that are described in §2. Then we analyze the local virial equilibrium and shocks in halos in §3. There we also differentiate between infall through voids and filaments and its associated virialization. We discuss the situations in which virial heating and turbulence occur. Next in §4, we decompose the velocity distribution in principle axes to explore virialization in both the DM and baryonic components. Furthermore we decompose velocities into shear and compressible flows to study turbulent flows in the virialized gas. We discuss the implications of these results on star and galaxy formation in §5. Finally we summarize in the last section.

3.2 The Simulations

To investigate protogalactic ($T_{\text{vir}} > 10^4$ K) halo virialization in the early universe, we utilize an Eulerian structured, adaptive mesh refinement (AMR), cosmological hydrodynamical code, *Enzo*¹ (Bryan & Norman, 1997, 1999; O’Shea et al., 2004). *Enzo* solves the hydrodynamical equations using the second order accurate piecewise parabolic method (Woodward & Colella, 1984; Bryan et al., 1995), while a Riemann solver ensures accurate shock capturing with minimal viscosity. Additionally *Enzo* uses an adaptive particle-mesh n -body method to calculate the dynamics of the collisionless dark matter particles (Couchman, 1991). Regions of the simulation grid are refined by two when one or more of the following conditions are met: (1) Baryon density is greater than 3 times $\Omega_b \rho_0 N^{l(1+\phi)}$, (2) DM density is greater than 3 times $\Omega_{\text{CDM}} \rho_0 N^{l(1+\phi)}$, and (3) the local Jeans length is less than 4 cell widths. Here $N = 2$ is the refinement factor; l is the AMR refinement level; $\phi = -0.3$ causes more frequent refinement with increasing AMR levels, i.e. super-Lagrangian behavior; $\rho_0 = 3H_0^2/8\pi G$ is the critical density; and the Jeans length, $L_J = \sqrt{15kT/4\pi\rho G\mu m_H}$, where H_0 , k , T , ρ , μ , and m_H are the Hubble constant, Boltzmann constant, temperature, gas density, mean molecular weight in units of the proton mass, and hydrogen mass, respectively. The Jeans length refinement ensures that we meet the Truelove criterion, which requires the Jeans length to be resolved by at least 4 cells on each axis (Truelove et al., 1997).

We conduct the simulations within the concordance Λ CDM model with WMAP first year parameters (WMAP1) of $h = 0.72$, $\Omega_\Lambda = 0.73$, $\Omega_M = 0.27$, $\Omega_b = 0.024h^{-2}$, and a primordial scale invariant ($n = 1$) power spectrum with $\sigma_8 = 0.9$ (Spergel et al., 2003). h is the Hubble parameter in units of $100 \text{ km s}^{-1} \text{ Mpc}^{-1}$. Ω_Λ , Ω_M , and Ω_b are the fractions of critical energy density of vacuum energy, total matter, and baryons, respectively. Last σ_8 is the rms of the density fluctuations inside a sphere of radius $8h^{-1} \text{ Mpc}$.

Using the WMAP1 parameters versus the significantly different WMAP third year parameters (WMAP3; Spergel et al., 2006) have no effect on the evolution of

¹See <http://lca.ucsd.edu/portal/software/enzo>

individual halos as are considered here. However these changes play an important role in statistical properties. For example, halos with mass $10^6 M_\odot$ at redshift 20 correspond to 2.8σ peaks with the WMAP1 but are 3.5σ peaks for WMAP3. The Ω_M/Ω_b ratio also only changed from 6.03 to 5.70 in WMAP3.

We also have verified that there is nothing atypical about the mass accretion rate histories of the objects we study. The mass accretion history of these objects exhibit smooth growth during minor mergers and accretion and dramatic increases when a major merger occurs. This behavior is consistent with typical halo assemblies in extended Press-Schechter calculations (Bond et al., 1991; Bower, 1991; Lacey & Cole, 1993, 1994; van den Bosch, 2002) and cosmological numerical simulations (e.g. De Lucia et al., 2004; Gao et al., 2005). The mass accretion histories in our simulations are well described by the fitting function of van den Bosch with $M_0 = 3 \times 10^7 M_\odot$, $z_f = 17$, and $\nu = 12.5$. We also compare our data against the mass accretion histories of Gao et al., who tested their data against an extended Press-Schechter calculation of the growth history of the halos. We find no major discrepancies between the two histories.

The initial conditions of this simulation are well-established by the primordial temperature fluctuations in the cosmic microwave background (CMB) and big bang nucleosynthesis (BBN) (Hu & Dodelson, 2002; Burles et al., 2001, and references therein).

We perform two realizations with different box sizes and random phases. In the first simulation (simulation A), we set up a cosmological box with 1 comoving Mpc on a side, periodic boundary conditions, and a 128^3 top grid with three nested child grids of twice finer resolution each. The other simulation is similar but with a box side of 1.5 comoving Mpc (simulation B). We provide a summary of the simulation parameters in Table 3.1. These volumes are adequate to study halos of interest because the comoving number density of $>10^4$ K halos at $z = 10$ is $\sim 6 \text{ Mpc}^{-3}$ according to an ellipsoidal variant of Press-Schechter formalism (Sheth & Tormen, 2002). We use the COSMICS package to calculate the initial conditions at $z = 129$ (119)[†] (Bertschinger,

[†]To simplify the discussion, simulation A will always be quoted first with the value from simulation B in parentheses.

1995, 2001), which calculates the linear evolution of matter fluctuations. We first run a dark matter simulation to $z = 10$ and locate the DM halos using the HOP algorithm (Eisenstein & Hut, 1998). We identify the first dark matter halo in the simulation with $T_{\text{vir}} > 10^4$ K and generate three levels of refined, nested initial conditions with a refinement factor of two, centered around the Lagrangian volume of the halo of interest. The nested grids that contain finer grids have 8 cells between its boundary and its child grid. The finest grid has an equivalent resolution of a 1024^3 unigrid. This resolution results in a DM particle mass of 30 (101) M_{\odot} and an initial gas resolution of 6.2 (21) M_{\odot} .

Table 3.1: Simulation Parameters

Name	l	z_{end}	N_{part}	N_{grid}	N_{cell}	Cooling model
	[Mpc]					
A0	1.0	15.87	2.22×10^7	30230	9.31×10^7 (453 ³)	Adiabatic
A6	1.0	15.87	2.22×10^7	40486	1.20×10^8 (494 ³)	H,He
A9	1.0	18.74	2.22×10^7	45919	1.21×10^8 (495 ³)	H,He,H ₂
B0	1.5	16.80	1.26×10^7	23227	6.47×10^7 (402 ³)	Adiabatic
B6	1.5	16.80	1.26×10^7	21409	6.51×10^7 (402 ³)	H,He
B9	1.5	23.07	1.26×10^7	20525	5.59×10^7 (382 ³)	H,He,H ₂

Note. — Col. (1): Simulation name. Col. (2): Number of dark matter particles. Col. (3): Number of AMR grids. Col. (4): Maximum number of unique grid cells. Col. (5): Maximum level of refinement reached in the simulation. Col. (6): Resolution at the maximum refinement level. Col. (7): Cooling model.

Enzo employs a non-equilibrium chemistry model (Abel et al., 1997; Anninos et al., 1997). We conduct three simulations for each realization with (i) the adiabatic equation of state with an adiabatic index $\gamma = 5/3$, (ii) a six species chemistry model (H, H⁺, He, He⁺, He⁺⁺, e⁻), and (iii) a nine species chemistry model that adds H₂, H₂⁺, and H⁻ to the six species model. In the nine species model, we use the molecular hydrogen cooling rates from Galli & Palla (1998). These models are differentiated

in the text by denoting 0, 6, and 9, respectively, after the simulation name (e.g. simulation B0). Compton cooling and heating of free electrons by the CMB and radiative losses from atomic and molecular cooling are also computed in the optically thin limit.

To restrict the analysis to protogalactic halos in the H_2 models, we suppress H_2 formation in halos that cannot undergo $\text{Ly}\alpha$ cooling by reducing the residual electron fraction to 10^{-12} instead of a typical value of $\sim 10^{-4}$ only at the initial redshift (Shapiro et al., 1994). This mimics an extreme case where all H_2 is dissociated by an extremely large radiation background, and the halo can only collapse and form stars when free electrons from ionized hydrogen can catalyze H_2 formation.

We end the simulations with non-equilibrium cooling when the gas begins to rapidly cool and collapse. We choose a final resolution limit of ~ 3000 (4000) proper AU, corresponding to a refinement level of 15. We end the adiabatic simulations at the same redshift. In a later paper, we will address the collapse of these halos to much smaller scales.

3.3 Virial Analysis

The equation of motion for an inviscid gas in tensor notation reads:

$$\rho \frac{Dv_i}{Dt} = -\frac{\partial}{\partial x_i} p + \rho g_i \quad (3.1)$$

where $D/Dt = \partial/\partial t + v_j \partial/\partial x_j$ is the total derivative. Here v is velocity; p is pressure; ρ is density; and $g = \nabla\Phi$ where Φ is the gravitational potential. From this Chandrasekhar & Fermi (1953) derived the general virial theorem for a region contained within a surface \mathbf{S} , in scalar form,

$$\frac{1}{2} \frac{D^2 I}{Dt^2} = 2\mathcal{T} + \mathcal{V} + 3(\gamma - 1)\mathcal{E} - \int p \mathbf{r} \cdot d\mathbf{S}, \quad (3.2)$$

where

$$\mathcal{V} = -\frac{1}{2} G \int_V \frac{\rho(\mathbf{x})\rho(\mathbf{x}')}{|\mathbf{x} - \mathbf{x}'|} d\mathbf{x}d\mathbf{x}', \quad (3.3)$$

$\mathcal{T} = \frac{1}{2} \int \rho \mathbf{v}^2 d\mathbf{x}$, $I = \int \rho \mathbf{x}^2 d\mathbf{x}$, and $\mathcal{E} = \int \varepsilon d\mathbf{x}$ denote the gravitational potential energy, the trace of the kinetic energy and inertia tensor, and the total internal thermal energy, respectively. The surface term E_s (the last term in eq. [3.2]) is often negligible in the outer regions of the halo. The system is not necessarily in virial equilibrium if $\dot{I} \neq 0$, but the time-averaged quantity is zero when the entire system is in virial equilibrium. A system is expanding or contracting when \dot{I} is positive or negative, respectively, based on energy arguments. Ballesteros-Paredes (2006) gives counterexamples to this simple interpretation. However, in the cases presented here, spherically averaged radial velocities are always negative.

We define the halo as the material contained in a sphere with a radius r_{200} enclosing an average DM overdensity of 200 and as such relates to mass by

$$r_{200} = \left[\frac{GM}{100\Omega_{\text{CDM}}(z)H^2(z)} \right]^{1/3}, \quad (3.4)$$

where M is the mass of the halo, $\Omega_{\text{CDM}}(z)$ is evaluated at a redshift z , and H is the Hubble parameter at z . The region where the cooling time is shorter than a Hubble time is denoted as the cooling radius r_{cool} ,

$$t_{\text{cool}}(r_{\text{cool}}) \equiv H(z)^{-1} \quad (3.5)$$

(White & Frenk, 1991). Mass and radius define a circular velocity and virial temperature, which are

$$V_c = \sqrt{\frac{GM}{r_{200}}} \quad \text{and} \quad T_{\text{vir}} = \frac{\mu m_p V_c^2}{2k}, \quad (3.6)$$

for a singular isothermal sphere (see Bryan & Norman, 1998, with $\beta = 1$ and $\Delta_c = 200$). 0.59 and 1.22 in units of the proton mass are appropriate values for μ for the fully ionized and completely neutral states of a primordial hydrogen and helium mixture of gas, respectively. We use $\mu = 1.22$ throughout this paper. We note that Iliev & Shapiro (2001) considered non-singular, truncated isothermal spheres, and the resulting virial temperature is $\sim 15\%$ lower than the one calculated in equation (3.6).

For $\gamma = 5/3$, T_{vir} is the temperature at which an ideal adiabatic gas reaches virial

equilibrium with the specified potential. Please note that for an isothermal gas where γ is close to unity virial equilibrium is established between the turbulent energies and the gravitational potential as the $3(\gamma - 1)\mathcal{E}$ term in equation (3.2) goes to zero.

3.3.1 Local Analysis

We evaluate the terms of equation (3.2) with respect to radius (i.e. the volume contained in a radius r). Figure 3.1 illustrates the radial structure of (a) the turbulent Mach number,

$$\mathcal{M}_{turb} = \frac{v_{rms}}{c_s}; \quad c_s = \sqrt{\frac{\gamma kT}{\mu m_h}} \quad (3.7)$$

(b) turbulent and (c) thermal energies per m_h , and (d) a “virialization” parameter³

$$\beta = \frac{3(\gamma - 1)\mathcal{E} + 2\mathcal{T}}{E_s - \mathcal{V}} - 1, \quad (3.8)$$

of the adiabatic and radiative cooling simulations when the cooling halo collapses. Here v_{rms} is the three-dimensional rms velocity and is assessed using the gas velocities relative to the mean gas velocity of each spherical shell. In the top row of Figure 3.1, we also plot the Mach number, using v_{rms} with respect to the mean velocity of the gas within r_{200} . In the six and nine species simulation, this occurs at $z_{c,H_2} = 18.7$ (23.4) and $z_{c,Ly\alpha} = 15.9$ (16.8), respectively. The radial profiles are centered on the densest point in the simulation with the collapsing halo. Several properties of the most massive halo in each simulation are detailed in Table 3.2. The sections of the Table compare the halo in the adiabatic, Ly α , and H₂ simulations.

Figure 3.2 shows the mass-weighted radial profiles of gas mass enclosed and gas density at $z = z_{c,Ly\alpha}$ in the adiabatic and cooling cases. Both realizations are remarkably similar. Halos in the adiabatic case have a central core with a radius ~ 50 pc and gas density of ~ 5.0 (3.5) cm^{-3} . Core densities in simulation A are slightly higher than simulation B, which has larger thermal and turbulent pressures (see Figure 3.1).

³This is a modified version of the β used in Shaw et al. (2006) to account for kinetic energies and so that it does not diverge when $\mathcal{V} \rightarrow 0$ in the center. It still has the same behavior of $\beta \rightarrow 0$ as $\dot{I} \rightarrow 0$.

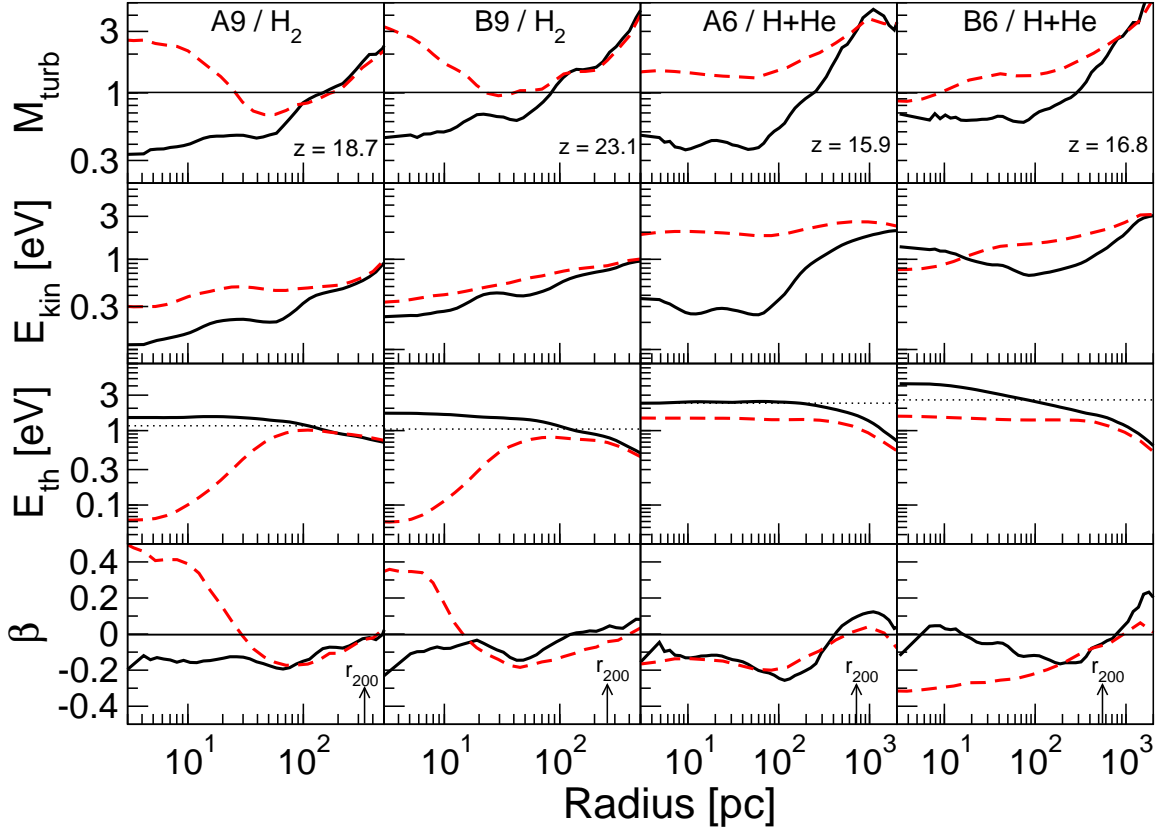


Fig. 3.1.— A comparison of (*top to bottom*) turbulent Mach numbers, turbulent and thermal energies, and virial parameters between simulations with radiative cooling (*dashed*) and adiabatic models (*solid*). The main coolant is listed at the top of each column. The *first* and *second* columns display the state of these variables at $z = z_{c,\text{H}_2} = 18.7$ (23.1) for Simulation A and B, respectively. The *third* and *fourth* columns are the data at $z = z_{c,\text{Ly}\alpha} = 15.9$ (16.8). The *top* row depicts the importance of radiative cooling in generating trans- and super-sonic turbulence throughout the halo during virialization. The *middle* two rows show that when radiative cooling is efficient the halo cannot virialize through heating but must virialize by increasing its kinetic (turbulent) energies. The dotted line in the *third* row marks T_{vir} (eq. [3.6]) with $\mu = 1.22$, estimated from the total halo mass. We plot the virialization parameter β (eq. [3.8]) to investigate the local virial equilibrium ($\beta = 0$), particularly at r_{200} . Furthermore, β allows us to determine the mass-averaged dynamics of the system at a given radius, where $\beta > 0$ and < 0 correspond to decelerating and accelerating collapses, respectively. r_{200} (eq. [3.4]) is marked on the bottom of each column.

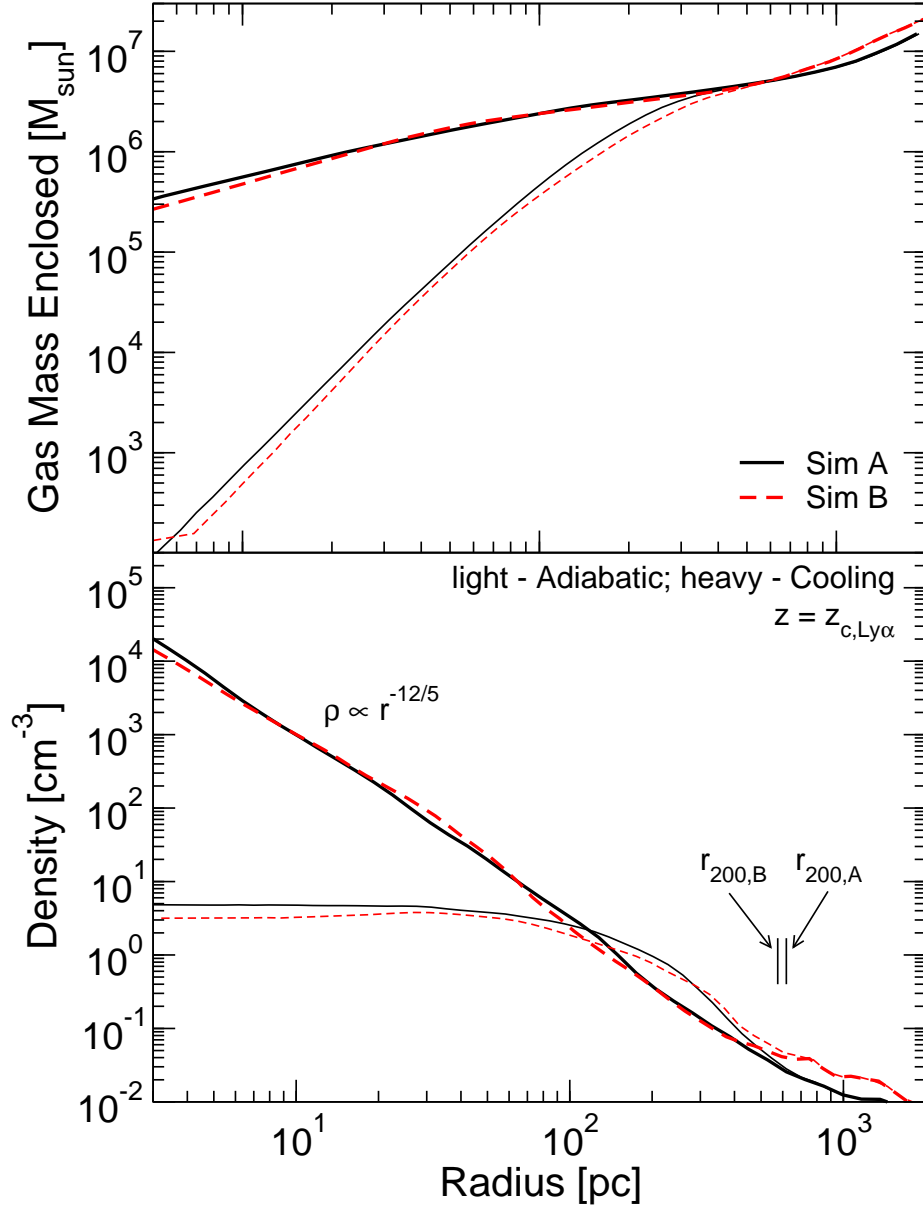


Fig. 3.2.— Mass-weighted radial profiles for gas mass enclosed (*top*) and number density (*bottom*) for Simulations A (*solid black*) and B (*dashed red*) at $z = z_{c, \text{Ly}\alpha} = 15.9$ (16.8). The *light* and *heavy* lines represent data for adiabatic and cooling models, respectively. The virial shock in the cooling halos occurs at $\frac{2}{3}r_{200}$, illustrated by the density increasing at smaller radii.

Table 3.2: Halo Properties

Name	z_{coll}	M_{tot} [M_{\odot}]	ρ_c [cm^{-3}]	T_{vir}^a [K]	T_c [K]	$\langle T \rangle$ [K]
H ₂ Induced Collapse						
A0	18.74	9.8×10^6	8.1	9200	10000	5700
A6	18.74	9.8×10^6	17	9200	7700	5500
A9	18.74	9.8×10^6	1.6×10^6	9100	590	5000
B0	23.07	6.2×10^6	13	8300	12000	6000
B6	23.07	6.2×10^6	15	8300	8900	5600
B9	23.07	6.7×10^6	3.0×10^6	8700	580	4200
Ly α Induced Collapse						
A0	15.87	3.6×10^7	4.9	19000	17000	12000
A6	15.87	3.6×10^7	1.8×10^6	19000	8700	7300
B0	16.80	3.5×10^7	3.8	19000	31000	11000
B6	16.80	3.6×10^7	4.0×10^6	20000	9000	7500

Note. — Col. (1): Simulation name. Col. (2): Redshift of collapse through H₂ or Ly α cooling. Col. (3): Total mass. Col. (4): Central density. Col. (5): Virial temperature (i.e. eq. 3.6). Col. (6): Central temperature. Col. (7): Mass-averaged temperature of the entire halo.

^bVirial temperatures are calculated with $\mu = 1.22$ in all cases.

With radiative cooling, gas infalls rapidly as it cools and undergoes a self-similar collapse with $\rho \propto r^{-12/5}$.

Virial Radius

We define the virial radius r_{vir} when $\beta = 0$ and $d\beta/dr < 0$. When we radially average the Ly α halo, $r_{\text{vir}} = 419$ (787) pc in the adiabatic simulations where the corresponding r_{200} value is 615 (576) pc.

A well defined shock exists on the interface between voids and the halo. This material shock-heats to T_{vir} and virializes at a radius comparable to r_{200} in the adiabatic cases. When we include radiative cooling, this radius decreases everywhere around the halo-void virial shock and is low as $r_{200}/2$. In contrast to the voids, the filamentary gas shock-heats at an even smaller radius. Dekel & Birnboim (2006) also studied the stability of cold inflows within a hot virialized medium and found similar results. Figures 3.2 and 3.3 illustrate these changes. At r_{200} , densities in the adiabatic case begin to increase more rapidly than the cooling case as material accretes at the virial shock. No significant increase in $d\rho/dr$ is seen in the cooling case, indicative of a self-similar collapse.

Adiabatic Model

We start with the discussion of the adiabatic model as it is the simplest case and later compare the calculations with radiative cooling to this model. Virialization should transfer potential energy to kinetic energy that dissipates in shocks to thermal energy, which is the implication of the dissipationless virial theorem. The solid lines in Figure 3.1 represent the energies in adiabatic models. The physics illustrated in this Figure are as follows:

1. *Thermal energy*— The gas shock-heats to the virial temperature at the virial shock. Virial heating continues with decreasing radius as the surface term becomes significant in the interior. The resulting central temperature of the halo is 10000 (12000) K, which is 1.2 (1.5) T_{vir} , at a redshift of $z_{\text{c,H}_2}$ when the H₂ model collapses. At the time ($z = z_{\text{c,Ly}\alpha}$) of collapse caused by Ly α cooling, the central temperature

is 17000 (31000) K, corresponding to 0.9 (1.6) T_{vir} .

2. *Kinetic energy*— It increases along with the thermal energy during virialization. The gas is generally turbulent, appearing as a velocity dispersion with a bulk radial inflow. At r_{200} , the kinetic energy is equivalent to the thermal energy, $\mathcal{T}/\mathcal{E} \sim 1$. This ratio steadily drops toward the center, where $\mathcal{T}/\mathcal{E} \sim 1/3$. This decrease in kinetic energy is apparent in all the calculations except simulation B at $z_{\text{c,Ly}\alpha}$, increasing by a factor of two in the center.

3. *Turbulent Mach number*— At r_{200} , the turbulent Mach number $\mathcal{M}_{\text{turb}}$ is maximal and varies from 1–3 in all adiabatic simulations. $\mathcal{M}_{\text{turb}}$ decreases to subsonic values ~ 0.15 but never below in the interior. Note that $\mathcal{M}_{\text{turb}}$ does not increase as the turbulent energy towards the center in simulation B because of the also growing sound speed there.

4. *Virialization parameter*— Virial equilibrium is quantified by the virialization parameter β , where the collapse is retarding or accelerating when it is negative or positive, respectively. At $z_{\text{c,H2}}$ and $z_{\text{c,Ly}\alpha}$ and in both simulations, β is within 20% of being virialized ($\beta = 0$). For comparison purposes, this corresponds to a halo having 80% of the required velocity dispersion for virialization in the dissipationless case. At r_{vir} , β is nearly zero which defines the virialized object. Within r_{vir} , the values decrease to values around -0.1 but stays $\lesssim 0$.

Characteristics of turbulence in our adiabatic models are similar to ones found in galaxy cluster simulations (Norman & Bryan, 1999; Dolag et al., 2005). Both groups find that turbulence provides $\sim 5\text{--}30\%$ of the total pressure, i.e. $\mathcal{T}/(\mathcal{T} + \mathcal{E})$, in the cluster cores. Our protogalactic halos have $\sim 25\%$ of the pressure in the turbulent form. Also the galaxy clusters in Norman & Bryan (1999) have comparable Mach numbers of ~ 1.6 at r_{vir} , ~ 0.5 at $r_{\text{vir}}/3$, and ~ 0.3 in the core. These similarities suggest that virial turbulence is generated over a large range of mass scales.

Ly α Cooling Model

At $z_{\text{c,Ly}\alpha}$, halos in calculations with the H+He cooling model start to rapidly collapse. The dashed lines in the third and fourth columns of Figure 3.1 illustrate the energies

of this model.

1. *Thermal energy*— Compared to the adiabatic models, the gas can radiatively cool through Ly α emission to $T \sim 8000$ K within $r_{\text{cool}} \sim r_{\text{vir}}$. The entire halo is isothermal at this equilibrium temperature. Below this temperature, the cooling function of pristine gas drops by several orders of magnitude, and the gas can no longer cool efficiently. The thermal energy is $\sim 65\%$ lower than the adiabatic case.

2. *Kinetic energy*— In response to the lesser thermal energy, the system tends toward virial equilibrium by increasing kinetic (turbulent) energy. The gravitational potential and surface terms do not appreciably change with the inclusion of radiative cooling. Turbulent energy within r_{vir} increases as much as a factor of 5 when compared to the adiabatic case.

3. *Turbulent Mach number*— The changes in thermal and kinetic energies equate to a increase of $\mathcal{M}_{\text{turb}}$ by a factor of 2–3 to values up to 1.5. The turbulence is supersonic in all cases at the virial shock, but when we include radiative cooling, this trait emanates inward as the halo begins to rapidly cool. When the central core becomes gravitationally unstable, the entire halo is supersonically turbulent.

4. *Virialization parameter*— The increased kinetic energies compensate for the loss in thermal energy and the halo remains in a similar virial state. This is apparent in the remarkably similar radial characteristics of β in the adiabatic and H+He models of simulation A.

H₂ Cooling Model

The collapses caused by H₂ cooling at $z = z_{\text{c,H}_2}$ have very similar dynamics as the halos described in the previous section. The dashed lines in the first and second columns of Figure 3.1 illustrate the energies of this model.

1. *Thermal energy*— H₂ cooling is efficient down to 300 K, so gas can depose a much larger fraction of its thermal energy. Inside $r_{\text{cool}} \sim 0.32$ (0.19) r_{vir} , thermal energies are only 5% of the values in the adiabatic models.

2. *Kinetic energy*— The turbulent energies must increase as in the Ly α case, and they increase by 93% (44%) on average inside r_{cool} .

3. *Turbulent Mach number*— Similarly, $\mathcal{M}_{\text{turb}}$ increases up to a factor of 10 to become supersonic at values up to 3 throughout the halo. They are somewhat larger than the Ly α cases since H₂ can cool to significantly lower temperatures than the virial temperature.

4. *Virialization parameter*— The virial equilibrium of the halos are also similar to the other models. β smoothly transitions from nearly equilibrium at r_{vir} to an increased radial infall with $\beta = -0.2$ at 70 pc. Then it increases to 0.4 inside 10 pc, which corresponds to the gas decelerating from the rapid infall as it encounters the central molecular cloud.

Model Summary

Baryons are close to virial equilibrium over three orders of magnitude in length scale by gaining both thermal and kinetic energies independent of cooling physics. Central temperatures of the adiabatic simulations are up to twice the nominal virial temperature. Similar to galaxy cluster studies, turbulence in the adiabatic model contributes $\sim 25\%$ to the energy budget with Mach numbers ~ 0.3 in the center. In cooling cases, atomic and molecular cooling inhibit virialization through heating, therefore the object must virialize by gaining kinetic energy up to five times the energy seen in the adiabatic models. This translates into the flow becoming supersonically turbulent with Mach numbers ranging from one to three.

3.3.2 Variations in the Virial Shock

Using the adiabatic invariant, $K = T/n^{2/3}$, which we label “entropy”, allows us to differentiate between gas accreting from voids and filaments. As a precaution, we note that K is not an invariant when γ varies; however, this is not the case in our simulations in which we permit molecular hydrogen cooling. Here molecular fractions remain low, $< 10^{-3}$, and $\gamma \approx 5/3$ even in the densest regions. The top row of Figure 3.3 depicts the variance of K with respect to radius in two-dimensional

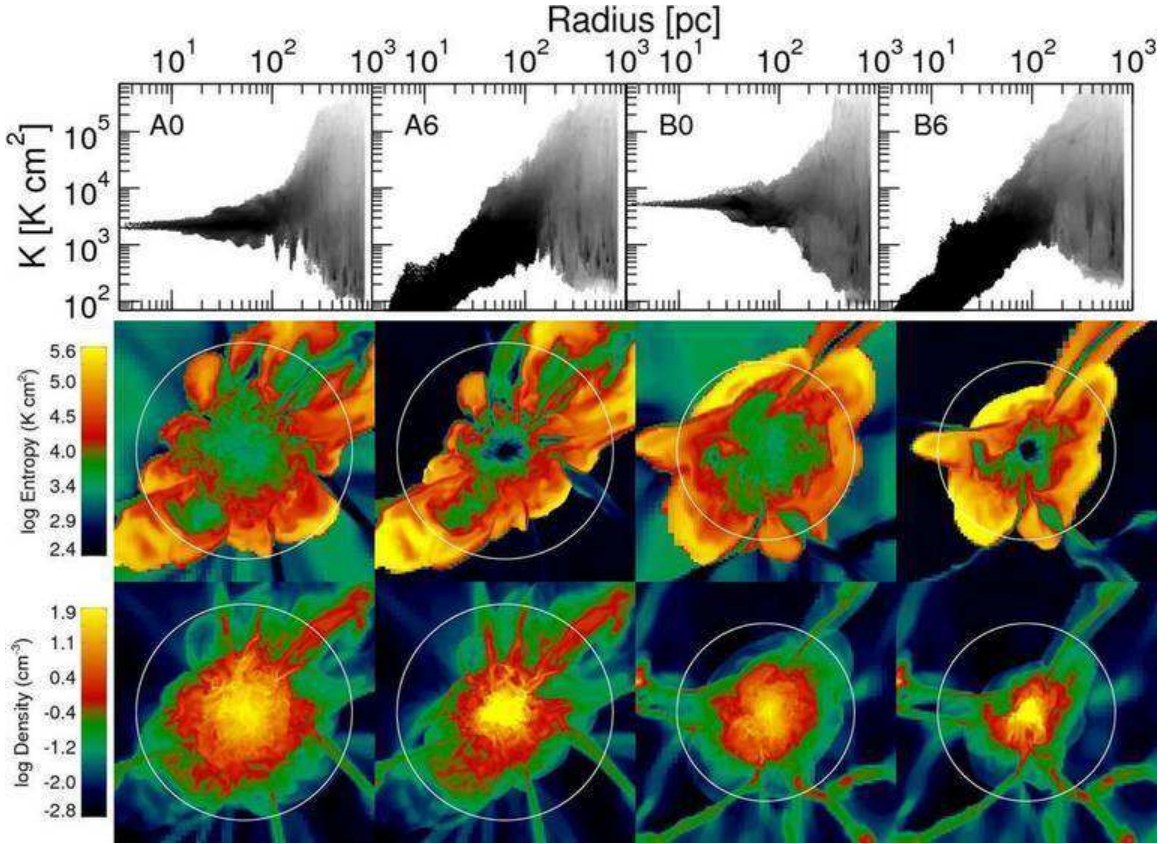


Fig. 3.3.— Differences in entropy and density in a protogalactic halo at $z = z_{c, \text{Ly}\alpha}$. *Left to right*: Simulations A0, A6, B0, B6. *Top row*: Mass-averaged radial scatter plots of the adiabatic invariant $K = T/n^{2/3}$. Radiative cooling allows the gas to cool and collapse in the center that accounts for the decrease in Simulations A6 and B6. The material at $r \gtrsim 100$ pc and $K \lesssim 10^{3.3}$ K cm² corresponds to the cold flows inside filaments that illustrates that virialization occurs at different radii depending on its origin. *Middle row*: Two-dimensional slices of entropy. The circle denotes $r_{200} = 615$ pc and 576 pc for Simulation A and B, respectively. The virial shock exists at approximately r_{200} in the adiabatic models; however it shrinks to $\sim 2/3$ of r_{200} when we consider radiative cooling. *Bottom row*: Two-dimensional slices of number density of baryons.

histograms, where the intensity of each pixel represents the mass having the corresponding K and r . The middle and bottom rows display two-dimensional slices of K and density, respectively, through the densest point in the halo. The virialized gas from the voids has low density and does not significantly contribute to the mass averaged radial profiles. Figure 3.3 illustrates this gas at $r \sim r_{200}$ and $K \gtrsim 10^{4.5}$ K cm². The gas in filaments has lower entropy than the rest of the halo at $r > 150$ pc and $K \lesssim 10^{3.3}$ K cm². In equation (3.2), the pressure in the surface term is the constant at a given radius. The accreting, denser, unshocked gas in filaments has lower temperatures than the more diffuse accreting gas. The gas remains cool until it shocks and mixes well inside r_{vir} and as small as $\sim r_{\text{vir}}/4$ in the most massive filaments. Similar characteristics of cold accretion flows have been noted and discussed by Nagai & Kravtsov (2003a), Kereš et al. (2005), and Dekel & Birnboim (2006).

Entropy in the exterior of the halo differ little between adiabatic and cooling runs outside of r_{cool} . But as the gas falls within r_{cool} , it cools and condenses, which gives a lower entropy, and the r - K histograms and entropy slices display this clearly. Another significant difference in the cooling simulations is the contraction of the virial shock by a factor of 1/3 when compared to adiabatic runs. This is caused by the contraction of the cooling gas. Here the cold filaments penetrate to even smaller radii. This is also evident in the radial density profiles of Figure 3.2.

3.3.3 Virial Heating and Turbulence

In order for a system to remain in virial equilibrium as it grows in mass, additional gravitational energy is balanced through two possible mechanisms: heating of the gas ($\dot{\mathcal{E}} > 0$) and increasing the kinetic energy of the gas ($\dot{\mathcal{T}} > 0$). We differentiate between two main cases of virialization by comparing the cooling time, $t_{\text{cool}} = kT/n\Lambda$, of the system to the heating time, $t_{\text{heat}} = T_{\text{vir}}/\dot{T}_{\text{vir}} \sim \frac{3}{2}M_{\text{vir}}/\dot{M}_{\text{vir}}$ in the case of rapid mass accretion. Birnboim & Dekel (2003), Dekel & Birnboim (2006), and Wang & Abel (2007) find that radiative cooling rates are greater than heating rates from virialization for halos with masses below $10^{12}M_{\odot}$.

1. *Thermalization* ($t_{\text{cool}} > t_{\text{heat}}$)— When no efficient radiative cooling mechanisms

(e.g. H_2 , $\text{Ly}\alpha$, He I) exist, the system virializes by injecting energy into heat \mathcal{E} and partly into kinetic energy \mathcal{T} . In the process, the halo becomes pressure supported and virialized. Traditional galaxy formation scenarios only consider this thermalization while neglecting the kinetic energy term of equation (3.2). However it is important to regard kinetic energy, even in adiabatic models, as the gas violently relaxes. Turbulence velocities are similar to the velocity dispersion of the system and contributes notably to the overall energy budget as seen in adiabatic cases in Figure 3.1.

2. *Turbulence generation* ($t_{\text{cool}} < t_{\text{heat}}$)— When a cooling mechanism becomes efficient, the system now dispenses its thermal energy and loses pressure support within r_{cool} . The gas will cool to a minimum equilibrium temperature. As the cooling halo collapses and radial velocities increase, the gas still lacks enough kinetic and thermal energy to match the gravitational energy and surface term in equation (3.2). The gas becomes more turbulent in order to virialize. We see this in the second row of Figure 3.1, where turbulent energies are significantly increased well inside the halo in the cooling models as compared to the adiabatic calculations.

Through virial analyses, we have shown that turbulent energies are comparable, if not dominant, to thermal energies in galaxy formation. In the next Section, we further investigate the significance and nature of the turbulence through velocity distributions and decompositions in order to study any small-scale anisotropies in the internal flows.

3.4 Velocity Distributions

In CDM cosmogony, collisionless dark matter dominates the gravitational potential and oscillates as it stabilizes. Lynden-Bell (1967) showed how a collisionless system undergoes violent relaxation if embedded within a rapidly time-varying potential. Individual mass elements do not conserve energy during violent relaxation, only the entire system conserves energy. This behavior randomizes the energies of the mass elements, and statistical mechanics makes the resulting energy (velocity) distribution to tend to Maxwellian. Furthermore, the system “forgets” its original configuration

during virialization or the incorporation of a lesser halo. Later studies have inferred two baryonic scenarios of virialization. First, violent relaxation and the accompanying phase mixing also applies to the gaseous component (van den Bosch et al., 2002; Sharma & Steinmetz, 2005). In the other case, the gaseous component dissipates all turbulent motions and finally rigidly rotates as a solid body with a velocity appropriate to the overall spin parameter (e.g. Loeb & Rasio, 1994; Mo et al., 1998; Bromm & Loeb, 2003).

Figure 3.4 shows the velocity distributions of the dark matter and baryonic components of the halo at z_{c,H_2} in the left column and $z_{c,Ly\alpha}$ in the right column. It also overplots the simulations with adiabatic and radiative cooling. We plot the radial and tangential velocity distribution on the top and bottom rows, respectively. The velocities are taken with respect to the bulk velocity of the halo. We also transform the velocity components to align the z-axis and total angular momentum vector of the DM halo.

The radial velocity distributions at $z = z_{c,H_2}$ are approximately Maxwellian in both dark matter and gas with a skew toward infall. The infall distributions are shifted by $\sim 1 \text{ km s}^{-1}$ in the cooling case when compared to adiabatic. However at $z = z_{c,Ly\alpha}$, the effects of Ly α cooling become more prevalent in the halo when compared to H₂ cooling, shifting the radial velocity distribution by $\sim 5 \text{ km s}^{-1}$ that is caused by faster infall. These distributions have two components that represent virialized gas and infalling gas in filaments. We further discuss this in the next Section.

The tangential velocity distributions are nearly Maxwellian in all cases except for the dark matter in simulation A at $z = z_{c,Ly\alpha}$ (right panels in Figure 3.4a). This deviation from Maxwellian arises from two major mergers that occur between 25 and 85 Myr ($z = 17\text{--}21$) before the final collapse. The residual substructure from the major merger causes three distinct populations with Gaussian distributions centered at -0.2 , $+13.6$, and -6.7 km s^{-1} with $\sigma = 11.6$, 4.2 and 3.6 km s^{-1} , respectively. These distributions clearly do not resemble a solid body rotator, whose velocity distribution would contain all positive velocities. In other words the turbulent velocities exceed the typical rotational speeds.

Distributions in dark matter are broader than the gas in both simulations and

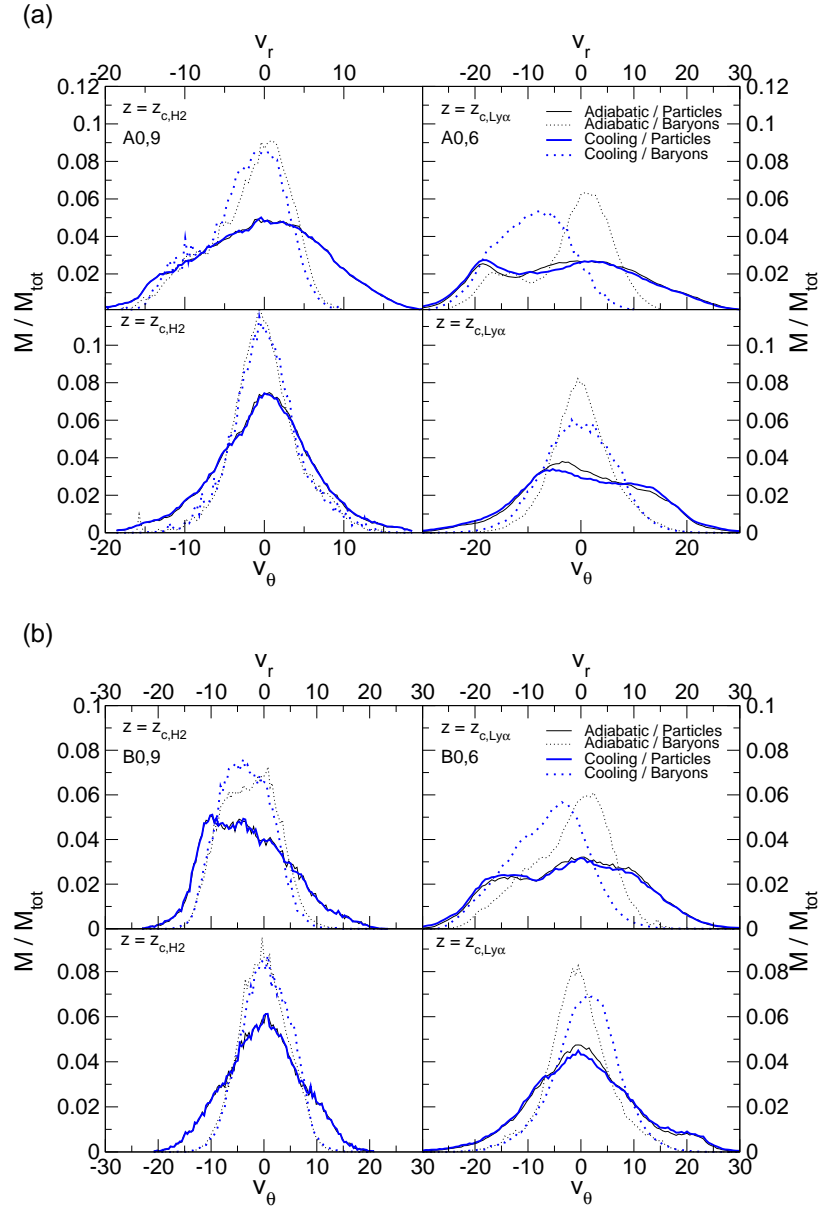


Fig. 3.4.— (a) Simulation A. (b) Simulation B. Radial (*top*) and tangential (*bottom*) velocity distributions of the most massive halo at $z = z_{c,H2}$ (*left*) and $z = z_{c,Ly\alpha}$ (*right*). The *heavy, blue* lines are the distributions of the adiabatic models, and the *light, black* lines are from the radiative cooling models. *Solid* and *dotted* lines correspond to the velocity distributions of DM and baryons, respectively. These distributions can be decomposed into single or multiple Gaussians, depending on substructure. This demonstrates that violent relaxation occurs for the baryons as well as the DM. The narrower distributions of the baryons is due to the dissipation in shocks.

collapse redshifts as expected because for the gas we only give the bulk velocities and do not add the microscopic dispersion (cf. van den Bosch et al., 2002; Sharma & Steinmetz, 2005).

3.4.1 Halo and Filament Contrasts

The dark matter velocity distributions are typical of a virialized system with the majority of the matter having a Maxwellian distribution with a dispersion corresponding to the main halo (Boylan-Kolchin & Ma, 2004; Dieman et al., 2004; Kazantzidis et al., 2004). Substructure appears as smaller, superposed Gaussians, which are stripped of its outer material as it orbits the parent halo. Dynamical friction acts on the substructure and decreases its pericenter over successive orbits, and the subhalo is gradually assimilated in the halo.

The filaments penetrate deep into the halo and provide mostly radial infall inside r_{200} . They do not experience a virial shock at r_{200} , and this contrast is apparent in the radial velocity distributions. When we restrict our analysis scope to the filaments (i.e. $r > 150$ pc and $K < 10^{3.3}$ K cm⁻²), the radial velocity distribution (Figure 3.4) is skewed toward infall, centered at -15 km/s, which is approximately the circular velocity of the halo. The rest of the gas outside of this region in $r - K$ space has already been virialized, shock heated, and roughly exhibits a Maxwellian distribution, centered at zero, with its associated substructures. Hence the mass in filaments dominate the radial velocity distributions at negative values in Figure 3.4.

3.4.2 Turbulence

Radial inflows can create turbulence in the halo. Filaments provide an influx material with distinct angular momentum. This gas virializes in the presence of an already turbulent medium that has a relatively high specific angular momentum at $r > r_{200}/4$. The Rayleigh inviscid instability criterion requires

$$\frac{dj^2}{dr} > 0 \quad \text{for rotational stability,} \quad (3.9)$$

where j is the specific angular momentum. If this is not satisfied, the system will become unstable to turbulence. The onset of turbulence can be delayed if viscosity were large enough so that Reynolds numbers are below the order of 10^2 or 10^3 . However there are many modes of instability if equation (3.9) is not met, and even a gas with low Reynolds number will eventually become fully turbulent (Shu, 1992).

Velocity dispersions can characterize the general magnitude of a turbulent medium, but its local nature is better detailed by applying the Cauchy-Stokes decomposition,

$$\mathbf{u}' = \mathbf{u} + \frac{1}{2} \boldsymbol{\omega} \times \mathbf{h} + \frac{1}{3} (\nabla \cdot \mathbf{u}) \mathbf{h} + \frac{1}{2} \mathcal{D} \cdot \mathbf{h} \quad (3.10)$$

that decomposes the velocity field into bulk motion \mathbf{u} , vorticity $\boldsymbol{\omega} = \nabla \times \mathbf{u}$, expansion and contraction $\nabla \cdot \mathbf{u}$, and a distortion \mathcal{D} without change in volume. Here the vector \mathbf{h} describes the separation between gas parcels at position \mathbf{x} and \mathbf{x}' , and \mathbf{u}' is the velocity at \mathbf{x}' .

We relate $\nabla \cdot \mathbf{u}$, which is plotted in Figure 3.5, to a convergence timescale through the continuity equation,

$$\dot{\rho} + \nabla \cdot (\rho \mathbf{u}) = 0, \quad (3.11)$$

that can be rewritten in terms of the total derivative D/Dt as

$$\frac{1}{\rho} \frac{D\rho}{Dt} = -\nabla \cdot \mathbf{u}. \quad (3.12)$$

$D\rho/Dt$ describes density changes along the fluid flow lines, and the $1/\rho$ factor converts this change into an inverse timescale on which local densities e-fold. We denote $-(\nabla \cdot \mathbf{u})^{-1}$ as the ‘‘Lagrangian convergence timescale’’ (LCT). Converging flows ($\nabla \cdot \mathbf{u} < 0$) are ubiquitous within the halo. On large scales, the smallest LCTs on the order of 20 kyr exist at the virial shock, adjacent to both the filaments and voids. In the cooling models, these timescales are also small in turbulent shocks well within r_{200} . Analogous to the dynamical time, typical shocked LCTs decrease toward the center as density increases.

The local magnitude and nature of turbulence is further illustrated by the vorticity $\boldsymbol{\omega}$, whose component perpendicular to the slice, ω_y , is shown in Figure 3.6. The local

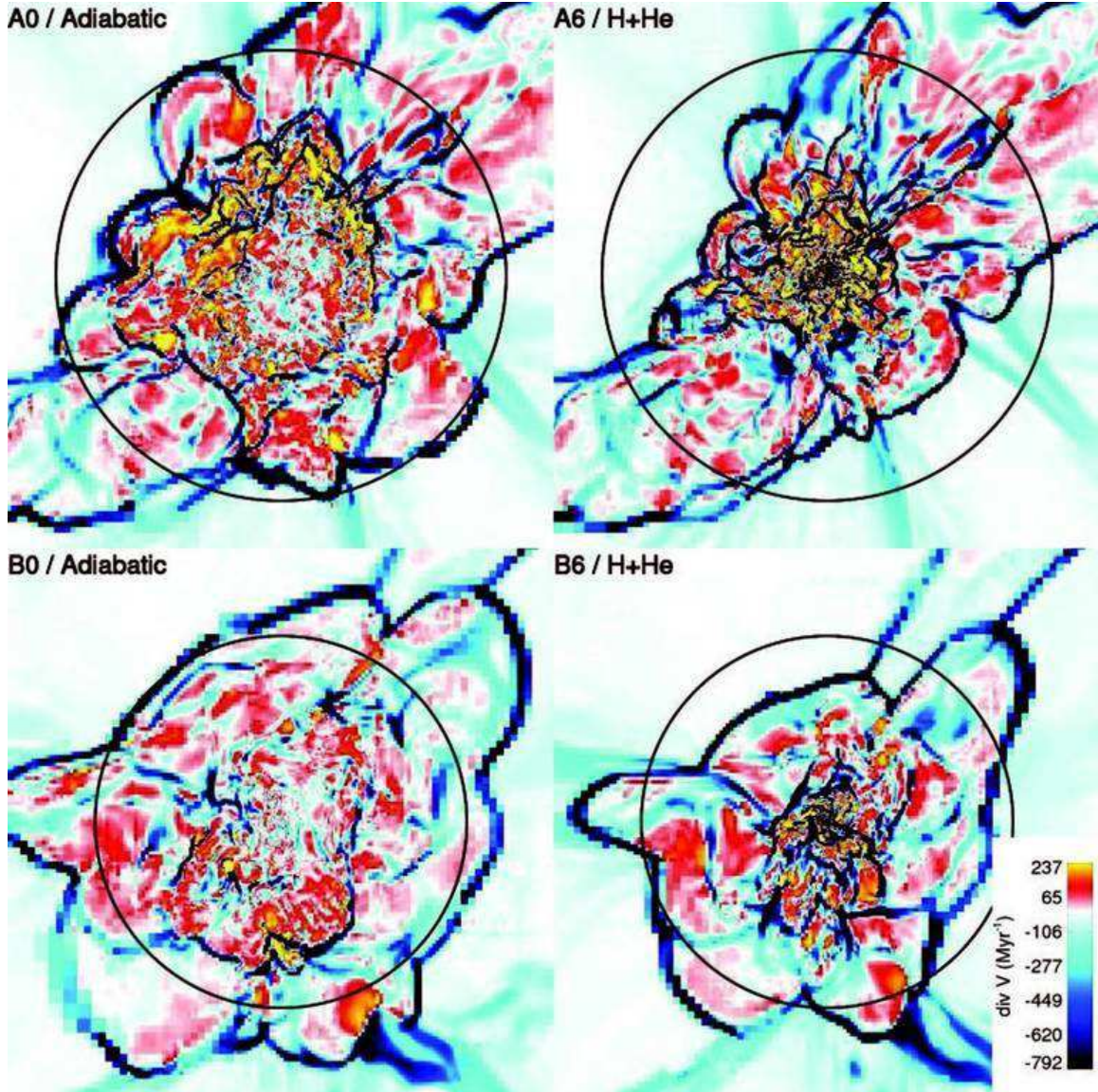


Fig. 3.5.— Two-dimensional slices of velocity divergence ($\nabla \cdot \mathbf{v}$) at $z = z_{c, \text{Ly}\alpha}$ for Simulations A0, A6, B0, and B6. The fields of view are 1.49 and 1.69 kpc for Simulations A and B, respectively. Shocks are clearly denoted by large, negative convergence values. In the adiabatic cases, these shocks mainly exist at large radii where the gas from the voids and filaments virializes. When we consider radiative cooling, supersonic turbulence increases the frequency of shock fronts in the interior of the halo.

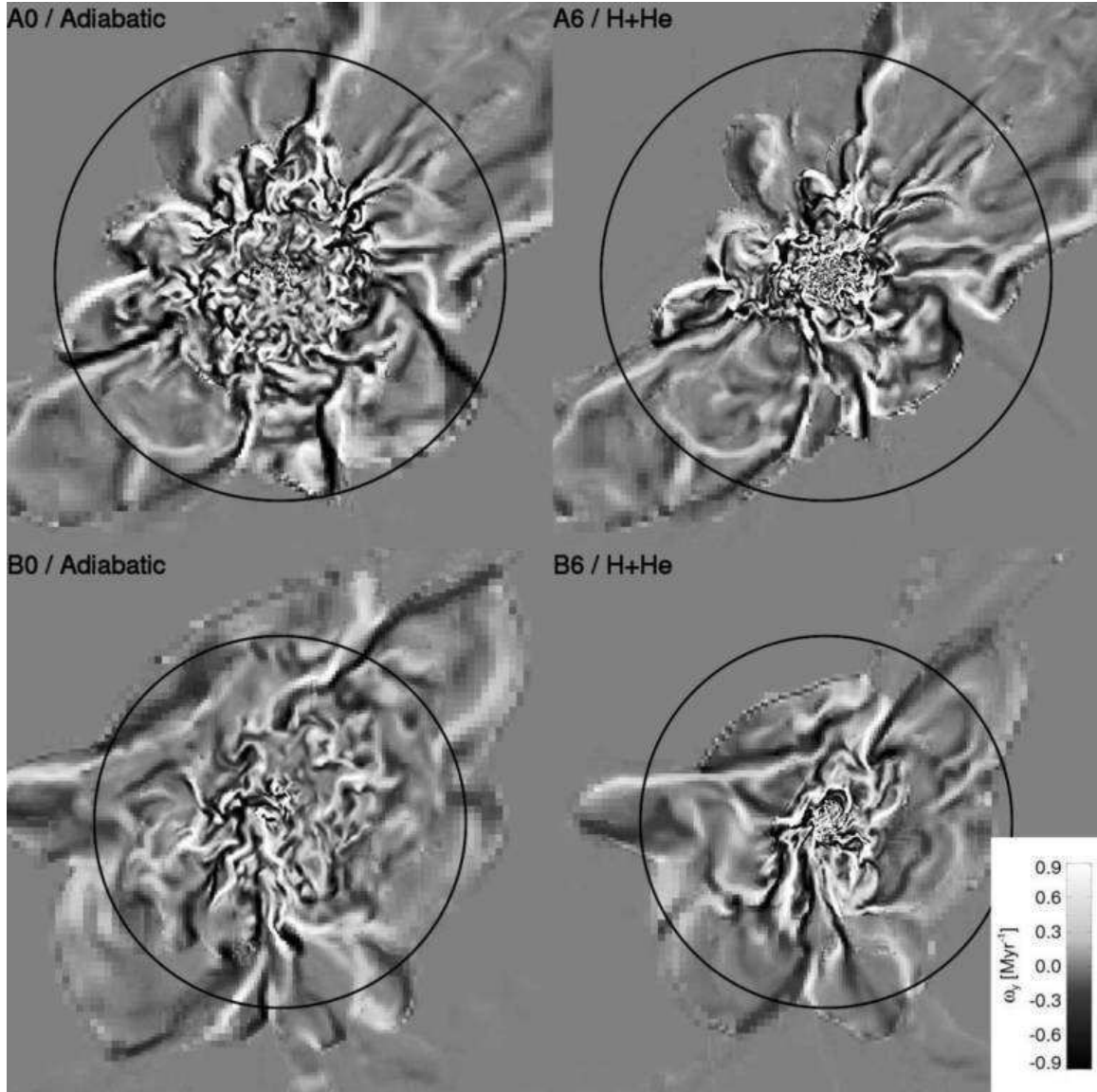


Fig. 3.6.— Two-dimensional slices of the component perpendicular to the slice of vorticity ($\nabla \times \mathbf{v}$) at $z = z_{c, Ly\alpha}$ for Simulations A0, A6, B0, and B6. The fields of view are the same as in Figure 3.5. This quantity emphasizes the large- and small-scale turbulent eddies in the halo.

rotation period, $4\pi/|\omega|$ is also helpful to quantify and visualize the nature of the flow. The vorticity equation reads

$$\frac{\partial \omega}{\partial t} + \nabla \times (\omega \times \mathbf{u}) = \frac{1}{\rho^2} \nabla \rho \times \nabla p, \quad (3.13)$$

where the source term is non-zero when the density and pressure gradients are not aligned, i.e. baroclinic vorticity generation. This occurs at and near shocks throughout the halo, regardless of radiative cooling. In the adiabatic models, vorticity exists even at modest but sufficient resolution in the large pressure-supported cores (see \mathcal{M}_{turb} for $r < 100$ pc in Figure 3.1) and generates a turbulent medium with $\mathcal{M}_{turb} = 0.3$. In the cooling models, this large-scale vorticity is still present but increases in the collapsing core. As shocks become abundant in the center, we do not see any dampening of kinetic energy. Perhaps this mechanism maintains turbulent motions during virialization, even in the presence of dissipative shocks. In Figure 3.6, adjacent, antiparallel fluid flows, i.e. a sign change in ω_y , are ubiquitous, which visually demonstrates that turbulence exists throughout the halo. The length scale of these eddies decrease with increasing density as with the LCTs.

Hence we believe significant turbulence generated during virialization should be present in all cosmological halos. The cooling efficiency of the gas, the total halo mass, and partly the merger history determines the magnitude of turbulence. We discuss some implications of virial turbulence in the following section.

3.5 Discussion

We have investigated the virialization of early pre-galactic cosmological halos in this paper with a suite of AMR simulations with varying chemistry and cooling models and collapse epochs. When analyzing the local virial equilibrium of the halo, we do not assume that it is in equilibrium but explicitly calculate all of the relevant terms in the virial theorem. In both adiabatic and radiative cooling cases, we find that the kinetic (turbulent) energy is comparable, if not dominant, with the thermal energy. Turbulence appreciates as radiative cooling becomes efficient because thermal energy

alone cannot bring the system into virial equilibrium. In this case, the gas attempts to virialize by increasing and maintaining its kinetic energy.

Besides violent relaxation, at least two other hydrodynamic processes will augment virial turbulence. The first occurs when radial inflow interacts with the virialized gas. Due to the Rayleigh criterion, the high angular momentum gas creates an instability when it is deposited by filaments at small radii. The second happens when minor and major mergers create Kelvin-Helmholtz instabilities and drives additional turbulence (e.g. Ricker & Sarazin, 2001; Takizawa, 2005). Our results show that this turbulence is acting to achieve close to virial equilibrium at all stages during assembly and collapse.

Virial turbulence may be most important in halos which can cool rapidly when compared to virial heating from mass accretion. Interestingly all halo masses below $\sim 10^{12} M_{\odot}$ that can cool by Ly α emission satisfy this condition (Birnboim & Dekel, 2003; Dekel & Birnboim, 2006; Wang & Abel, 2007).

Turbulence appears to mix angular momentum efficiently so that it redistributes to a radially increasing function, and thus only the lowest specific angular momentum material sinks to the center. This segregation allows a collapse to proceed if it were self-similar and basically non-rotating. Similar results have been reported in cosmological simulations of collapses of the first stars (Abel et al., 2000, 2002; Yoshida et al., 2003, 2006b; O’Shea & Norman, 2007). Here and in protogalactic collapses, the turbulent velocities become supersonic. One would expect even higher Mach numbers in larger potential wells that still have $t_{\text{cool}} < t_{\text{dyn}}$.

The inclusion of the surface term allows us to study the virial equilibrium in the halo’s interior where the gravitational potential is not influential. Here our simulations show thermal and kinetic energies balancing the surface term and potential energy to achieve virial equilibrium. Before cooling is efficient, gas virially heats and its temperature can exceed the traditional virial temperature within $r_{200}/2$ as seen in our adiabatic simulations. The consequences of this additional heating is substantial because halos can collapse and form stars before the virial temperature reaches the critical temperature, such as $\sim 10,000\text{K}$ for Ly α cooling.

The timescale at which the center collapse occurs is crucial to the type of object that forms there. If the collapse occurs faster than a Kelvin-Helmholtz time for a

massive star (~ 300 kyr), a black hole might form from the lowest angular momentum gas. Conversely if the collapse is delayed by turbulent pressure, star formation could occur in the density enhancements created by turbulent shocks. The ensuing radiative feedback may create outflows and thus slow further infall and possibly prevent the formation of a central black hole. The nature of the first galaxies poses an important question in the high-redshift structure formation, and to address this problem we must consider their progenitors – the first stars.

3.5.1 Pop III Feedback

Numerical simulations have shown that the first, metal-free (Pop III) stars form in isolation in its host halo. They are believed to have stellar masses $\sim 100 M_{\odot}$ (Abel et al., 2002; Omukai & Palla, 2003; Tan & McKee, 2004; Yoshida et al., 2006b) and produce $\sim 10^{50}$ photons s^{-1} that can ionize hydrogen and dissociate H_2 (Schaerer, 2002). One-dimensional radiative hydrodynamical calculations (Whalen et al., 2004; Kitayama et al., 2004) and recently three-dimensional radiative hydrodynamical AMR (Abel et al., 2007) and SPH (Yoshida et al., 2006a) simulations found that pressure forces from the radiatively heated gas drive a ~ 30 km s^{-1} shock outwards and expels the majority of the gas in the host halo. Additionally the star ionizes the surrounding few kpc of the intergalactic medium (IGM).

Pop III stellar feedback invalidates some of our assumptions in the calculations presented here, but the general aspect of kinetic energy being dominant should hold in the presence of these feedback processes. In a later paper, we will expand our simulations to include radiative feedback from primordial stars (cf. Yoshida et al., 2006a; Abel et al., 2007) and the metal enrichment from pair instability supernovae (Barkat et al., 1967; Bond et al., 1984; Heger & Woosley, 2002) of the IGM and subsequent star formation.

3.6 Summary

We have investigated the process of virialization in pre-galactic gas clouds in two cosmology AMR realizations. Our virial analyses included the kinetic (turbulent) energies and surface pressures of the baryons in the system. The significance of each energy component of the gas varies with the effectiveness of the radiative cooling, which we quantify by performing each realization with adiabatic, hydrogen and helium, and H_2 cooling models. We highlight the following main results of this study as:

1. Inside r_{cool} , gas cannot virialize alone through heating but must gain kinetic energy. It is up to a factor of five greater than thermal energy throughout the proto-galactic halos. This manifests itself in a faster bulk inflow and supersonic turbulent motions.
2. In the radiative cooling models, supersonic turbulence ($\mathcal{M} = 1\text{--}3$) leads to additional cooling within turbulent shocks. We expect turbulence in larger galaxies, up to $10^{12}M_{\odot}$, to be even more supersonic.
3. Baryonic velocity distributions are Maxwellian that shows violent relaxation occurs for gas as well as dark matter. Turbulent velocities exceed typical rotational speeds, and these halos are only poorly modeled as solid body rotators.
4. Virial shocks between the void-halo interface occur between $r_{200}/2$ and r_{200} . Dense, cold flows in filaments do not shock-heat until well within r_{200} and as small as $r_{200}/4$.
5. Turbulence generated during virialization mixes angular momentum so that it redistributes to a radially increasing function (the Rayleigh criterion).

After the halo virializes, its central part will undergo turbulent collapse, such as in primordial star formation and galactic molecular clouds. These collapses should be ubiquitous in early structure formation as turbulence can be generated through virialization, merging, and angular momentum segregation. We conclude that *turbulence plays a key role in virialization and galaxy formation*.

Chapter 4

Central Gas Collapse of a Atomic Hydrogen Cooling Halo

Classical and modern galaxy formation models involve the gravitational collapse of an initially homogeneous cosmological gaseous cloud. In the 1970's, evidence from theoretical and observational studies arose that galaxies were embedded in a dark halo that outweighed baryons by a factor of 10. The gas condensed until it was rotationally supported and formed a gaseous disk, where stars formed. We study this long-standing scenario with adaptive mesh refinement simulations that follows the evolution of the collapse of cosmological halo. We achieve a dynamical range of 10^{15} in length scale and 10^{25} in density that permits the investigation of the collapse to stellar scales in a cosmological volume.

These simulations are continuations of simulations with hydrogen and helium radiative cooling discussed in the previous chapter. We neglect primordial star formation and feedback in these simulations, which we will later show to be an important factor in early galaxy formation. However, these simulations provide an excellent testbed for studying turbulent collapses, which are also applicable to current theories of star formation.

This chapter is in preparation for publication in *The Astrophysical Journal*. It is co-authored by Matthew Turk, who modified the cosmological hydrodynamics code *Enzo* to accurately follow the collapse of such systems to dynamic ranges greater than

10^{10} in length scale, and Tom Abel, who helped with the organization and clarity of this chapter and suggested some of the analysis techniques.

4.1 Motivation & Previous Work

Since the first investigations of galaxy interactions (Holmberg, 1941) using light bulbs, the use of numerical simulations in galaxy formation has developed dramatically. Not only gravity but also hydrodynamics and cooling are standard ingredients in the sophisticated computer models studying galaxy formation and interactions. In hierarchical structure formation, dark matter (DM) halos merge to form larger halos while the gas infalls into these potential wells (Peebles & Dicke, 1968; White & Rees, 1978). White & Rees provided the basis for modern galaxy formation. In this picture, small galaxies form early and continuously merge into larger systems.

As more high redshift galaxies were observed in the following 10 years, White & Frenk (1991) expanded and refined the ideas in White & Rees to explain and model the observed characteristics in these galaxies. In their model, the halo accumulates mass until the gas cools faster than a Hubble time, t_H , which usually occurs when atomic hydrogen line, specifically $\text{Ly}\alpha$, cooling is efficient. This happens when the halo has $T_{\text{vir}} > 10^4$ K, where the cooling function sharply rises by several orders of magnitude because the number of free electrons able to excite hydrogen greatly increases at this temperature (Spitzer, 1978). One can define a cooling radius, r_{cool} , in which the interior material is able to cool. Once the halo reaches this first milestone, r_{cool} increases through additional accretion and cooling. A rapid baryonic collapse ensues when $t_{\text{cool}} < t_{\text{dyn}}$ (Rees & Ostriker, 1977). The material accelerates towards the center, and its density quickly increases. In the model discussed in White & Frenk, this collapse will halt once a gaseous disk forms stars. In the first scenario, angular momentum prevents the gas from collapsing further and becomes rotationally supported. Afterwards, this disk fragments and star formation follows. In the latter scenario, star formation does not necessarily develop in a disk component, but the energy released by stars during their lifetimes and associated supernovae (SNe) terminates the collapse.

These concepts have been applied also to the earliest galaxies in the universe (Mo et al., 1998; Oh & Haiman, 2002; Begelman et al., 2006; Lodato & Natarajan, 2006). Many studies (e.g. Ostriker & Gnedin, 1996; Haiman et al., 1997; Cen, 2003a; Somerville & Livio, 2003; Wise & Abel, 2005) demonstrated that OB-stars within protogalaxies at $z > 6$ produce the majority of photons required for reionization. These protogalaxies contain an ample gas reservoir for widespread star formation, and the accompanying radiation propagates into and ionizes the surrounding neutral intergalactic medium. Several high redshift starburst galaxies have been observed that support ubiquitous star formation at $z > 6$ (Stanway et al., 2003; Mobasher et al., 2005; Bouwens & Illingworth, 2006). Additionally, supermassive black holes (SMBH) more massive than $10^8 M_\odot$ are present at these redshifts (e.g. Becker et al., 2001; Fan et al., 2002). Finally, a reionization signature at $z \sim 10$ (Page et al., 2006) further supports and constrains stellar and SMBH activity at high redshifts.

Stars formed in these earliest galaxies are part of present day galaxies. Thus constraints on protogalactic environments may be derived from local dwarf galaxies (e.g. Tolstoy et al., 2003, 2004; Gnedin & Kravtsov, 2006; Helmi et al., 2006). The distinction between SMBH formation and a starburst galaxy should depend on the initial ingredients (e.g. seed BHs, metallicity, merger histories) of the host halo, but the evolution of various initial states is debatable. It is essential to study the hydrodynamics of high redshift halo collapses because the initial luminous object that emerges will chemically and thermally alter its surroundings. For example, as the object emits ultraviolet radiation, the nearby gas heats and thus the characteristic Jeans mass increases, which may inhibit the accretion of new gas for future star formation (Efstathiou, 1992; Thoul & Weinberg, 1996).

The following work will attempt to clarify early galaxy formation by focusing on $T_{\text{vir}} > 10^4$ K halos and following their evolution in the early universe. Wise & Abel (2007a, hereafter Paper I) studied the virialization of protogalactic halos and the virial generation of supersonic turbulence. In this paper, we only address the gas dynamics of the continued, turbulent collapse of a halo and study the evolution and characteristics of the central object. In later studies, we will introduce the effects from star and SMBH formation and feedback and H_2 cooling. The progressive introduction

of new processes is essential to understand the relevance of each mechanism. We argue that our results are highly relevant for scenarios that envisage SMBH formation from gaseous collapses.

Loeb & Rasio (1994) and Bromm & Loeb (2003) conducted smoothed particle hydrodynamics (SPH) simulations that focused on the collapse of idealized, isolated protogalactic halos. The former group concluded that a central $10^6 M_\odot$ SMBH must exist to stabilize the thin gaseous disk that forms in their calculations. Bromm & Loeb considered cases with and without H_2 chemistry and a background UV radiation field. They observed the formation of a dense object with a mass $M \sim 10^6$, or $\gtrsim 10\%$ of the baryonic matter, in simulations with no or suppressed H_2 formation. Spaans & Silk (2006) analytically studied the collapse of 10^4 K halos with an atomic equation of state. They find that $\sim 0.1\%$ of the baryonic mass results in a pre-galactic BH with a mass $\sim 10^5 M_\odot$. Additionally, Lodato & Natarajan (2006) also found that $\sim 5\%$ of the gas mass in $M = 10^7 M_\odot$ halos at $z \sim 10$ become unstable in a gaseous disc and form a SMBH. These calculations without metal cooling and stellar feedback are useful to explore the hydrodynamics of the collapse under simplified conditions.

A runaway gaseous collapse requires angular momentum transport so material can inflow to small scales and form a central object. The stability of rotating gaseous objects have been subject of much interest over the last four centuries and was thoroughly detailed by the work of Chandrasekhar (1969, hereafter EFE). In the 1960's and 1970's, studies utilizing virial tensor techniques (EFE; Lebovitz, 1967; Ostriker & Tassoul, 1969; Ostriker & Bodenheimer, 1973), variational techniques (Lynden-Bell & Ostriker, 1967; Bardeen et al., 1977), and N-body simulations (Ostriker & Peebles, 1973) all focused on criteria in which a stellar or gaseous system becomes secularly or dynamically unstable. The first instability encountered is an $m = 2$ bar-like instability, which is conducive for angular momentum transport in order to form a dense, central object. Begelman et al. (2006) investigated the conditions where a gaseous disc would become rotationally unstable to bar formation (see Christodoulou et al., 1995a,b). They adapt the “bars within bars” scenario (Shlosman et al., 1989, 1990), which was originally formulated to drive SMBH accretion from a gaseous bar that forms in a stellar galactic bar, to the scenario of pre-galactic BH formation. Here a

cascade of bars form and transport angular momentum outwards, and the system can collapse to small scales to form a quasistar with runaway neutrino cooling, resulting in a central SMBH. In one of our realizations, a central bar-like instability forms, for which we reveal the causing mechanism.

As briefly mentioned before, angular momentum plays a dominant role in halo contractions. The standard picture of galaxy formation inside this paradigm includes the following elements: tidal torques from cosmological neighbors create angular momentum (Hoyle, 1949; Peebles, 1969); baryonic angular momentum is conserved while cooling (Mestel, 1963); both DM and baryonic components of a virialized halo have equivalent initial angular momentum distributions (Fall & Efstathiou, 1980). The halo is subject to turbulence from gravitational instabilities (Elmegreen, 1993) and angular momentum transport (see Paper I; Toomre, 1964; Lin & Pringle, 1987) as it collapses, and cosmological virialization (see Paper I).

In §2 we describe our simulations and their cosmological context. In the following section, we detail the analytical models of rotational instabilities. Next in §4, we present our analysis of the halo collapse simulations. Here we investigate the structural and hydrodynamical evolution, the initial halo collapse, rotational instabilities, and the importance of turbulence. In §5, we discuss its implications on the field of early galaxy formation. There we also examine the applicability and limitations of our results and desired improvements in our simulations. Finally we conclude in the last section.

4.2 Simulation Techniques

To investigate protogalactic ($T_{\text{vir}} > 10^4$ K) halo collapses in the early universe, we utilize an Eulerian structure, adaptive mesh refinement (AMR), cosmological hydrodynamical code, *Enzo*¹ (Bryan & Norman, 1997, 1999; O’Shea et al., 2004). *Enzo* solves the hydrodynamical equations using a second order accurate parabolic method (Woodward & Colella, 1984; Bryan et al., 1994), while a Riemann solver ensures accurate shock capturing with minimal viscosity. Additionally *Enzo* uses

¹See <http://cosmos.ucsd.edu/enzo/>

a particle-mesh N-body method to calculate the dynamics of the collisionless dark matter particles (Couchman, 1991). Regions of the simulation grid are refined by two when one of the following conditions are met: (1) Baryon density is greater than 3 times $\Omega_b \rho_0 N^{l(1+\phi)}$, (2) DM density is greater than 3 times $\Omega_{\text{CDM}} \rho_0 N^{l(1+\phi)}$, and (3) the local Jeans length is less than 16 cell widths. Here $N = 2$ is the refinement factor; l is the AMR refinement level; $\phi = -0.3$ causes more frequent refinement with increasing AMR levels, i.e. super-Lagrangian behavior; $\rho_0 = 3H_0^2/8\pi G$ is the critical density; and the Jeans length, $L_J = \sqrt{15kT/4\pi\rho G\mu m_H}$, where H_0 , k , T , ρ , μ , and m_H are the Hubble constant, Boltzmann constant, temperature, gas density, mean molecular weight in units of the proton mass, and hydrogen mass, respectively. The Jeans length refinement insures that we meet the Truelove criterion, which requires the Jeans length to be resolved by at least 4 cells on each axis (Truelove et al., 1997). Runs with a refinement criterion of 4, 8, and 16 Jeans lengths have indistinguishable mass weighted radial profiles.

We conduct the simulations within the concordance Λ CDM model with WMAP 1 year parameters of $h = 0.72$, $\Omega_\Lambda = 0.73$, $\Omega_M = 0.27$, $\Omega_b = 0.024h^{-2}$, and a primordial scale invariant ($n = 1$) power spectrum with $\sigma_8 = 0.9$ (Spergel et al., 2003). h is the Hubble parameter in units of $100 \text{ km s}^{-1} \text{ Mpc}^{-1}$. Ω_Λ , Ω_M , and Ω_b are the fractions of critical energy density of vacuum energy, total matter, and baryons, respectively. Lastly σ_8 is the rms of the density fluctuations inside a sphere of radius $8h^{-1} \text{ Mpc}$.

Using the WMAP1 parameters versus the significantly different WMAP third year parameters (WMAP3; Spergel et al., 2006) have no effect on the evolution of individual halos that are considered here. However these changes play an important role in statistical properties. For example, halos with mass $10^6 M_\odot$ at redshift 20 correspond to 2.8σ peaks with the WMAP1 but are 3.5σ peaks for WMAP3. The Ω_M/Ω_b ratio also only changed from 6.03 to 5.70 in WMAP3. Also we have verified that there is nothing atypical about the mass accretion rate histories of the objects we study.

The initial conditions of this simulation are well-established by the primordial temperature fluctuations in the cosmic microwave background (CMB) and big bang nucleosynthesis (BBN) (Hu & Dodelson, 2002; Burles et al., 2001, and references

therein).

Table 4.1: Simulation Parameters

Name	l	N_{part}	N_{grid}	N_{cell}	L_{max}	Δx
	[Mpc]					[R_{\odot}]
A	1.0	2.22×10^7	44712	1.23×10^8 (498 ³)	41	9.3×10^{-3}
B	1.5	1.26×10^7	22179	7.40×10^7 (420 ³)	41	1.4×10^{-2}

Note. — Col. (1): Simulation name. Col. (2): Number of dark matter particles. Col. (3): Number of AMR grids. Col. (4): Maximum number of unique grid cells. Col. (5): Maximum level of refinement reached in the simulation. Col. (6): Resolution at the maximum refinement level.

We perform two simulations in which we vary the box size to study different scenarios and epochs of halo collapse. In the first simulation, we setup a cosmological box with 1 comoving Mpc on a side (Simulation A), periodic boundary conditions, and a 128^3 top grid. The other simulation is similar but with a box side of 1.5 comoving Mpc (Simulation B). We provide a summary of the simulation parameters in Table 4.1. These volumes are adequate to study halos of interest because the comoving number density of $>10^4$ K halos at $z = 10$ is $\sim 6 \text{ Mpc}^{-3}$ according to Press-Schechter formalism (Press & Schechter, 1974; Sheth & Tormen, 2002). We use the COSMICS package to calculate the initial conditions at $z = 129$ (119)[†] (Bertschinger, 1995, 2001). It calculates the linearized evolution of matter fluctuations. We first run a dark matter simulation to $z = 10$ and locate the DM halos using the HOP algorithm (Eisenstein & Hut, 1998). We identify the first dark matter halo in the simulation that has $T_{vir} > 10^4$ K and generate three levels of refined, nested initial conditions with a refinement factor of two that are centered around the Lagrangian volume of the halo of interest. The nested grids that contain finer grids have 8 cells between its boundary and its child grid. The finest grid has an equivalent resolution of a

[†]To simplify the discussion, simulation A will always be quoted first with the value from simulation B in parentheses.

1024³ unigrid and a side length of 250 (300) comoving kpc. This resolution results in a DM particle mass of 30 (101) M_\odot and an initial gas resolution of 6.2 (21) M_\odot . These simulations continue from the endpoints of Simulations A6 and B6 of Paper I. Table 4.2 lists the parameters of the most massive halo in each realization. We evolve the system until the central object has collapsed and reached our resolution limit. There are 1.23×10^8 (498³) and 7.40×10^7 (420³) unique cells in the final simulation output of the 1 and 1.5 Mpc simulation, respectively. The finest grid then has a refinement level of 41 and a spatial resolution of roughly 0.01 of a solar radius in both simulations.

Table 4.2: Halos of interest

l	z	M_{tot}	σ	ρ_c	T_c	M_{BE}
[Mpc]		[M_\odot]		[cm^{-3}]	[K]	[M_\odot]
1.0	15.87	3.47×10^7	2.45	5.84×10^{21}	8190	4.74×10^5
1.5	16.80	3.50×10^7	2.59	7.58×10^{21}	8270	1.01×10^5

Note. — The subscript “c” denotes central quantities.

Note. — Col. (1): Box size of the simulation. Col. (2): Final redshift of simulation. Col. (3): Total halo mass. Col. (4): σ of the total mass compared to matter fluctuations. Col. (5): Central halo density. Col. (6): Central gas temperature. Col. (7): Gravitationally unstable central mass.

Enzo employs a non-equilibrium chemistry model (Abel et al., 1997; Anninos et al., 1997), and we consider six species in a primordial gas (H, H⁺, He, He⁺, He⁺⁺, e⁻). Compton cooling and heating of free electron from the CMB and radiative losses from atomic cooling are computed in the optically thin limit. At high densities in the halo cores, the baryonic component dominates the material. However, the discrete sampling of the DM potential by particles can become inadequate, and artificial heating (cooling) of the baryons (DM) can occur. To combat this effect, we smooth the DM particles in cells with a width <0.24 (<0.36) comoving pc, which corresponds

to a refinement level of 15.

4.3 Results

In this section, we first describe how the halo collapses when it starts to cool through Ly α line emission. Then we discuss the role of turbulence in the collapse. Lastly we describe the rotational properties and stability of the halo and central object.

4.3.1 Halo Collapse

At $z = 21.1$ in simulation A, the progenitor of the final halo ($M_{\text{vir}} = 4.96 \times 10^6 M_{\odot}$) starts to experience two major mergers, which continues until $z = 17.2$ when $M_{\text{vir}} = 2.36 \times 10^7 M_{\odot}$. We define M_{vir} as the mass M_{200} in a sphere that encloses an average DM overdensity of 200. In simulation B, no major merger occurs before the cooling gas starts to collapse, but it accumulates mass by accretion and minor mergers. Mergers disrupt the relaxed state of the progenitor and create turbulence as these systems collide and combine. Additional turbulence arises during virialization, as discussed in Paper I. In the density slices of Figure 4.1, more small scale density fluctuations are present in simulation A. These fluctuations penetrate farther into the potential well in simulation A to scales³ of 5 pc, compared to simulation B that contains nearly no fluctuations between 5 and 50 pc. The virial temperatures are now $\geq 10^4$ K, and therefore they can efficiently cool by atomic hydrogen transitions. The gas fulfills the critical condition for contraction, $t_{\text{dyn}} > t_{\text{cool}}$, and proceeds to continuously collapse in approximately a dynamical time.

The halo collapses in two stages. We denote the beginning of the first stage when $t_{\text{dyn}} > t_{\text{cool}}$ for the first time. The second stage begins when the central object becomes gravitationally unstable.

1. *Cooling stage*— As mass infalls toward the center, the increased cooling rate,

³Note that all masses concerning the collapse are gas mass, not total mass. The central regions of $r < 10$ pc are baryon dominated so that $M_{\text{enc, gas}} \approx M_{\text{enc, tot}}$. All length scales are in proper units unless otherwise noted.

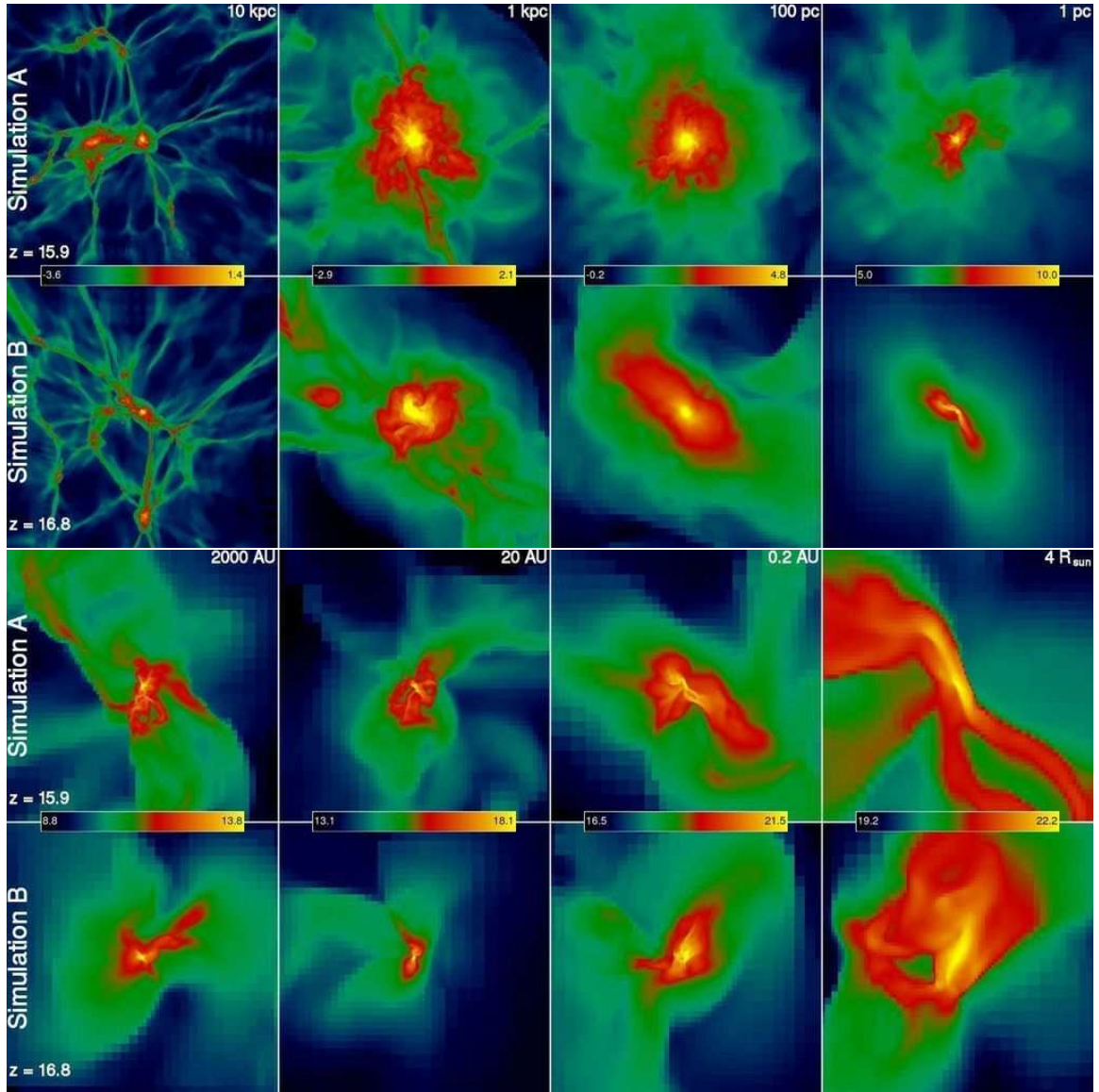


Fig. 4.1.— An overview of the final state of the collapsing protogalactic gas cloud. Slices of gas density in cm^{-3} are shown through the densest point in the halo. The *first* and *third* rows show Simulation A, and the *second* and *fourth* rows show Simulation B. The columns in the top two rows are slices with a field of view of 10 kpc, 1 kpc, 100 pc, and 1 pc. For the bottom two rows, the fields of view are 0.01pc, 20AU, 0.2AU, and $4 R_{\odot}$. Note that each color scale is logarithmic (values increases with *black, blue, green, red, and yellow*), spans 5 orders of magnitude, and is unique for every panel. At the 10 kpc scale, the filamentary large-scale structure is shown, and the protogalactic halo exists at the intersection of these filaments. In the next scale, we show the protogalactic gas cloud. At the 100 pc scale, a thick disk is seen in Simulation B. It is nearly edge-on in this view. In the inner 10 pc, the panels focus on the gravitationally unstable central mass that has a radius of 7.9 pc and 1.5pc for Simulation A and B, respectively. In Simulation B at 1 pc, a bar forms from a rotational secular instability that transports angular momentum outwards. Similar instabilities exist at radii of 0.2 pc, 90 AU, 0.7 AU, and 0.02 AU in Simulation B. Simulation A also undergoes a secular bar instability at smaller scales at radii of 140 AU and 0.02 AU but shows a more disorganized medium at larger scales.

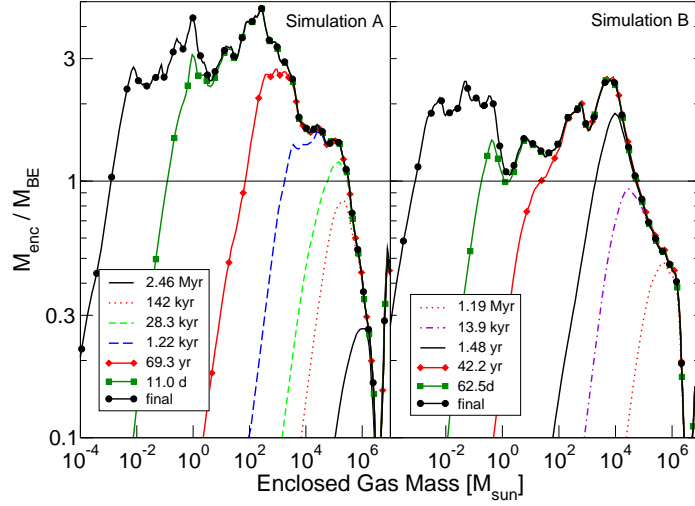


Fig. 4.2.— The ratio of the enclosed gas mass and Bonnor-Ebert mass (eq. 4.1) for the final output (*black with circles*) and selected previous times that are listed in the legend. Simulation A (*left*) and B (*right*). For values above the horizontal line at $M_{\text{enc}}/M_{\text{BE}} = 1$, the system is gravitationally unstable.

which is $\propto nn_e$, catalyzes the collapse as atomic line transitions convert kinetic energy to radiation. Here n and n_e are the number density of baryons and electrons, respectively. The first stage starts 520 (36) kyr before the last output. The inner 100 pc have a steady decrease in electron fraction that indicates atomic hydrogen cooling is now efficient in this region. However, only the gas within 1.5 (1.0) pc has $t_{\text{dyn}} \gtrsim t_{\text{cool}} = 383$ (100) kyr at this epoch.

2. *Gravitationally unstable stage*— We observe the start of the second collapse stage when the central region becomes unstable to gravitational collapse. Ebert (1955) and Bonnor (1955) investigated the stability of an isothermal sphere with an external pressure P_{ext} and discovered that the critical mass (BE mass hereafter) for gravitational collapse is

$$M_{\text{BE}} = 1.18 \frac{c_s^4}{G^{3/2}} P_{\text{ext}}^{-1/2} M_{\odot}. \quad (4.1)$$

If we set P_{ext} to the local pressure, then

$$M_{\text{BE}} \approx 20 T^{3/2} n^{-1/2} \mu^{-2} \gamma^2 M_{\odot}. \quad (4.2)$$

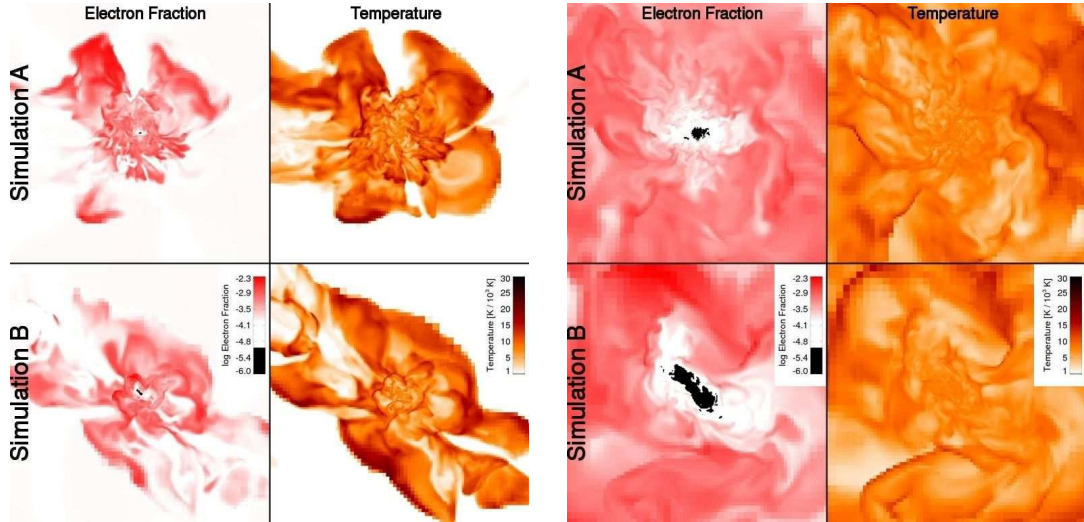


Fig. 4.3.— Slices of electron fraction (*left*) and temperature (*right*) of Simulation A (*top*) and B (*bottom*). The field of view is 1.5 kpc (*left panels*) and 200 pc (*right panels*). The color scale is logarithmic for electron fraction and linear for temperature. Electron fractions below 10^{-5} are shown in black. Supersonic turbulent shocks are ubiquitous throughout the halos.

For both simulations, this stage occurs between 10 and 100 kyr before we end the simulation. We plot the ratio of the enclosed gas mass and BE mass in Figure 4.2 for several epochs in the collapse. When the clump becomes gravitationally unstable, the central 3.3×10^5 (5.5×10^4) M_{\odot} in the central $r_{\text{BE}} = 5.8$ (0.9) pc exceeds the BE mass, and its $t_{\text{dyn}} = 520$ (80) kyr. Thus our numerical results agree with these analytic expectations.

We follow the evolution of the accretion and contraction until the simulation⁴ reaches a refinement level of 41 (41) that corresponds to a resolution of 0.01 (0.014) R_{\odot} . At this point, the central 4.7×10^5 (1.0×10^5) M_{\odot} are gravitationally unstable and *not* rotationally supported. The central mass is nearly devoid of free electrons where the electron fraction, $n_e/n < 10^{-6}$, and the temperature is ~ 8000 K. It has a radius of 7.9 (1.5) pc. The central number density is 5.8 (7.6) $\times 10^{21}$ cm^{-3} . Two-dimensional slices of gas density in both simulations are displayed at various length

⁴We stop the simulation due to ensuing round-off errors from a lack of precision. We use 80-bit precision arithmetic for positions and time throughout the calculation.

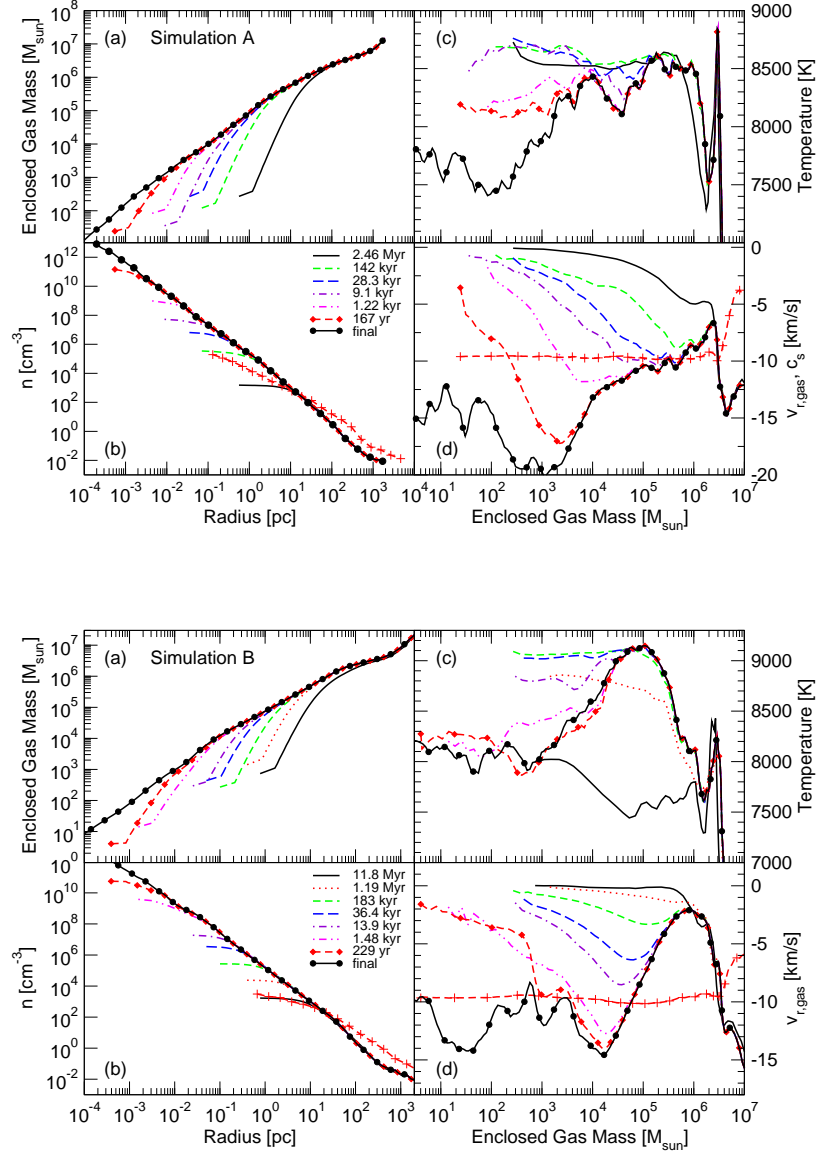


Fig. 4.4.— Mass-weighted radial profiles at various times of (a) gas mass enclosed, (b) number density, (c) mass-weighted temperature, and (d) mass-weighted radial velocity for simulation A (*upper panels*) and simulation B (*lower panels*). The quantities in the left and right panels are plotted with respect to radius and gas mass enclosed, respectively. In (b), the dashed line with crosses is the dark matter density in units of $m_H \text{ cm}^{-3}$. In (d), the dashed line with crosses is the negative of the sound speed in the final output. The times in the legends correspond to time before the end of the simulation.

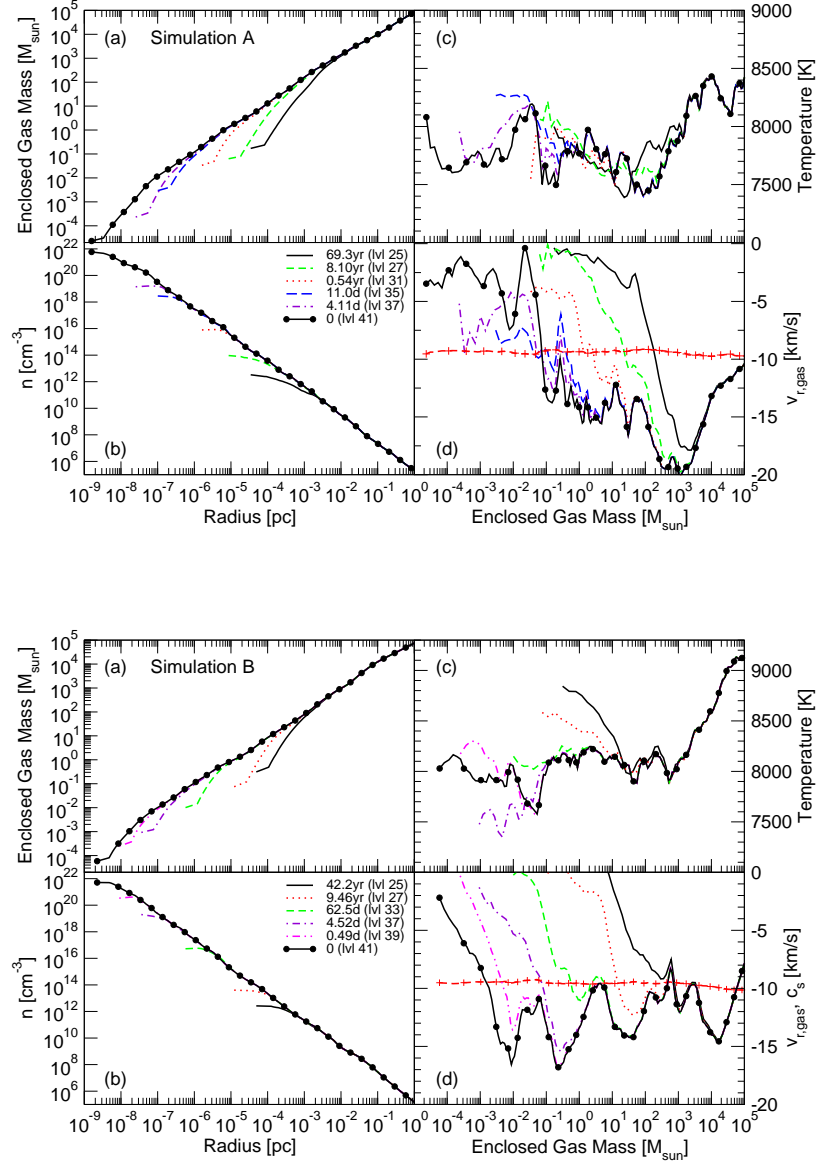


Fig. 4.5.— Same as Figure 4.4 for the inner parsec of Simulation A (*upper panels*) and Simulation B (*lower panels*). The maximum AMR level is listed next to the times in the legend. In Simulation B, the local minima in radial velocities at 2×10^4 , 40, 0.3, and $0.01 M_{\odot}$ occur as angular momentum is transported outwards in secular bar-like instabilities.

scales in Figure 4.1. Figure 4.3 gives slices of electron fraction and temperature with fields of view of 1.5 kpc and 200 pc.

Next we show the radial profiles of the final and preceding outputs in Figures 4.4 and 4.5, where we plot (a) enclosed gas mass, (b) number density, (c) mass-weighted temperature, and (d) mass-weighted radial velocity. Figure 4.4 focuses on length scales greater than 20 AU to $r > r_{\text{vir}}$. The halo collapses in a self-similar manner with $\rho(r) \propto r^{-12/5}$. We also overplot the DM density in units of $m_{\text{H}} \text{ cm}^{-3}$ in the *b* panels. The DM density in simulation A does not flatten as in simulation B with $\rho_{\text{DM}} \propto r^{-4/3}$ and $r^{-2/3}$, respectively. In the *c* panels, one sees that the entire system is isothermal within 10% of 8000 K. In the *d* panels, the sound speed in the final epoch is plotted, and one sees a clear shock at a mass scale when M_{enc} first exceeded M_{BE} where $v_r > c_s$. Here v_r is the radial velocity, and c_s is the local sound speed.

Figure 4.5 shows the data within 1 pc and later times. Here one sees the self-similar, isothermal collapse continues to stellar scales. However, the structure in the radial velocity in simulation B exhibits a striking behavior with four successive minima at mass scales 2×10^4 , 10^3 , 6, and $10^{-3} M_{\odot}$. We attribute this to rotational bar-like instabilities that we discuss later in the paper.

If we consider v_r constant from the last output, we can determine the infall times, which are shown in Figure 4.6. The infall time, $t_{\text{in}} = r/v_r$, of the shocked BE mass is 350 (50) kyr.

4.3.2 Turbulence

Kolmogorov (1941) described a theory of the basic behavior of incompressible turbulence where turbulence is driven on a large scale that forms eddies at that scale. Then these eddies interact to form smaller eddies and transfer some of their energy to the smaller scale. This cascade continues until the dissipation scale is reached, and energy is dissipated through viscosity. In supersonic turbulence, most of the turbulent energy is dissipated through shock waves, which removes the local nature of cascades found in incompressible turbulence.

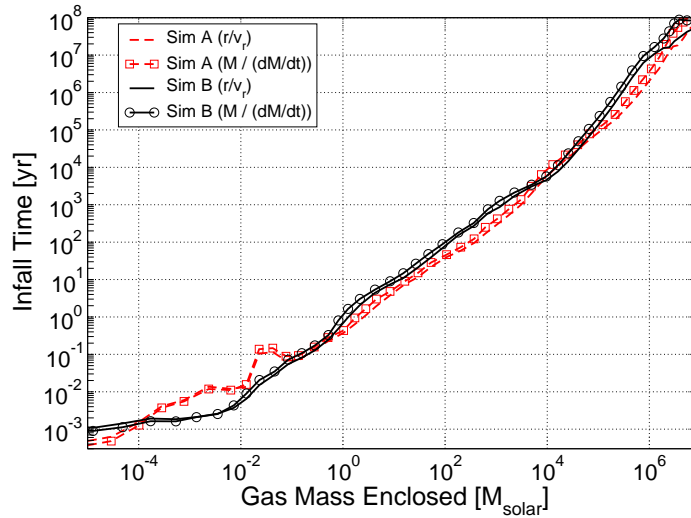


Fig. 4.6.— Radial profiles of gas infall times. To approximate a collapse timescale, the quantities r/v_r (*solid*) and $M/(dM/dt)$ (*dashed*) are calculated and plotted here.

In Paper I, we found that turbulence is stirred during virialization. When radiative cooling is efficient, the gas cannot virialize by gaining thermal energy and must increase its kinetic energy in order to reach equilibrium, which it achieves by radial infall and turbulent motions.

In addition to virial turbulence generation, mergers create turbulence. Here the largest driving scale will be approximately the scale of the merging objects, and the turbulent cascade starts from that length scale. Additional driving may come from Kelvin-Helmholtz instabilities as the mergers occur (Takizawa, 2005). Takizawa considered mergers of galaxy clusters, however his work is still applicable to the formation of protogalactic halos since similar temperature contrasts also exist in this regime of mergers. As the lesser halo infalls into the massive halo, a bow shock and small-scale eddies from the Kelvin-Helmholtz instability form between the two interacting objects. At later times, a dense, cool core remains in the substructure of the lesser halo. As they grow, these instabilities destroy the baryonic substructure, and this gas mixes with the existing gas in the massive halo and becomes highly turbulent.

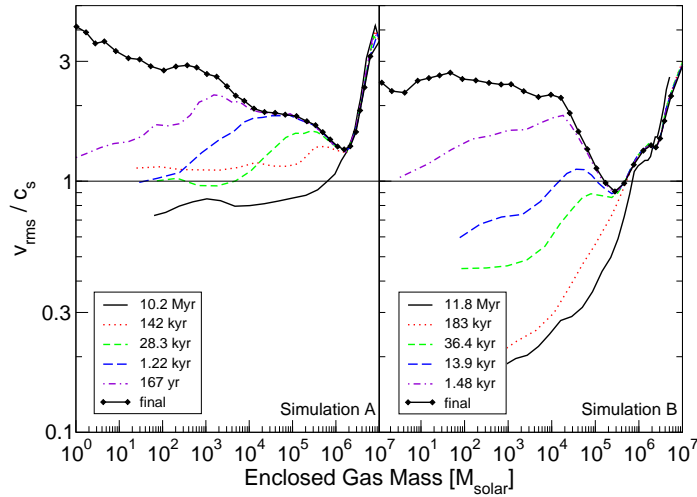


Fig. 4.7.— The turbulent Mach number, v_{rms}/c_s , for the final output (*black with diamonds*) and selected previous times that are listed in the legend. Simulation A (*left*) and B (*right*).

To quantify aspects of this turbulence, we inspect the turbulent Mach number,

$$\mathcal{M} = \frac{v_{rms}}{c_s}; \quad c_s^2 = \frac{dP}{d\rho} = \frac{\gamma kT}{\mu m_H}. \quad (4.3)$$

Here P is pressure, v_{rms} is the 3D velocity dispersion, and γ is the adiabatic index that we set to 5/3. Radial profiles of \mathcal{M} are shown in Figure 4.7. Before the core becomes gravitationally unstable, the turbulence is subsonic within the virial shock. After the core becomes gravitationally unstable, the turbulent Mach number rises to 2–3. The collapse produces turbulence on a timescale that is faster than it can be dissipated.

The initial turbulence may impact the nature of the central collapse. In simulation A, the core initially has $\mathcal{M} \approx 1$, and this results in a central object with $4.7 \times 10^5 M_\odot$ and a radius of 7.9 pc. Alternatively, the core in simulation B has $\mathcal{M} \approx 0.2$, and the central object is about five times less massive and smaller, which corresponds to a free-fall time approximately five times shorter as well.

4.3.3 Spin Parameter Evolution

During the hierarchical buildup of structure, tidal forces from neighboring structures impart angular momentum to a halo, particularly when its radius is maximal at the turn-around time (Hoyle, 1949; Peebles, 1969). However in recent years, several groups have recognized that the mergers impart a considerable fraction of angular momentum to the system (Steinmetz & Bartelmann, 1995; Gardner, 2001; Vitvitska et al., 2002; Maller et al., 2002). Over many realizations of mergers, the net angular momentum change would be zero. In reality, an angular momentum residual remains after the last major merger occurs because there are too few events to cancel the randomization of halo spin. Although each halo has unique rotational properties, it is useful to define a dimensionless spin parameter

$$\lambda \equiv \frac{|L|\sqrt{|E|}}{GM^{5/2}}, \quad (4.4)$$

where G is the gravitational constant and L , E , and M are the angular momentum, energy, and mass of the object, that measures the rigid body rotation of the halo (Peebles, 1971). In Figure 4.8, we display the time evolution of λ of the DM and baryons in our simulations and mark the occurrence of the major merger in simulation A. Eisenstein & Loeb (1995b) (preceded by Barnes & Efstathiou, 1987) calculated that the mean spin parameter, $\langle\lambda\rangle \approx 0.04$, is weakly dependent on object mass and cosmological model, and this value is also marked in Figure 4.8. Also λ weakly depends on its merger history, where $\langle\lambda\rangle$ increases in halos with the number of mergers. Most of the angular momentum is acquired from steady minor mergers and accretion because major mergers only happen rarely (usually only once per logarithmic mass interval). In 96% of mergers, the majority of the internal spin originates from the orbital energy of the infalling halo (Hetznecker & Burkert, 2006).

At $z \approx 22$ in simulation A, the spin parameter is large, $\lambda = 0.06$, before the last major merger. Then the spin parameter increases by a factor of 3 during its major merger due to the system being far from dynamical equilibrium. The system becomes virialized after approximately a sound crossing time, and the spin parameter

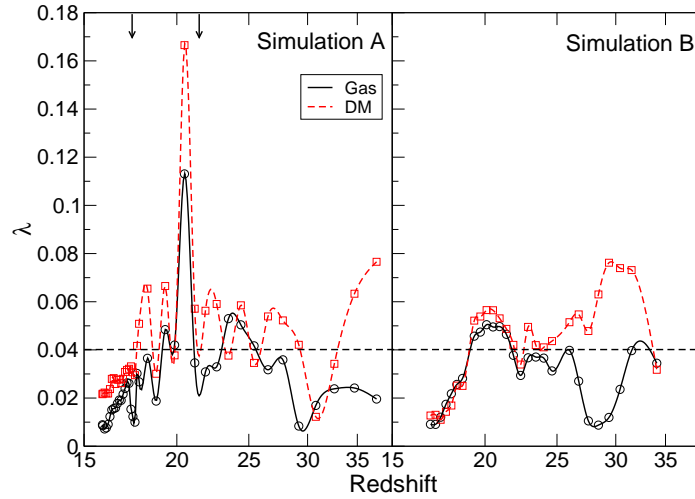


Fig. 4.8.— Spin parameter, $\lambda \equiv |L|\sqrt{|E|}/GM^{5/2}$, evolution of the main halo in the simulation. (*left*) Simulation A. (*right*) Simulation B. The dashed and solid lines are the interpolated values for the DM and baryonic spin parameter. The squares and circles correspond to the actual measurements from the DM and gas data, respectively. The horizontal dashed line at $\lambda = 0.04$ marks the mean cosmological spin parameter. In Simulation A, two major mergers, whose beginning and end are marked by arrows, causes the large increase at $z \approx 21$. The oscillations occur as the merging halos orbit each other until they virialize.

stabilizes at $\lambda \approx 0.03$ and proceeds to decrease with time until $\lambda = 0.022$ at the time of collapse. The above evolution of λ agrees with the findings of Hetznecker & Burkert. Simulation B describes a halo that does not undergo a recent major merger and its final $\lambda = 0.013$.

Both halos have less angular momentum than $\langle \lambda \rangle$ when the cooling gas collapses. The probability distribution of λ can be described with the log-normal function

$$p(\lambda)d\lambda = \frac{1}{\sigma_\lambda\sqrt{2\pi}} \exp\left[-\frac{\ln^2(\lambda/\lambda_0)}{2\sigma_\lambda^2}\right] \frac{d\lambda}{\lambda}, \quad (4.5)$$

where $\lambda_0 = 0.042 \pm 0.006$ and $\sigma_\lambda = 0.5 \pm 0.04$ (e.g. Bullock et al., 2001). From the cumulative probability function resulting from equation (4.5), 11% (1.2%) of the cosmological sample of halos have larger spin parameters than the halos described here. Eisenstein & Loeb (1995a) demonstrated that halos with low spin parameters

are candidates for BH formation and quasar seeds. However they argue that the angular momentum needs to be at least an order of magnitude lower than the mean. Next we present further evidence that reveal that a gaseous collapse is possible with not too atypical spin parameters.

4.3.4 Global Disk

In Simulation B, a thick disk with a radius of 50 pc and disk scale height of ~ 10 pc forms that is pressure supported and only partially rotationally supported. This equates to a shape parameter $f = 0.89$ in Equation 4.11. The circular velocities within this disk achieve only a third of Keplerian velocities. The lack of full rotational support and large scale height suggests that a central collapse occurs before any fragmentation in this large-scale disk. In contrast, we see a disorganized, turbulent medium and no large scale disk formation in Simulation A that corresponds to $f = 2/3$, i.e. a sphere.

4.3.5 Instability of Maclaurin Spheroids

The dynamics of rotating systems is a classic topic in astrophysics (see EFE §§1–6). These self-gravitating systems are susceptible to two types of instability. Secular instability occurs when small dissipative forces, e.g. viscosity, amplify perturbations to become unstable in an otherwise stable inviscid configuration. Dynamical (also referred to as ordinary) instability results when some oscillatory mode exponentially grows with time, regardless of any dissipative forces. Here we concentrate on Maclaurin spheroids relevant for a uniform body rotating with a fixed angular velocity. Maclaurin spheroids are a special case of Jacobi ellipsoids that are axisymmetric. The onset of the $m = 2$ bar-like instability in gaseous Maclaurin spheroids happens for a given eccentricity,

$$e = \left(1 - \frac{a_3^2}{a_1^2}\right)^{1/2} \geq \begin{cases} 0.8127 & \text{(secular)} \\ 0.9527 & \text{(dynamical)} \end{cases}, \quad (4.6)$$

where a_3 and a_1 are the principle axes with $a_3 \leq a_1$ (EFE §33). Eccentricity is related to the ratio, $t = T/|W|$, of rotational kinetic energy to gravitational potential by

$$t = \frac{1}{2}[(3e^{-2} - 2) - 3(e^{-2} - 1)^{1/2}(\sin^{-1} e)^{-1}], \quad (4.7)$$

and the secular and dynamical instabilities correspond to $t = (0.1375, 0.27)$, respectively (e.g. Ostriker & Peebles, 1973).

When t is larger than 0.1375 but smaller than 0.27, both the Maclaurin spheroid and Jacobi ellipsoid are perfectly stable against small perturbations in the non-viscous case. For a given e , the Jacobi configuration has a lower total energy than its Maclaurin counterpart and is therefore a preferred state. Here any dissipative force induces a secular bar-like instability. The system slowly and monotonically deforms through a series of Riemann S-type ellipsoids until its final state of a Jacobi ellipsoid with an equal angular momentum (Press & Teukolsky, 1973) and lower angular velocity (EFE §32) as specific angular momentum is transported outward. The instability grows on an e -folding timescale

$$\tau = \phi a_1^2 / \nu, \quad (4.8)$$

where ϕ is a constant of proportionality that asymptotes at $t = 0.1375$, decays to zero at $t = 0.27$, and is plotted in Figure 4.9 (EFE §37). Here ν is the kinematic viscosity.

Christodoulou et al. (1995a,b) generalized the formulations for bar-like instabilities to account for self-gravity. In addition, they consider different geometries, differential rotation, and non-uniform density distributions. They devised a new stability criterion

$$\alpha \equiv \frac{T/|W|}{\Omega/\Omega_J} = \sqrt{\frac{f}{2} \frac{T}{|W|}} \quad (4.9)$$

where Ω is the rotation frequency,

$$\Omega_J^2 = 2\pi G\rho \left[\frac{(1 - e^2)^{1/2}}{e^3} \sin^{-1} e - \frac{1 - e^2}{e^2} \right] \quad (4.10)$$

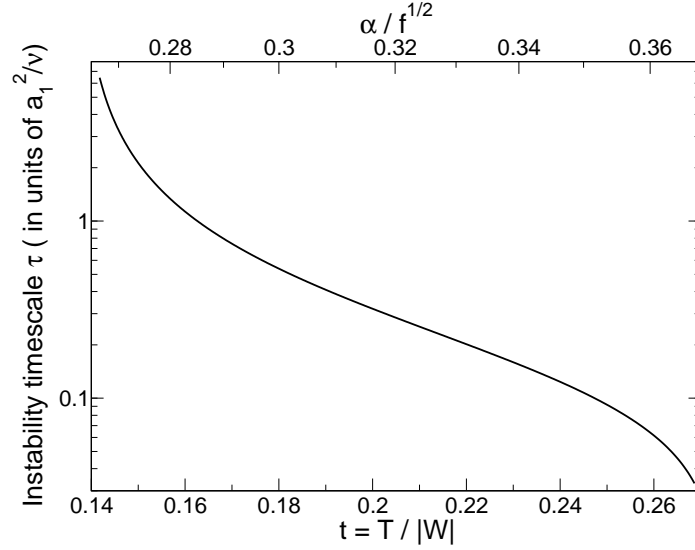


Fig. 4.9.— Secular instability e -folding timescale in units of a_1^2/ν as a function of $t = T/|W|$ and $\alpha = (tf/2)^{1/2}$ (eq. 4.9). At $t < 0.1375$, the system is stable to all perturbations. Above 0.27, the system is dynamically unstable, and this timescale is not applicable.

is the Jeans frequency in the radial direction for a Maclaurin spheroid, and

$$f = \frac{1}{e^2} \left[1 - \frac{e}{\sin^{-1} e} \sqrt{1 - e^2} \right] \quad (4.11)$$

accounts for differing geometries⁵ with $f = 2/3$ for a sphere and $f = 1$ for a disk. Secular and dynamical instabilities for Maclaurin spheroids occur above $\alpha = (0.228, 0.341)$, respectively.

From N-body simulations of disk galaxies, Ostriker & Peebles (1973) found that a massive dark halo with comparable mass to the disk could suppress secular instabilities. In the case of a gaseous collapse into a SMBH, the baryonic component dominates over the dark matter component in the central 10 pc. Secular instabilities cannot be prevented through this process, which we demonstrate next.

⁵See Christodoulou et al. (1995b) for more generalized geometries.

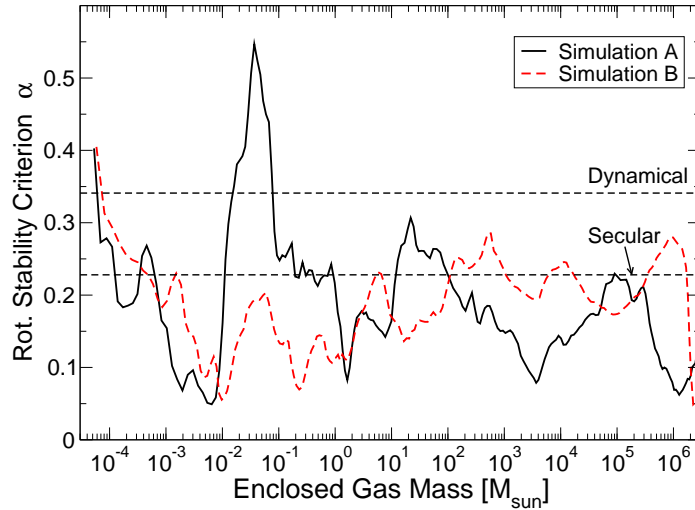


Fig. 4.10.— Rotational instability parameter $\alpha = \sqrt{fT/2|W|}$ for the thick disk with $r \simeq 50$ pc in simulations A (black solid line) and B (red dashed line). For $\alpha > 0.22$ denoted by the horizontal line, a secular instability occurs in the disk and leads to bar formation. In simulation A, instabilities occur at mass scales of 100, 0.1, and $10^{-4}M_{\odot}$. In simulation B, the same happens at 2×10^6 , 2×10^4 , 10^3 , 6, and $10^{-3}M_{\odot}$. We also mark $\alpha = 0.341$ where a rotating system becomes dynamically unstable. Only simulation A at $0.1 M_{\odot}$ experiences a dynamical instability.

4.3.6 Rotational Instabilities

In the $l = 1$ pc panel of Simulation B in Figure 4.1, it is apparent a bar-like instability exists in the gravitationally unstable central object. Figure 4.10 shows the instability criterion α (eq. 4.9) against enclosed gas mass. Here we transform the velocities to align the z -axis with the baryonic angular momentum vector of the entire halo. We use the tangential velocities to calculate the rotational kinetic energy T .

As discussed before, Maclaurin spheroids are subject to secular $m = 2$ bar-like instabilities when $\alpha > 0.228$. In simulation A, the central object becomes unstable three approximate mass scales, 100, 0.1, and 10^4M_{\odot} . The instability at $0.1 M_{\odot}$ is dynamically unstable with α peaking at 0.55. In simulation B, instabilities occur at 2×10^6 , 2×10^4 , 10^3 , 6, and $5 \times 10^{-4}M_{\odot}$.

It is interesting to note that the innermost instability in both simulations becomes

dynamical ($\alpha > 0.341$), and α continues to increase rapidly toward the center. However these features should be taken with caution since it occurs near our resolution limit, where the particular location used as the center will influence the rotational energy one would calculate.

The e -folding time of secular instabilities τ is proportional to a_1^2 (see eq. 4.8). Hence small-scale instabilities collapses on a faster timescale than its parent, large-scale bar instability. Viscosity, turbulent viscosity in this case, is the main dissipative force that drives the instability. τ is inversely proportional to the viscosity. Therefore in the data presented, this further shortens the τ because supersonic turbulence is maintained to the smallest scales. We also note that the radial velocity (see Figure 4.5) increases after it becomes comparable to the sound speed.

4.3.7 Rotational Properties

During the collapse of the gas in our simulations, rotational support never impedes the collapse. In Figures 4.11 and 4.12, we show (a) coherent rotational velocity divided by Keplerian velocity v_{kep} , (b) rotational velocity, (c) specific angular momentum, and (d) rotational velocity divided by the sound speed. We note that the rotational velocity L/r plotted here is different than organized rotation, i.e. a disk. The radial profiles only sample gas in radial shells, where the angular momentum vectors are not necessarily parallel.

1. *Simulation A*— At $r > 1$ AU ($M_{enc} = 1M_{\odot}$), the typical rotational speed is two or three times lower than the Kepler velocity, which is required for rotational support. At this radius, the infall becomes marginally rotationally supported, i.e. $L/r \sim v_{kep}$, around 0.1 AU ($M_{enc} = 0.07M_{\odot}$) in Figure 4.12. The radial velocities react by slowing from 15 km s^{-1} to around zero. At late times, the rotational support is steady at 0.1 AU, however the rotational velocities vary significantly over time to the interior.

2. *Simulation B*— As discussed in Section 4.3.6, the collapse object experiences rotational bar instabilities. After an instability occurs, the radial velocities increase due to angular momentum transport. Then this material begins to gain rotational

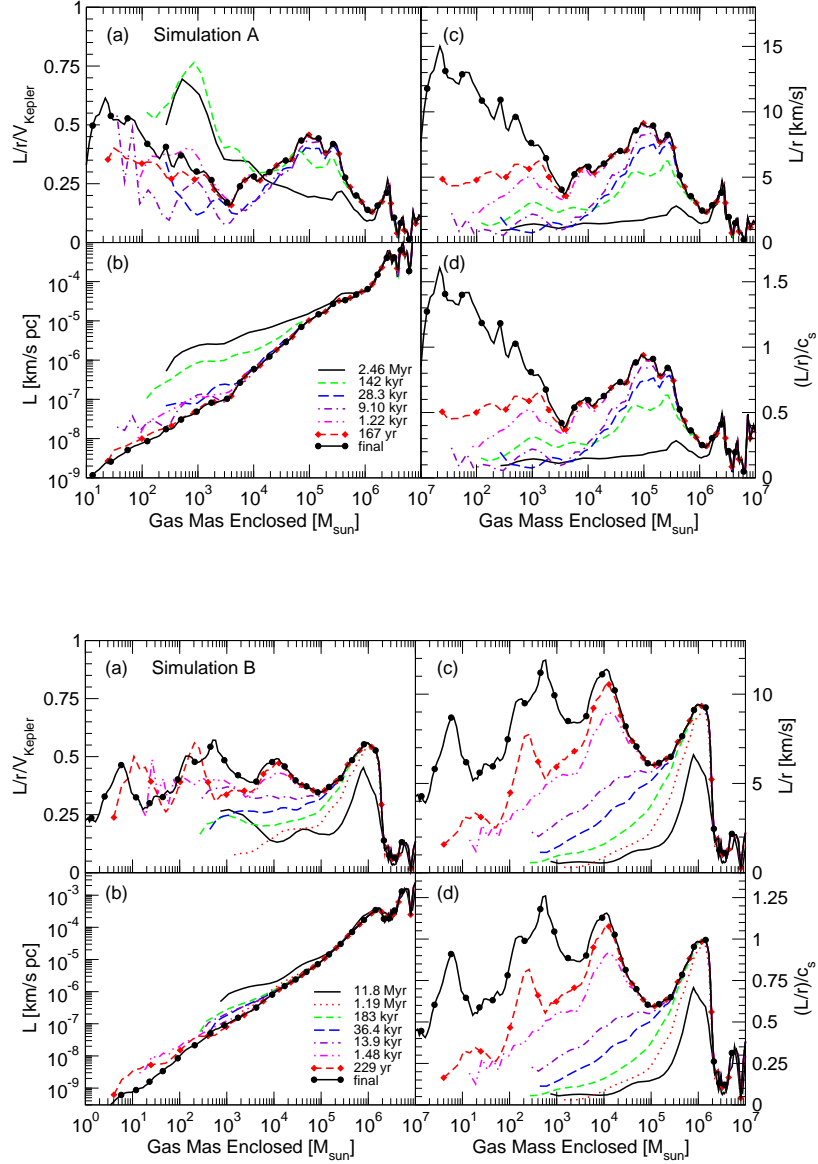


Fig. 4.11.— Mass-weighted radial profiles of various rotational quantities in simulation A (*left panels*) and simulation B (*right panels*). In panel A, we show the rotational velocity compared to the Kepler velocity $= \sqrt{GM/r}$. In panel B, we display the specific angular momentum (in units of [km/s] pc). In panels C and D, the typical rotational velocity and the ratio of the rotational velocity and sound speed are shown, respectively. The line styles correspond to the same times in Figure 4.4.

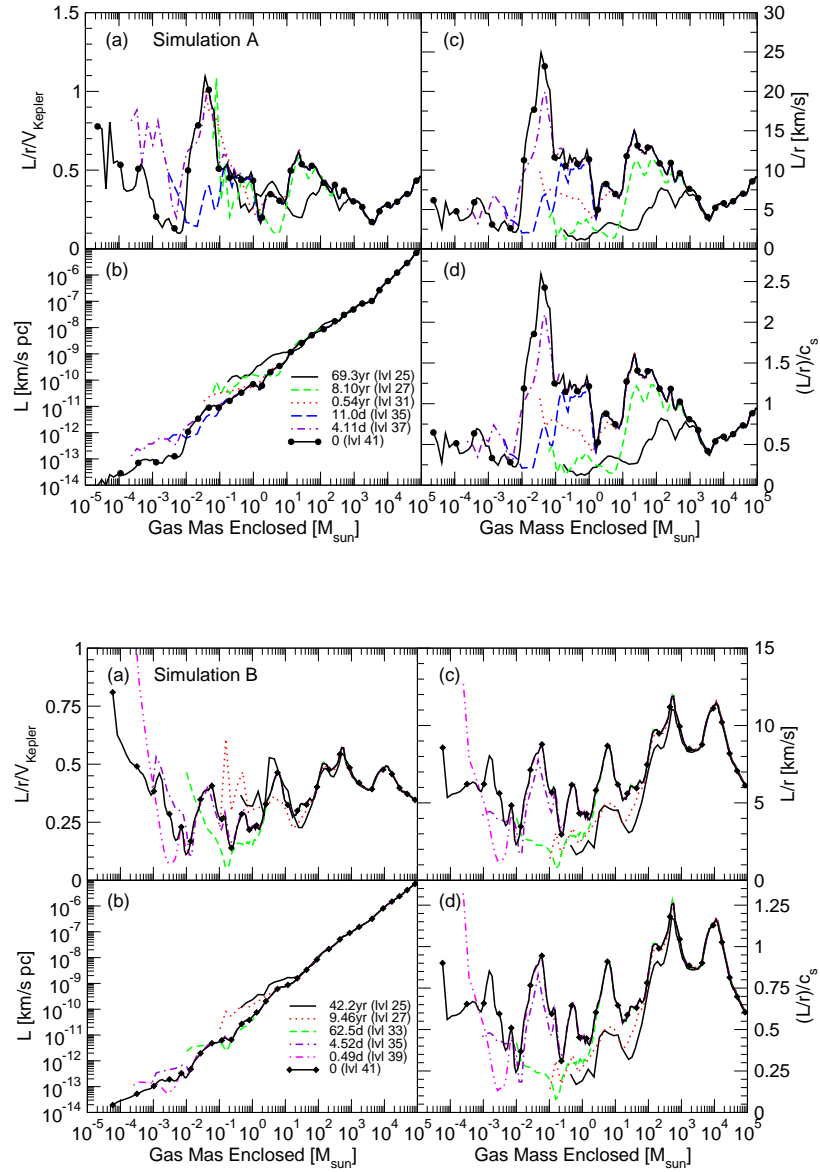


Fig. 4.12.— The same as Figure 4.11 but with the inner parsec of simulation A and B and the output times as listed in Figure 4.5.

velocities caused by conservation of angular momentum. However this causes another instance of a bar instability to occur. The increased infall velocity and associated decrease in rotational velocities (i.e. the dips in Figures 4.5d and 4.12d) depict this behavior. At the final output, the infalling material exhibits no rotational support similar to Simulation A at $r > 1$ AU. At the outputs that are 27 and 4.5 days before the final output, there is a hint of rotational support at $r < 1.7R_{\odot}$ ($M_{\text{enc}} = 0.33$ Jupiter masses), but this decays in the two later outputs.

We interpret the inner points where $L/r/V_{\text{Kepler}}$ fluctuations greatly or increases above unity with caution due to the nature of choosing a center in a turbulent medium. If the central sphere is smaller than a radius where the turbulent velocities average to zero, we introduce errors into the angular momentum profiles by sampling the turbulent gas incompletely. Thus we do not conclude that the inner regions are rotationally supported.

In the *b*-panels of Figure 4.11, one sees that specific angular momentum inside $M_{\text{enc}} < 10^6 M_{\odot}$ decreases over time and is transported outwards in the collapse. As discussed in Section 4.3.2 and shown in Figure 4.7, supersonic turbulence typically exists at all radii. Additionally, the rotational speed never exceeds the local sound speed, and we interpret this as further evidence for the efficient angular momentum transport. In a turbulent medium, transport is different than in a disk. At any radius, both high and low angular momentum gas exists, whereas in a Keplerian disk all gas have equal amounts of angular momentum. Rayleigh's criterion (Rayleigh, 1920; Chandrasekhar, 1961) states that specific angular momentum in a system must be a monotonically increasing function with radius. If this does not hold, the lower angular momentum gas at large radii will preferentially sink to smaller radii and vice versa that is similar to Couette flow. As this occurs, the system becomes unstable to turbulence. The onset of turbulence can be delayed if viscosity is large enough so that Reynolds numbers are below the order of 10^2 or 10^3 . However there are many modes of instability if Rayleigh's criterion is not met, and a gas with low Reynolds number will eventually become fully turbulent (Shu, 1992).

With a typical spin parameter, the thick disk with $r \sim 50$ pc is not rotationally supported. In simulation A, a global disk does not exist at all. We attribute this

behavior to the nature of angular momentum transport in a turbulent medium. Even with a higher spin parameter, we do not expect a disk to fragment before the central collapse due to the intrinsic amount of low angular momentum gas and shorter dynamical timescales in the center. This gas can collapse to such small radii without fragmentation so that a central mass of $\sim 10^5 M_\odot$ or 2% of the halo gas mass forms. After the initial collapse, the thick disk may become rotationally supported as more higher angular momentum gas infalls.

4.4 Discussion

In our cosmological simulations, we find that a $\sim 10^5 M_\odot$ dense object forms in the center of a metal-free protogalactic halo that supports atomic hydrogen cooling. Although we have neglected some important processes, such as H_2 chemistry, star and BH formation and feedback, our results show that rotational support cannot prevent matter from collapsing to a dense, massive object with $r < 5$ pc. Before the central collapse, there is no global, rotationally supported disk formation on the order of 50 pc (cf. Mo et al., 1998). However this does not preclude this type of disk formation, but the initial collapse into a central object must precede it. Disk formation and its associated star formation may also be dependent on the feedback and outcome of the central object. This additional stage of galaxy formation should be included in the most frequently employed models, where the earliest star formation occurs in high redshift disk galaxies.

4.4.1 Secular Instabilities

Our calculations show that the “bars within bars” cascade (Shlosman et al., 1989, 1990) occurs for gaseous systems due to a secular instead of dynamical instability (cf. Begelman et al., 2006). For a given morphology, this allows bar-like structures to form in systems having $T/|W|$ values 45% smaller than the ones calculated in Begelman et al.. We also find that rotational instabilities are possible without a global disk as in simulation A.

Our results should be applicable to any turbulent gaseous collapse, in particular galactic molecular clouds. Imagine the following scenario of an initially turbulent, slowly rotating, and uniform sphere beginning to collapse. In a turbulent medium, the gas with low specific angular momentum preferentially falls toward the center, leaving the high specific angular momentum at the outskirts of the cloud. This is seen in our specific angular momentum profiles of turbulent collapses (also see Abel et al., 2002; Yoshida et al., 2006b). Material with similar angular momentum now obtains some organized rotational velocity. Some shells become rotationally unstable to bar formation as it gains rotational velocity in its attempt to conserve angular momentum. In this example, the instabilities are secular and occur at $T/|W| \geq 0.14$ because turbulent viscosity provides the dissipative force. Then these rotational bar-like instabilities transport high angular momentum outwards so that the gas with low specific angular momentum can flow to a smaller radius. Afterwards, the “bars within bars” scenario drives gas to even smaller radius, eventually forming a central object, whether it be a star or BH. Angular momentum segregation in a turbulent medium and during the bar instability cascade could alleviate “the angular momentum problem” of a gravitational collapse, in which a cloud must somehow shed several orders of magnitude of angular momentum in order to form a central star or, in this case, a pre-galactic SMBH.

Nevertheless, we do not advocate our simulations as evidence of pre-galactic SMBH formation because we have neglected many important processes related to H_2 cooling and primordial star formation that we detail shortly afterwards. We expect the stellar feedback from Pop III stars to alter the “initial conditions” of early galaxy formation, as shown by recent radiation hydrodynamical simulations of the first stars (Yoshida et al., 2006a; Abel et al., 2007).

4.4.2 The Fate of the Central Object

Although we study the idealized collapse of a protogalactic collapse, it is still possible to infer the fate of the central object. In our simulations, the merger history and the subsequent turbulence influence the nature of the collapse. In simulation A, a

major merger precedes the collapse, and the turbulence is significant throughout the halo before and during the collapse. In the final output, turbulence extends inward to r_{BE} and may have caused the central object to be more massive and less dense. In simulation B, we find a less massive but more compact central object, which leads to a faster collapse. Since this halo did not experience a major merger before its collapse, the turbulence is smaller, and the medium is more homogeneous and has coherent rotational motions in the thick disk.

These two different environments may result in different types of objects. If the crossing and dynamical timescales are greater than the Kelvin-Helmholtz timescale, t_{KH} , for a massive star, star formation may commence and provide sufficient feedback to prevent further collapse. Alternatively, the collapse could proceed faster than t_{KH} and initially forms a BH. To further study the central dynamics, it will be necessary to employ sink particles (Bate et al., 1995; Krumholz et al., 2004) in order to avoid the decreasing timescales of the collapsing object(s).

4.4.3 The Role of Low Angular Momentum Gas

To form a central dense object, a sufficient amount of gas needs to have low angular momentum to infall to small radii. The origin and transport of this gas are integral to our comprehension of protogalactic gas cloud collapses. According to Rayleigh's inviscid stability criterion, angular momentum segregates such that the lowest angular momentum material piles up at the center of dark matter potential wells. We observe this behavior in the angular momentum distributions. The low angular momentum material may originate in lower mass progenitors. Here the gas resides in a shallower potential well that results in lower turbulent and random thermal velocities or equivalently an angular momentum distribution skewed to lower values. We argue that this effect is intimately linked to the gas acting to achieve virial equilibrium at all stages during the collapse (cf. Paper I). As this gas infalls, it gains rotational energy as it conserves angular momentum. It then experiences a secular bar instability as discussed in Section 4.3.6 that transports angular momentum outward so only the lowest angular momentum gas collapses toward the center. This picture is true also

in simulations of the very first stars (Abel et al., 2002).

The angular momentum distribution also influences the manner in which the halo collapses. It should be noted that the angular momentum distribution, not the total angular momentum of a halo, dictates the nature of its collapse because gas parcels within the halo will segregate into different regions of the halo. In principle, the low angular momentum material sinks inward and forms the central structures. If an insufficient amount of low angular momentum matter exists in the halo, it cannot monolithically collapse and will form a disk (Fall & Efstathiou, 1980).

4.4.4 Applicability

Limitations of Current Approach

Our results depict the importance of turbulence, accretion, and the hydrogen cooling in the initial collapse of these halos. However we are missing some essential processes, such as H_2 chemistry, primordial and Population II stellar formation and feedback, SMBH formation and feedback, and metal transport and cooling. It was our intention to study only the hydrogen and helium cooling case first and gradually introduce other processes at a later time to investigate the magnitude and characteristics of their effects, which we will present in later papers.

Gas becomes optically thick to $\text{Ly}\alpha$ radiation above number densities of 10^7cm^{-3} , but we continue to use optically thin cooling rates above this density. We overestimate the cooling within 0.1 pc. As a consequence, we do not suggest that these simulated objects ever form in nature. However this scenario poses an excellent problem of a turbulent collapse. This should be common in galaxy formation, where turbulence is generated during virialization, and star formation within turbulent molecular clouds.

Desired Improvements

Clearly local dwarf spheroidals contain stars with ages consistent with formation at very high redshifts (Ferrara & Tolstoy, 2000; Tolstoy et al., 2002, 2003; Helmi et al., 2006). To develop a model that desires to fit galaxy luminosity functions down to the faintest observed galaxies one may need a star formation and feedback

model that follows molecular clouds as small as one thousand solar masses in order to allow for the dominant mode of star formation observed locally. It should be already technologically feasible with current cosmological hydrodynamical models to simulate these galaxies one star at a time.

Correct initial conditions for early galaxy formation require prior star and BH formation and feedback. The typically adopted conditions for phenomenological star formation are velocity convergence, a density that exceeds some critical value, $t_{\text{dyn}} > t_{\text{cool}}$, and a low temperature (Cen & Ostriker, 1992). Phenomenological primordial star formation is possible if we include two additional conditions as utilized in Abel et al. (2007). First, the H_2 fraction must exceed 10^{-3} (Abel et al., 2002), and second, the metallicity of the gas must not exceed the “critical metallicity” of $10^{-3} - 10^{-4}$ of the solar value (Bromm et al., 2001). From prior studies (e.g. Abel et al., 2002; Bromm & Loeb, 2003; O’Shea et al., 2005), we expect these stars to form in halos that can support H_2 cooling and in relic H II regions. The Lyman-Werner radiation from massive stars can dissociate H_2 from large distances, suppress star formation in lower mass halos (Machacek et al., 2001; Wise & Abel, 2005), and must be considered to accurately model future star formation.

BH formation in the death of some primordial stars can also have a profound effect on surrounding structure formation as it accretes infalling matter during later mergers. Therefore it is necessary to include its effects from seed BHs from primordial stars with masses outside of the range between 140 and 260 solar masses. Also it is possible to phenomenologically model SMBH formation in a similar manner to the stellar case. If the protogalactic collapse occurs faster than the stellar formation timescale of a massive star, a SMBH may form inside this region. Using the stellar formation conditions plus this condition and allowing the particle to accrete (i.e. sink particles; Bate et al., 1995; Krumholz et al., 2004), SMBH formation can be followed in cosmological hydrodynamic simulations. These sink particles should regulate the accretion with an appropriate subgrid model. Important processes include an appropriate accretion rate (e.g. Eddington or Bondi-Hoyle), turbulence (Krumholz et al., 2006), rotational support of the infalling gas, and a viscosity timescale for accretion disks.

For small galaxies radiative transfer effects can have a great impact (e.g. Haehnelt, 1995; Whalen et al., 2004; Kitayama et al., 2004; Alvarez et al., 2006) and should not be neglected. The approach of Gnedin & Abel (2001), although promising, has not been implemented and coupled with an adaptive hydrodynamics code that is capable of high dynamic range calculations. However, the novel technique of adaptive ray tracing (Abel & Wandelt, 2002) has recently been implemented into *Enzo* and used to study the outflows and ionizing radiation from a primordial star (Abel et al., 2007). There ionization front instabilities create cometary small-scale structure and shadowing effects as a result from the explicit treatment of three-dimensional radiative hydrodynamics. Lastly as used in many stellar formation routines (Cen & Ostriker, 1992; Tassis et al., 2003), we hope to include thermal and radiative feedback from Population II stars in future studies.

4.5 Conclusions

We have simulated the hydrodynamics and collapse of a protogalactic gas cloud in two cosmology AMR realizations. Our focus on the hydrodynamics presents a basis for future studies that consider stellar and BH feedback. In the idealized case presented, we find a central dense object forms on the order of $10^5 M_\odot$ and $r \lesssim 5$ pc. This central object is not rotationally supported and does not form a disk in our simulations. However our results do not dismiss disk formation in protogalaxies, and rotationally supported disk formation may begin after the initial central collapse. Disk formation could also depend on the feedback and outcome of the central object. This initial central collapse adds another phase to the most frequently employed galaxy formation models, where star formation commences in a gaseous disk.

These simulations highlight the relevance of secular bar-like instabilities in galaxy formation. Similar bar structures are witnessed in primordial star formation simulations. As low angular momentum infalls, it gains rotational energy as it conserves angular momentum. This induces an $m = 2$, bar-like instability that transports angular momentum outwards, and the self-similar collapse can proceed without becoming rotationally supported and exhibits $\rho \propto r^{-12/5}$. This process repeats itself as material

infalls to small scales that is indicative of the “bars within bars” scenario. We see three and five occurrences of embedded secular instabilities in the two realizations studied here.

We also find that gas turbulence influences the collapse in two different mechanisms. First, supersonic turbulence provides a channel for the gas to preferentially segregate according to specific angular momentum. The low angular momentum material sinks to the center and provides the material necessary for a central collapse. Second, the degree of turbulence created from the previous mergers can delay the central collapse. The final characteristics of the central object depend on the balance of collapse and star formation timescales. Possible outcomes are BH formation, a starburst, or a combination of both.

All of these cases are viable in the early universe, and the occurrence of these cases depends on the merger history, local abundances in the halo, and the existence of a seed BH. Moreover, star formation should occur whether a central BH exists or not. Perhaps the frequency of these different protogalactic outcomes may be traced with either 3D numerical simulations that consider star and SMBH formation and feedback along with metal transport or Monte Carlo merger trees that trace Pop III star formation, metallicities, and BHs. We will attempt the former option in later studies to investigate protogalactic formation in more detail.

Chapter 5

Suppression of H₂ Cooling in the UVB

We have studied the standard model of galaxy formation, where dark matter halos of masses greater than $10^8 M_\odot$ are the first luminous objects in the universe. However, it has been known since the 1960's that molecular hydrogen plays an important role in structure formation in the early universe. Molecular hydrogen is a delicate species that can be dissociated from large distances since the universe is optically thin to the H₂ dissociating radiation between 11.2 and 13.6 eV. This effect has been argued that a soft ultraviolet background renders the relevance of H₂ unimportant in this epoch. To investigate this claim, we include H₂ cooling in our simulations while including such radiation backgrounds, adding yet more physics to our study. The implications of luminous objects existing before the first galaxies are significant because their feedback processes will change the initial density and temperature structures where the first galaxies form.

This chapter is in preparation for publication in *The Astrophysical Journal*. It is co-authored by Tom Abel, who suggested the initial motivation of this work and provided excellent critique in the arguments used to stress the importance of H₂ cooling in early structure formation.

5.1 Motivation

Cosmic structure forms hierarchically. Any object in the universe today started with copious numbers of small progenitors at redshifts currently inaccessible to direct observations. Traditionally in galaxy formation (Rees & Ostriker, 1977; White & Rees, 1978; Dekel & Rees, 1987; White & Frenk, 1991; Baugh et al., 2003) $T_{\text{vir}} = 10^4$ K halos are assumed to be the first cooling halos. Nevertheless since the late 1960's it has been known that molecular hydrogen, formed in the gas phase, can dominate cooling in objects of smaller virial temperature and mass (Saslaw & Zipoy, 1967; Peebles & Dicke, 1968; Yoneyama, 1972; Haiman et al., 1996; Tegmark et al., 1997; Abel et al., 1998, 2000). Neglecting this early phase of H_2 cooling halos has been justified by arguing that H_2 is destroyed via radiative feedback effects (cf. Dekel & Rees, 1987; Haiman et al., 1997, 2000; Glover & Brand, 2001; Bromm & Loeb, 2003). The photo-dissociation of H_2 via the Solomon process by an early soft ultraviolet background (UVB) is generally assumed as the main reason (Oh & Haiman, 2002; Ciardi & Ferrara, 2005; Haiman & Bryan, 2006).

The mass scale of halos considered enters exponentially in the collapsed mass fraction and the abundance of halos. Figure 5.1 shows the predicted abundances of the earliest building blocks of galaxy formation as a function of redshift for the latest concordance cosmology using the Sheth-Tormen formalism (Press & Schechter, 1974; Sheth & Tormen, 2002). The different lines correspond to different virial masses. The solid line corresponds to halos with virial temperatures of 10^4 K, the temperature at and above which atomic hydrogen line cooling is dominant. At redshift 30, e.g., the difference of abundances of $2 \times 10^5 M_{\odot}$ and $T_{\text{vir}} = 10^4$ K halos is five orders of magnitude. Even at redshift 10 this disparity is still a factor of a thousand. When studying reionization and chemical evolution of galaxies and the intergalactic medium, one needs to consider stellar feedback. The simple fact that the binding energy of the gas of smaller mass halos is even less than the kinetic energy deposited by even one supernova (SN) is illustrated in Figure 5.1B. Surely whether the atomic hydrogen line ($\text{Ly}\alpha$) cooling halos are formed from pristine primordial gas or are mergers of many tens of progenitors that massive stars have enriched and expelled the gas from

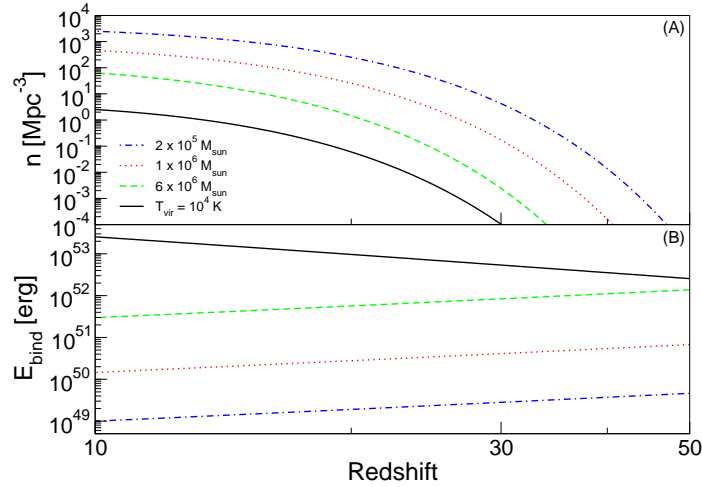


Fig. 5.1.— *Panel A*: Sheth Tormen number density of dark matter halos as a function of redshift for $T_{\text{vir}} = 10^4 \text{ K}$, $M = 2 \times 10^5$, 10^6 , and $6 \times 10^6 M_{\odot}$ using WMAP 3 year data for parameters. *Panel B*: Binding energies as a function of redshift for the corresponding halos (same line styles as in panel A)

should make a significant change in their further evolution. The minimum mass of star forming halos is undoubtedly an important issue independent of the techniques employed to study structure formation.

Advances in cosmological hydrodynamics and its numerical methods (Cen & Ostriker, 1992; Zhang et al., 1995; Katz & Hernquist, 1996; Abel et al., 1997; Anninos et al., 1997; Bryan & Norman, 1998; Gnedin & Abel, 2001; Ricotti et al., 2002a,b) allow now detailed investigations of all the relevant physical processes. Modeling the expected negative feedback from an early soft UVB is straightforward as a background flux only causes a spatially constant photo-dissociation rate in the chemical reaction network being solved when H_2 does not exist at high enough abundances to self-shield. Machacek et al. (2001, MBA01 hereafter) used Eulerian adaptive mesh refinement (AMR) simulations to investigate the role of such a H_2 dissociating (Lyman-Werner; LW) background on the minimum mass of halos within which primordial gas can first cool for a variety of radiation amplitudes. In addition to a LW background, the collapse of halos within relic H II regions can be either delayed or catalyzed. Mesinger et al. (2006) used AMR simulations with a short-lived 3 Myr hydrogen ionizing UVB

that simulates a nearby massive, metal-free (Pop III) star. They found that halo collapses are prolonged if $J_{UV} \gtrsim 0.1$ and catalyzed if below this critical value, where J_{UV} is in units of $10^{-21} \text{ erg s}^{-1} \text{ cm}^{-2} \text{ Hz}^{-1} \text{ sr}^{-1}$ at a wavelength of 912 \AA . In the case of a large UVB, the collapse is delayed due to lower gas densities and higher cooling times. In the small UVB regime, excess free electrons in the relic H II region accelerate H_2 formation. In both cases, feedback in relic H II subsides after $\sim 30\%$ of a Hubble time. Strong suppression of H_2 formation also occurs in $10^6 M_\odot$ halos with a LW background $J_{LW} > 0.01$. Yoshida et al. (2003, YAHS03 hereafter) similarly addressed this issue using smoothed particle hydrodynamics (SPH). They found an additional effect on the minimum collapse mass of dynamical heating from the mass accretion history of the halo. As the heat input increases, the virial temperature must rise before H_2 cooling can start to dominate, and a cool phase develops in the center of the potential well.

Self-consistent calculations in which the sources produce the radiation backgrounds which in turn affect the number of new sources are feasible so far only with semi-analytic approaches (Haiman et al., 2000; Wise & Abel, 2005, WA05 hereafter) and small volume cosmological simulations at low spatial resolutions (Ricotti et al., 2002a,b). From these studies, one can derive realistic upper limits on the amplitude of the expected soft UVB. In all studies that include radiation sources in halos less than $10^4 K$ halos, the largest the soft UVB flux can get before the $T > 10^4 K$ halos dominate the emission is $J_{LW} \sim 1$ (cf. Haiman et al., 2000; Ricotti et al., 2002a,b, WA05). Interestingly, for a LW intensity of $J_{LW} \sim 0.1$, MBA01 found that $2 \times 10^6 M_\odot$ halos were still able to cool and collapse. On the other hand at that J_{LW} , YAHS03 suggest negative feedback should become so strong that the critical H_2 fraction for cooling cannot be reached and cooling will not occur. However, they did not explore this further with detailed higher resolution simulations to check whether their analytical expectation would hold.

We present a series of fourteen very high resolution Eulerian AMR simulations designed to see how the largest possible feedback may raise the minimum mass in which primordial gas will cool by molecular hydrogen. The simulations techniques and details of the suite of calculations is the topic of the next section. In the following

sections, we describe the results that show H_2 cooling cannot be neglected in early structure formation. In the discussion, we describe the nature of the UVB and why H_2 cooling can occur in such large radiation backgrounds. We also comment on the large range of questions in cosmological structure formation that this conclusion affects.

5.2 Simulations and Assumptions

We use the Eulerian AMR hydrodynamic code *Enzo* (Bryan & Norman, 1997, 1999) to study the importance of H_2 cooling in early galaxy formation. *Enzo* uses an n -body adaptive particle-mesh solver (Couchman, 1991) to follow the dark matter (DM) dynamics. We perform two cosmological realizations with different box sizes and random phases and WMAP 1 year parameters of $(h, \Omega_\Lambda, \Omega_M, \Omega_b, \sigma_8, n) = (0.72, 0.73, 0.27, 0.024h^{-2}, 0.9, 1)$ (Spergel et al., 2003). The significantly different third year WMAP (WMAP3; Spergel et al., 2006) results favor lesser small-scale power that delays high-redshift structure formation by $\sim 40\%$ and alters the statistical properties of DM halos (Alvarez et al., 2006). The ratio Ω_M/Ω_b also only lowered by 5% to 5.70. However these differences have no effect on the evolution and assembly of individual halos studied here that have typical mass accretion histories.

The initial conditions are the same as in Wise & Abel (2007). Both realizations have a top grid with a resolution of 128^3 with three nested subgrids with twice finer resolution and are initialized at $z = 129$ (119)¹ with the COSMICS package (Bertschinger, 1995, 2001). The box size is 1.0 (1.5) comoving Mpc. The innermost grid has an effective resolution of 1024^3 with DM particle masses of 30 (101) M_\odot and a side length of 250 (300) comoving kpc. We refine the AMR grids when either the DM (gas) exceeds three times the mean DM (gas) density on the same level. We also refine so that the local Jeans length is resolved by at least 4 cells.

We focus on the region containing the most massive halo in the simulation box and follow its evolution until it collapses to an overdensity of 10^7 that corresponds to

¹To simplify the discussion, simulation A will always be quoted first with the value from simulation B in parentheses.

a refinement level of 15 and a spatial resolution of ~ 3000 (4000) proper AU.

We perform each realization with seven sets of assumptions. Table 3.1 summarizes them. We use a nine-species (H, H⁺, He, He⁺, He⁺⁺, e⁻, H₂, H₂⁺, H⁻) non-equilibrium chemistry model (Abel et al., 1997; Anninos et al., 1997) for all runs except the H+He runs that do not include H₂ cooling. The nine-species runs are specified by “H2”. Runs with H₂ dissociating (Lyman-Werner; LW) radiation are denoted by “LW” followed by its negative log-flux. We set F_{LW} to 10^{-22} , 10^{-21} , and 10^{-20} erg s⁻¹ cm⁻² Hz⁻¹ because the first two are typical values one finds in semi-analytic models of reionization and the latter investigates the case of a very large UVB (e.g. Haiman et al., 2000; Wise & Abel, 2005). We use the H₂ photo-dissociation rate coefficient for the Solomon process from Abel et al. (1997) of $k_{\text{diss}} = 1.1 \times 10^8 F_{\text{LW}} \text{ s}^{-1}$.

Table 5.1: Simulation Properties

Name	H ₂	Residual e ⁻	F_{LW}	z_a	z_b
H2	Yes	Yes	0	29.7	31.1
H2LW22	Yes	Yes	10^{-22}	28.3	27.5
H2LW21	Yes	Yes	10^{-21}	24.4	24.7
H2LW20	Yes	Yes	10^{-20}	20.5	22.4
noe-H2	Yes	No	0	18.7	23.4
noe-H2LW20	Yes	No	10^{-20}	16.8	21.4
H+He	No	Yes	0	15.9	16.8

Note. — These simulations are performed for both realizations.

Free electrons are necessary to form H₂ in the gas phase. In order to restrict H₂ formation to Ly α line cooling halos in our “noe-” calculations, we reduce the residual free electron fraction from $\sim 10^{-4}$ (Peebles, 1968; Shapiro et al., 1994) to a physically low 10^{-12} at the initial redshift. This setup is designed to find the first halos that can collapse and form stars once free electrons from collisionally ionized hydrogen becomes available to catalyze H₂ formation (Shapiro & Kang, 1987).

This work is an extension of the original work of MBA01, adding the calculations with $F_{\text{LW}} = 10^{-20}$ and ones in which H_2 cannot cool until $\text{Ly}\alpha$ cooling becomes efficient. We consider these extreme cases to strengthen the point made in MBA01 in which a UVB only increases the critical halo collapse mass, never completely suppressing the crucial importance of H_2 formation and cooling. Our maximum spatial resolution in the finest AMR level is a factor of four smaller than MBA01; however, this does not cause any differences between our work and MBA01 because these finest grid patches only exist in the dense, central core during the final 150 kyr of the collapse.

5.2.1 Virial Temperature

In galaxy formation models, the virial temperature is a key quantity as it controls the cooling and star formation rates in a given halo. We define a halo as the material contained in a sphere of radius r_{200} enclosing an average DM overdensity Δ_c of 200. For an isothermal singular sphere, the virial temperature

$$T_{\text{vir}} = \frac{\mu m_p V_c^2}{2k}, \quad (5.1)$$

where $V_c^2 = GM/r_{200}$ is the circular velocity (see Bryan & Norman, 1998, with $\beta = 1$). Here μ is the mean molecular weight in units of the proton mass m_p , and k is Boltzmann's constant. We use this definition of T_{vir} in this paper with $\mu = 0.59$. We choose this value of μ to be consistent with the literature on galaxy formation even though the halos presented in this paper are neutral and have $\mu = 1.22$.

5.3 Results

We first describe the halo properties at collapse. Then we compare them to previous studies of collapsing halos in the presence of a soft UVB.

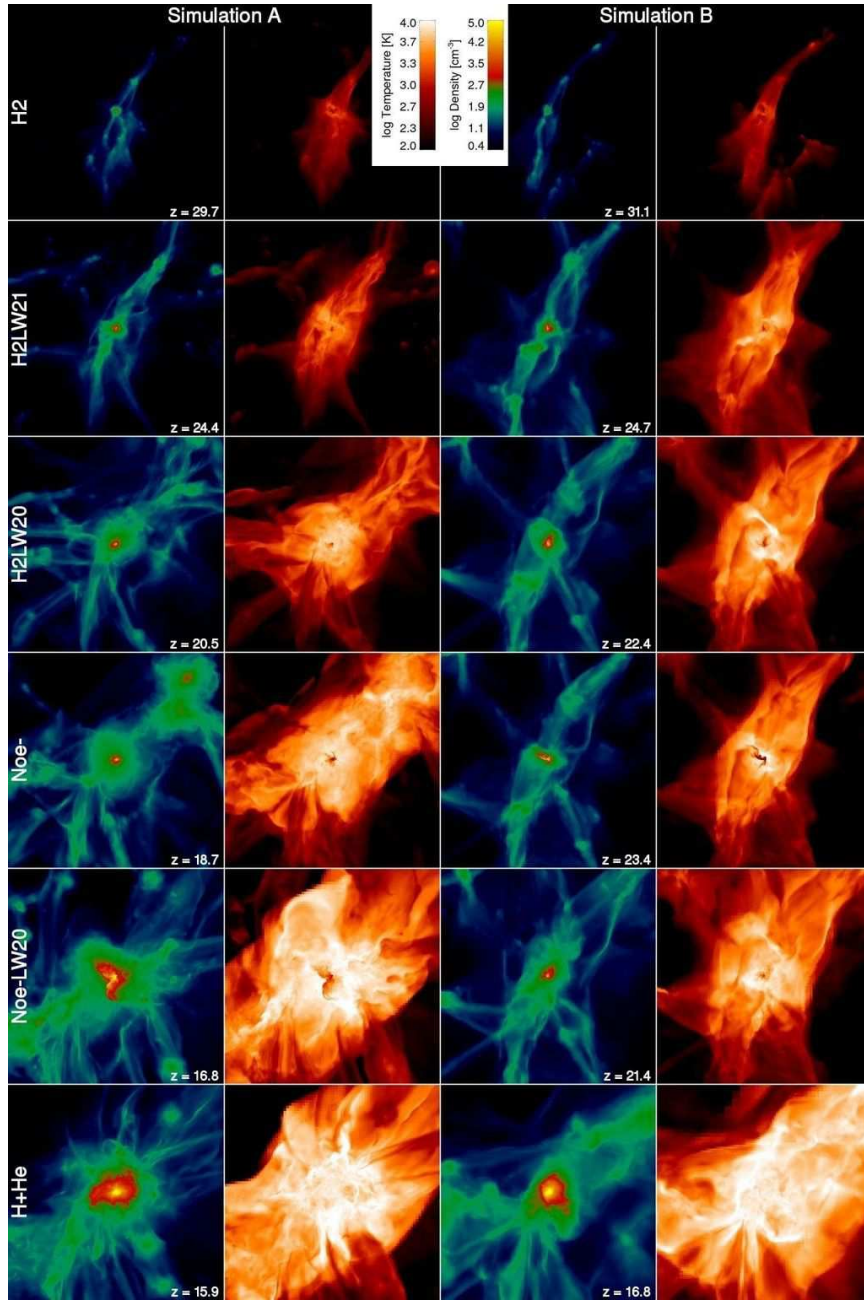


Fig. 5.2.— Projections in simulation A (left two columns) and B (right two columns) of the gas density (first and third columns) and temperature (second and fourth columns) at the times when the most massive halo starts to cool and collapse above an overdensity of 10^7 in the models. The rows show the H2, H2LW21, H2LW20, and noe-H2, noe-H2LW20, and H+He runs from top to bottom, respectively. Note the complex structure for the SimA-Noe-LW20 and SimB-Noe-H2 run in which central shocks lead to the formation of free electrons that promote the formation of H_2 and trigger the collapse. The field of view in all panels is 1.2 proper kpc. The color maps are equal for all runs.

5.3.1 Halo Properties

Figure 5.2 shows density-squared weighted projections of gas density and temperature when each calculation can cool and collapse to an overdensity of 10^7 . It illustrates the large difference in the sizes and morphologies of the collapsing halos in the various cases of negative feedback. All panels have the same field of view of 1.2 proper kpc and same color scales. It is clear from the relative sizes of the collapsing halos that the critical halo mass to cool increases with the amount of negative feedback. The virial shock and numerous central shocks heat the gas to the virial temperature. The central shocks create fine structure seen in the temperature projections. In all of the H₂ cases, we see neither fragmentation nor large-scale disk formation. The internal structures of the halos with H₂ cooling and residual free electrons are similar to previous studies of Pop III star forming halos (MBA01; Abel et al., 2000, 2002; Bromm et al., 2002; Yoshida et al., 2003), exhibiting a turbulent medium with a radially monotonically decreasing density profile and a cool central core.

Figure 5.3A depicts the halo mass and redshift when the halo collapses for all of the runs, and Figure 5.3B shows their central temperature at the same epoch. The collapse redshifts, z_a and z_b , are also listed in Table 3.1 for simulations A and B, respectively. As seen in other studies (MBA01, YAHS03), the minimum DM halo mass to collapse increases with the background intensity. The H+He case predictably collapses at $T_{\text{vir}} \sim 10^4$ K, and all of the halos with H₂ cooling collapse at much smaller masses. The temperature of the central core increases with halo mass from 300 K to 1000 K for halo masses $4 \times 10^5 M_\odot$ and $10^7 M_\odot$. Restricting the data to models with residual electrons, the central temperature increases as a power-law, $T_c = AM_{\text{vir}}^B$, where $A = 3.1_{-0.9}^{+1.3}$, $B = 0.355 \pm 0.024$, and M_{vir} is in units of solar masses. This relationship is plotted in Figure 5.3.

With neither residual electrons nor an UVB (noe-H2), the most massive halo collapses at $9.8 (6.2) \times 10^6 M_\odot$ at $z = 18.7 (23.4)$. Here H₂ formation in the gas phase can only become important when sufficient free electrons are created by collisional ionization. Virial heating in the center of halos can increase temperatures up to twice the virial temperature (Wise & Abel, 2007) that collisionally ionizes hydrogen in the central shocks and initiates H₂ cooling (Shapiro & Kang, 1987) in halos well

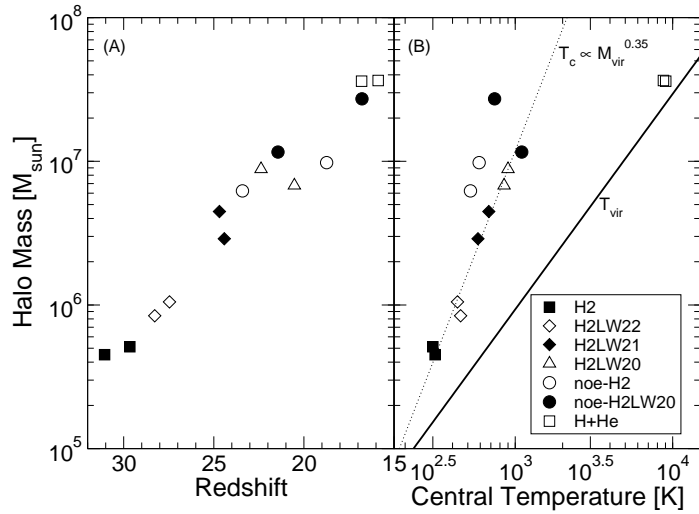


Fig. 5.3.— *Panel A*: Halo masses of the most massive halos as function of redshift when they reach a central overdensity of 10^7 . This allows to translate the mass values in Panel B to be converted to cooling redshifts. It marks the runs with H+He (*filled squares*), H_2 (*open squares*), $F_{\text{LW}} = 10^{-22}$ (*open diamonds*), $F_{\text{LW}} = 10^{-21}$ (*filled diamonds*), no residual electrons (*open circles*), and extreme feedback noe-LW20 (*filled circles*) runs. The two data points for each symbol represent simulations A and B. Even for the most extreme cases of feedback cooling occurs much earlier than in the atomic line cooling only case. *Panel B*: Central temperatures of the most massive halo in the simulation as a function of its mass at different redshifts. The virial temperature computed from the dark matter halo mass at redshift 20 is the solid line. The dotted line is the fitted relationship between the central gas temperatures and the halo mass in models with residual electrons and H_2 cooling.

below virial temperatures of 10^4 K. These shocks are abundant throughout the central regions. Figure 5.4 shows radial profiles of temperature and electron fraction for both simulations and depicts gas shock-heating up to 2×10^4 K and electron fractions up to 10^{-3} . The electron fractions remain at unrealistically low values less than 10^{-6} in low density regions where gas has not been collisionally ionized. The higher density regions have condensed to densities above $3 \times 10^2 \text{ cm}^{-3}$ after free electrons in protogalactic shocks induced H_2 cooling.

A similar but extreme model demonstrates that even in the presence of a very large UVB of $F_{\text{LW}} = 10^{-20}$ gas is able to form a cool and dense central molecular

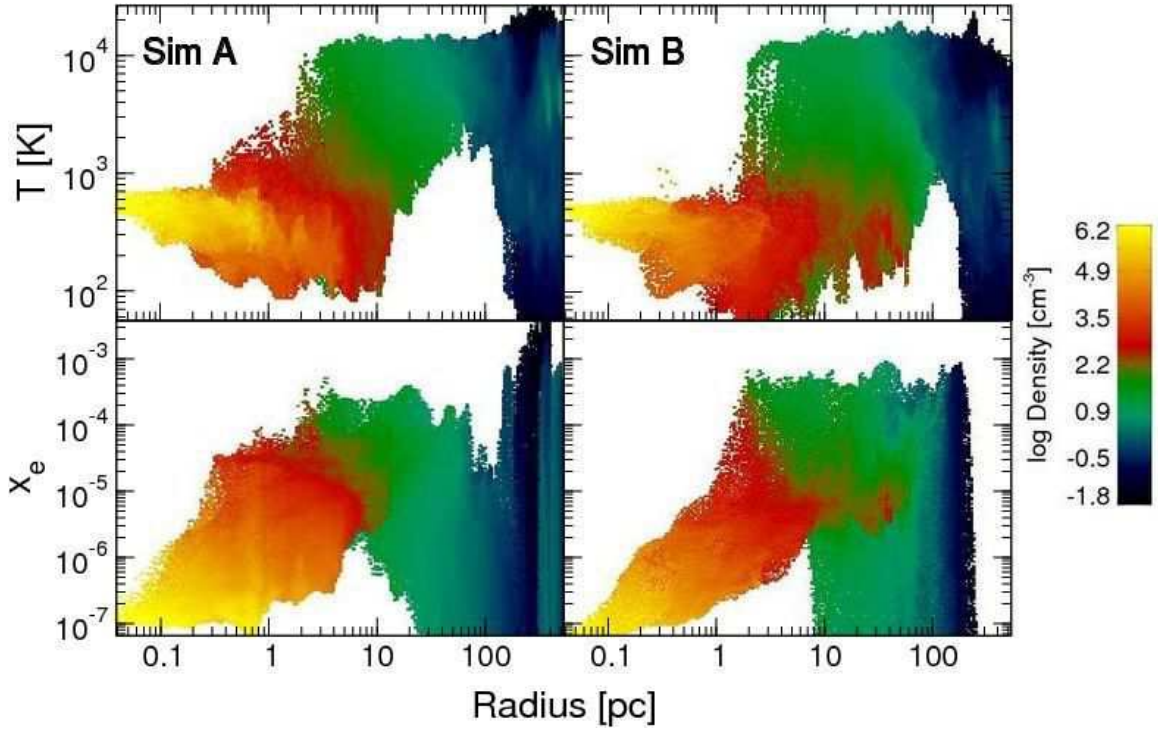


Fig. 5.4.— Radial profiles of temperature (*top*) and electron fraction (*bottom*) colored by density for the “noe-” simulations with no residual free electrons or UVB in simulation A (*left*) and B (*right*). The virial temperatures of these halos are 4600K and 4200K for simulation A and B, using equation (5.1) with $\mu = 0.59$.

core at a mass of $2.7 (1.1) \times 10^7 M_\odot$ at redshift 16.8 (21.4). Two major mergers in simulation A occur between $z = 17$ – 21 , and the associated heating allows the halo to begin cooling by H_2 . A central core only forms once the system is adequately relaxed after the mergers, which causes the collapse mass difference between the realizations.

The combination of a recent major merger and collisional ionization produces complex structures as seen in the density and temperature projections of the SimA-Noe-LW20 and SimB-Noe- calculations in Figure 5.2, unlike the other H_2 models with a single cool central core.

5.3.2 Comparison to Previous Studies

Through a series of AMR calculations with varying UVB intensities, MBA01 found the minimum DM halo mass to be $2.5 \times 10^5 + 1.7 \times 10^6 (F_{\text{LW}}/10^{-21})^{0.47} M_{\odot}$ in order to cool and condense 4% of the baryons. This fraction of cool and dense gas agrees with simulations of the formation of Pop III stars (Abel et al., 2002; Yoshida et al., 2006b). There is some scatter of ~ 0.5 dex in this threshold mass (see also YAHS03). For the UVB intensities used in our models ($F_{\text{LW}} = 0, 10^{-22}, 10^{-21}, 10^{-20}$), the critical collapse masses are $2.5 \times 10^5, 8.4 \times 10^5, 2.0 \times 10^6$, and $5.4 \times 10^6 M_{\odot}$. Our calculations with H₂ cooling and residual free electrons agree with the results of MBA01.

YAHS03 studied the minimum collapse mass but also included the effects of self-shielding. Through their SPH simulations and arguments using equilibrium H₂ abundances, they conclude that an UVB intensity of $J_{21} = 0.1$ nearly prevents halo collapses below $T_{\text{vir}} \simeq 7000$ K where Ly α cooling becomes efficient. They also deduce that $J_{21} = 1.0$ completely prevents any H₂ cooling in these low-mass halos, based on H₂ dissociation timescales. We find the contrary in our H2LW21 and H2LW20 calculations where the most massive halo collapses with a mass of $4.5 (2.9) \times 10^6 M_{\odot}$ and $8.8 (6.8) \times 10^6 M_{\odot}$, respectively. Even in our noe- runs, the halo collapses when $T_{\text{vir}} \sim 4000$ K, i.e. before Ly α cooling becomes important, which is around the same mass scale that the H2LW20 runs condense. We ignore self-shielding in our calculations, but this would only decrease the critical collapse mass. This difference is most likely a consequence of our high resolution shock capturing numerical method and high spatial resolution as compared to the SPH approach of YAHS03 that was designed to study the statistical aspects of these objects.

The halo characteristics and the collapse redshift will likely depend on halo merger histories as seen in these two realizations. The better statistics of MBA01 sampled this effect well. Here the scatter of threshold mass is ~ 0.5 dex and is smaller than the mass difference between halos with virial temperatures of 4000K and 10000K. Thus our limited sample of halos should not change our result of the importance of H₂ cooling in halos well below $T_{\text{vir}} = 10^4$ K, even with very large LW radiation backgrounds.

5.4 Discussion

Structure formation in the high-redshift universe is contained within shallow potential wells that are sensitive to negative feedback from a UVB. Additionally local positive and negative feedback will influence star formation and further complicate estimates of halo mass scales. Some examples include

- *Positive feedback*— Enhanced H_2 formation in relic H II regions (e.g. Ferrara, 1998; O’Shea et al., 2005; Johnson et al., 2007) and ahead of the H II ionization front (Ricotti et al., 2001; Ahn & Shapiro, 2007), dust and metal line cooling (Glover, 2003; Schneider et al., 2006; Jappsen et al., 2007),
- *Negative feedback*— Baryonic expulsion from host halos (Whalen et al., 2004; Kitayama et al., 2004; Yoshida et al., 2006a; Abel et al., 2007), photo-evaporation (Susa & Umemura, 2006), entropy floors (Oh & Haiman, 2003).

These processes are not within the scope of this paper and will be considered in later publications that utilize three-dimensional radiation hydrodynamic simulations with Pop III star formation. Here we only focused on the effects of a UVB on low-mass halos.

5.4.1 The Nature of the UVB

The intensity of the UVB is a monotonically increasing function of redshift as more halos form stars. The UVB increases on the order of a Hubble time, which is much shorter than a dynamical time of a collapsing halo and justifies the use of a constant intensity in our calculations.

Self-consistent studies that evolve the UVB according to star formation rates only find J_{LW} to be in the range of 0.01 and 0.1 at redshifts 15–20 (YAHS03, WA05). WA05 calibrated their model against the WMAP1 measurement of $\tau = 0.17$. With the WMAP3 result of the electron scattering optical depth $\tau = 0.09$ and less small-scale power, UVB intensities will be even lower at these redshifts.

We can relate reionization to LW radiation by equating J_{21} in the LW band to a common quantity in reionization models, the ratio of emitted hydrogen ionizing

photons to baryons, $n_{\gamma,\text{HI}}/\bar{n}_b$, where $\bar{n}_b \simeq 2 \times 10^{-7}(1+z)^3 \text{ cm}^{-3}$ is the cosmic mean of the baryon number density. Assuming that J_{LW} is constant in the LW band, the number density of LW photons is

$$\begin{aligned} n_{\gamma,\text{LW}} &= \frac{4\pi}{c} \int_{\nu_1}^{\nu_2} \frac{J_{\text{LW}}}{h_p \nu} d\nu \\ &= 1.19 \times 10^{-5} J_{\text{LW}} \text{ cm}^{-3}, \end{aligned} \quad (5.2)$$

where h_p is Planck's constant and $\nu_1, \nu_2 = 2.70 \times 10^{15} \text{ Hz}, 3.26 \times 10^{15} \text{ Hz}$ bound the LW band. To relate J_{21} to $n_{\gamma,\text{HI}}/\bar{n}_b$, we must consider the intrinsic ionizing spectrum and absorption from the IGM and host halo. At redshift 20, the majority of star forming halos host Pop III stars that emit a factor $\phi_{\text{HI}} \simeq 10$ more hydrogen ionizing photons than LW photons because of its $\sim 10^5 \text{ K}$ surface temperature. Since the number density of sources exponentially increases with redshift, the majority of the early UVB at a given redshift originates from cosmologically nearby ($\Delta z/z \sim 0.1$) sources. Lyman line resonances absorb a fraction $f_{\text{abs}} \sim 0.1$ of the LW radiation in the intergalactic medium in this redshift range, producing a sawtooth spectrum (Haiman & Loeb, 1997). Additionally, absorption in the host halo reduces the number of ionizing photons that escape into the IGM by a fraction f_{esc} . For Pop III halos, this factor is close to unity (Yoshida et al., 2006a; Abel et al., 2007). By considering these multiplicative processes, we now estimate

$$\begin{aligned} \frac{n_{\gamma,\text{HI}}}{\bar{n}_b} &= \frac{n_{\gamma,\text{LW}}}{\bar{n}_b} \left(\frac{1+z}{20}\right)^{-3} \phi_{\text{HI}} f_{\text{esc}} f_{\text{abs}}^{-1} \\ &= 0.64 J_{21} \left(\frac{1+z}{20}\right)^{-3} \left(\frac{\phi_{\text{HI}}}{10}\right) \left(\frac{f_{\text{esc}}}{1}\right) \\ &\quad \times \left(\frac{f_{\text{abs}}}{0.1}\right)^{-1} \end{aligned} \quad (5.3)$$

This estimate is in agreement with the reionization models of Haiman et al. (2000) and WA05 (see also Gnedin & Ostriker, 1997). These models find that sources produce a large UVB of $J_{21} \sim 1$ prior to reionization. When Pop III stars dominate the UVB, the LW radiation will be small in comparison to the volume averaged hydrogen

ionizing emissivity because of the intrinsically hard Pop III spectra that peaks at $\sim 300\text{\AA}$. Hence high-redshift halos should not be exposed to a large UVB, i.e. $J_{21} \gtrsim 0.1$, and H₂ formation will remain important before reionization.

Nearby star formation can boost the LW radiation over its background value, but these bursts are short-lived as Pop III lifetimes are only ~ 3 Myr (Schaerer, 2002). For example, a $100 M_{\odot}$ star produces 10^{50} LW photons s^{-1} and will produce $J_{\text{LW}} > 0.1$ in the surrounding 3 proper kpc, neglecting any H₂ self-shielding.²

The LW background is uniform outside these spheres of influence. The bursting nature of Pop III star formation does not affect the time evolution of the background. The intensity only depends on the number of sources in a redshift range $\Delta z/z = 13.6 \text{ eV} / 11.18 \text{ eV} - 1$, where the two energies bound the LW band, because any radiation redward of the Lyman break contributes to the LW background. Using a conservative minimum halo mass for Pop III star forming halos of $3 \times 10^6 M_{\odot}$ at redshift 20, there are ~ 42000 halos that have hosted a Pop III star in the volume contained within Δz , using WMAP3 parameters with Sheth-Tormen formalism. Clearly the background is uniform considering the sheer number of sources within this optically thin volume. Local perturbations from Pop III star formation should only affect the timing of nearby star formation but not the global star formation rate.

5.4.2 H₂ Cooling within a UVB

YAHS03 used cosmological SPH simulations and H₂ formation and dissociation timescales to argue that a LW background intensity of $J_{\text{LW}} > 0.1$ suppresses H₂ formation so halos cannot cool before virial temperatures of 7000 K are reached. Employing the same argument, we see that the H₂ formation timescale

$$t_{\text{H}_2} = \frac{n_{\text{H}_2}}{k_{\text{H}^-} n_{\text{H}} n_{\text{e}}} = \frac{f_{\text{H}_2}}{0.92 k_{\text{H}^-} f_{\text{e}} n} \approx 30 \text{ kyr}, \quad (5.4)$$

with typical central values found in high-redshift halos before any radiative cooling becomes efficient (see Wise & Abel, 2007). Here $f_{\text{H}_2} = 10^{-6}$ and $f_{\text{e}} = 10^{-4}$ are the

²LW self-shielding may be unimportant up to column densities of $10^{20} - 10^{21} \text{ cm}^{-2}$ if the medium contains very large velocity gradients and anisotropies (Glover & Brand, 2001).

H_2 and electron number fraction, respectively, and $n = 10 \text{ cm}^{-3}$ is the baryon number density. $k_{H^-} \approx 10^{-15} \text{ cm}^3 \text{ s}^{-1}$ is the H^- formation rate coefficient by electron photo-attachment at $T = 1000 \text{ K}$ (Abel et al., 1997). This timescale is a factor of 1000 smaller than the value calculated in YAHS03 because we use the quantities from the halo center as compared to the mean values. The H_2 dissociation timescale is $k_{diss}^{-1} = 23/J_{21} \text{ kyr}$, which is comparable with t_{H_2} using the values above.

Figure 5.5 shows SimB-LW20 twenty million years before the central core condenses. At this time, the core is just beginning to cool by H_2 , catalyzed by the free electrons created in the central shocks. In these shocks, temperatures reach $1.4 \times 10^4 \text{ K}$ and electron fractions up to 10^{-3} exist there. These conditions result in H_2 formation timescales less than 25 kyr, which is necessary to cool in a UVB of $J_{21} \sim 1$. Within the central 10 pc, hot and cold gas phases exist. The hot phase exists behind the shocks that have lower densities around 10 cm^{-3} and $t_{H_2} < 25 \text{ kyr}$. This is where H_2 cooling is catalyzed by collisional ionization in these shocks. The cold phase has already cooled through H_2 and has high densities and larger t_{H_2} values. Both phases are apparent in the panels of Figure 5.5. Similar conditions create H_2 in the collapses in the “noe-” calculations, which have sufficient gravitational potential energy, resulting in temperatures above 10^4 in central shocks.

Hence H_2 formation is possible in the centers of high-redshift halos with virial temperatures below 10^4 K , even with a UVB of intensity $J_{LW} \sim 1$, larger than expected from semi-analytic models of reionization.

5.4.3 Impact on Semi-analytic Models

Two consequences of a lower critical $\text{Ly}\alpha$ cooling halo mass are more frequent and earlier galaxy formation and higher mass fractions in cooling halos. At redshift 20, e.g., abundances of $T_{\text{vir}} = 4000 \text{ K}$ halos are an order of magnitude larger than $T_{\text{vir}} = 10^4 \text{ K}$ halos, resulting from the exponential nature of Press-Schechter formalism. The mass fraction contained in these halos is three times higher than 10^4 K halos. In semi-analytic models of reionization and chemical enrichment, the star formation rate (SFR) is linearly dependent on the collapsed mass fraction since the SFR is usually

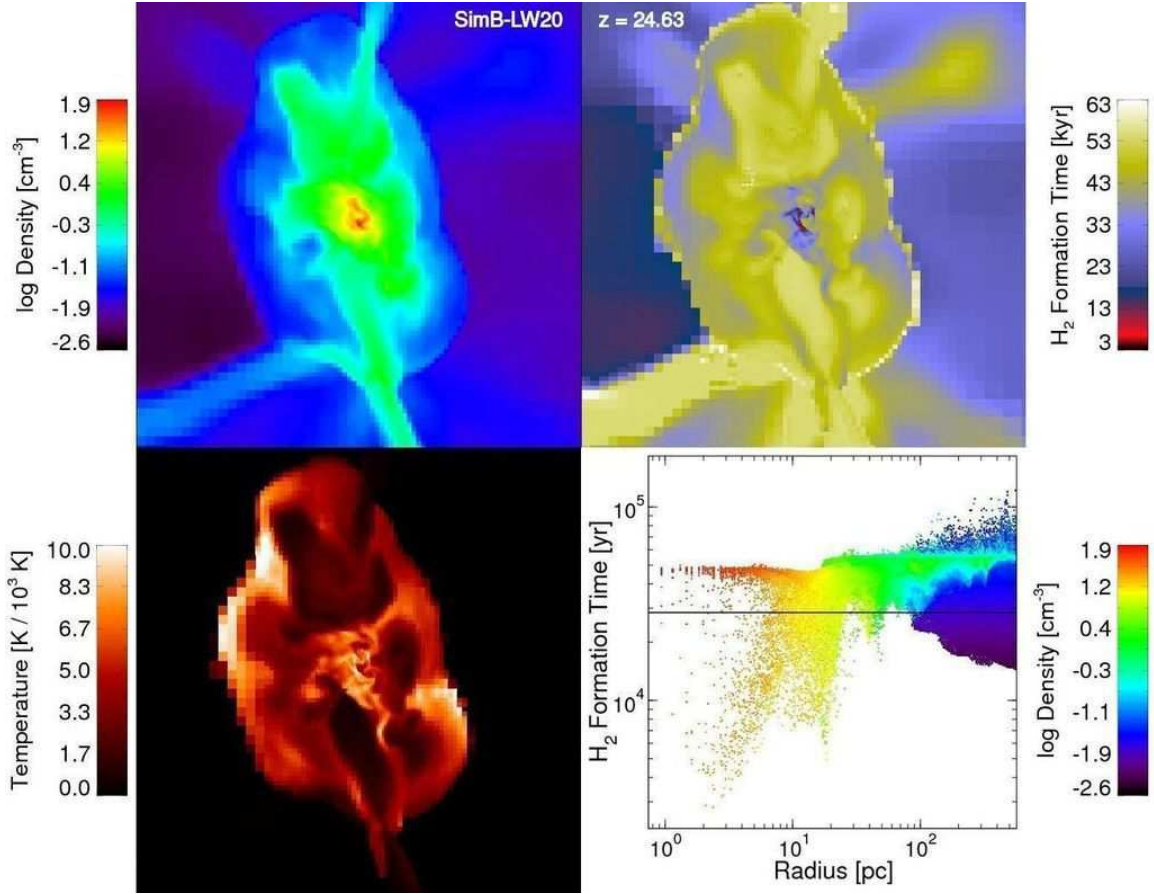


Fig. 5.5.— The most massive halo in SimB-LW20 ($F_{\text{LW}} = 10^{-20}$) twenty million years before the cooling core collapses. Slices of gas density (*left*) and the H_2 formation timescale (Eq. [5.4]; *right*) through the densest point in the halo are in the *top* row. The *bottom* row contains a slice of temperature (*left*) and a radial profile of the H_2 formation timescale, colored by gas density. The phase diagram and density slice have the same color scale. The slices have a field of view of 500 proper pc. In the central shocks, H_2 formation timescales are lower than the dissociation timescale of 28 kyr with $F_{\text{LW}} = 10^{-20}$ that is denoted by the horizontal line in the radial profile. The central core is now efficiently cooling and will collapse 20 Myr after these data.

a product of mass fraction and star formation efficiency, which is the fraction of gas collapsing into stars (e.g. Haiman & Loeb, 1997). The star formation efficiency for primordial stars is $\sim 10^{-3}$ with a single massive star forming in dark matter halos with mass $\sim 10^6 M_\odot$ (Abel et al., 2002; Bromm et al., 2002; Yoshida et al., 2006b). This fraction may rise to a few percent in dwarf galaxies as widespread star formation occurs (Taylor et al., 1999; Gnedin, 2000; Walter et al., 2001). Various studies predict that a majority of the reionizing flux originates from dwarf galaxies (e.g. Cen, 2003a; Sokasian et al., 2004; Haiman & Bryan, 2006). If the mass contained in star forming halos is three times greater than previously thought, some of the predicted attributes, e.g. photon escape fractions and star formation efficiencies, of high-redshift dwarf galaxy will require appropriate adjustments to match observations, such as the WMAP3 measurement of optical depth to electron scattering (Page et al., 2006) and Gunn-Peterson troughs at $z \sim 6$ (Becker et al., 2001; Fan et al., 2002).

5.5 Summary

We conducted a suite of fourteen cosmology AMR simulations that focus on the importance of H_2 cooling with various degrees of negative feedback. We summarize the findings of each model below.

1. The calculations with a UVB of $F_{\text{LW}} = (0, 10^{-22}, 10^{-21})$ agree with the results of MBA01, where the critical collapse halo mass increases as a function of UVB intensity.
2. Above $F_{\text{LW}} = 10^{-21}$, it had been argued that an H_2 dissociating background would inhibit any H_2 formation until the halo could cool through $\text{Ly}\alpha$ cooling. We showed that central shocks provide sufficient free electrons from collisional ionization to drive H_2 formation faster than dissociation rates even in a $F_{\text{LW}} = 10^{-20}$ background.
3. In our “noe-” models, we explored when collisional ionization becomes important and conducive for H_2 formation. This occurs at $T_{\text{vir}} \sim 4000$ K. Recent major mergers above this mass scale create complex cooling structures, unlike the non-fragmented central cores in smaller halos.

4. Even our most extreme assumptions of $J_{21} = 1$ ($F_{\text{LW}} \simeq 10^{-20}$) and no residual free electrons cannot defeat the importance of H_2 cooling in the early universe.

In any case, H_2 cooling triggers collapses in halos with virial temperatures well below 10^4 K. The lower critical halo mass, corresponding to $T_{\text{vir}} \sim 4000$ K, increases mass fraction contained in these halos by three times at redshift 20 and the number density of high-redshift star forming halos by an order of magnitude! By considering additional cases of extremely large negative feedback, we have strengthened the results of MBA01 that H_2 cooling plays a key role in high-redshift structure formation. We conclude that a UVB only delays and never completely suppresses H_2 formation and cooling and subsequent star formation in these low-mass halos.

Chapter 6

The Nature of Early Dwarf Galaxies

All observed galactic and extragalactic stars and intergalactic Lyman forest clouds have some fraction of gas enriched by elements heavier than helium. This applies to even the oldest stars, whose ages are comparable to the age of the universe, in our galaxy and surrounding dwarf galaxies. Big Bang nucleosynthesis produces hydrogen and helium with trace amounts of deuterium and lithium (Alpher, Bethe, & Gamow, 1948; Wagoner et al., 1967). The first stars formed from this pristine gas, but this prompts the question: *How did the first generation of stars enrich the universe with the first metals?*

After quantifying the relevance of the hydrodynamics, hierarchical assembly, and cooling physics in the previous chapters, we can finally include the main focus of this thesis: the impact of primordial stellar feedback on early galaxy formation. These models probe the same questions that were addressed in Chapter 2 but with a self-consistent treatment of primordial star formation in adaptive mesh refinement simulations. We have developed an accurate radiation transport model that utilizes adaptive ray tracing (Abel & Wandelt, 2002) and has been parallelized and optimized for shared and distributed computing systems. This allows us to follow the radiative feedback from the first stars and to investigate its impact on the formation of the first galaxies. We also follow the propagation of metal ejecta from the supernovae of

massive, metal-free stars. We investigate the global nature of the early dwarf galaxies that ultimately form in our calculations. These results may result in a better understanding of the origin of the oldest stars in our galaxy and some of the neighboring dwarf galaxies.

This is the final iteration of the gradual inclusion of physical models in this thesis; however we note that many other processes may be relevant in early galaxy formation, e.g. metal-line and dust cooling, self-shielding of H_2 dissociating radiation, and magnetic fields.

This chapter is in preparation for publication in *The Astrophysical Journal*. It is co-authored by Tom Abel, who developed the original version of the adaptive ray tracing code used in these simulations.

6.1 Motivation

The majority of galaxies in the universe are low-luminosity, have masses of $\sim 10^8$ solar masses, and are known as dwarf galaxies (Schechter, 1976; Ellis, 1997; Mateo, 1998). Galaxies form hierarchically through numerous mergers of smaller counterparts (Peebles & Dicke, 1968; White & Rees, 1978), whose properties will inevitably influence the parent galaxy. Dwarf galaxies are the smallest galactic building blocks, and this leads to the question on even smaller scales: how were dwarf galaxies influenced by their progenitors? To answer this intriguing question, we let observations of local dwarf galaxies and numerical simulations guide us.

A subset of dwarf galaxies, dwarf spheroidals (dSph), have the highest mass-to-light ratios (de Blok & McGaugh, 1997; Mateo, 1998) and contain a population of metal-poor stars that are similar to Galactic halo stars (Tolstoy et al., 2004; Helmi et al., 2006). Stellar metallicities increase with time as previous stars continually enrich the interstellar medium (ISM). There is a metallicity floor of 10^{-3} and 10^{-4} of solar metallicity in dSph and halo stars, respectively (Beers & Christlieb, 2005; Helmi et al., 2006). Hence the lowest metallicity stars are some of the oldest stars in the system and can shed light on the initial formation of dwarf galaxies. This metallicity floor also suggests that metal enrichment was widespread in dark matter halos before

low-mass stars could have formed (e.g. Ricotti et al., 2002b). Supernovae (SNe) from metal-free (Pop III) stars generate the first metals in the universe and may supply the necessary metallicity to form the most metal-poor stars observed (Ferrara, 1998; Madau et al., 2001; Norman et al., 2004).

Dwarf galaxy formation can be further constrained with observations that probe reionization and semi-analytic models. Observations of luminous quasars powered by supermassive black holes (SMBH) of mass $\sim 10^9 M_\odot$ (Becker et al., 2001; Fan et al., 2002, 2006) and low-luminosity galaxies (Hu & Dodelson, 2002; Iye et al., 2006; Kashikawa et al., 2006; Bouwens & Illingworth, 2006; Stark et al., 2007) at and above redshift 6 indicate that active star and BH formation began long before this epoch. Semi-analytic models have shown that cosmological reionization was largely caused by low-luminosity dwarf galaxies (Haiman et al., 1997; Cen, 2003a; Somerville & Livio, 2003; Wise & Abel, 2005; Haiman & Bryan, 2006). Some of the most relevant parameters in these models control star formation rates, ionizing photon escape fractions, metal enrichment, and the minimum mass of a star forming halo. They are usually constrained using (i) the cosmic microwave background (CMB) polarization observation from WMAP that measures the optical depth of electron scattering to the CMB (Page et al., 2006), (ii) Gunn-Peterson troughs in $z \sim 6$ quasars, and (iii) numerical simulations that examine negative and positive feedback of radiation backgrounds (Machacek et al., 2001; Yoshida et al., 2003; Mesinger et al., 2006). Radiation hydrodynamical *ab initio* simulations of the first stars (Yoshida et al., 2006a; Abel et al., 2007) and galaxies can further constrain the parameters used in semi-analytic models by analyzing the impact of stellar feedback on star formation rates and the propagation of H II regions in the early universe. Moreover, these simulations contain a wealth of information pertaining to the properties of Pop III star forming halos and early dwarf galaxies that can increase our understanding of the first stages of galaxy formation.

First we need to consider Pop III stars, which form in the progenitor halos of the first galaxies, to fully understand the initial properties of dwarf galaxies. Cosmological numerical studies have shown that massive Pop III stars form in dark matter halos with masses $\sim 10^6 M_\odot$. Recently, Yoshida et al. (2006b) followed the gaseous collapse of

a molecular cloud that will host a Pop III star to cosmologically high number densities of 10^{16} cm^{-3} . They thoroughly analyzed the gas dynamics, cooling, and stability of this free-fall collapse. They found no fragmentation in the fully molecular core that collapses into a single, massive $\sim 100 M_{\odot}$ star (see also Abel et al., 2002). Furthermore, Omukai & Palla (2003) determined that accretion will halt at the same mass scale, using protostellar models while considering different mass accretion histories.

Pop III stars with stellar masses roughly between 140 and 260 M_{\odot} end their life in a pair-instability SN that releases $10^{51} - 10^{53}$ ergs of energy and tens of solar masses of heavy elements into the ambient medium (Barkat et al., 1967; Bond et al., 1984; Heger & Woosley, 2002). These explosions are an order of magnitude larger than typical Type II SNe in both quantities (Woosley & Weaver, 1986). Pair-instability SN energies are larger than the binding energies of their low-mass hosts, e.g., 2.8×10^{50} ergs for a $10^6 M_{\odot}$ halo at redshift 20. Gas structures in the host halo are totally disrupted and expelled, effectively enriching the surrounding intergalactic medium (IGM) with the SN ejecta (Bromm & Loeb, 2003; Kitayama & Yoshida, 2005). The combination of the shallow potential well and large explosion energy suggests that these events are good candidates for enriching the first galaxies and IGM. Outside of the pair-instability mass range, Pop III stars die by directly collapsing into a BH (Heger et al., 2003), possibly providing the seeds of high-redshift quasars in galaxies that are associated with the rarest density fluctuations (e.g. Madau & Rees, 2001; Volonteri et al., 2005).

One-dimensional calculations (Whalen et al., 2004; Kitayama et al., 2004; Kitayama & Yoshida, 2005) and recent three-dimensional radiation hydrodynamical simulations (Yoshida et al., 2006a; Abel et al., 2007) have investigated how the Pop III stellar feedback affects its host halo and nearby cosmic structure. In addition to SNe, stellar radiation from Pop III stars, which have luminosities $\sim 10^6 L_{\odot}$ (Schaerer, 2002), alone can dynamically affect gas at distances up to a few proper kpc, for which ionization fronts are mainly responsible. Ionization fronts and H II regions (see Yorke, 1986, for a review) have been extensively studied in literature on star formation since Strömberg (1939). Stellar radiation generates an ionization front that begins as a R-type front and transforms into a D-type front when its speed slows to twice the

sound speed of the ionized gas. Then a strong shock wave forms at the front and recedes from the star at $\sim 30 \text{ km s}^{-1}$. The ionization front decouples from the shock wave and creates a final H II region that is 1 – 3 proper kpc in radius for massive Pop III stars residing in low-mass halos. The ionized gas is warm ($\sim 3 \times 10^4 \text{ K}$) and diffuse ($\sim 1 \text{ cm}^{-3}$). The shock wave continues to accumulate gas and advance after the star dies. Eventually it stalls in the IGM, but in the process, it reduces the baryon fraction of the halo below one percent (Yoshida et al., 2006a; Abel et al., 2007).

Clearly the number of progenitors of a given galaxy as well as the star formation and feedback history of the progenitors will play a role in shaping all of its properties. But how much? If most stars of a galaxy are formed later, will the earliest episodes not be entirely negligible? To start addressing these questions, we have carried out a suite of simulations that include accurate three dimensional radiative transfer and the SN explosions of Pop III stars and have followed the buildup of several dwarf galaxies from those Pop III star hosting progenitors. The Pop III radiative and SN feedback dramatically alters the properties of high redshift dwarf galaxies, and we discuss some of the most striking differences here. We leave a more detailed exposition of star formation rates, star forming environments, and the beginning of cosmic reionization for a later paper.

In the following section, we detail our cosmological, radiation hydrodynamics simulations and the star formation algorithm. Then we describe the global characteristics of dwarf galaxies that form in our simulations in §6.3. There we also focus on metal enrichment of star forming halos and the IGM, arising from pair-instability SNe. In §6.4, we discuss the implications of our findings on the paradigm of high-redshift galaxy formation by including H_2 chemistry and Pop III star formation and feedback. We summarize in the last section.

6.2 Radiation Hydrodynamical Simulations

We use the Eulerian AMR hydrodynamic code *Enzo* (Bryan & Norman, 1997, 1999) to study the importance of primordial stellar feedback in early galaxy formation. *Enzo* uses an n -body adaptive particle-mesh solver (Couchman, 1991) to follow the

dark matter (DM) dynamics. We first describe the setup of our simulations. We then detail our star formation recipe for primordial star formation. Also we have implemented adaptive ray tracing into *Enzo* that concludes this section.

6.2.1 Simulation Setup

We perform two cosmological realizations with different box sizes and random phases and WMAP 1 year parameters of $(h, \Omega_\Lambda, \Omega_M, \Omega_b, \sigma_8, n) = (0.72, 0.73, 0.27, 0.024h^{-2}, 0.9, 1)$ (Spergel et al., 2003). Table 6.1 summarizes the details of these simulations. The characteristics of the individual halos studied here are not affected by the significantly different WMAP third year parameters (WMAP3; Spergel et al., 2006), which do affect the statistical properties of such halos. We have verified that nothing atypical occurs during the assembly of the halos studied here.

Table 6.1: Simulation Parameters

Name	l [Mpc]	SF	SNe	N_{part}	N_{grid}	N_{cell}
SimA-HHe	1.0	No	No	2.22×10^7	40601	1.20×10^8 (494 ³)
SimA-RT	1.0	Yes	No	2.22×10^7	44664	1.19×10^8 (493 ³)
SimB-HHe	1.5	No	No	1.26×10^7	21409	6.51×10^7 (402 ³)
SimB-RT	1.5	Yes	No	1.26×10^7	24013	6.54×10^7 (403 ³)
SimB-SNe	1.5	Yes	Yes	1.26×10^7	24996	6.39×10^7 (400 ³)

Note. — Col. (1): Simulation name. Col. (2): Box size. Col. (3): Star formation. Col. (4): Supernova feedback. Col. (5): Number of dark matter particles. Col. (6): Number of AMR grids. Col. (7): Number of unique grid cells.

The initial conditions are the same as in Wise & Abel (2007a). They both have a top grid with a resolution of 128^3 with three nested subgrids with twice finer resolution and are initialized at $z = 129$ (119) with the COSMICS package¹ (Bertschinger, 1995,

¹To simplify the discussion, simulation A will always be quoted first with the value from simulation B in parentheses.

2001). The box size is 1.0 (1.5) comoving Mpc. The innermost grid has an effective resolution of 1024^3 with DM particle masses of 30 (101) M_\odot and a side length of 250 (300) comoving kpc. We refine the AMR grids when either the DM (gas) exceeds three times the mean DM (gas) density times a factor of 2^l , where l is the AMR refinement level. We also refine so that the local Jeans length is resolved by at least 16 cells. Refinement only occurs in the initial innermost grid that has a comoving side length of 250 (300) kpc. We enforce a maximum AMR level of 12 in these simulations that corresponds to a resolution limit of 2.9 (1.9) comoving parsecs.

We use the nine species (H, H⁺, He, He⁺, He⁺⁺, e⁻, H₂, H₂⁺, H⁻) non-equilibrium chemistry model in *Enzo* (Abel et al., 1997; Anninos et al., 1997). Compton cooling and heating of free electrons by the CMB and radiative losses from atomic and molecular cooling are computed in the optically thin limit.

We focus on the region containing the most massive halo in the simulation box. We perform three calculations – simulation A with star formation (SimA-RT), simulation B with star formation (SimB-RT), and simulation B with star formation and SNe (SimB-SN). We end the calculations at the same redshift the halo with a virial temperature of 10^4 K collapses at $z = 15.9$ (16.8) in the hydrogen and helium cooling runs (HHe) of Wise & Abel (2007a).

6.2.2 Star Formation Recipe

Star formation is modelled through an extension (Abel et al., 2007) of the Cen & Ostriker (1992) algorithm that automatically forms a star particle when a grid cell has

1. an overdensity exceeding 5×10^5
2. a converging velocity field ($\nabla \cdot \mathbf{v} < 0$)
3. rapidly cooling gas ($t_{\text{cool}} < t_{\text{dyn}}$)
4. an H₂ fraction greater than 5×10^{-4} .

Then we remove half of the gas from the grid cells in a sphere that contains twice the stellar mass, which is a free parameter. Once these criteria are met, Abel et al.

(2002) showed that a Pop III star forms within 10 Myr. For this reason, we do not impose the Jeans instability requirement used in Cen & Ostriker and do not follow the collapses to stellar scales. We allow star formation to occur in the Lagrangian volume of the surrounding region out to three virial radii from the most massive halo at $z = 10$ in the dark matter only runs as discussed in Wise & Abel (2007a). This volume has a side length of 195 (225) comoving kpc at $z = 30$ and 145 (160) comoving kpc at the end of the calculation.

Runs with star formation only model all Pop III stars with $M_\star = 100 M_\odot$ that live for 2.7 Myr and emit 1.23×10^{50} hydrogen ionizing photons per second. After its death, the star particle is converted into an inert $100 M_\odot$ tracer particle. The SNe runs use $M_\star = 170 M_\odot$ that results in a lifetime of 2.3 Myr and 2.57×10^{50} ionizing photons per second, in accordance with the no mass loss stellar models of Schaerer (2002).

When a $170 M_\odot$ star dies, it injects $E_{\text{SN}} = 2.7 \times 10^{52}$ erg of thermal energy and $81 M_\odot$ of metals, appropriate for a pair-instability SN of a $170 M_\odot$ star (Heger & Woosley, 2002), into a sphere with radius $r_{\text{SN}} = 1$ pc centered on the star's position. The mass contained in the star particle and associated metal ejecta are evenly distributed in this sphere. The mass of the star particle is changed to zero, and we track its position in order to determine the number of stars associated with each halo. We also evenly deposit the SN energy in the sphere, which changes the specific energy by

$$\Delta\epsilon = \frac{\rho_0\epsilon_0 + \rho_{\text{SN}}\epsilon_{\text{SN}}}{\rho_0 + \rho_{\text{SN}}} - \epsilon_0, \quad (6.1)$$

where ρ_0 and ϵ_0 are the original gas density and specific energy, respectively. Here $\rho_{\text{SN}} = M_\star/V_{\text{SN}}$ is the ejecta density; $\epsilon_{\text{SN}} = E_{\text{SN}}/M_\star/V_{\text{SN}}$ is the ejecta specific energy; V_{SN} is the volume of a sphere with radius r_{SN} . In order not to create unrealistically strong shocks at the blast wave and for numerical stability reasons, we smoothly transition from this energy bubble to the ambient medium, using the function

$$f(r) = A \left\{ 0.5 - 0.5 \tanh \left[B \left(\frac{r}{r_{\text{SN}}} - 1 \right) \right] \right\}. \quad (6.2)$$

Here A is a normalization factor that ensures $\int f(r)dr = 1$, and B controls the rate of transition to the ambient medium, where the transition is steeper with increasing B . We use $A = 1.28$ and $B = 10$ in our calculations.

We continue to use the nine-species chemistry model as we do not consider the additional cooling from metal lines. We follow the hydrodynamic transport of metals from the SNe to the enrichment of the surrounding IGM and halos.

6.2.3 Radiative Transfer

For point sources of radiation, ray tracing is an accurate method to calculate and evolve radiation fields. However millions of rays must be cast in order to obtain adequate ray sampling at large radii. We use adaptive ray tracing (Abel & Wandelt, 2002) to overcome this dilemma associated with ray tracing (cf. Abel et al., 2007). We initially cast 768 rays, i.e. level three in HEALPix (Górski et al., 2005), from the radiation source. The photons contained in the initial rays are equal, and their sum is the stellar luminosity. Rays are split into 4 child rays, whose angles are calculated with the next HEALPix level, if their associated solid angle is greater than 20% of the cell area Δx^2 . Photons are distributed evenly among the children. This occurs if the ray travels to a large distance from its source, or the ray encounters a highly refined AMR grid, in which adaptive ray tracing accurately samples and retains the fine structure contained in high resolution regions.

The rays cast in these simulations have an energy E_{ph} that is the mean energy of hydrogen ionizing photons from the stellar source. For $100 M_{\odot}$ and $170 M_{\odot}$, this energy is roughly equal at 28.4 and 29.2 eV, respectively, due to the weak dependence of the surface temperature of primordial stars on stellar mass. The rays are transported at the speed of light on constant timesteps $\Delta t_{\text{ph}} = 800$ years, which is always less than the hydrodynamical timesteps at the finest resolution.

To model the H_2 dissociating (Lyman-Werner; LW) radiation between 11.2 and 13.6 eV, we use an optically thin $1/r^2$ radiation field with luminosities calculated from Schaerer (2002). We use the H_2 photo-dissociation rate coefficient for the Solomon process of $k_{\text{diss}} = 1.1 \times 10^8 F_{\text{LW}} \text{ s}^{-1}$, where F_{LW} is the LW flux in units of $\text{erg s}^{-1} \text{ cm}^{-2}$

Hz^{-1} (Abel et al., 1997).

The radiation transport is coupled with the hydrodynamical, chemistry, and energy solvers of *Enzo*. Here we only consider hydrogen photo-ionization. We first calculate the photo-ionization and heating rates caused by each ray and then sub-cycle the chemistry and heating solvers with these additional rates. Next we advance the hydrodynamics of the system with the usual adaptive timesteps.

The hydrogen photo-ionization rate is computed by

$$k_{ph} = \frac{P_0(1 - e^{-\tau})}{n_{\text{HI}} V_{\text{cell}} \Delta t_{\text{ph}}}, \quad (6.3)$$

where P_0 is the incoming number of photons, n_{HI} is the number density of neutral hydrogen, V_{cell} is the volume of the computational grid cell, and $\tau = n_{\text{HI}} \sigma_{\text{HI}} dl$ is the optical depth. Here σ_{HI} is the cross section of hydrogen, and dl is the distance travelled by the ray through the cell. The heating rate is computed from the excess photon energies of the photo-ionizations by

$$\begin{aligned} \Gamma_i &= k_{ph}(E_{\text{ph}} - E_i) \\ &= \frac{P_0(1 - e^{-\tau})}{n_{\text{HI}} V_{\text{cell}} \Delta t_{\text{ph}}} (E_{\text{ph}} - E_i). \end{aligned} \quad (6.4)$$

In the case of hydrogen ionizing photons, $E_i = 13.6$ eV. In each radiation timestep, the number of photons absorbed, i.e. $P_0(1 - e^{-\tau})$, is subtracted from the ray. The ray is eliminated once most of the associated photons (e.g. 99%) are absorbed or the ray encounters a highly optically thick region (e.g. $\tau > 20$).

6.3 Results

In this section we first discuss star formation in dwarf galaxy progenitors. Then we focus on the global characteristics of the most massive halo. We detail the different ISM phases. Metal transport from pair-instability SNe and the associated metal-enriched star formation history are discussed lastly.

6.3.1 Number of Star Forming Halos

Gas in halos with masses $\lesssim 10^6 M_\odot$ is evacuated by a $\sim 30 \text{ km s}^{-1}$ D-type front, leaving a diffuse (1 cm^{-3}) and warm ($3 \times 10^4 \text{ K}$) medium (Whalen et al., 2004; Kitayama et al., 2004; Yoshida et al., 2006a; Abel et al., 2007). The aftermath of SN explosions in relic H II regions is explored in spherical symmetry in one-dimensional calculations by Kitayama & Yoshida (2005). Even without SNe, star formation is suppressed for $\sim 100 \text{ Myr}$ before gas is reincorporated into the potential well. Pair-instability SNe provide an extra $\sim 10^{52} \text{ erg}$ of thermal energy and can evacuate halos up to $10^7 M_\odot$. Hence star formation within these low-mass halos are highly dependent on their star formation and merger histories, as illustrated by Yoshida et al. (2006a).

Table 6.2: Global halo properties with star formation

Name	$N_\star(<r_{\text{vir}})$	$N_\star(<3r_{\text{vir}})$	$M_{\text{gas}}/M_{\text{tot}}$	λ_g
SimA-HHe	0.14	0.010
SimA-RT	14	16	0.081	0.053
SimB-HHe	0.14	0.010
SimB-RT	13	19	0.11	0.022
SimB-SN	7	13	0.049	0.097

Note. — Col. (1): Simulation name. Col. (2): Number of stars hosted in the halo and its progenitors. Col. (3): Number of stars formed in the Lagrangian volume within $3r_{\text{vir}}$ of the most massive halo. Col. (4): Baryon fraction within r_{vir} . Col. (5): Baryonic spin parameter [Eq. 6.5].

Table 6.2 summarizes the global properties of the most massive halo at the time of collapse in the HHe calculations. Approximately ten Pop III stars form in the progenitors, whose original gas structures are nearly destroyed by radiative feedback, of the 10^4 K halo. More specifically at $z = 15.9$ (16.8), there are 22, 27, and 24 stars that form after redshift 30 in the SimA-RT, SimB-RT, and SimB-SN runs, respectively. The most massive halo and its progenitors have hosted 14, 13, and 7

stars in the same simulations. When we look at the Lagrangian volume contained within three times the virial radius of the most massive halo, there have been 16, 19, and 13 instances of star formation.

6.3.2 Global Nature of Objects

In addition to providing the first ionizing photons and metals to the universe, Pop III stars change the global gas dynamics of $T_{\text{vir}} \sim 10^4$ K star forming halos. Figures 6.1 and 6.2 compare the structure of the most massive halo in all simulations, depicting density-squared weighted projections of gas density and temperature. All of the halos have a virial mass of $3.5 \times 10^7 M_{\odot}$. The models with neither star formation nor H_2 chemistry show a condensing $T_{\text{vir}} = 10^4$ K halo with its associated virial heating. In comparison, feedback from primordial star formation expels the majority of the gas in low-mass star forming progenitors. This induces the formation of an inhomogeneous medium, where the radiation anisotropically propagates, creating champagne flows in the directions with lower column densities. The temperature projections illustrate both the ultraviolet heated ($\sim 10^4$ K) and optically thick, cool ($\sim 10^3$ K) regions in the host halo and IGM. SN explosions alter the gas structure by further stirring and ejecting material after main sequence. Next we quantify these visual features with the baryon fraction of the halo and an inspection of phase diagrams of density and temperature.

As the gas in the progenitors is mostly evacuated, the baryon fraction of high-redshift star forming halos are greatly reduced. In halos with masses $\lesssim 10^6 M_{\odot}$, the baryon fraction lowers to 5×10^{-3} ten million years after the star's death without a SN (cf. Yoshida et al., 2006a). When we include SNe, the baryon fraction decreases further to 1×10^{-5} six million years after the explosion (cf. Kitayama & Yoshida, 2005). This is in stark contrast with the cosmic fraction $\Omega_b/\Omega_M = 0.17$.

Within these shallow potential wells, outflows from stellar feedback impede subsequent star formation until sufficient gas is reincorporated, occurring through mergers and smooth IGM accretion. After the halo mass surpasses $\sim 10^7 M_{\odot}$, total evacuation does not occur but significant outflows are still generated. Near the same mass

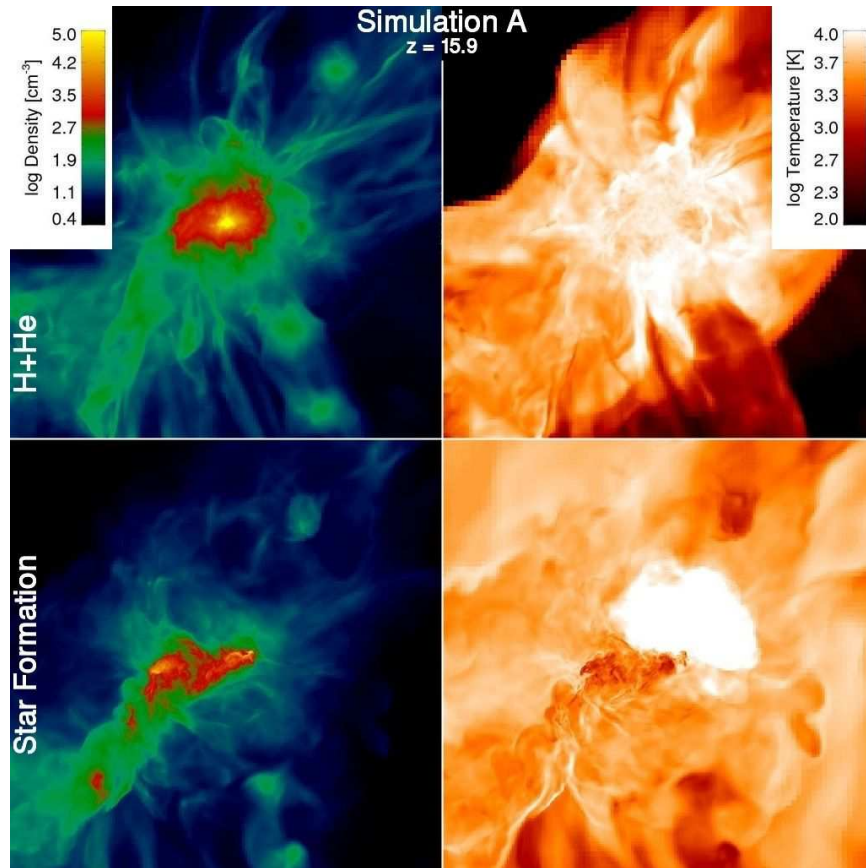


Fig. 6.1.— Density-squared weighted projections of gas density (*left*) and temperature (*right*) of the most massive halo in simulation A. The field of view is 1.2 proper kpc. The *top* row shows the model without star formation and only atomic hydrogen and helium cooling. The *bottom* row shows the same halo affected by primordial star formation.

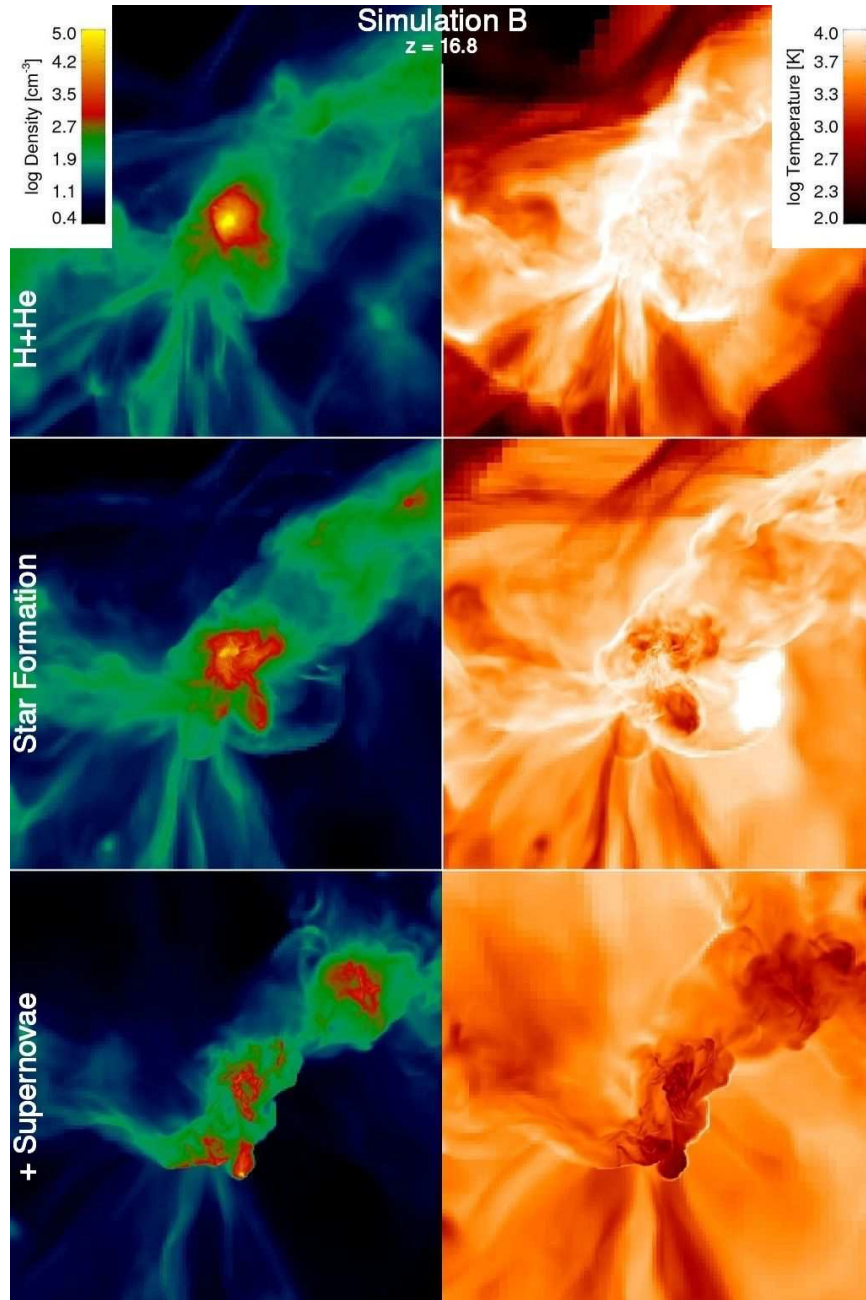


Fig. 6.2.— Same as Figure 6.1 for simulation B. Here the *bottom* row shows the halo with primordial stellar feedback and supernovae.

scale, multiple sites of star formation occur in the same halo. These stars rarely shine simultaneously since we neglect H_2 self-shielding, which only affects the timing of star formation and not the global star formation rate. Here after the first star dies, the second star, whose dense, cool core survived the UV heating, condenses and forms a star a few million years afterwards. This scenario of adjacent star formation is similar to the one presented in Abel et al. (2007), but the multiple sites of star formation are caused by H_2 and $\text{Ly}\alpha$ cooling in central protogalactic shocks (cf. Shapiro & Kang, 1987), not from residual cores from a recent major merger.

When the most massive halo reaches $T_{\text{vir}} \sim 10^4$ K, the baryon fraction within the virial radius has only partially recovered to 0.081, 0.11, and 0.049 in the SimA-RT, SimB-RT, and SimB-SN calculations. Without any stellar feedback, these fractions are 0.14 in the HHe runs.

These outflows also create inhomogeneities in and around halos and increase the baryonic spin parameter

$$\lambda_{\text{g}} = \frac{L_{\text{g}}|E_{\text{g}}|^{1/2}}{GM_{\text{g}}^{5/2}}, \quad (6.5)$$

where L_{g} , E_{g} , and M_{g} are the total baryonic angular momentum, kinetic energy, and mass of the system. The DM spin parameter λ uses the total DM angular momentum, kinetic energy, and mass of the system. At the time of collapse in the HHe runs, $\lambda = 0.022$ (0.013) and is marginally lower than the average $\langle\lambda\rangle \simeq 0.04$ found in numerical simulations (Barnes & Efstathiou, 1987; Eisenstein & Loeb, 1995). It is not affected by stellar feedback as DM dominates the potential well. Without star formation, the baryonic spin parameter $\lambda_{\text{g}} = 0.010$ (0.010) and is slightly lower than λ . However with stellar and SNe feedback, λ_{g} increases up to a factor of 10. The effect is smaller without SNe but still significant, raising λ_{g} to 0.053 (0.022).

The increase of λ_{g} may be caused by cosmological tidal forces on the expelled gas, which gains angular momentum when it is at large radii. At this point, tidal forces are at its greatest influence. Then a fraction of the expelled gas, now with a higher specific angular momentum, falls back to the dwarf galaxy and thus increasing its spin parameter.

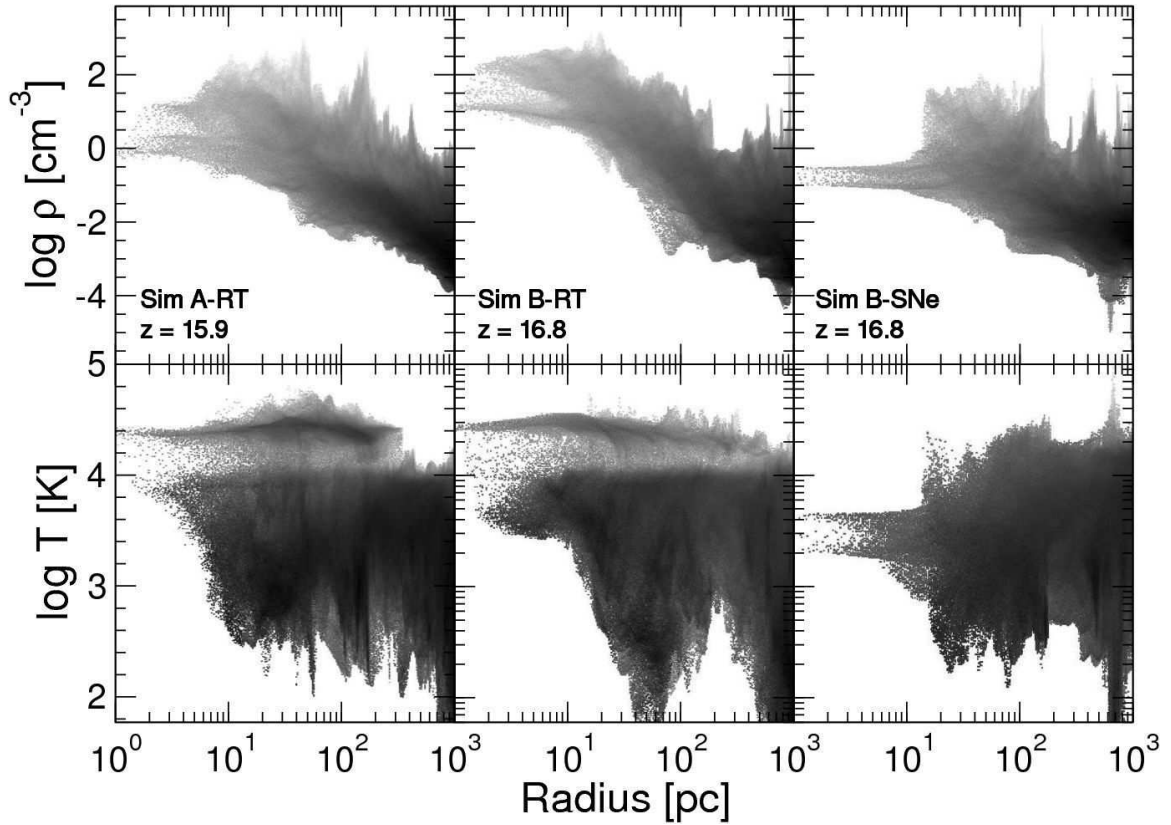


Fig. 6.3.— Mass-weighted radial profiles of density (*top*) and temperature (*bottom*), centered on the densest DM particle. The columns show data from SimA-RT (*left*), SimB-RT (*middle*), and SimB-SN (*right*). Note how the cool and warm gas phases coexist at similar radii throughout the halo.

6.3.3 ISM Phases

The combination of molecular cooling, stellar feedback, and SN explosions create a multi-phase ISM in star forming halos. These phases are interspersed throughout the halo. They are marginally seen in the temperature projections in Figures 6.1 and 6.2. However they are better demonstrated by the mass-weighted radial profiles in Figure 6.3 and density-temperature phase diagrams in Figure 6.4. The radial profiles are centered on the densest DM particle. For a given radius within the halo, the gas density can span up to 3 orders of magnitude, and the temperature ranges from ~ 100 K in the cool phase to 30,000 K in the warm, ionized phase. Below we describe the

different ISM phases at redshift 15.9 and 16.8 for simulation A and B, respectively.

Cool phase— The relatively dense ($\rho > 100 \text{ cm}^{-3}$) and cool ($T > 1000 \text{ K}$) gas has started to condense by H_2 cooling. Current star formation dissociates H_2 in nearby condensations through LW radiation in our simulations as we neglect self-shielding. In many cases, especially when $M_{\text{vir}} \gtrsim 10^7 M_{\odot}$, nearby clumps remain cool and optically thick. After the star dies, H_2 formation can proceed again to form a star in these clumps. There are two other sources of cool gas. First, the filaments are largely shielded from being photo-heated and provide the galaxy with cold accretion flows. Second, after SN explosions, the material within the expanding shell cools through adiabatic expansion and Compton cooling to temperatures as low as 100 K, which is seen in the ρ - T phase diagram at very low densities.

Warm, neutral phase— Gas that cools by atomic hydrogen line transitions, but not molecular, has $T \sim 8000 \text{ K}$ and densities ranging from 10^{-3} to 10^2 cm^{-3} . Gas in relic H II regions and virially shock-heated gas compose this phase.

Warm, ionized phase— In the RT simulations at the final redshift, a Pop III star is creating an H II region with temperatures up to 30,000 K. These regions are approximately 300 and 800 pc in radius with a non-spherical geometry because of the inhomogeneity of the ISM.

Hot, X-ray phase— The 3×10^{52} ergs of energy deposited by one pair-instability SN in the SimB-SN simulation heats the gas to over 10^8 K immediately after the explosion. Figure 6.5 shows the density and temperature of the ISM 30 kyr after a SN, where the adiabat of the hot phase is clearly visible at $T > 10^5 \text{ K}$. A blastwave initially travelling at 4000 km s^{-1} sweeps through the ambient medium during the free expansion phase. The gas behind the shock cools adiabatically and through Compton cooling as the SN shell expands.

6.3.4 Metallicity

Metallicities of second and later generations of stars depend on the locality of previous SNe. In the SimB-SN calculation, outflows carry most of the SN ejecta to radii up to ~ 1 proper kpc after 30 Myr. Interestingly they approximately fill the relic H II region

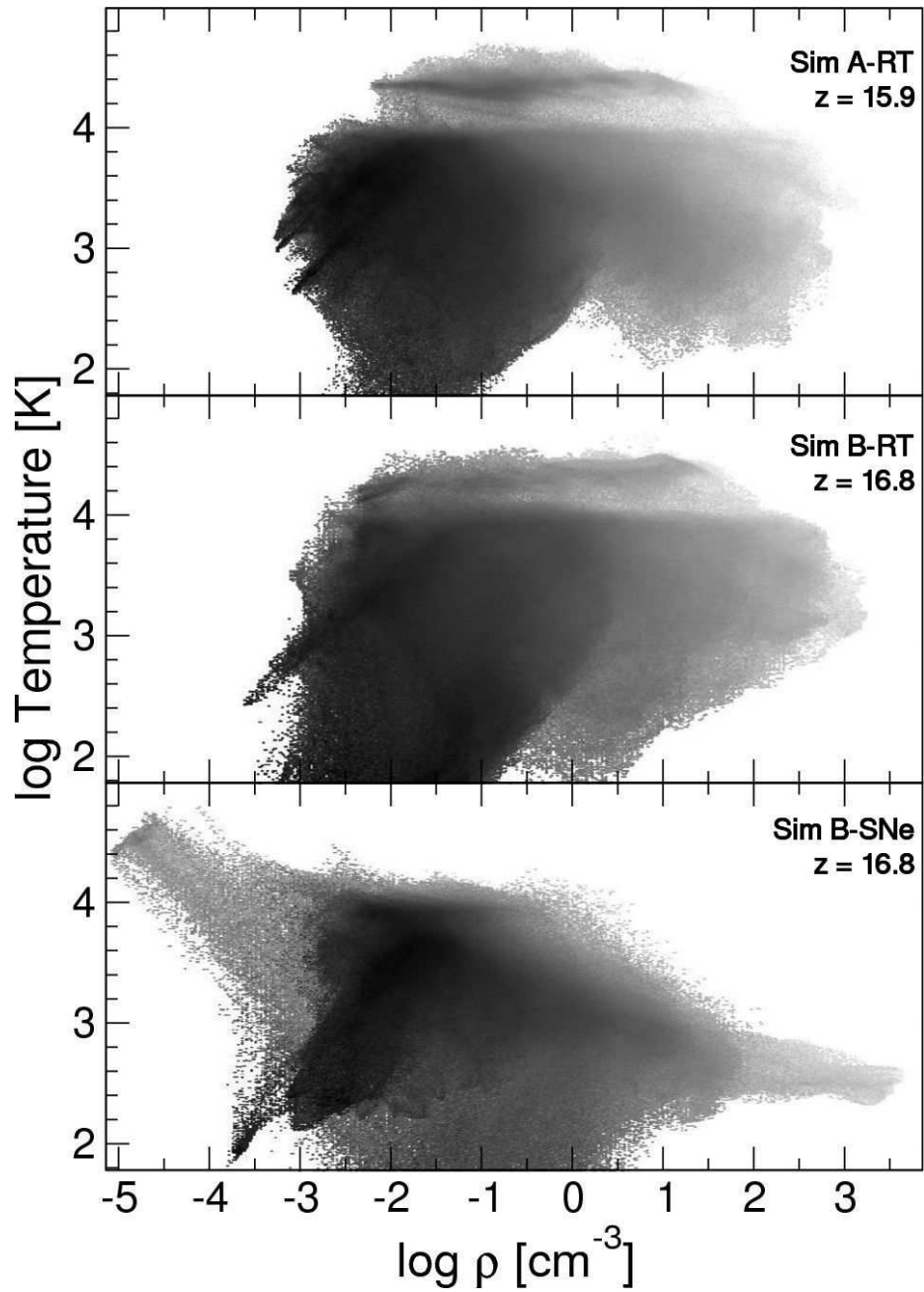


Fig. 6.4.— Mass-weighted ρ - T phase diagrams of a sphere with radius 1 kpc, centered on the most massive halo in SimA-RT (*top*), SimB-RT (*middle*), and SimB-SN (*bottom*). At $T > 10^4$ K, one can see the H II regions created by current star formation. The warm, low density ($\rho < 10^{-3} \text{ cm}^{-3}$) gas in SimB-SN are contained in SNe shells.

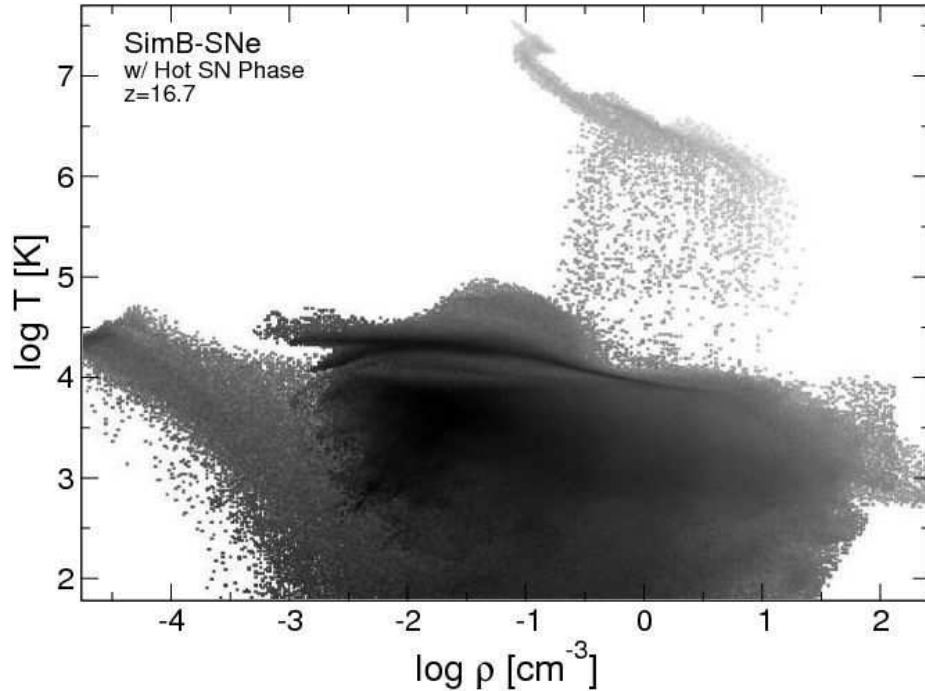


Fig. 6.5.— Mass-weighted ρ - T phase diagram of a sphere with radius 1 kpc, centered on the most massive halo in SimB-SN, 30 kyr after a pair-instability SN. In addition to the ISM phases seen in Figure 6.4, the SN ejecta is still hot and X-ray emitting at temperatures of 10^{6-7} K.

and expand little beyond that. The low density IGM marginally resists the outflows, and it is preferentially enriched instead of the surrounding filaments and halos.

It should be noted that this calculation is an upper limit of metallicities since all stars end with a SN. Nevertheless the mixing and transport of the first metals is a fundamental element of the transition to Pop II stars and is beneficial to study in detail. All quoted metallicities are in units of solar metallicity. The metallicities also scale linearly with metal yield of each SN because we treat the metal field as a tracer field that is advected with the fluid flow. We quote the metallicities according to this scaling.

When the most massive halo reaches a virial temperature of 10^4 K at $z = 16.8$, metals are thoroughly mixed in the halo, and its mean metallicity is $10^{-4.8}(M_{\text{yield}}/M_{\odot})$, where M_{yield} is the metal ejecta from one SN in units of solar masses. The metallicity

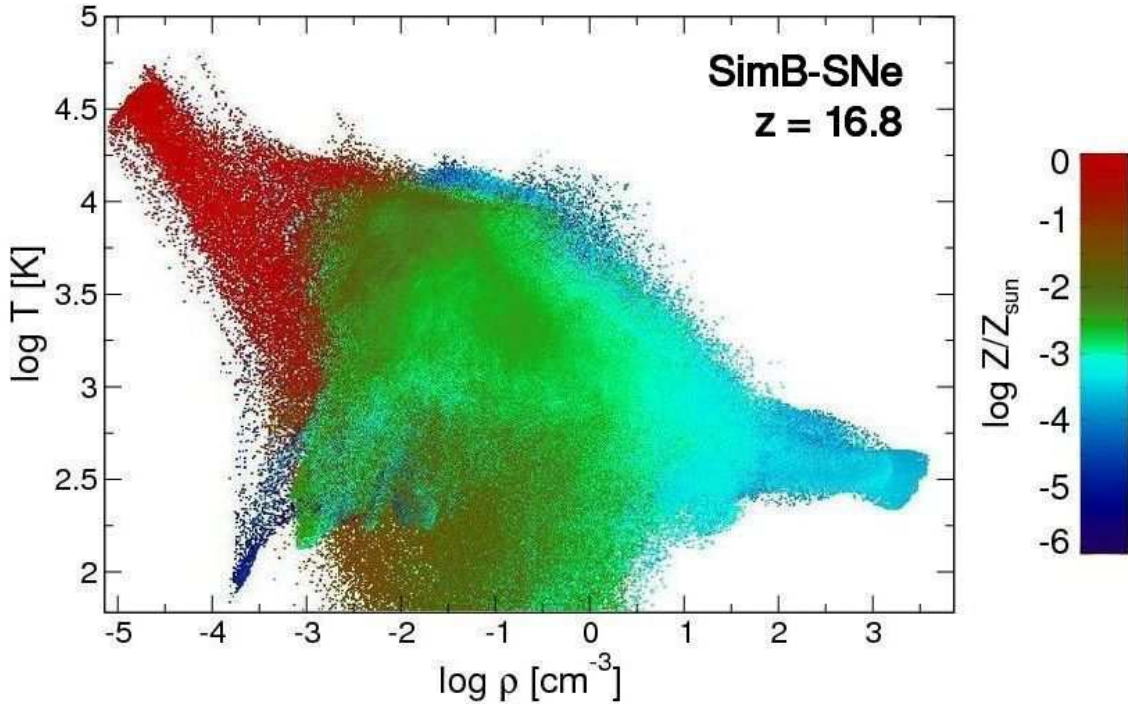


Fig. 6.6.— The same phase diagram of SimB-SNe in Figure 6.4 but colored by mean metallicity. The SN remnants that are warm and diffuse ($\rho < 10^{-3} \text{ cm}^{-3}$) have solar metallicities or greater. The majority of the ISM has metallicities $\sim 10^{-2.5}$ solar. The densest, collapsing material has a metallicity $\sim 10^{-3.5}$ solar.

of this halo fluctuates around this value because stars continue forming but ejecting most of their metals into the IGM. Also the filaments are still mostly pristine and provide a source of nearly metal-free cold gas. The volume averaged metallicity of the enriched IGM ($\delta < 10$) is $10^{-3.7}(M_{\text{yield}}/M_{\odot})$, compared to the filaments and halos ($\delta > 10$) that are less enriched with $10^{-4.5}(M_{\text{yield}}/M_{\odot})$. The metal volume filling fraction is 4.3% of the volume where we allow star formation to occur. This percentage should be higher than the cosmic mean because this comoving volume of $(205 \text{ kpc})^3$ is a biased with an overdensity $\delta \equiv \rho/\bar{\rho} = 1.8$. Thus star formation rates are greater than the mean since there are more high- σ peaks, and the metal filling fraction should scale with this bias.

Figure 6.6 shows the same ρ -T phase diagram as in Figure 6.4 but colored by the

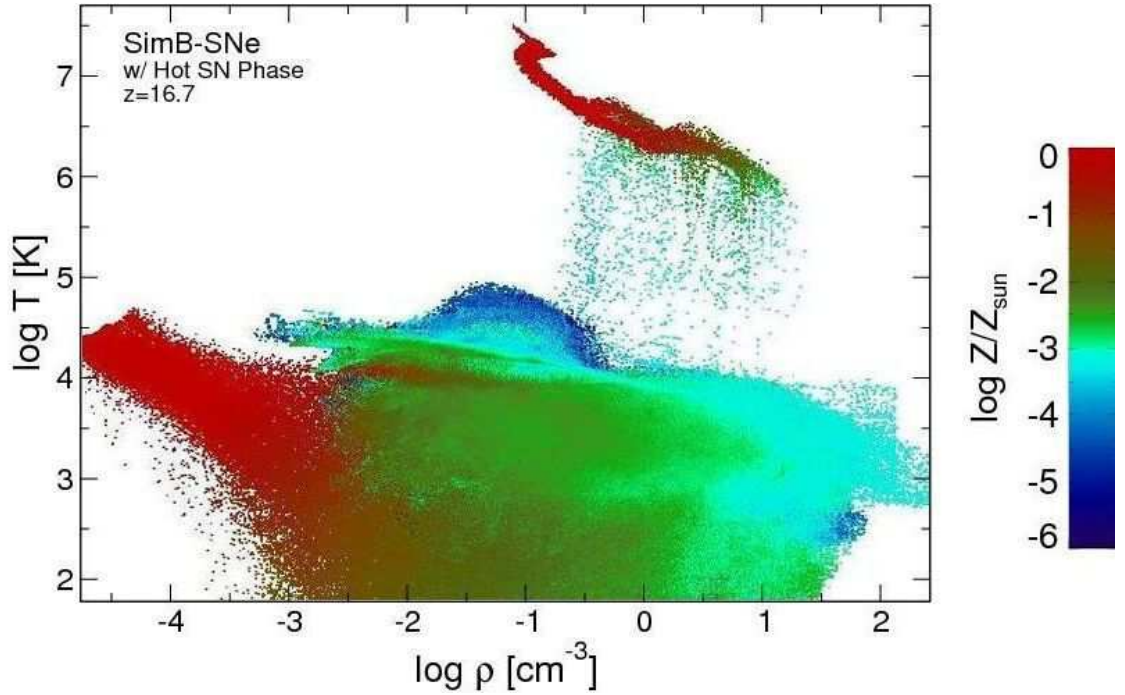


Fig. 6.7.— The same phase diagram of SimB-SNe in Figure 6.5 but colored by mean metallicity.

mean metallicity of the gas. These data are taken immediately before the formation of a star with a metallicity of $10^{-5.5}(M_{\text{yield}}/M_{\odot})$. There are three distinct metallicity states in the halo. The majority of the gas in the halo has a density between 10^{-3} and 1 cm^{-3} . This gas has a mean metallicity of $10^{-4.4}(M_{\text{yield}}/M_{\odot})$. At higher densities, the metallicity is slightly lower at $10^{-5.4}(M_{\text{yield}}/M_{\odot})$. The same preferential enrichment of diffuse regions may have caused the lower metallicities in this dense cloud. The third phase is the warm, low density ($\rho < 10^{-4} \text{ cm}^{-3}$) gas that exists in recent SN remnants and has solar metallicities and greater. Figure 6.7 depicts the state of the most massive halo 30 kyr after a SN, where the hot phase produced by a SN is super-solar. The high-density tail of the ejecta is the SN shell and is mixing with the lower metallicity ambient medium. As the ejecta expands and cools, it will contribute to the warm, low density, solar material in the lower-left of the phase diagram.

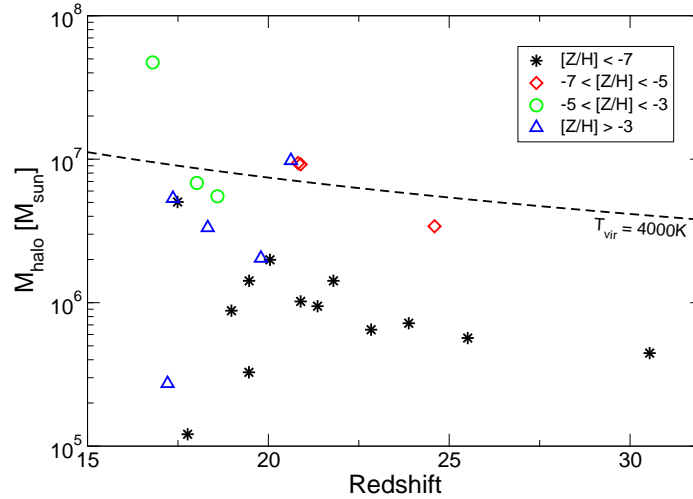


Fig. 6.8.— Star formation history of SimB-SN. The y -axis shows the total mass of the host halo. The symbols indicate the different metallicities of the stars and are labeled in the legend. The dashed line marks the mass of a halo with a virial temperature of 4000 K, approximately at which multiple sites of star formation occur.

6.3.5 Metal-enriched Star Formation History

The star formation history of SimB-SN is depicted in Figure 6.8 by plotting the total mass of the host halo versus the formation redshift. The different symbols represent the metallicity of the star. Before redshift 20, zero metallicity stars form in low-mass halos, whose masses increase from $5 \times 10^5 M_\odot$ to $2 \times 10^6 M_\odot$ due to negative feedback from the LW flux and UV heating from earlier stars. This agrees with the results of Machacek et al. (2001), who demonstrated the critical halo mass to cool increases with the LW radiation background intensity. There are two stars that form in halos with masses of $3 - 5 \times 10^5 M_\odot$ because of the positive feedback from a SN blastwave impacting a satellite halo and creating excess electrons that induce H_2 cooling (Ferrara, 1998).

The first instance of a metal enriched star occurs at $z = 24.6$ with a metallicity of $10^{-8.4} (M_{\text{yield}}/M_\odot)$ in the most massive halo with a mass of $3.4 \times 10^6 M_\odot$. The gas that was reincorporated into the host halo was enriched by the star that formed at $z = 31$. The resulting SN again expels the gas from the halo. The gas is reincorporated

again so stars can form in the same halo around redshift 21. Here three instances of star form with metallicities of $[-8.2, -8.1, -4.3]$ ($M_{\text{yield}}/M_{\odot}$). The aggregate energy from these three SNe expel most of the gas from the potential well yet again, and the most massive halo does not form any stars until $z = 16.8$. Similar instances of reincorporation of enriched material happens for smaller halos at redshifts less than 20. There is one metal enriched star with a metallicity of $10^{-4.8}(M_{\text{yield}}/M_{\odot})$ that forms in a low-mass halo with a mass of $2.7 \times 10^5 M_{\odot}$ at $z = 17.2$. This halo was a satellite of a more massive star forming halo that was enriched by a SN blastwave originating from the parent halo.

6.4 Discussion

We find that the combination of Pop III stellar feedback and continued H_2 cooling in $T_{\text{vir}} < 10^4$ K halos alters the landscape of high-redshift galaxy formation. The most drastic changes are as follows:

1. *Dynamic assembly of dwarf galaxies*— A striking difference when we include Pop III radiative feedback are the outflows and gas inhomogeneities in the halos and surrounding IGM. The outflows enrich the IGM and reduce the baryon fraction of the 10^4 K halo as low as 0.05, much lower than the cosmic fraction $\Omega_b/\Omega_M = 0.17$ (cf. Yoshida et al., 2006a; Abel et al., 2007). This substantially differs from the current theories of galaxy formation where relaxed isothermal gas halos hierarchically assemble a dwarf galaxy. Furthermore, Pop III feedback increases the total baryonic angular momentum of the system by a factor of 2–5 without SNe and up to 10 with SNe.

2. *Pop III sphere of influence*— Pop III feedback is mainly a local phenomenon except its contribution to the UVB. How far its H II region, outflows, and metal ejecta (if any) extend will predominately determine the characteristics of the next generation of stars. Highly biased (clustered) regions are significantly affected by Pop III feedback, whereas isolated halos will feel little feedback. The first galaxies will form in these biased regions and thus should be significantly influenced by their

progenitors.

3. *Dependence on star forming progenitors*— Although our study of calculations with SNe only provided an upper limit of metal enrichment, it is clear that the metallicity, therefore metal-line and dust cooling and low-mass star formation, depends on the nature of the progenitors of the dwarf galaxy. If the galaxy was assembled by smaller halos that hosted a Pop III star that did not produce a SN, the galaxy will continue to have a top-heavy initial mass function (IMF).

4. *Complex protogalactic ISM*— The interplay between stellar and SNe feedback, cold inflows, and molecular cooling produce a truly multi-phase ISM that is reminiscent of local galaxies. The cool, warm, and hot phases are interspersed throughout the dwarf galaxy, whose temperatures and densities can span up to three orders of magnitude at a given radius.

5. *Metallicity floor*— When the halo is massive enough to host multiple sites of star formation, the metal ejecta does not significantly increase the mean metallicity of the host halo. There seems to be a balance between galactic outflows produced from SNe, inflowing metal-enriched and pristine gas, and SNe ejecta that is not blown out of the system. In our high yield models, the metallicity interestingly fluctuates around $10^{-3}Z_{\odot}$ in the most massive halo when this balance occurs at and above mass scales $\sim 10^7 M_{\odot}$.

Clearly the first and smallest galaxies are complex entities, contrary to their low mass and generally assumed simplicity. Our calculations reflect the important role of Pop III stellar feedback in early galaxy formation.

These high-redshift galaxies have a $\sim 5\text{--}15\%$ chance of being undisturbed by mergers until the present day, being “fossils” of reionization (Gnedin & Kravtsov, 2006). Dwarf spheroidals (dSph) galaxies are some of the darkest galaxies in the universe, having high mass-to-light ratios up to 100 (Mateo, 1998). Gas loss in dSph’s close to the Milky Way or M31 can be explained by gas tidal stripping during orbital encounters (Mayer et al., 2007). However there are some galaxies (e.g. Tucana, Cetus) removed from both the Milky Way and Andromeda galaxies and cannot be explained by tidal stripping. In addition to ultraviolet heating from reionization (Bullock et

al., 2000; Susa & Umemura, 2004) and intrinsic star formation (Mac Low & Ferrara, 1999), perhaps stellar feedback from Pop III stars influenced the gas-poor nature of dSph's. Even at the onset of widespread star formation in the objects studied here, the baryon fraction can be three times lower than the cosmic mean, and the dwarf galaxy may never fully recover from the early mass loss. This initial deficit may play an important role in future star formation within these low-mass galaxies and could partially explain the lack of gas in isolated dSph's.

With the radiative and chemical feedback from the progenitors of the early dwarf galaxies, we have an adequate set of cosmological “initial conditions” to study the transition from Pop III to metal-enriched (Pop II) stars. In this setup, the current metal tracer field would actually contribute to the radiative cooling. To accomplish this, we need to include a metal-line and dust cooling model to investigate the dynamical effect of this additional cooling. However, metal-line cooling might not be important at these low metallicities. Jappsen et al. (2007) showed that metal-line cooling at metallicities below $10^{-2}Z_{\odot}$ does not significantly affect the dynamics of a collapsing halo. Conversely, dust cooling can induce fragmentation of solar mass fragments at metallicities as low as $\sim 10^{-6}$ (Schneider et al., 2006).

Perhaps when the protogalactic gas cloud starts to host multiple sites of star formation, the associated SNe produce sufficient dust in order for a transition to Pop II. In lower mass halos, the SN ejecta is blown out of the halo, and future star formation cannot occur until additional gas is reincorporated into the halo. However in these halos with masses $\gtrsim 10^7 M_{\odot}$, the SN does not totally disrupt the halo. A fraction of the SN ejecta is contained within the halo and could contribute to subsequent sites of star formation. Now this SN ejecta and associated dust could instigate the birth of the first Pop II stars.

As discussed above, the metallicity of the most massive halo fluctuates around $10^{-3}Z_{\odot}$. This is intriguingly the same value as a sharp cutoff in stellar metallicities in four local dSph's: Sculptor, Sextans, Fornax, and Carina (Tolstoy et al., 2004; Helmi et al., 2006). This is in contrast with the galactic halo stars, whose metal-poor tail extends to $Z/Z_{\odot} = 10^{-4}$ (Beers & Christlieb, 2005). We must take care when comparing our results to observations since we made the simplification that

every Pop III star produces a pair-instability SN. As discussed in Helmi et al., the galactic halo may be composed of remnants of galaxies that formed from high- σ density fluctuations, and dwarf galaxies originate from low- σ peaks. In this scenario, the objects (or its remnants) simulated here would most likely reside in galactic halos at the present day. If we attempt to match this metallicity floor of $10^{-4}Z_{\odot}$ in the galactic halo, this requires $\sim 8M_{\odot}$ of metals produced for every Pop III star or roughly one in ten Pop III stars ending in a pair-instability SN.

6.5 Summary

Radiative feedback from Pop III stars play an important role in shaping the first galaxies. We studied the effects of this feedback on the global nature of high-redshift dwarf galaxies, using a set of five cosmology AMR simulations that accurately model radiative transfer with adaptive ray tracing. Additionally, we focused on the metal enrichment of the star forming halos and their associated star formation histories. Our key findings in this paper are listed below.

1. Dynamical feedback from Pop III stars expel nearly all of the baryons from low-mass host halos. The baryon fractions in star forming halos never fully recover even when it reaches a virial temperature of 10^4 K. The baryon fraction is reduced as low as ~ 0.05 with SNe feedback, three times lower than the cases without stellar feedback.
2. The expelled gas gains angular momentum as it exists at large radii. When it is reincorporated into the halo, it increases the spin parameter by a factor of 2–5 without SNe and up to 10 with SNe.
3. The accurate treatment of radiative transfer produces a complex, multi-phase ISM that has densities and temperatures that span up to 4 orders of magnitude at a given radius.
4. Pair-instability SN preferentially enrich the IGM to a metallicity an order of magnitude higher than the surrounding overdensities.
5. Once a SN explosion cannot totally disrupt its host halo, the mean metallicity fluctuates around $10^{-4.8}(M_{\text{yield}}/M_{\odot})$ as there may be a balance between SN outflows,

cold inflows, and contained SNe ejecta.

We conclude that Pop III stars play an integral part in the early universe as they determine the characteristics of the first galaxies, which then reionize the universe and may survive until the present day. Their feedback is essential to consider in the early universe because of their large masses and luminosities and being hosted in shallow potential wells. Although our high-resolution simulations included an accurate model of radiative transfer, there are still uncertainties in the true nature of the first galaxies, arising from the unknown primordial IMF. With future observations of early dwarf galaxies at $z > 6$, it will be possible to infer some details about the first stars by using theoretical predictions from cosmological simulations that accurately model their stellar feedback.

Chapter 7

How Massive Metal-Free Stars Start Cosmological Reionization

We considered the impact of Pop III star formation on early dwarf galaxies in the last section. Now we focus on the global impact of these stars on cosmological reionization and the nature of star formation during this epoch. We show that Pop III stars reionize the universe to $\sim 10\%$, where reionization is completed by low-luminosity galaxies. Nevertheless, it is important to gauge the transition from isolated primordial star forming regions to galaxies. The heating and reionization of the IGM by Pop III stars suppresses galaxy formation that are forming from pre-heated gas. Star formation in these galaxies are regulated by Jeans smoothing instead of the ability to radiatively cool through atomic line transitions.

As we noted in Chapter 2, the SNe from Pop III stars will only be detectable by JWST but not the main sequence radiation. It is timely to establish other constraints on Pop III star formation. One of these constraints is the thermal history of the universe. In these simulations, we can directly track this and perhaps connect them with observed IGM temperatures at $z \sim 4$. Furthermore, some local dwarf galaxies may hold clues about the first stars in their structures and properties, e.g. mass-to-light ratios, metallicity gradients, stellar ages, and abundance patterns.

This chapter specifically concentrates on the properties of star formation in these

low-mass halos in the presence of stellar feedback and the characteristics of the beginning of cosmological reionization caused by these massive, metal-free stars. This chapter is in preparation for publication in *The Astrophysical Journal*. It is co-authored by Tom Abel, who developed the original version of the adaptive ray tracing code used in these simulations.

7.1 Motivation

It is clear that quasars are not responsible to keep the universe ionized at redshift 6. The very brightest galaxies at those redshifts alone also provide few photons. The dominant sources of reionization so far are observationally unknown despite remarkable advances in finding sources at high redshift (e.g. Shapiro, 1986; Bouwens et al., 2004; Fan et al., 2006; Thompson et al., 2006; Eyles et al., 2006) and hints for a large number of unresolved sources at very high redshifts (Spergel et al., 2006; Kashlinsky et al., 2007). At the same time, ab initio numerical simulations of structure formation in the concordance model of structure formation have found that the first luminous objects in the universe are formed inside of cold dark matter (CDM) dominated halos of total masses $2 \times 10^5 - 10^6 M_{\odot}$ (Haiman et al., 1996; Tegmark et al., 1997; Abel et al., 1998). Fully cosmological ab initio calculations of Abel et al. (2000, 2002) and more recently Yoshida et al. (2006b) clearly show that these objects will form isolated very massive stars. Such stars will be copious emitters of ultraviolet (UV) radiation and are as such prime suspects to get the process of cosmological reionization started. In fact, one dimensional calculations of Whalen et al. (2004) and Kitayama et al. (2004) have already argued that the earliest H II regions will evaporate the gas from the host halos and that in fact most of the UV radiation of such stars would escape into the intergalactic medium. Recently, Yoshida et al. (2006a) and Abel et al. (2007) demonstrated with full three-dimensional radiation hydrodynamical simulations that indeed the first H II regions break out of their host halos quickly and fully disrupt the gaseous component of the cosmological parent halo. The initially circumstellar material of the first stars finds itself radially moving away from the star at $\sim 30 \text{ km s}^{-1}$ at a distance of $\sim 100 \text{ pc}$ at the end of the stars life. At this time, the photo-ionized

regions have high electron fractions and little destructive Lyman-Werner band radiation fields, creating ideal conditions for molecular hydrogen formation which may in fact stimulate further star formation above levels that would have occurred without the pre-ionization. Such conclusion have been obtained in calculations with approximations to multi dimensional radiative transfer or one dimensional numerical models (Ricotti et al., 2002a; Nagakura & Omukai, 2005; O’Shea et al., 2005; Yoshida et al., 2006a; Ahn & Shapiro, 2007; Johnson et al., 2007). These early stars may also explode in supernovae and rapidly enrich the surrounding material with heavy elements, deposit kinetic energy and entropy to the gas out of which subsequent structure is to form. This illustrates some of the complex interplay of star formation, primordial gas chemistry, radiative and supernova feedback and readily explains why any reliable results will only be obtained using full ab initio three dimensional hydrodynamical simulations. In this paper, we present the most detailed such calculations yet carried out to date and discuss issues important to the understanding of the process of cosmological reionization.

It is timely to develop direct numerical models of early structure formation and cosmological reionization as considerable efforts are underway to

1. Observationally find the earliest galaxies with the James Webb Space Telescope (JWST; Gardner et al., 2006) and the Atacama Large Millimeter Array (ALMA; Wilson et al., 2005),
2. Further constrain the amount and spatial non-uniformity of the polarization of the cosmic microwave background radiation (Page et al., 2006),
3. Measure the surface of reionization with LOFAR (Rottgering et al., 2006), MWA (Bowman et al., 2007), GMRT (Swarup et al., 1991) and the Square Kilometer Array (SKA; Schilizzi, 2004), and
4. Find high redshift gamma ray bursts with SWIFT (Gehrels et al., 2004) and their infrared follow up observations.

We begin by describing the cosmological simulations that include primordial star formation and accurate radiative transfer. In §7.3, we report the details of the star

formation environments and host halos in our calculations. Then in §7.4, we describe the resulting cosmological reionization, and investigate the environments in which these primordial stars form and the evolution of the clumping factor. We compare our results to previous calculations and further describe the nature of the primordial star formation and feedback in §7.5. Finally we summarize our results in the last section.

7.2 Radiation Hydrodynamical Simulations

We use radiation hydrodynamical simulations with a modified version of the cosmological AMR code *Enzo* to study the radiative effects from the first stars (Bryan & Norman, 1997, 1999). We have integrated adaptive ray tracing (Abel & Wandelt, 2002) into the chemistry, energy, and hydrodynamics solvers in *Enzo* that accurately follow the evolution of the H II regions from stellar sources and their relevance during structure formation and cosmic reionization.

Seven different simulations are discussed here. Table 3.1 gives an overview of the parameters and the physics included in these calculations. We perform two cosmological realizations, Sim A and B, with three sets of assumptions about the primordial gas chemistry. The simplest calculations here assume only adiabatic gas physics and provide the benchmark against which the more involved calculations are compared. We compare this to one model with atomic hydrogen and helium cooling only and one that includes H₂ cooling. Massive, metal-free star formation is included only in the H₂ cooling models.

Table 7.1: Simulation Parameters

Name	l [Mpc]	Cooling model	SF	SNe	N_{part}	N_{grid}	N_{cell}
SimA-Adb	1.0	Adiabatic	No	No	2.22×10^7	30230	9.31×10^7 (453^3)
SimA-HHe	1.0	H, He	No	No	2.22×10^7	40601	1.20×10^8 (494^3)
SimA-RT	1.0	H, He, H_2	Yes	No	2.22×10^7	44664	1.19×10^8 (493^3)
SimB-Adb	1.5	Adiabatic	No	No	1.26×10^7	23227	6.47×10^7 (402^3)
SimB-HHe	1.5	H, He	No	No	1.26×10^7	21409	6.51×10^7 (402^3)
SimB-RT	1.5	H, He, H_2	Yes	No	1.26×10^7	24013	6.54×10^7 (403^3)
SimB-SN	1.5	H, He, H_2	Yes	Yes	1.26×10^7	24996	6.39×10^7 (400^3)

Note. — Col. (1): Simulation name. Col. (2): Box size. Col. (3): Cooling model. Col. (4): Star formation. Col. (5): Supernova feedback. Col. (6): Number of dark matter particles. Col. (7): Number of AMR grids. Col. (8): Number of unique grid cells.

These calculations are initialized at redshift $z = 130$ (120)* when the intergalactic medium has a temperature of 325 (280) K in box sizes 1 comoving Mpc (1.5 Mpc) for Sim A (B). We use the cosmological parameters of $(\Omega_B h^2, \Omega_M, h, \sigma_8, n) = (0.024, 0.27, 0.72, 0.9, 1)$ from first year WMAP results, where the constants have the usual meaning (Spergel et al., 2003). The changes in the third year WMAP results (Spergel et al., 2006) does not affect the evolution of individual halos studied here but only delays structure formation by $\sim 40\%$ (Alvarez et al., 2006b). The adiabatic simulations as well as the atomic hydrogen and helium cooling only calculations are described in Wise & Abel (2007a). The new models presented here have the exact same setup and random phases in the initial density perturbation and only differ in that they include star formation as well as follow the full radiation hydrodynamical evolution of the H II regions and supernova feedback in Sim B. We use the designations RT and SN to distinguish cases in which only star formation and radiation transport were included (RT) and the one model which also includes supernovae (SN) in Sim B. We use the same refinement criteria as in our previous work, where we refine if the DM (gas) density becomes three times greater than the mean DM (gas) density times a factor of 2^l , where l is the AMR refinement level. We also refine to resolve the local Jeans length by at least 16 cells. Cells are refined to a maximum AMR level of 12 that translates to a spatial resolution of 1.9 (2.9) comoving parsecs. Refinement is restricted to the innermost initial nested grid that has a side length of 250 (300) comoving kpc.

The star formation recipe and radiation transport are detailed in Wise & Abel (2007c). Here we overview the basics about our method. Star formation is modelled using the Cen & Ostriker (1992) algorithm with the additional requirement that an H_2 fraction of 5×10^{-4} must exist before a star forms. We allow star formation to occur in the Lagrangian volume of the surrounding region out to three virial radii from the most massive halo at $z = 10$ in the dark matter only runs as discussed in Wise & Abel (2007a). This volume that has a side length of 195 (225) comoving kpc at $z = 30$ and 145 (160) comoving kpc at the end of the calculation. The calculations with SNe

*To simplify the discussion, simulation A will always be quoted first with the value from simulation B in parentheses.

use a stellar mass M_* of $170M_\odot$, whereas the ones without SNe use a mass of $100M_\odot$. The ionizing luminosities are taken from no mass loss models of Schaerer (2002), and we employ the SN energies from Heger & Woosley (2002). Star particles after main sequence are tracked but are inert. There is evidence of lower mass primordial stars forming within relic H II regions (O’Shea et al., 2005; Yoshida et al., 2006a), but we neglect this to avoid additional uncertain parameters. This is a desired future improvement, however.

We use adaptive ray tracing (Abel & Wandelt, 2002) to calculate the photo-ionization and heating rates caused by stellar radiation. We consider photo-ionization from photons with an energy of 28.4 (29.2) eV that is the mean energy of ionizing radiation from a metal-free star with 100 (170) M_\odot . We account for H₂ photo-dissociation with a $1/r^2$ Lyman-Werner radiation field without self-shielding. We use a non-equilibrium, nine-species (H, H⁺, He, He⁺, He⁺⁺, e⁻, H₂, H₂⁺, H⁻) chemistry solver in *Enzo* (Abel et al., 1997; Anninos et al., 1997) that takes into account the additional photo-ionization from the radiation transport.

We present results from SimA to a redshift of 20, which we stop because of computing constraints. In SimB, we end the simulations when the most massive halo begins to rapidly collapse (i.e. $t_{\text{cool}} < t_{\text{dyn}}$) in the hydrogen and helium cooling only runs at redshift 16.8. The virial temperature T_{vir} of the halo is $\sim 10^4$ K at this redshifts.

7.3 Star Formation

Here we describe the aspects of massive metal-free star formation in our simulations. The first star forms at redshift 29.7 (30.8) in halo typical of Pop III star formation without any feedback that has a mass of $\sim 5 \times 10^5 M_\odot$ (cf. Abel et al., 2000, 2002; Machacek et al., 2001; Yoshida et al., 2003, 2006a). Afterwards there are a total of 6, 27, and 20 instances of star formation in SimA-RT, SimB-RT, and SimB-SN, respectively.

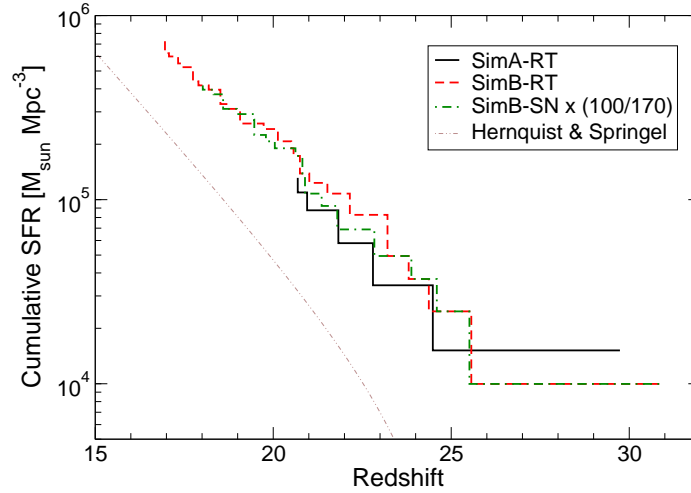


Fig. 7.1.— Cumulative star formation rate in units of comoving $M_{\odot} \text{ Mpc}^{-3}$ of SimA-RT (*black solid*), SimB-RT (*red dashed*), and SimB-SN (*green dot-dashed*). The star formation rate of SimB-SN has been scaled by 100/170, which is the ratio of Pop III stellar masses used in SimB-RT and SimB-SN, in order to make a direct comparison between the two simulations. The *brown dot-dot-dashed* line represents the cumulative star formation rate in atomic hydrogen cooling halos from Hernquist & Springel (2003).

7.3.1 Star Formation Rate

We show the cumulative star formation rate (SFR) in units of comoving $M_{\odot} \text{ Mpc}^{-3}$ in Figure 7.1. This quantity is simply calculated by taking the total mass of stars formed at a given redshift divided by the comoving volume where stars are allowed to form (see §7.2). In this figure, we decrease the SFR of SimB-SN by a factor of 1.7 in order to directly compare the rates from the other two simulations. This minimizes some of the uncertainties entered into our calculations when we chose the free parameter of Pop III stellar mass. The cumulative rates are very similar in both realizations. The refined volume of Sim A (Sim B) has an average overdensity $\delta \equiv \rho/\bar{\rho} = 1.4$ (1.8). The more biased regions in Sim B allows for a higher density of star-forming halos that leads to the increased cumulative SFR.

We also overplot the cumulative SFR in atomic hydrogen cooling halos from Hernquist & Springel (2003) in this figure. It is up to an order of magnitude lower than

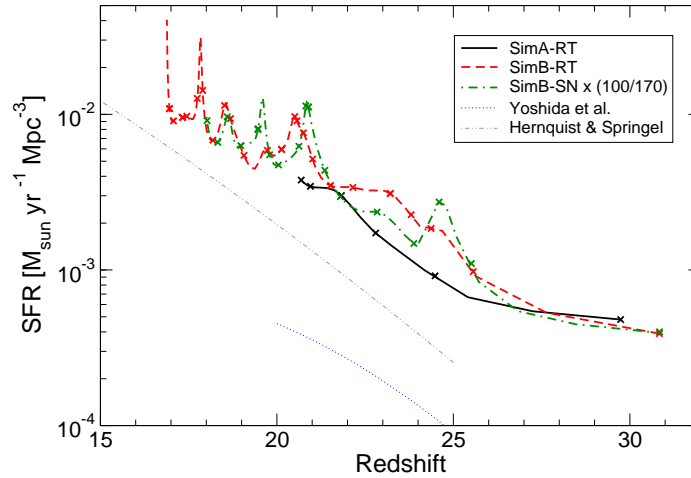


Fig. 7.2.— Comoving star formation rate in units of $M_{\odot} \text{ yr}^{-1} \text{ Mpc}^{-3}$. The lines representing the simulation data have the same meaning as in Figure 7.1. The crosses show at which redshifts stars form. The rates in SimB-SN are scaled for the same reason as in Figure 7.1. For comparison, we overplot the star formation rates from Hernquist & Springel (2003) in atomic hydrogen line cooling halos and Yoshida et al. (2003) for $100M_{\odot}$ Pop III stars.

the rates seen in our calculations up to redshift 20. They only focused on larger mass halos in their simulations. The disparity between the rates is caused by our simulations only sampling a highly biased region, where we focus on a region containing a $3\text{-}\sigma$ density fluctuation, and from the contribution from Pop III stars. The rates of Hernquist & Springel (2003) are calculated from an extensive suite of smoothed particle hydrodynamics simulations that encompasses both large and small simulation volumes and give a more representative global SFR due to their larger sampled volumes. However, our adaptive spatial resolution allows us to study both the small- and large-scale radiative feedback from Pop III stars, which is the main focus of the paper, in addition to the quantitative measures such as a SFR.

To calculate a true SFR (i.e. Madau et al., 1996, in units of comoving $M_{\odot} \text{ yr}^{-1} \text{ Mpc}^{-3}$) from the cumulative SFR, we first fit the cumulative SFR with a cubic spline with 10 times the temporal resolution. Then we smooth the data back to its original time resolution and evaluate its time derivative to obtain the SFR that we show in

Figure 7.2. We also mark the redshifts of star formation with crosses. We again compare our rates to ones calculated in Hernquist & Springel (2003) for metal-enriched stars and Yoshida et al. (2003) for Pop III stars with a mass of $100 M_{\odot}$. Our rates are higher for reasons discussed previously. We do not advocate these SFRs as cosmic averages but give them as a useful diagnostic of the performed simulations.

We see an increasing function from $4 \times 10^{-4} M_{\odot} \text{ yr}^{-1} \text{ Mpc}^{-3}$ at redshift 30 to $\sim 6 \times 10^{-3} M_{\odot} \text{ yr}^{-1} \text{ Mpc}^{-3}$ at redshift 20. Here only one star per halo forms in objects with masses $\lesssim 5 \times 10^6 M_{\odot}$. Above this mass scale, star formation is no longer isolated in nature and can be seen by the bursting nature of the star formation after redshift 20, where the SFR fluctuates around $10^{-2} M_{\odot} \text{ yr}^{-1} \text{ Mpc}^{-3}$ (cf. Ricotti et al., 2002b). Since we neglect H_2 self-shielding, the strong Lyman-Werner (LW) radiation dissociates almost all H_2 in the host halo and surrounding regions. Thus we rarely see simultaneous instances of star formation. However, the regions that were beginning to collapse when a nearby star ignites form a star 3 – 10 million years after the nearby star dies. This only results in a minor change in the timing of star formation. Furthermore this delay is minimal compared to the Hubble time and does not affect SFRs.

7.3.2 Star Forming Halo Masses

We show the star formation history versus the host halo DM masses as a function of redshift in Figure 7.3. The DM halo masses are calculated with the HOP algorithm (Eisenstein & Hut, 1998). First we focus on star formation in the largest halo. Around redshift 30, the first star forms in all three simulations within a halo with a mass $\sim 5 \times 10^5 M_{\odot}$. The stellar radiation drives a $\sim 30 \text{ km s}^{-1}$ shock wave that removes almost all of the gas from the shallow potential well. It takes approximately 40 million years for gas to reincorporate into the potential well from smooth IGM accretion and mergers. At $z \sim 24$, the second star forms in the most massive progenitor that now has a mass of $\sim 3 \times 10^6 M_{\odot}$. Yet again, the stellar feedback expels most of the gas from its host. For Sim A (Sim B), another 50 (30) million years passes before the next star forms in this halo. Now it has a mass of $10^7 M_{\odot}$, which is a sufficient amount

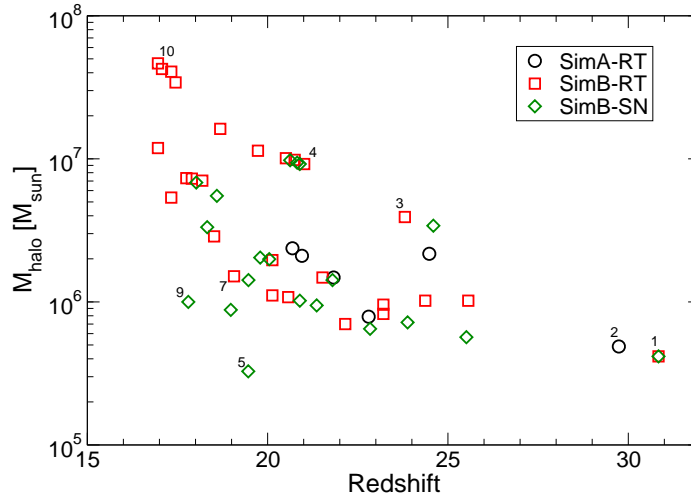


Fig. 7.3.— Star formation history versus host halo DM mass for SimA-RT (*black circles*), SimB-RT (*red squares*), and SimB-SN (*green triangles*). One symbol represents one star. The numbers correspond to the halo numbers listed in Table 7.2.

of potential energy to confine most of the stellar and SNe outflows. In SimA-RT and SimB-RT, the halo now hosts multiple sites of star formation that is seen in the nearly continuous bursts of star formation in the most massive halo. However in SimB-SN at $z = 20.8$, three stars form in succession in the most massive halo. Their aggregate stellar and SNe feedback expels the gas from its halo one more time.

Most of the stars form in low-mass halos with masses $\sim 10^6 M_\odot$ that are forming its first star between redshifts 18 – 25 in our calculations. A slight increase in host halo masses with respect to redshift occurs because of the negative feedback from ionization, ultraviolet heating, and H_2 dissociation from previous stars that increases the critical halo mass in which gas can cool and condense (e.g. Machacek et al., 2001; Yoshida et al., 2003; Mesinger et al., 2006).

One interesting difference in SimB-SN from the other calculations is that it forms stars in halos with masses with $\lesssim 5 \times 10^5 M_\odot$ when stars are mainly forming in more massive halos. In these cases, the SN shell expands into the ambient medium and impacts the surrounding satellite halos. The blast wave induces star formation in low-mass halos that otherwise would not have formed a star (Ferrara, 1998).

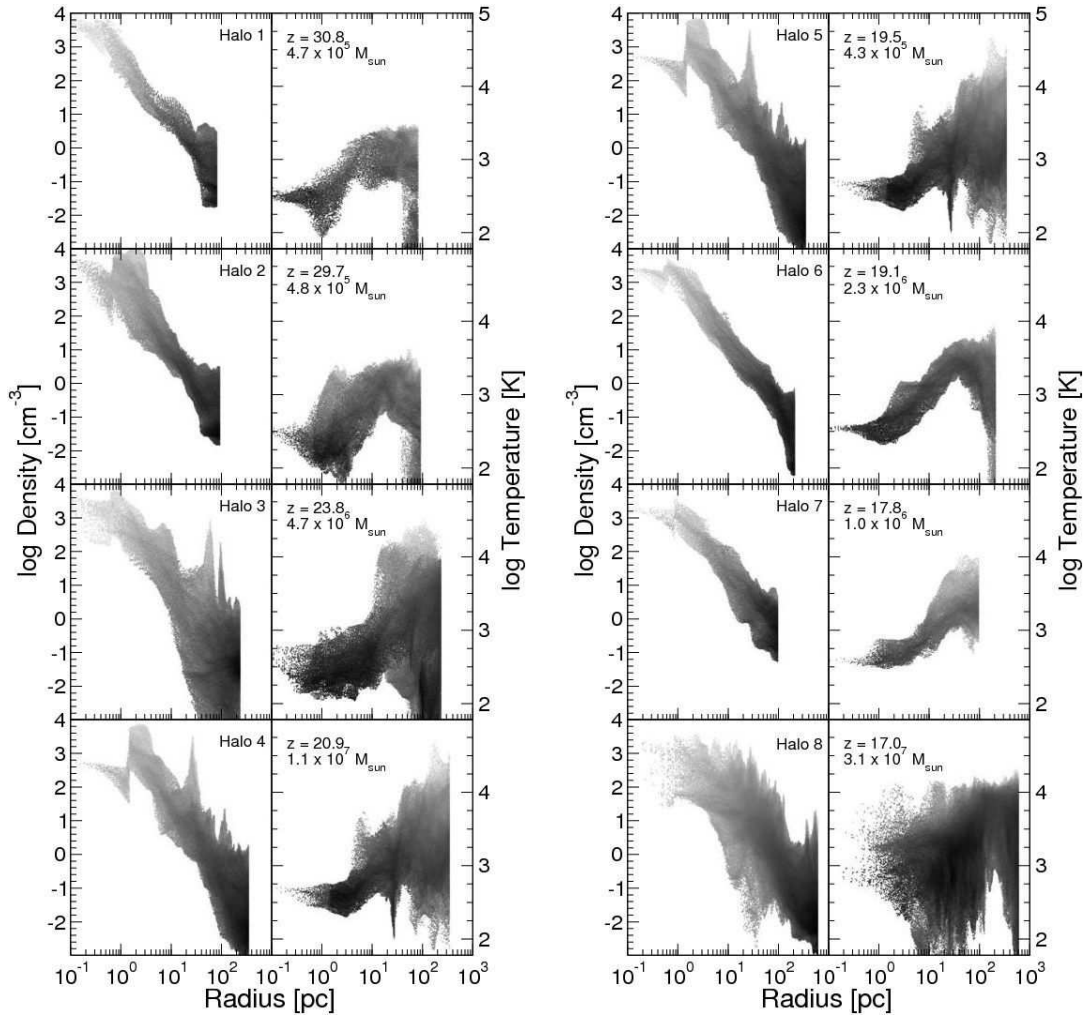


Fig. 7.4.— Radial profiles of number density (*left column*) and temperature (*right column*) for selected star forming halos inside the virial radius. These data represent the state of the region immediately before star formation. Notice the added complexity (range) in the density and temperature with increasing host halo mass, especially if the region has been affected by stellar radiation, as in Halos 3, 4, 5, 10, 11, and 12. The discontinuities in density in the inner parsec arise from our star formation recipe when we remove half the mass in a sphere containing twice the stellar mass.

Table 7.2: Selected Star Forming Halo Parameters

#	Sim	z	M_{vir} [M_{\odot}]	f_b	ρ_c [cm^{-3}]	T_c [K]
1	SimB-RT	30.8	4.7×10^5	0.089	3000	330
2	SimA-RT	29.7	4.8×10^5	0.094	3000	310
3	SimB-RT	23.8	4.7×10^6	0.036	1400	310
4	SimB-SN	20.9	1.1×10^7	0.051	350	460
5	SimB-SN	19.5	4.3×10^5	0.017	470	170
6	SimB-RT	19.1	2.3×10^6	0.13	1500	360
7	SimB-SN	17.8	1.0×10^6	0.18	1100	390
8	SimB-RT	17.0	3.1×10^7	0.10	440	1000

Note. — Col. (1): Halo number. Col. (2): Simulation source. Col. (3): Redshift. Col. (4): Virial mass. Col. (5): Baryon mass fraction. Col. (6): Central number density. Col. (7): Central temperature.

7.3.3 Star Formation Environments

We further study the nature of high-redshift star formation by selecting eight star forming regions and studying the surrounding interstellar medium (ISM) prior to star formation. The ISM in the 10^4 K halos are described in more detail in Wise & Abel (2007c). The sample of regions are chosen in order to compare different star formation environments. These regions can be categorized into (1) first star inside an undisturbed halo, (2) first star that is delayed by LW radiation, (3) induced star formation by positive feedback, (4) star formation after gas reincorporation, and (5) star formation in a halo with a virial temperature over 10^4 K. The represented halos and their parameters are listed in Table 7.2 and annotated in Figure 7.3.

We plot the mass-weighted radial profiles of number density (*left columns*) and temperature (*right columns*) within the virial radius for these eight halos in Figure 7.4 and describe them below.

1. *First star* (Halo 1, 2)— These stars are the first to form in the simulation

volume. The structure of the host halos within our resolution limit exhibit similar characteristics, e.g., a self-similar collapse and central temperatures of 300 K, as in previous studies (Abel et al., 2000, 2002; Bromm et al., 2002; Yoshida et al., 2006b). The halo masses are $4.8(4.7) \times 10^5 M_{\odot}$. Heating from virialization raises gas temperatures to 3000 K, and in the central parsec, H_2 cooling becomes effective and cools the gas down to 100 K that drives the free-fall collapse. The central gas densities and temperatures are approximately 3000 cm^{-3} and 320 K, respectively.

2. *Delayed first star* (Halo 6, 7)— The host halos have similar radial profiles as the halos that hosted the first stars but with masses of $1 - 3 \times 10^6 M_{\odot}$. Here the H_2 cooling has been stifled by the LW radiation from nearby star formation. Only when the halo mass passes a critical mass, the core can cool and condense by H_2 formation (Machacek et al., 2001; Yoshida et al., 2003). The central densities are slightly lower than the first stars with 1500 and 1100 cm^{-3} in SimB-RT and SimB-SN, respectively. The central temperatures are marginally higher at 360 and 390 K.

3. *Induced star formation* (Halo 5)— At $z = 19.61$, a massive star explodes in a SN, whose shell initially propagates outward at 4000 km s^{-1} . After two million years, the shell passes a satellite halo with $4 \times 10^5 M_{\odot}$ that is 480 pc from the origin of the SN. The combination of the shock passage and excess free electrons in the relic H II catalyze H_2 formation in this low-mass halo (e.g. Ferrara, 1998; O’Shea et al., 2005; Mesinger et al., 2006). The SN blast wave heats the gas over 10^4 K to radii as low as five parsecs. In the density profile, both low and high density gas exists at similar radii. Here the shock passage creates a tail of gas streaming from the central core, whose asymmetries can be seen in the density profile. However, the core survives and benefits from the excess electrons created during this event. The central temperature is interestingly a factor of two lower than the previous cases at 170 K. The H_2 criterion for star formation is reached faster because of the excess electrons, which creates a star particle at a lower density (470 cm^{-3}).

4. *Star formation after reincorporation* (Halo 3, 4)— After a sufficient amount of gas that was expelled by dynamical feedback of the first star is reincorporated into the halo, star formation is initiated again. Here virial temperatures of the halos are

under 10^4 K. Halo 3 is the second instance of star formation in this halo, whereas the other halos are forming their third star. These halos have a larger spread in gas densities and temperatures than the halos forming their first star. Gas is heated by virialization and prior stars to over 10^4 K outside 10 pc. The central quantities in halo 3 are similar to the regions described in the delayed star formation section. Halos 4 shows a more diffuse and warmer core with densities of 350 cm^{-3} and temperatures of 460 K.

5. *Star formation in 10^4 K halos* (Halo 8)— In this halo, H_2 formation is aided by atomic hydrogen cooling. The ISM becomes increasingly complex as more stars form in the halo. The temperatures range from 100 K to 20,000 K throughout the halo. It has hosted eight massive stars since it started to continually form stars at redshift 21. The densities are similar to the other regions that have been affected by other stars.

7.4 Starting Cosmological Reionization

In this section, we first describe the ionizing radiation from massive stars that starts cosmological reionization. Then we discuss the effects of recombinations in the inhomogeneous IGM and kinetic energy feedback from Pop III stars. Lastly the evolution of the average IGM thermal energy is examined.

To illustratively demonstrate radiative feedback from massive stars on the host halos and IGM, we show projections of gas density and temperature that are density-squared weighted in Figures 7.5 and 7.6 for all of the simulations at redshift 20 and 18, respectively. These projections have the same field of view of 8.5 proper kpc and the same color maps. The large-scale density structure is largely unchanged by the stellar feedback, and the adjacent filaments remain cool since they are optically thick to the incident radiation. H_2 cooling produces more centrally concentrated objects, and the dynamical stellar feedback destroys the baryonic structure in $\sim 10^6 M_\odot$ halos. Kinematic feedback from SNe has an even larger effect on the surrounding gas. In SimB-SN, this effect is seen in the reduced small-scale structure and low-mass halos with no gas counterparts. However, the most apparent difference in the radiative

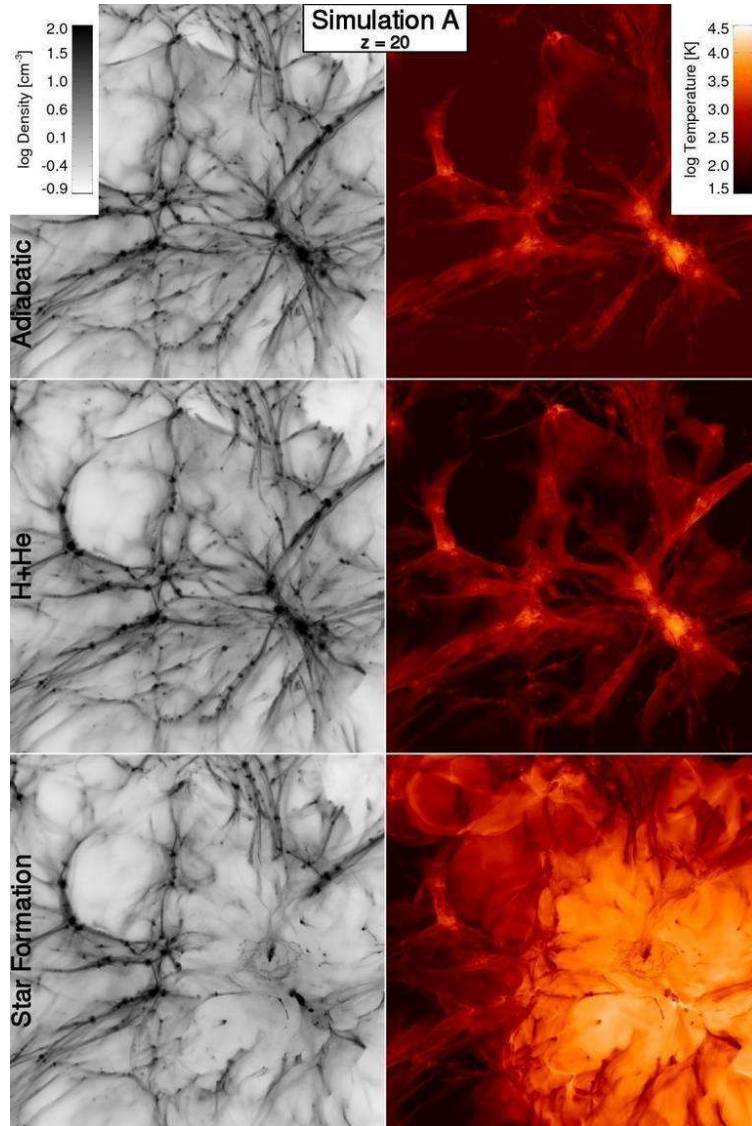


Fig. 7.5.— Density-squared weighted projections of gas density (*left*) and temperature (*right*) of Sim A. The field of view is 8.5 proper kpc (1/216 of the simulation volume) and the color scale is the same for all simulations.

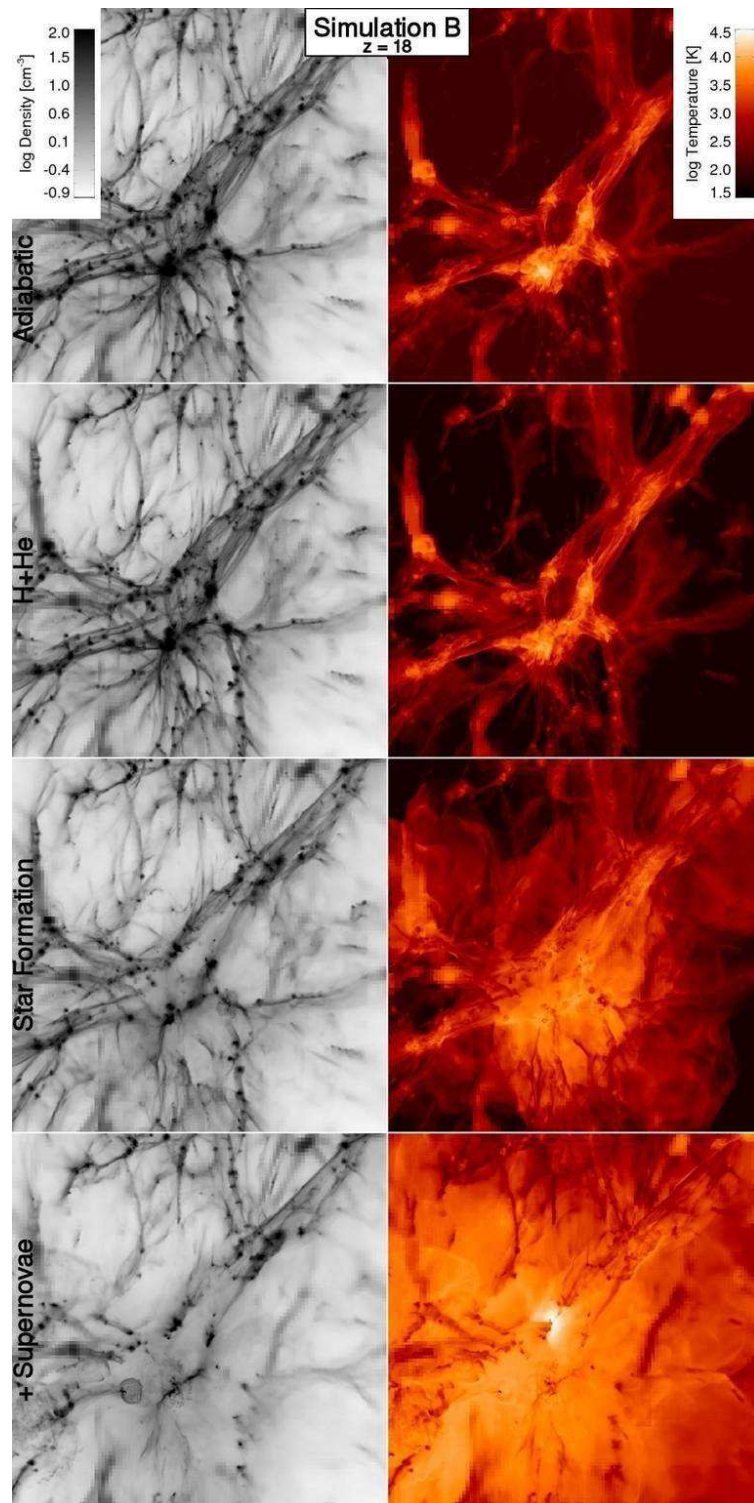


Fig. 7.6.— Same as Figure 7.5 but for Sim B.

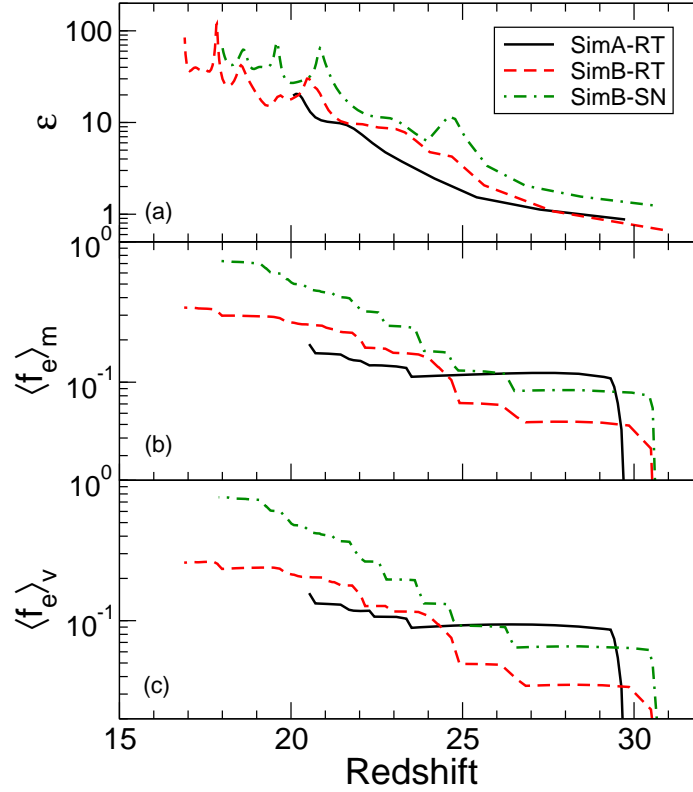


Fig. 7.7.— (a) Averaged emissivity in units of ionizing photons per baryon per Hubble time that is calculated from the star formation rate in Figure 7.2. (b) Mass-averaged ionization fraction of the inner 250 (300) comoving kpc for SimA (SimB). (c) Volume-averaged ionization fraction for the same runs.

simulations is the IGM heating by Pop III stars, especially in SimB-SN.

7.4.1 UV Emissivity

A key quantity in reionization models is volume-averaged emissivity of ionizing radiation. We utilize the comoving SFR $\dot{\rho}_*$ to calculate the proper volume-averaged UV emissivity

$$\epsilon = \frac{\dot{\rho}_* Q_{\text{HI}} t_{\text{H}}}{\bar{\rho}_b} \quad (7.1)$$

in units of ionizing photons per baryon per Hubble time. Here Q_{HI} is the number of ionizing photons emitted in the lifetime of a star per solar mass, $\bar{\rho}_b \simeq 2 \times 10^{-7} \text{ cm}^{-3}$ is the comoving mean number density, and

$$t_{\text{H}} \approx \frac{2}{3H_0\sqrt{\Omega_m}}(1+z)^{-3/2} \quad (7.2)$$

is the Hubble time in a Einstein de-Sitter universe, which is valid for Λ CDM cosmology at $z \gg 1$. For Pop III stellar masses greater than $100 M_{\odot}$, $Q_{\text{HI}} \approx 10^{62}$ photons per solar mass, corresponding to 84000 ionizing photons per stellar proton (Schaerer, 2002). We plot the emissivity ϵ in Figure 7.7a. It follows the same behavior as the SFR, but now can be directly used in semi-analytic reionization models. The emissivity increases from unity at redshift 30 to ~ 100 at the end of our simulations. Our results agree with the emissivity calculated in semi-analytic models that include Pop III stars (e.g. Onken & Miralda-Escudé, 2004).

7.4.2 Effective Number of Ionizations per UV Photon

Although there are approximately 50 photons emitted per baryon at the end of the RT simulations, the simulation volumes remain approximately 25% ionized. We show the mass-averaged and volume-averaged ionization fraction within the innermost initial grid in Figures 7.7b and 7.7c. At $z > 20$, the ionization fraction is $\sim 10\%$ with occasional sharp increases that happen when a star ignites. In the star formation only runs, the volume only becomes slightly more ionized even though the emissivity is increasing at a faster rate. This happens because of the strong recombinations in the inhomogeneous IGM and the partial containment of H II regions in host halos with masses greater than $10^7 M_{\odot}$. Kitayama et al. (2004) provided a useful approximation of the critical halo mass

$$M_{\text{crit}}^{\text{ion}} \sim 2.5 \times 10^6 \left(\frac{M_{\star}}{200 M_{\odot}} \right)^{3/4} \left(\frac{1+z}{20} \right)^{-3/2} M_{\odot}, \quad (7.3)$$

in which an ionization front (I-front) cannot escape. This approximation is valid for stellar masses between 80 and $500 M_{\odot}$, redshifts between 10 and 30, and singular

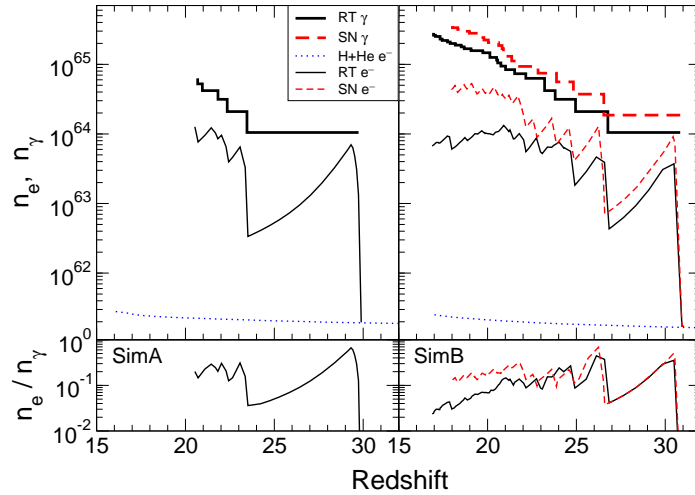


Fig. 7.8.— *Top panels:* Total number of ionizing photons emitted (*thick lines*) and total number of electrons (*thin lines*) for simulations with cooling only (*dotted blue*), star formation only (*solid black*), and supernovae (*dashed red*) in the inner 250 and 300 comoving kpc for SimA (*left*) and SimB (*right*). The H II regions are completely contained in these volumes. *Bottom panels:* The ratio of total number of electrons to the total number of ionized photons emitted.

isothermal spheres. Our simulations exhibit this same trait in which I-fronts only partially breakout from the host halo above this mass scale.

In the SN runs, the mass- and volume-averaged ionization fractions dramatically increase to 0.2 and 0.75 between $z = 21$ and 18. At this time, three stars form in succession in the most massive halo. After the first star goes SN, a diffuse and hot medium is left behind, but the blastwave has not completely disrupted two other nearby condensing clumps. The radiation from the second star now does not have to ionize its host halo and has an escape fraction of near unity. The same happens for the third star in this halo. The combination of the radiation and SN explosions from this stars create a sharp IGM ionization transition that is three times more ionized than before this event.

To examine the strength of recombinations, we compare the total number of electrons to the total number of ionizing photons emitted in Figure 7.8. The ratio of these two quantities is the number of UV photons needed for one effective ionization.

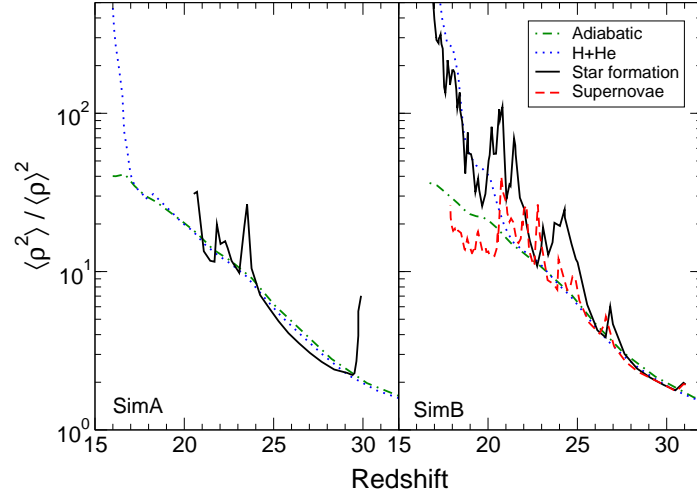


Fig. 7.9.— Clumping factor $C = \langle \rho^2 \rangle / \langle \rho \rangle^2$ for SimA (*left*) and SimB (*right*), comparing the cases of the adiabatic equation of state (*dot-dashed*), atomic hydrogen and helium cooling (*dotted*), star formation only (*solid*), and supernovae (*dashed*).

This ratio is approximately two after the first star dies. The total number of electrons remains basically constant with the increasing SFR that drives this ratio to ~ 50 at redshifts less than 20. The effects of SNe as previously discussed increases the number of electrons by a factor of 3, but effective ionizations per UV photons is still quite low $\sim 1/10$.

7.4.3 Clumping Factor Evolution

Volume averaged recombination rates in an inhomogeneous IGM scale with the clumping factor $C = \langle \rho^2 \rangle / \langle \rho \rangle^2$, where the angled brackets denote volume averaged quantities. The recombination rate for hydrogen, e.g., is simply

$$\left(\frac{dn_{\text{HII}}}{dt} \right)_{\text{rec}} = C k_{\text{rec}} f_e \bar{\rho}_b (1+z)^3, \quad (7.4)$$

where k_{rec} is the case B recombination rate for hydrogen at $T \approx 10^4$ K. Both the increased recombinations in overdense regions and photon escape fractions lower than unity result in the high number of UV photons needed for one effective ionization that

we see in our simulations.

Figure 7.9 compares the clumping factor in the adiabatic, cooling only, star formation, and supernovae calculations. Since we resolve the local Jeans length by at least 4 cells in all simulations, the clumping factor is not underestimated, given our assumptions about gas cooling in each model. The RT and SN calculations capture the full evolution of the clumping factor since gas can fully condense by H_2 cooling in the pristine gas, accurately following the small-scale structure at low metallicities and high redshifts.

The clumping factor in the adiabatic case smoothly increases to ~ 40 at $z = 17$ from unity at $z > 30$ because of the increase in number density of halos with masses above the cosmological Jeans mass. The cooling run only deviates from the adiabatic case when the most massive halo can start cooling by $\text{Ly}\alpha$ cooling, and the center begins a free-fall collapse, which causes the rapid increase in C . The clumping factor in the star formation only simulations become larger than the other simulations as several halos start to condense by H_2 cooling. The clumping decreases as these central concentrations are disbanded by stellar radiation. The combination of collapsing halos and stellar radiation generates fluctuations in the clumping factor around twice the value in the adiabatic case. SN explosions disperse gas more effectively than radiative feedback alone in larger halos and can have a bigger impact on the clumping factor. At redshift 20, the three stars and their SNe energy in the most massive halo destroy the surrounding baryonic structures and reduce the clumping back to the values seen in non-radiative cases.

We show the clumping factor C_{ion} in ionized regions above $f_e > 10^{-3}$ in Figure 7.10. It fluctuates around and slightly below the values found in adiabatic simulations. When an H II is still confined within its parent halo, the ionized material is still at high densities that causes the spikes in C_{ion} . As the shock wave caused by the stellar radiation propagates into the IGM, baryon expulsion and photo-evaporation of small gas clumps in the H II regions cause C_{ion} to decrease. This repeats as star formation ensues and causes the fluctuations in C_{ion} .

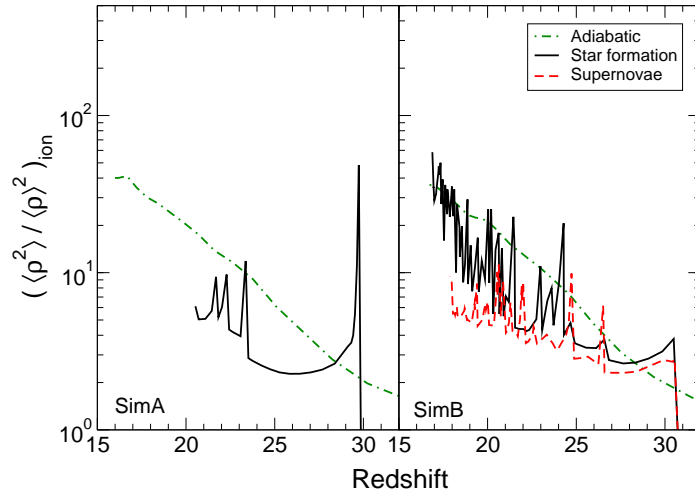


Fig. 7.10.— Clumping factor in ionized regions with $f_e > 10^{-3}$ for SimA (*left*) and SimB (*right*). The line styles are the same as in Figure 7.9.

7.4.4 Kinetic Energy Feedback

SN explosion energy and kinetic energy generated in D-type I-front play a key role in star formation in low-mass halos, which are easily affected due to their shallow potential well (e.g. Haehnelt, 1995; Bromm & Loeb, 2003; Whalen et al., 2004; Kitayama et al., 2004; Kitayama & Yoshida, 2005). The kinetic energy created by SNe is sufficient to expel the gas from these low-mass halos. For example, the binding energy of a $10^6 M_\odot$ halo is only 2.8×10^{50} erg at $z = 20$, which is two orders of magnitude smaller than a typical energy output of a pair instability SN (Heger & Woosley, 2002). For a $T_{\text{vir}} > 10^4$ K halo at the same redshift, it is 9.4×10^{52} erg. With our chosen stellar mass of $170 M_\odot$, it takes 3 – 4 SNe to overcome this potential energy.

The shock wave created by the D-type I-front travels at a velocity $v_s = 25 - 35$ km s^{-1} for density gradients (i.e. $\rho(r) \propto r^{-w}$) with slopes between 1.5 and 2.25 (Shu et al., 2002; Whalen et al., 2004; Kitayama et al., 2004). This velocity is the escape velocity for halos with masses greater than $3 \times 10^8 M_\odot$ at $z = 15$, which is an order of magnitude greater than the most massive halos studied here. However less massive halos can contain these I-fronts because pressure forces slow the I-front after the star dies.

Using the position of the shock wave when the star dies (eq. 7.6) and energy arguments, we can estimate the critical halo mass where the material in the D-type I-front can escape from the halo by comparing the binding energy E_b of the halo and kinetic energy in the shell. For most massive stars, the shock wave never reaches the final Strömngren radius,

$$R_{\text{str}} = 150 \left(\frac{\dot{N}_{\text{HI}}}{10^{50} \text{ph s}^{-1}} \right)^{1/3} \left(\frac{n_f}{1 \text{ cm}^{-3}} \right)^{-2/3} \text{ pc}, \quad (7.5)$$

before the star dies. Here \dot{N}_{HI} is the ionizing photon rate of the star, and n_f is the number density contained in this radius. After the lifetime of the star, the shock reaches a radius

$$R_s = 83 \left(\frac{v_s}{30 \text{ km s}^{-1}} \right) \left(\frac{t_\star}{2.7 \text{ Myr}} \right) \text{ pc}, \quad (7.6)$$

where t_\star is the stellar lifetime (see also Kitayama et al., 2004). We can neglect isolated, lower mass ($M \lesssim 30 M_\odot$) Pop III stars whose shock wave reaches R_{str} within its lifetime. In this case, the I-front stops at R_{str} , and the shock wave becomes a pressure wave that has no associated density contrast in the neutral medium (Shu, 1992). Thus we can safely ignore these stars in this estimate.

Assume that the source is embedded in a single isothermal sphere. The mass contained in the shell is

$$M_{\text{sw}} = \frac{(\Omega_b/\Omega_M) M_{\text{vir}} R_s}{r_{\text{vir}}} - V_s \rho_i \quad (7.7)$$

that is the mass enclosed in the radius R_s in an isothermal sphere, corrected for the warm, ionized medium behind the I-front. Here V_s is the volume contained in a sphere of radius R_s , and ρ_i is the gas density of the ionized medium, whose typical number density is 1 cm^{-3} for stellar feedback from a massive primordial star (Whalen et al., 2004; Kitayama et al., 2004; Yoshida et al., 2006a; Abel et al., 2007). For massive stars ($M_\star \gtrsim 30 M_\odot$), the mass of the central homogeneous medium is small (i.e. 10%) compared to the shell. We compensate for this interior mass by introducing the

fraction η , so the shell mass is simply

$$M_{\text{sw}} = \eta \frac{(\Omega_b/\Omega_M) M_{\text{vir}} r_s}{r_{\text{vir}}}. \quad (7.8)$$

For these outflows to escape from the halo, the kinetic energy contained in the shell must be larger than the binding energy, which is

$$\frac{1}{2} M_{\text{sw}} v_s^2 > \frac{GM_{\text{vir}}^2}{2r_{\text{vir}}}. \quad (7.9)$$

Using equations (7.6) and (7.8) in this condition, we obtain the maximum mass

$$\begin{aligned} M_{\text{max}} &\sim \frac{r_s v_s^2 \Omega_b}{G \Omega_M} \\ M_{\text{max}} &\sim 3.20 \times 10^6 \left(\frac{r_s}{100 \text{pc}} \right) \left(\frac{v_s}{30 \text{ km s}^{-1}} \right)^2 \\ &\quad \times \left(\frac{\eta}{0.9} \right) \left(\frac{\Omega_b/\Omega_M}{0.17} \right) M_{\odot} \end{aligned} \quad (7.10)$$

of a halo where the material in the shock wave becomes unbound, expelling the majority of the gas from the halo.

In Figure 7.11, we use the stellar lifetimes and ionizing luminosities from Schaerer (2002) to calculate the critical halo mass for outflows for stellar masses $5 - 500 M_{\odot}$ and for shock velocities of 20, 25, 30, and 35 km s^{-1} with $\eta = 0.9$. For stellar masses smaller than $30 M_{\odot}$, the D-type I-front reaches the final Strömgren sphere and cannot expel any material from the host. Hence they are not plotted in this figure. For the more massive stars, the star dies before the D-type I-front can reach the Strömgren radius, thus being limited by t_* . This maximum halo mass is in good agreement with our simulations as we see halos with masses greater than $5 \times 10^6 M_{\odot}$ retaining most of their gas in the star formation only cases. However in larger halos, stellar sources still generate champagne flows, but this material is still bound to the halo and returns in tens of million years.

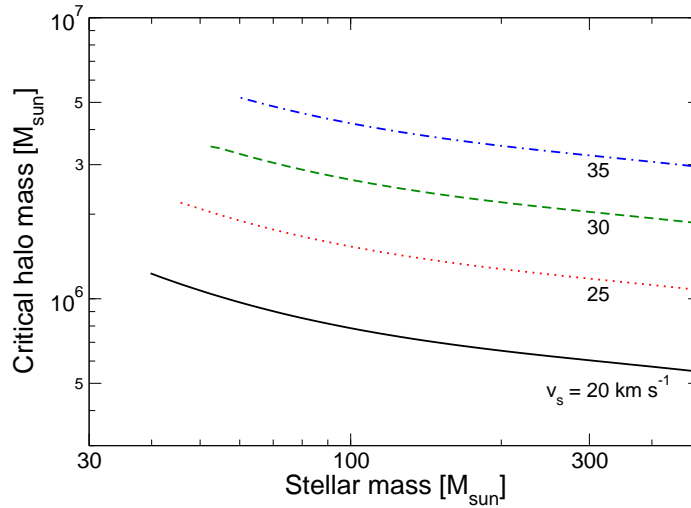


Fig. 7.11.— Maximum halo mass in which a D-type ionization front can create outflows as a function of primordial stellar mass for shock velocities v_s of 20, 25, 30, and 35 km s^{-1} . Here the fraction η of mass contained in the shell is 0.9.

7.4.5 Thermal Energy

Thermal feedback is yet another mechanism by which Pop III stars leave their imprint on the universe. The initial heating of the IGM will continue and intensify from higher SFRs at lower redshifts (e.g. Hernquist & Springel, 2003; Onken & Miralda-Escudé, 2004). It is possible to constrain the reionization history by comparing temperatures in the Ly α forest to different reionization scenarios (Hui & Haiman, 2003). Temperatures in the Ly α forest are approximately 20,000 K at $z = 3 - 5$ (Schaye et al., 2000; Zaldarriaga et al., 2001). Although our focus was not on redshifts below 15 due to the uncertainty of the transition to the first low-mass metal-enriched (Pop II) stars, we can utilize the thermal data in our radiation hydrodynamical simulations to infer the thermal history of the IGM at lower redshifts.

The excess energy from hydrogen ionizing photons over 13.6 eV photo-heat the gas in the H II region. The mean temperature within H II regions in our calculations is $\sim 30,000$ K. When the short lifetime of a Pop III star is over, the H II region cools mainly through Compton cooling off the cosmic microwave background. The same

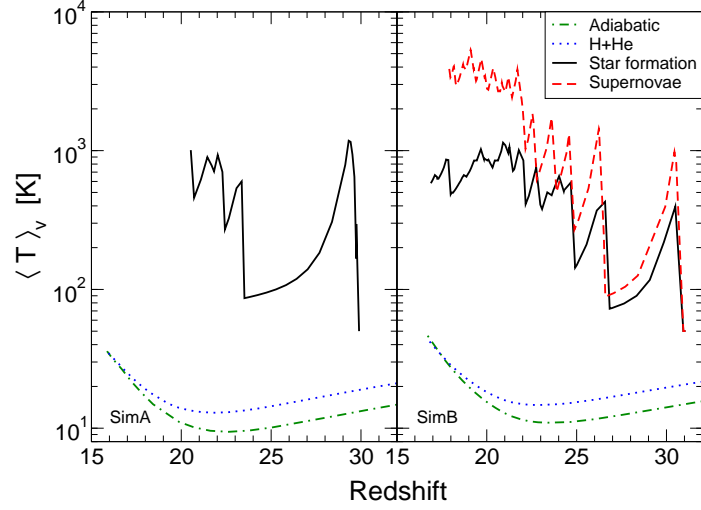


Fig. 7.12.— Evolution of the volume-averaged temperature in the inner 250 and 300 comoving kpc for Sim A (*left*) and Sim B (*right*), respectively. The simulations for the adiabatic (*green dot-dashed*), cooling only (*blue dotted*), star formation only (*black solid*), and supernovae (*red dashed*) simulations are plotted.

framework applies to SNe remnants as well. The timescale for Compton cooling is

$$t_C = 1.4 \times 10^7 \left(\frac{1+z}{20} \right)^{-4} f_e^{-1} \text{ yr.} \quad (7.11)$$

This process continues until the gas recombines, and Compton cooling is no longer efficient because of its dependence on electron fraction. Radiation preferentially propagates into the voids and leaves the adjacent filaments and its embedded halos virtually untouched. Hence we can restrict the importance of Compton cooling to the diffuse IGM since Compton cooling cools the gas to low temperatures without being impeded by recombinations that are proportional to n_e^2 . This causes the relic H II region to cool to temperatures down to 300 K. The temperature evolution in our radiative calculations agrees with the analytic models of relic H II (Oh & Haiman, 2003).

We plot the volume-averaged temperature $\langle T \rangle_v$ and mass-averaged temperature $\langle T \rangle_m$ in the volume where we allow star formation, i.e. the inner 250 (300) comoving

kpc, in Figures 7.12 and 7.13. The first star in the calculations raises the volume averaged temperatures to ~ 100 K. The mass-averaged temperatures are slightly higher at ~ 125 K since the star has heated a larger fraction of mass, its host halo, when compared to the volume of the H II region. The supernovae calculations are even higher due to the hot SN bubble that has an initial temperature of 10^8 K. The high initial temperature causes the mass-averaged temperature in the SN simulations to spike when SNe occur to several times higher than the RT simulations. Afterwards the remnant cools from Compton and adiabatic processes as it expands to temperatures similar to the RT simulations.

Because photo-heating is confined to the H II regions, the trends seen in average temperatures follows the same behavior as the ionization fraction with the exception of the spikes associated with SNe. In the RT simulations, the volume-averaged temperature rises gradually from 60 K to ~ 200 K from redshifts 25 to 15. The mass-averaged temperature increases more than $\langle T \rangle_v$ because of the photo-heating of the host halo and virial heating of the halos, which is the cause of the increase in the simulations without star formation. Without SNe, $\langle T \rangle_m$ is only up to two times the temperatures in the no star formation runs. Both $\langle T \rangle_v$ and $\langle T \rangle_m$ in the SN calculations exhibit a sharp transition to higher temperatures around 4000 K at $z = 21$, corresponding to the same transition to a more ionized state of $f_e = 0.75$.

The photo-heating is better represented by the average temperature $\langle T \rangle_v^{\text{ion}}$ in ionized regions, which is plotted in Figure 7.14b. The first few stars heat the gas up to 20,000 K that then cool by adiabatic expansion and Compton cooling. When star formation occurs in several halos and the ionized filling fraction increases, the average temperature fluctuates around 4000 K because there are both active and relic H II in the simulation, causing $\langle T \rangle_v^{\text{ion}}$ to be lower than 20,000 K that happens during the formation of the first few H II regions. The increased temperatures cause the photo-evaporated and Jeans smoothing of the gas in the relic H II regions. We discuss these effects in the next section.

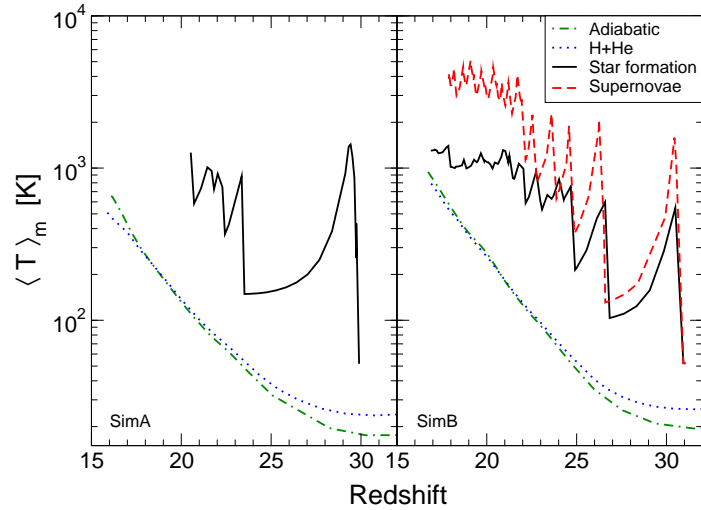


Fig. 7.13.— Same as Figure 7.12 but for the mass-averaged temperature.

7.5 Discussion

We have studied the details of massive metal-free star formation and its role in the start of cosmological reionization. We have treated star formation and radiation in a self-consistent manner, allowing for an accurate investigation of the evolution of cosmic structure under the influence of early Pop III stars. Stellar radiation from these stars provides thermal, dynamical, and ionizing feedback to the host halos and IGM. Although Pop III stars do not provide the majority of ionizing photons needed for cosmological reionization, they play a key role in the early universe because early galaxies that form in these relic H II regions are significantly affected by Pop III feedback. Hence it is important to consider primordial stellar feedback while studying early galaxy formation. In this section, we compare our results to previous numerical simulations and semi-analytic models of reionization and then discuss any potential caveats of our methods and possible future directions of this line of research.

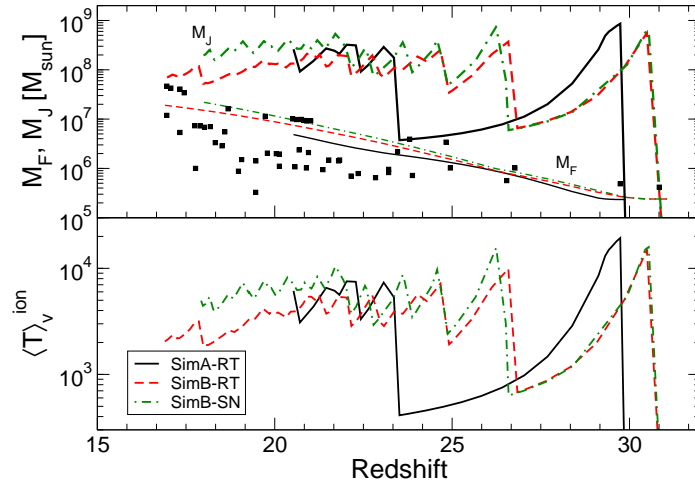


Fig. 7.14.— (a) The Jeans mass M_J and filtering mass M_F that can form bound objects. The squares denote the total mass of star forming halos in all three simulations. (b) Volume-averaged temperature in the ionized regions ($f_e > 10^{-3}$) that is used in computing the filtering mass.

7.5.1 Comparison to Previous Models

Filtering Mass

One source of negative feedback is the suppression of gas accretion into potential wells when the IGM is preheated. The lower limit of the mass of a star forming halo is the Jeans filtering mass

$$M_F^{2/3}(a) = \frac{3}{a} \int_0^a da' M_J^{2/3}(a') \left[1 - \left(\frac{a'}{a} \right) \right], \quad (7.12)$$

where a and M_J are the scale factor and time dependent Jeans mass in the H II region (Gnedin & Hui, 1998; Gnedin, 2000b). Additionally, the virial shocks are weakened if the accreting gas is preheated and will reduce the collisional ionization in halos with $T_{\text{vir}} \gtrsim 10^4$ K. To illustrate the effect of Jeans smoothing, we take the large H II region of SimB-SN because it has the largest ionized filling fraction, which is constantly being heated after $z = 21$. Temperatures in this region fluctuates between 1,000 K and 30,000 K, depending on the proximity of the currently living stars. In Figure

7.14, we show the volume-averaged temperature and the resulting filtering mass of regions with an ionization fraction greater than 10^{-3} along with the total mass of star forming halos.

Gnedin (2000b) found the minimum mass of a star forming halo is better described by M_F instead of M_J . Our simulations are in excellent agreement for halos that are experiencing star formation after reincorporation of their previously expelled gas. The filtering mass is the appropriate choice for a minimum mass in this case as the halo forms from preheated gas. However for halos that have already assembled before they become embedded in a relic H II region, the appropriate minimum mass M_{\min} is one that is regulated by the LW background (Machacek et al., 2001; Wise & Abel, 2005). This is evident in the multitude of star forming halos below M_F . With the exception of star formation induced by SN blast waves or I-fronts, this verifies the justification of using M_{\min} and M_F for Pop III and galaxy formation, respectively, as a criterion for star forming halos in semi-analytic models.

Star Formation Efficiency

Semi-analytic models rely on a star formation efficiency f_* , which is the fraction of collapsed gas that forms stars, to calculate quantities such as emissivities, chemical enrichment, and IGM temperatures. Low-mass halos that form a central star have $f_* \sim 10^{-3}$ whose value originates from a single $100 M_\odot$ star forming in a dark matter halo of mass $10^6 M_\odot$ (Abel et al., 2002; Bromm et al., 2002; Yoshida et al., 2006b). Pop II star forming halos are usually calibrated with star formation efficiencies from local dwarf and high-redshift starburst galaxies and are usually on the order of a few percent (e.g. Taylor et al., 1999; Gnedin, 2000).

This leads to the question: how efficient is star formation in these high-redshift halos while explicitly considering feedback? This is especially important when halos start to form multiple massive stars and when metallicities are not sufficient to induce Pop II star formation. The critical metallicity for a transition to Pop II is still unclear. Recently, Jappsen et al. (2007) showed that metal line cooling is dynamically unimportant until metallicities of $10^{-2} Z_\odot$. On the other hand, dust that is produced in SNe can generate efficient cooling down in gas with $10^{-6} Z_\odot$ (Schneider et al.,

2006). If the progenitors of the more massive halos did not result in a pair-instability SN, massive star formation can continue until it becomes sufficiently enriched. Hence our simulations can probe the efficiency of this scenario of massive metal-free star formation.

We calculate f_\star with the ratio of the sum of the stellar masses to the total gas mass of unique star-forming halos. For example at the final redshift of 15.9 in SimA-RT, the most massive halo and its progenitors had hosted 14 stars and the gas mass of this halo is $2.6 \times 10^6 M_\odot$, which results in $f_\star = 5.4 \times 10^{-4}$ for this particular halo. Expanding this quantity to all star forming halos, $f_\star/10^{-4} = 5.0, 4.1, 6.3$ for SimA-RT, SimB-RT, and SimB-SN, respectively. Our efficiencies are smaller than the isolated Pop III case because halos cannot form any stars after the first star expels the gas, and 30 – 60 million years must pass until stars can form again when the gas is reincorporated into the halo. f_\star is larger in the SN case because more stars form in lower mass halos. There are two reasons for this occurring. First, the positive feedback happens when SN blast waves induces star formation in low-mass satellite halos. Second, the local LW radiation field originating from the most massive halos has been reduced since star formation is suppressed from the SNe kinetic energy feedback.

A better comparison can be made by using the same techniques used in semi-analytic models. Most models calculate the SFR by taking the product of f_\star and the collapsed mass fraction ψ in halos above some minimum mass. We can calculate f_\star by taking the same approach but the inverse: determine f_\star from the SFRs in our calculations and by assuming a critical star-forming halo mass. We take the cumulative SFR ρ_\star^{tot} (Fig. 7.1) to calculate

$$f_\star(z) = \frac{\rho_\star^{\text{tot}}(z)}{\psi(z, M_{\text{min}}) \rho_b}, \quad (7.13)$$

where ρ_b is the comoving mean gas density. As a simple example of a fixed minimum mass of a star forming halo, the collapsed mass fraction $\psi = 0.07$ in $10^6 M_\odot$ halos at redshift 15, using WMAP first year parameters and Press-Schechter formalism (Press & Schechter, 1974; Sheth & Tormen, 2002). This results in $f_\star = 1.5 \times 10^{-3}$ and 2.6×10^{-3} for the RT and SN calculations, respectively. The difference between the

two fractions merely comes from the different choices of primordial stellar masses. The efficiencies are lower than the explicitly calculated values because of our fiducial choice of the minimum mass of a star forming halo, which should be $\sim 3 \times 10^5 M_\odot$ when the UV background is insignificant and increasing with redshift by an order of magnitude (Machacek et al., 2001; Wise & Abel, 2005). It should be noted that this approach is sensitive to the choice of minimum mass, arising from the exponential nature of the collapsed mass fraction of high- σ peaks in Press-Schechter formalism.

By regarding the feedback created by Pop III stars and associated complexities during the assembly of these halos, the f_* values of $\sim 5 \times 10^{-4}$ that are explicitly determined from our radiation hydrodynamical simulations provide a more accurate estimate on the star formation efficiencies.

Intermittent & Anisotropic Sources

Our treatment of star formation and feedback produces intermittent star formation, especially in low-mass halos. If one does not account for this, star formation rates might be overestimated in this phase of star formation. Kinetic energy feedback is the main cause of this behavior. As discussed in sections 7.3.2 and 7.4.4, shock waves created by D-type I-fronts and SN explosions expel most of the gas in halos with masses $\lesssim 10^7 M_\odot$. A period of quiescence follows these instances of star formation. Then stars are able to form after enough material has accreted back into the halo. Only when the halo becomes massive enough to retain most of the outflows and cool efficiently through Ly α and H $_2$ radiative processes does star formation becomes more regular with successive stars forming.

The central gas structures in the host halo are usually anisotropic as it is acquiring material through smooth IGM accretion and mergers. At scales smaller than 10 pc, the most optically thick regions produce shadows where the gas radially behind the dense clump is not photo-ionized or photo-heated by the source. This produces cometary and so-called elephant trunk structures that are also seen in local star forming regions and have been discussed in detail since Pottasch (1958). At a larger distance, the surrounding cosmic structure is composed of intersecting or adjacent filaments and satellite halos that break spherical symmetry. The filaments and nearby

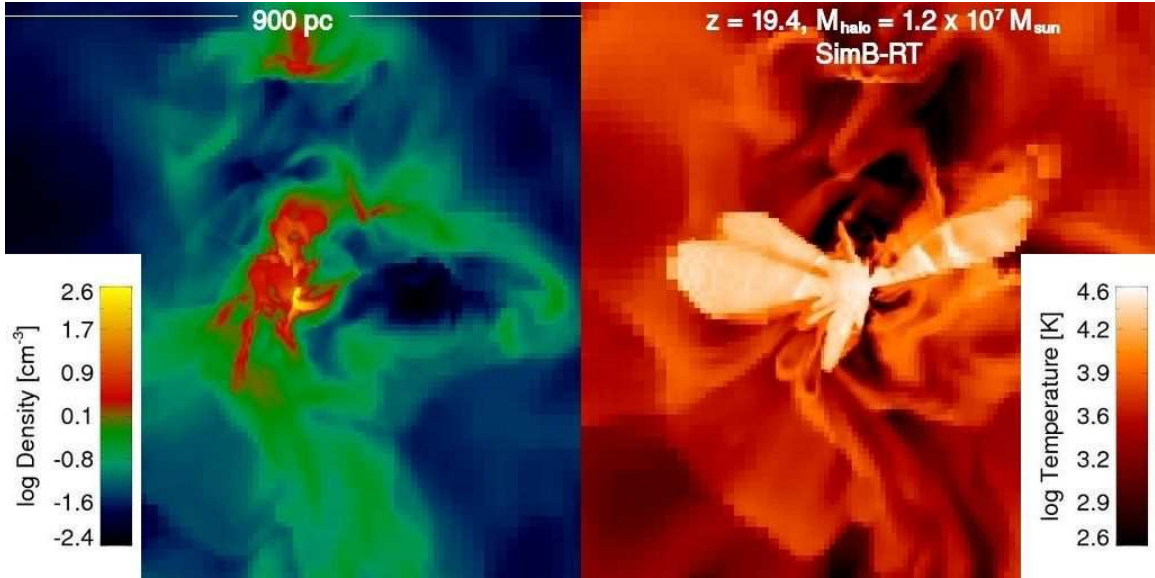


Fig. 7.15.— Density (*left*) and temperature (*right*) slices of an anisotropic H II region in the most massive halo of SimB-RT. The star has lived for 2.5 Myr out of its 2.7 Myr lifetime. The field of view is 900 proper parsecs.

halos are optically thick and remain cool and thus the density structures are largely unchanged. The entropy of dense regions is not increased by stellar radiation and will feel little negative feedback from an entropy floor that only exists in the ionized IGM (cf. Oh & Haiman, 2003). Ray-tracing allows for accurate tracking of I-fronts in this inhomogeneous medium. Radiation propagates through the least optically thick path and generates champagne flows that have been studied extensively in the context of present day star formation (e.g. Franco et al., 1990; Churchwell, 2002; Shu et al., 2002; Arthur & Hoare, 2006). In the context of massive primordial stars, these champagne flows spread into the voids and are impeded by the inflowing filaments. The resulting H II regions have “butterfly” morphologies (Abel et al., 1999, 2007; Alvarez et al., 2006a; Mellema et al., 2006; Yoshida et al., 2006a). We also point out that sources embedded in relic H II largely maintain or increase the ionization fraction, depending on the overdensities in the nearby IGM. Here the already low optical depth of the recently ionized medium (within a recombination time) allows the radiation to travel to greater distances than a halo embedded in a completely neutral IGM. The H II

regions become increasingly anisotropic in higher mass halos. We show an example of an H II region near the end of the star’s lifetime in a dark matter halo with mass $1.2 \times 10^7 M_\odot$ in Figure 7.15.

7.5.2 Potential Caveats and Future Directions

Although we have simulated the first generations of stars with radiation hydrodynamic simulations, our methods have neglected some potentially important processes and made an assumption about the Pop III stellar masses.

One clear shortcoming of our simulations is the small volume and limited statistics of the objects studied here. However, it was our intention to focus on the effects of Pop III star formation on cosmological reionization and on the formation of an early dwarf galaxy instead of global statistics. We have verified even in a $3\text{-}\sigma$ peak that Pop III stars cannot fully reionize the universe, which verified previous conclusions that low-luminosity galaxies provide the majority of ionizing photons. Furthermore, it is beneficial to study Pop III stellar feedback because it regulates the nature of star formation in these galaxies that form from pre-heated material. Further radiation hydrodynamics simulations of primordial star and galaxy formation with larger volumes while still resolving the first star forming halos of mass $\sim 3 \times 10^5 M_\odot$ will improve the statistics of early star formation, especially in more typical overdensities, i.e. $1\text{-}\sigma$ peaks that may survive to become dwarf spheroidal galaxies at $z = 0$.

In this work, we treated the LW radiation field as optically thin, but in reality, H_2 produces a non-zero optical depth above column densities of 10^{14} cm^{-2} (Draine & Bertoldi, 1996). Conversely, Doppler shifts of the LW lines arising from large velocity anisotropies and gradient may render H_2 self-shielding unimportant up to column densities of $10^{20} - 10^{21} \text{ cm}^{-2}$ (Glover & Brand, 2001). If self-shielding is important, it will lead to increased star formation in low-mass halos even when a nearby source is shining. Moreover, H_2 production can also be catalyzed ahead of I-fronts (Ricotti et al., 2001; Ahn & Shapiro, 2007). In these halos, LW radiation will be absorbed before it can dissociate the central H_2 core. On the same topic, we neglect any type of soft UV or LW background that is created by sources that are cosmologically nearby

($\Delta z/z \sim 0.1$). A soft UV background either creates positive or negative feedback, depending on its strength (Mesinger et al., 2006), and a LW background increases the minimum halo mass of a star-forming halo (Machacek et al., 2001; Yoshida et al., 2003; Wise & Abel, 2007b). However in our calculations, the lack of self-shielding, which suppresses star formation in low-mass halos, and the neglect of a LW background, which allows star formation in these halos, virtually counterbalance each other. Hence we do not expect any significant deviations in the SFRs and reionization history if we treat these processes explicitly.

To address the incident radiation and the resulting UV background from more rare density fluctuations outside of our simulation volume, it will be useful to bridge the gap between the start of reionization on Mpc scales to larger scale (10 – 100 Mpc) simulations of reionization, such as the work of Sokasian et al. (2003), Iliev et al. (2006), Zahn et al. (2007), and Kohler et al. (2007). Radiation characteristics from a volume that has similar overdensities as our Mpc-scale simulations can be sampled from such larger volumes to create a radiation background that inflicts the structures in our Mpc scale simulations. Inversely, perhaps the small-scale evolution of the clumping factor, filtering mass, and average temperature and ionization states can be used to create an accurate subgrid model in large volume reionization simulations.

Another potential caveat is the continued use of primordial gas chemistry in metal enriched regions in the SN runs. As discussed in §7.5.1, metal line cooling may be dynamically unimportant until metallicities of $10^{-2}Z_{\odot}$, but dust cooling could be important as low as $10^{-6}Z_{\odot}$. Our simulations with SNe give excellent initial conditions to self-consistently treat the transition to low-mass star formation. In future work, we plan to introduce metal-line and dust cooling models (e.g. from Glover & Jappsen, 2007) to study this transition.

The one main assumption about Pop III stars in our calculations is the fixed, user-defined stellar mass. The initial mass function (IMF) of these stars is largely unknown, therefore we did not want to introduce an uncertainty by choosing a fiducial IMF. It is possible to calculate a rough estimate of the stellar mass by comparing the accretion rates and Kelvin-Helmholtz time of the contracting molecular cloud (Abel et al., 2002; O’Shea et al., 2005). Protostellar models of primordial stars have also

shown that the zero-age main sequence (ZAMS) is reached at $100 M_{\odot}$ for typical accretion histories after the star halts its adiabatic contraction (Omukai & Palla, 2003; Yoshida et al., 2006b). Based on accretion histories of star forming halos, one can estimate the ZAMS stellar mass for each halo and create a more self-consistent and ab initio treatment of Pop III star formation and feedback.

7.6 Summary

We conducted three radiation hydrodynamical, adaptive mesh refinement simulations that supplement our previous cosmological simulations that focused on the hydrodynamics and cooling during early galaxy formation. These new simulations concentrated on the formation and feedback of massive, metal-free stars. We used adaptive ray tracing to accurately track the resulting H II regions and followed the evolution of the photo-ionized and photo-heated IGM. We also explored the details of early star formation in these simulations. Theories of early galaxy formation and reionization and large scale reionization simulations can benefit from the useful quantities and characteristics of the high redshift universe, such as SFR and IGM temperatures and ionization states, calculated in our simulations. The key results from this work are listed below.

1. SFRs increase from 4×10^{-4} at redshift 30 to $6 \times 10^{-3} M_{\odot} \text{ yr}^{-1} \text{ Mpc}^{-3}$ at redshift 20. Afterwards the SFR begins to have a bursting nature in halos more massive than $10^7 M_{\odot}$ and fluctuates around $10^{-2} M_{\odot} \text{ yr}^{-1} \text{ Mpc}^{-3}$. These rates are larger than the ones calculated in Hernquist & Springel (2003) because our simulation volume samples a highly biased region that contains a $3\text{-}\sigma$ density fluctuation. The associated emissivity from these stars increase from 1 to ~ 100 ionizing photons per baryon per Hubble time between redshifts 15 and 30.

2. In order to provide a comparison to semi-analytic models, we calculate the star formation efficiency to be $\sim 5 \times 10^{-4}$ averaged over all redshifts and the simulation volume. For Pop III star formation, this is a factor of two lower than stars that are not affected by feedback (Abel et al., 2002; Bromm et al., 2002; Yoshida et al., 2006b; O’Shea & Norman, 2007).

3. Shock waves created by D-type I-fronts expel most of the gas in the host halos below $\sim 5 \times 10^6 M_\odot$. Above this mass, significant outflows that are still bound to the halo are generated. This feedback creates a dynamical picture of early structure formation, where star formation is suppressed in halos because of this baryon depletion, which is more effective than UV heating or the radiative dissociation of H_2 .

4. We see two instances of induced star formation in low-mass ($\sim 5 \times 10^5 M_\odot$) satellite halos that recently had a SN blastwave overtake it. Central temperatures in these halos are half the central temperatures of star forming halos with similar masses.

5. Although the volume-averaged emissivities are high, only 1 in 50 UV photons result in a sustainable ionization in the RT simulations. Interestingly, the SN calculations contain a sharp transition where the volume filling fraction increases by a factor of three in a mere 25 million years. Multiple star formation in a single halo and their SNe increase the photon escape fraction to nearly unity after the first star dies, which leads to the dramatic increase in ionized IGM. In this simulation, the effective number of ionizations per UV photon is 1 in 10, which is still small but significantly higher than its star formation only counterpart.

6. Our simulations that include star formation and H_2 formation capture the entire evolution of the clumping factor that is used in semi-analytic models to calculate the effective enhancement of recombinations in the IGM. We showed that clumping factors in the ionized medium fluctuate around the values found in adiabatic simulations. They evolve from unity at high redshifts and steadily increase to ~ 100 at redshift 15. Dynamical stellar feedback causes the fluctuations of the clumping factor.

7. We calculated the Jeans filtering mass with the volume-averaged temperature only in fully and partially ionized regions, which yields a better estimate than the temperature averaged over both ionized and neutral regions. The filtering mass depends on the thermal history of the IGM, which mainly cools through Compton cooling. It increases by two orders of magnitude to $\sim 3 \times 10^7 M_\odot$ at $z \sim 15$. It describes the minimum mass a halo requires to collapse after hosting a Pop III star. For halos forming their first star, the minimum mass found in Machacek et al. (2001) is appropriate, which is regulated by a LW background.

Pop III stellar feedback plays a key role in early star formation and the beginning of cosmological reionization. The shallow potential wells of their host halos only amplify their radiative feedback. Our understanding of the formation of the oldest galaxies and the characteristics of isolated dwarf galaxies may benefit from including the earliest stars and their feedback in galaxy formation models. Although these massive stars only partially reionized the universe, their feedback on the IGM and galaxies is crucial to include since it affects the characteristics of low-mass galaxies that are primarily responsible for cosmological reionization. Harnessing observational clues about reionization, observations of local dwarf spheroidal galaxies, and numerical simulations that accurately handle star formation and feedback may provide great insight on the formation of the first galaxies, their properties, and how they completed cosmological reionization.

Chapter 8

Conclusions and Future Work

The first stars in the universe form in isolation in their parent dark matter halos with masses $\sim 10^6 M_\odot$, starting as early as 100 million years after the Big Bang (Tegmark et al., 1997; Abel et al., 2002; Yoshida et al., 2006b). Because big bang nucleosynthesis does not create anything heavier than lithium, the first stars are mainly composed of hydrogen and helium. The most efficient coolant in this pristine gas is H_2 , forming in the gas-phase. Because of the differences in radiative cooling of metal-free gas, the first stars are approximately 100 times more massive than the Sun (Abel et al., 2002) and have a large impact on their surroundings and future structure formation.

The purpose of this thesis has been to assess this impact on early galaxies. We have methodically approached this problem by introducing each piece of the puzzle progressively. In general, this allows one to judge the relevance of each physical process; in our case, we have learnt about the importance of turbulence, radiative feedback, H_2 formation, and Pop III stars in the early universe and how they affect the first galaxies. Low-luminosity galaxies have been known to be responsible to reionize the universe (e.g. Shapiro, 1986). Thus their properties and formation have been of great interest for the past few decades. Only in the last decade has it been possible to study these galaxies in numerical simulations with adequate resolution. The cosmological simulations of Abel et al. (2000, 2002) first resolved the formation of the first protostar with AMR calculations that covered 10^{12} orders of magnitude in length scale. Star formation and feedback in galaxies before reionization ($z > 6$) have

been explored by Gnedin & Ostriker (1997), Ricotti et al. (2002b), and many others. Furthermore, some have argued that H_2 cooling is unimportant (Oh & Haiman, 2002; Ciardi & Ferrara, 2005; Haiman & Bryan, 2006) in early structure formation as it can be dissociated from large distances and have thus ignored the effects of primordial stellar feedback. This thesis attempts to bridge the gap in between these calculations of the first stars and early galaxies and how the isolated mode of primordial star formation transitions to dwarf galaxy formation. Additionally, we have explored the validity of neglecting H_2 formation and the ensuing scenario of galaxy formation without H_2 chemistry, which has been frequently used in galaxy formation models in the early universe.

8.1 Supernovae from Primordial Stars

We developed a semi-analytical method that calculates the abundances of primordial stars and the observed SNe rates. This method uses results from AMR simulations that determines the minimum halo mass of an object that can host a cool, dense core, which then forms a Pop III star (Machacek et al., 2001). We find that star formation in early galaxies contribute the most to cosmological reionization, which is in agreement with other studies (Cen, 2003a; Somerville & Livio, 2003; Ciardi et al., 2003). The main conclusions of this study are:

- Radiation from star formation in protogalaxies suppresses primordial star formation. We expect ~ 0.34 primordial SNe per square degree per year. These rates can vary from 0.1 to $>1.5 \text{ deg}^{-2} \text{ yr}^{-1}$ depending on the choice of primordial stellar mass and protogalaxy parameters while still constrained by WMAP results. The peak of SNe rates occurs earlier with increasing primordial stellar masses. These results are upper limits since the rate of visible primordial SNe depends on the IMF because only a fraction will lie in the pair instability SNe mass range. The other massive primordial stars might result in jet-driven SNe or long duration GRBs.
- Stellar metal abundances and star formation rates in local dwarf galaxies aid

in estimating the protogalaxy properties. Our best models find that 4% of the gas form stars and 5% of their radiation escapes into and reionizes the IGM.

- Primordial stars enrich the IGM to a maximum volume-averaged $[\text{Fe}/\text{H}] \simeq -4.1$ if the IMF is skewed toward the pair-instability mass range. A proper IMF will lessen this metallicity since only a fraction of stars will exist in this mass range.
- The entire error bar in the first year WMAP measurement of the optical depth to electron scattering can be explained by a higher/lower star formation efficiency and photon escape fraction. Massive primordial stars provides $\sim 10\%$ of the necessary ionizing photons to achieve cosmological reionization. No exotic processes or objects are necessary.
- Only the upper mass range of pair-instability SNe will be observable by JWST since the low mass counterparts do not produce enough ^{56}Ni to be very luminous.

8.2 Galaxy Formation without Molecular Hydrogen

Our first cosmological simulations in this thesis involved the scenario of galaxy formation without H_2 cooling. The first objects to form have a virial temperature of 10^4 K, which translates to $10^8 M_\odot$ at redshift 10 (Rees & Ostriker, 1977). Previous works concluded that the angular momentum acquired from tidal torques induces disc formation in the initial collapse of the gas cloud (Fall & Efstathiou, 1980; Mo et al., 1998; Begelman et al., 2006). We investigate this scenario with AMR simulations that first focus on the virialization of such objects and then the central gaseous collapse. Our main results are as follows:

- Baryons cannot virialize through heating alone but must gain kinetic energy that manifests in a faster bulk inflow and, in the case of efficient gas cooling, supersonic turbulent motions up to Mach numbers of three. We expect turbulence in larger galaxies, up to $10^{12} M_\odot$, to be even more supersonic.

- Baryonic velocity distributions are Maxwellian, which shows violent relaxation occurs for gas as well as dark matter. Turbulent velocities exceed typical rotational speeds, and these halos are only poorly modeled as solid body rotators.
- Turbulence generated during virialization mixes angular momentum so that it redistributes to a radially increasing function. This allows the gas with the lowest specific angular momentum to infall and form a $\sim 10^5 M_\odot$ central dense object within the central five parsecs. It forms before any multiple fragmentation occurs in the global disc.
- The final characteristics of the central object depend on the merger history of the parent halo because these mergers influence the amount of turbulence and morphologies in the halo.
- Our simulations of the central collapse highlight the relevance of secular bar-like instabilities in galaxy formation, as well as star formation. Similar bar structures are witnessed in primordial star formation simulations. These structures transport angular momentum outwards, so the collapse can continue. Smaller scale bars form within the larger bars, which shows the “bars within bars” scenario is also applicable to a gaseous collapse. We follow the collapse to length scales smaller than a solar radius and show that it follows a self-similar collapse with $\rho \propto r^{-12/5}$.

However, we do not advocate that these objects form in this way because we have neglected H_2 cooling and primordial stellar feedback. We focused next on the key role of H_2 cooling in early galaxy formation.

8.3 Importance of Molecular Hydrogen

We conducted a suite of fourteen simulations that focused on the importance of H_2 cooling with various degrees of negative feedback. Our work is an extension of Machacek et al. (2001), who showed that a LW radiation background only increases

the minimum mass a halo must obtain before forming stars but never fully suppressing primordial star formation. We made the following conclusions in these calculations.

- Our simulations with an UVB of $F_{\text{LW}} = (0, 10^{-22}, 10^{-21})$ agree with previous results of Machacek et al. (2001). Above $F_{\text{LW}} = 10^{-21}$, it had been argued that a LW background would inhibit any H_2 formation until the halo could cool through atomic transitions. We showed that central shocks provide sufficient free electrons from collisional ionization (Shapiro & Kang, 1987) to drive H_2 formation faster than dissociation rates even in a $F_{\text{LW}} = 10^{-20}$ background.
- We investigated at what halo mass collisional ionization becomes conducive for H_2 formation. This occurs at a virial temperature ~ 4000 K. Here we remove all residual free electrons from recombination, in which H_2 formation can only occur once collisional ionizations induce H_2 cooling.
- Recent major mergers above this mass scale create complex cooling structures, unlike the non-fragmented central cores in smaller halos.
- Even our most extreme assumptions of a large radiation background ($F_{\text{LW}} = 10^{-20}$) and no residual free electrons cannot defeat the importance of H_2 cooling in the early universe.

Molecular hydrogen cooling triggers collapses in halos with virial temperatures well below 10^4 K. This increases the mass fraction contained in these halos by three times at redshift 20 and the abundance of high-redshift star forming halos by an order of magnitude! This chapter has strengthened the results of Machacek et al. (2001) that H_2 cooling plays a key role in high-redshift structure formation.

8.4 Primordial Stellar Feedback and the First Galaxies

The last iteration of the simulations presented in this thesis include accurate radiative transfer, using adaptive ray tracing (Abel & Wandelt, 2002). We include self-consistent star formation and feedback in our simulations and use the same initial

conditions as before but only including these additional processes. We also track the SNe ejecta in one simulation and the propagation of the first metals in the universe. We find that primordial stars have a large impact on future galaxy formation and conclude with the following key points:

- Dynamical feedback from Pop III stars expel nearly all of the baryons from low-mass host halos. The baryon fractions in star forming halos never fully recover even when it reaches a virial temperature of 10^4 K. The baryon fraction is reduced as low as ~ 0.05 with SNe feedback, three times lower than the cases without stellar feedback.
- The expelled gas gains angular momentum by tidal torques as it exists at large radii. When it is reincorporated into the halo, it increases the spin parameter by a factor of 2–5 without SNe and up to 10 with SNe.
- Radiative and SNe feedback produces a complex, multi-phase interstellar medium that resembles the conditions in larger galaxies. It is clear that the first and earliest galaxies are complex entities, contrary to their generally assumed simplicity due to their low masses.
- Pair-instability SNe preferentially enrich the IGM to a metallicity an order of magnitude higher than the surrounding halos and filaments.
- Once a SN explosion cannot totally disrupt its host halo, the mean metallicity fluctuates around a mean value as there may be a balance between SN outflows, cold inflows, and contained SN ejecta.

8.5 Starting Cosmological Reionization

We then addressed the impact of Pop III stellar radiation on cosmological reionization. Previous studies have shown that low-luminosity galaxies are mainly responsible for this, but the first stars must have at least started reionization. Our main conclusions about reionization by Pop III stars are listed below.

- The comoving star formation rates (SFR) increase from 4×10^{-4} at redshift 30 to $6 \times 10^{-3} M_{\odot} \text{ yr}^{-1} \text{ Mpc}^{-3}$ at redshift 20. When halos become more massive than $10^7 M_{\odot}$, stars form in a more bursting nature, where the SFR fluctuates around $10^{-2} M_{\odot} \text{ yr}^{-1} \text{ Mpc}^{-3}$. These rates are larger than Hernquist & Springel (2003) because our simulation volume samples a highly biased region that contains a 3σ density fluctuation.
- In order to provide a comparison to semi-analytic models, we calculate the star formation efficiency to be $\sim 5 \times 10^{-4}$ averaged over all redshifts and the simulation volume. For Pop III star formation, this is a factor of two lower than stars that are not affected by feedback.
- We see two instances of induced star formation in low-mass ($\sim 5 \times 10^5 M_{\odot}$) satellite halos that recently had a SN blastwave overtake it. Central temperatures in these halos are half the central temperatures of star forming halos with similar masses.
- Only 1 in 50 UV photons result in a sustainable ionization in our simulations without SNe. This ratio interestingly increases to 1 in 10 when we consider SNe. Here multiple star formation and their SNe increase the photon escape fraction to nearly unity after the first star dies, which allows later stars to more effectively ionize the IGM.
- We showed that the Jeans filtering mass (Gnedin & Hui, 1998) is in excellent agreement with the star forming halos that are forming from reincorporated gas that was previously expelled by stellar and SNe feedback. This increases by two orders of magnitude to $\sim 3 \times 10^7 M_{\odot}$ at redshift 15. For halos forming their first star, the minimum mass found in Machacek et al. (2001) is appropriate.

8.6 Future Work

We have included an accurate treatment of the formation and feedback of the first stars in the universe; however, there are still several important processes that we

have neglected and will include in future studies. In this thesis, we have treated the H_2 dissociating radiation as optically thin, but in reality, H_2 produces a non-zero optical depth above column densities above 10^{14} cm^{-2} (Draine & Bertoldi, 1996). Currently it is computationally prohibitive to ray-trace optically thin radiation, even with adaptive techniques, in cosmological simulations. This will undoubtedly improve as computational power relentlessly increases. However, this does not preclude us from devising an ingenious scheme to treat small- and large-scale radiation scales accurately and efficiently. This will allow the study of many radiation sources in a cosmological or galactic setting. Perhaps this new method will be abstractly comparable to the adaptive P^3M algorithm that efficiently computes the gravitational field at all length scales.

Besides considering larger volumes with the same resolution, it will be useful to connect our simulations on Mpc-scales to larger volume simulations (10 – 100 Mpc) that focus on cosmological reionization. The properties of the radiation field in large-scale calculations can be sampled to a radiation background in our simulations. One must ensure that the sampled region in the large-scale calculations has similar overdensities as the Mpc-scale ones. We can also regard the inverse process of composing an accurate sub-grid model with the clumping factor, filtering mass, and average temperatures from our simulations to reionization simulations.

Another necessary improvement to our simulations is the inclusion of metal-line and dust cooling. We already have the appropriate “initial conditions” for this as we track the heavy elements from SNe of massive, metal-free stars. Perhaps it will be possible to follow the transition from a top-heavy IMF of Pop III to a more regular Salpeter IMF, associated with metal-enriched Pop II stars. This requires the introduction of metal-enriched cooling models, such as the ones described in Glover & Jappsen (2007) and Smith & Sigurdsson (2007).

We note one last possible improvement in our simulations of removing the assumption of a fixed Pop III stellar mass. We can estimate the stellar mass from the accretion rates and the Kelvin-Helmholtz time (Abel et al., 2002; O’Shea et al., 2005). Alternatively, we could follow the collapse to stellar scales and include protostellar models to calculate where its radiation effectively suppresses further accretion, thus

giving an accurate estimate of the stellar mass.

Even after centuries of development, there are still many unanswered questions in galaxy formation. In this thesis, we have demonstrated the importance of H_2 cooling and primordial star formation and feedback in early galaxy formation. Models of the first galaxies are necessary to interpret future observations of the earliest galaxies that should be available within the next decade. With the observations in hand, both theorists and observers will benefit from the wealth of knowledge contained in these data and their comparisons to accurate models of early galaxy formation.

Bibliography

- Aarseth, S. J. 1963, MNRAS, 126, 223
- Abel, T., Bryan, G. L., & Norman, M. L. 2000, ApJ, 540, 39
- Abel T., Bryan G. L., & Norman M. L., 2002, Science, 295, 93
- Abel, T. & Wandelt, B. D. 2002, MNRAS, 330, L53
- Abel, T., Wise, J. H., & Bryan, G. L. 2007, ApJ, 659, L87
- Abel, T., Anninos, P., Zhang, Y., & Norman, M. L. 1997, New Astronomy, 2, 181
- Abel, T., Anninos, P., Norman, M. L., & Zhang, Y. 1998, ApJ, 508, 518
- Abel, T., Norman, M. L., & Madau, P. 1999, ApJ, 523, 66
- Ahn, K., & Shapiro, P. R. 2007, MNRAS, 375, 881
- Aitken, R. G. 1906, PASP, 18, 111
- Alexander, D. M., et al. 2003, AJ, 126, 539
- Alexander, S. 1852, AJ, 2, 95
- Alpher, R. A., Bethe, H., & Gamow, G. 1948, Phys. Rev., 73, 803
- Alvarez, M. A., Bromm, V., & Shapiro, P. R. 2006, ApJ, 639, 621
- Alvarez, M. A., Bromm, V., & Shapiro, P. R. 2006a, ApJ, 639, 621
- Alvarez, M. A., Shapiro, P. R., Ahn, K., & Iliev, I. T. 2006, ApJ, 644, L101

- Anninos, P., Norman, M. L., & Clarke, D. A. 1994, *ApJ*, 436, 11
- Anninos, P., Zhang, Y., Abel, T., & Norman, M. L. 1997, *New Astronomy*, 2, 209
- Appel, A. W. 1985, *SIAM J. Sci. Stat. Comp.*, 6, 85
- Arthur, S. J., & Hoare, M. G. 2006, *ApJS*, 165, 283
- Ballesteros-Paredes, J. 2006, *MNRAS*, 372, 443
- Bardeen, J. M., Friedman, J. L., Schutz, B. F., & Sorkin, R. 1977, *ApJ*, 217, L49
- Bardeen, J. M., Bond, J. R., Kaiser, N., & Szalay, A. S. 1986, *ApJ*, 304, 15
- Barkana, R., & Loeb, A. 2001, *Phys. Rep.*, 349, 125
- Barkana, R. & Loeb, A. 2004, *ApJ*, 601, 64
- Barkat, Z, Rakavy, G., & Sack, N. 1967, *Phys. Rev. Lett.*, 18, 379
- Barnes, J., & Hut, P. 1986, *Nature*, 324, 446
- Barnes, J., & Efstathiou, G. 1987, *ApJ*, 319, 575
- Bate, M. R., Bonnell, I. A., & Price, N. M. 1995, *MNRAS*, 277, 362
- Baugh, C. M., Benson, A. J., Cole, S., Frenk, C. S., & Lacey, C. 2003, *The Mass of Galaxies at Low and High Redshift*, 91
- Becker, R. H. et al. 2001, *AJ*, 122, 2850
- Becker, R. H. et al. 2001, *AJ*, 122, 2850
- Beers, T. C., & Christlieb, N. 2005, *ARA&A*, 43, 531
- Begelman, M. C., Volonteri, M., & Rees, M. J. 2006, *MNRAS*, 370, 289
- Benson, A. J., Cole, S., Frenk, C. S., Baugh, C. M., & Lacey, C. G. 2000, *MNRAS*, 311, 793

- Benson, A. J., Frenk, C. S., Baugh, C. M., Cole, S., & Lacey, C. G. 2003, MNRAS, 343, 679
- Bertschinger, E. 2001, ApJS, 137, 1
- Bertschinger, E. 1995, ArXiv Astrophysics e-prints, arXiv:astro-ph/9506070
- Birnboim, Y., & Dekel, A. 2003, MNRAS, 345, 349
- Blumenthal, G. R., Faber, S. M., Primack, J. R., & Rees, M. J. 1984, Nature, 311, 517
- Bond, J. R., Arnett, W. D., & Carr, B. J. 1984, ApJ, 280, 825
- Bond, J. R., Cole, S., Efstathiou, G., & Kaiser, N. 1991, ApJ, 379, 440
- Bonnor, W. B. 1955, MNRAS, 116, 351
- Bonnor, W. B. 1956, Z. Astrophys., 39, 143
- Bouwens, R. J., et al. 2004, ApJ, 606, L25
- Bouwens, R. J., & Illingworth, G. D. 2006, Nature, 443, 189
- Bower, R. G. 1991, MNRAS, 248, 332
- Bowman, J. D., et al. 2007, AJ, 133, 1505
- Boylan-Kolchin, M., & Ma, C.-P. 2004, MNRAS, 349, 1117
- Bromm, V., Ferrara, A., Coppi, P. S., & Larson, R. B. 2001, MNRAS, 328, 969
- Bromm, V., Coppi, P. S., & Larson, R. B. 2002, ApJ, 564, 23
- Bromm, V. & Loeb, A. 2002, ApJ, 575, 111
- Bromm, V. & Loeb, A. 2003, ApJ, 596, 34
- Bryan, G. L., Abel, T., & Norman, M. L. 2001, ArXiv Astrophysics e-prints, arXiv:astro-ph/0112089

- Bryan, G. L., Cen, R., Norman, M. L., Ostriker, J. P., & Stone, J. M. 1994, *ApJ*, 428, 405
- Bryan, G. L., Norman, M. L., Stone, J. M., Cen, R., Ostriker, J. P. 1995, *Computer Physics Communication* 89, 149
- Bryan, G. L. & Norman, M. L. 1997, in *Computational Astrophysics*, eds. D. A. Clarke and M. Fall, ASP Conference #123
- Bryan, G. L., & Norman, M. L. 1998, *ApJ*, 495, 80
- Bryan, G. L. & Norman, M. L. 1999, in *Workshop on Structured Adaptive Mesh Refinement Grid Methods*, IMA Volumes in Mathematics 117, ed. N. Chrisochoides (New York: Springer), 165
- Bullock, J. S., Kravtsov, A. V., & Weinberg, D. H. 2000, *ApJ*, 539, 517
- Bullock, J. S., Dekel, A., Kolatt, T. S., Kravtsov, A. V., Klypin, A. A., Porciani, C., & Primack, J. R. 2001, *ApJ*, 555, 240
- Burles, S., Nollett, K. M., & Turner, M. S. 2001, *ApJ*, 552, L1
- Cen, R. 2003b, *ApJ*, 591, 12
- Cen, R. 2003a, *ApJ*, 591, L5
- Cen, R. 2005, *ApJ*, 620, 191
- Cen, R. Y., Ostriker, J. P., Jameson, A., & Liu, F. 1990, *ApJ*, 362, L41
- Cen, R. & Ostriker, J. P. 1992, *ApJ*, 399, 115
- Cen, R., & Ostriker, J. P. 1992, *ApJ*, 399, L113
- Cen, R. 1992, *ApJS*, 78, 341
- Cen, R., & Ostriker, J. P. 1992, *ApJ*, 399, L113
- Chamberlain, T. A. 1901, *ApJ*, 14, 17

- Chandrasekhar, S., & Fermi, E. 1953, ApJ, 118, 116
- Chandrasekhar, S. 1961, *Hydrodynamic and hydromagnetic stability*, (Oxford: Clarendon)
- Chandrasekhar, S. 1969, *Ellipsoidal Figures of Equilibrium*. Yale Univ. Press, New Haven
- Christodoulou, D. M., Shlosman, I., & Tohline, J. E. 1995, ApJ, 443, 551
- Christodoulou, D. M., Shlosman, I., & Tohline, J. E. 1995a, ApJ, 443, 551
- Christodoulou, D. M., Shlosman, I., & Tohline, J. E. 1995b, ApJ, 443, 563
- Churchwell, E. 2002, ARA&A, 40, 27
- Ciardi, B., Ferrara, A., & White, S. D. M. 2003, MNRAS, 344, L7
- Ciardi, B., & Ferrara, A. 2005, Space Science Reviews, 116, 625
- Cole, S., Lacey, C. G., Baugh, C. M., & Frenk, C. S. 2000, MNRAS, 319, 168
- Cole, S. 1991, ApJ, 367, 45
- Cole, S., Aragon-Salamanca, A., Frenk, C. S., Navarro, J. F., & Zepf, S. E. 1994, MNRAS, 271, 781
- Colella, P., & Woodward, P. R. 1984, Journal of Computational Physics, 54, 174
- Couchman, H. M. P. & Rees, M. J. 1986, MNRAS, 221, 53
- Couchman, H. M. P. 1991, ApJ, 368, L23
- Cowie, L. L., Songaila, A., Kim, T., & Hu, E. M. 1995, AJ, 109, 1522
- Crampin, D. J., & Hoyle, F. 1964, ApJ, 140, 99
- de Blok, W. J. G., & McGaugh, S. S. 1997, MNRAS, 290, 533
- Dekel, A., & Birnboim, Y. 2006, MNRAS, 368, 2

- Dekel, A., & Rees, M. J. 1987, *Nature*, 326, 455
- De Lucia, G., Kauffmann, G., Springel, V., White, S. D. M., Lanzoni, B., Stoehr, F., Tormen, G., & Yoshida, N. 2004, *MNRAS*, 348, 333
- de Vaucouleurs, G. 1959, *Handbuch der Physik*, 53, 275
- Diemand, J., Moore, B., & Stadel, J. 2004, *MNRAS*, 352, 535
- Dolag, K., Jubelgas, M., Springel, V., Borgani, S., & Rasia, E. 2004, *ApJ*, 606, L97
- Dolag, K., Vazza, F., Brunetti, G., & Tormen, G. 2005, *MNRAS*, 364, 753
- Doroshkevich, A. G., Sunyaev, R. A., & Zeldovich, I. B. 1974, *Confrontation of Cosmological Theories with Observational Data*, ed. M. S. Longair (Holland: Reidel), 213
- Doroshkevich, A. G., Shandarin, S. F., & Saar, E. 1978, *MNRAS*, 184, 643
- Draine, B. T., & Bertoldi, F. 1996, *ApJ*, 468, 269
- Dubinski, J. 1996, *New Astronomy*, 1, 133
- Ducloux, E., Leorat, J., Gerbal, D., & Alecian, G. 1992, *A&A*, 257, 425
- Ebert, R. 1955, *Zeitschrift für Astrophysics*, 37, 217
- Efstathiou, G., & Jones, B. J. T. 1979, *MNRAS*, 186, 133
- Efstathiou, G., & Eastwood, J. W. 1981, *MNRAS*, 194, 503
- Efstathiou, G., Davis, M., White, S. D. M., & Frenk, C. S. 1985, *ApJS*, 57, 241
- Efstathiou, G. 1992, *MNRAS*, 256, 43P
- Eggen, O. J., Lynden-Bell, D., & Sandage, A. R. 1962, *ApJ*, 136, 748
- Eisenstein, D. J., & Loeb, A. 1995, *ApJ*, 439, 520
- Eisenstein, D. J., & Loeb, A. 1995, *ApJ*, 443, 11

- Eisenstein, D. J., & Loeb, A. 1995, *ApJ*, 439, 520
- Eisenstein, D. J. & Hut, P. 1998, *ApJ*, 498, 137
- Ellis, R., Santos, M. R., Kneib, J., & Kuijken, K. 2001, *ApJ*, 560, L119
- Ellis, R. S. 1997, *ARA&A*, 35, 389
- Elmegreen, B. G. 1993, *ApJ*, 419, L29
- Miralda-Escudé, J. 2003, *Science*, 300, 1904
- Evrard, A. E. 1988, *MNRAS*, 235, 911
- Eyles, L. P., Bunker, A. J., Ellis, R. S., Lacy, M., Stanway, E. R., Stark, D. P., & Chiu, K. 2006, *MNRAS*, 1348
- Faber, S. M., & Jackson, R. E. 1976, *ApJ*, 204, 668
- Fall, S. M. & Efstathiou, G. 1980, *MNRAS*, 193, 189
- Fan, X., Narayanan, V. K., Strauss, M. A., White, R. L., Becker, R. H., Pentericci, L., & Rix, H. 2002, *AJ*, 123, 1247
- Fan, X., et al. 2006, *AJ*, 132, 117
- Ferrara, A. & Tolstoy, E. 2000, *MNRAS*, 313, 291
- Ferrara, A. 1998, *ApJ*, 499, L17
- Field, G. B., Somerville, W. B., & Dressler, K. 1966, *ARA&A*, 4, 207
- Flower, D. R., Le Bourlot, J., Pineau des Forêts, G., & Roueff, E. 2000, *MNRAS*, 314, 753
- Franco, J., Tenorio-Tagle, G., & Bodenheimer, P. 1990, *ApJ*, 349, 126
- Frenk, C. S., et al. 1999, *ApJ*, 525, 554
- Fryer, C. L., Woosley, S. E., & Heger, A. 2001, *ApJ*, 550, 372

- Fuller, T. M. & Couchman, H. M. P. 2000, ApJ, 544, 6
- Furlanetto, S. R., Sokasian, A., & Hernquist, L. 2004, MNRAS, 347, 187
- Galli, D., & Palla, F. 1998, A&A, 335, 403
- Gamow, G. & Teller, E. 1939, Phys. Rev., 55, 654
- Gamow, G. 1946, Physical Review, 70, 572
- Gamow, G. 1952, Phys. Rev., 21, 367
- Gao, L., White, S. D. M., Jenkins, A., Frenk, C. S., & Springel, V. 2005, MNRAS, 363, 379
- Gardner, J. P. 2001, 557, 616
- Gardner, J. P., et al. 2006, Space Science Reviews, 123, 485
- Gehrels, N., et al. 2004, ApJ, 611, 1005
- Gehrels, N., & Michelson, P. 1999, Astroparticle Physics, 11, 277
- Gingold, R. A., & Monaghan, J. J. 1977, MNRAS, 181, 375
- Glover, S. C. O., & Brand, P. W. J. L. 2001, MNRAS, 321, 385
- Glover, S. C. O. 2003, ApJ, 584, 331
- Glover, S. C. O., & Jappsen, A.-K., 2007, ApJ, *submitted*
- Gnedin, N. Y. 2000, ApJ, 535, L75
- Gnedin, N. Y. 2000, ApJ, 535, L75
- Gnedin, N. Y. 2000b, ApJ, 542, 535
- Gnedin, N. Y., & Abel, T. 2001, New Astronomy, 6, 437
- Gnedin, N. Y., & Kravtsov, A. V. 2006, ApJ, 645, 1054

- Gnedin, N. Y. 1995, *ApJS*, 97, 231
- Gnedin, N. Y., & Ostriker, J. P. 1997, *ApJ*, 486, 581
- Gnedin, N. Y., & Hui, L. 1998, *MNRAS*, 296, 44
- Goldman, I. 2000, *ApJ*, 541, 701
- Górski, K. M., Hivon, E., Banday, A. J., Wandelt, B. D., Hansen, F. K., Reinecke, M., & Bartelmann, M. 2005, *ApJ*, 622, 759
- Gou, L. J., Mészáros, P., Abel, T., & Zhang, B. 2004, *ApJ*, 604, 508
- Governato, F., Baugh, C. M., Frenk, C. S., Cole, S., Lacey, C. G., Quinn, T., & Stadel, J. 1998, *Nature*, 392, 359
- Guth, A. H. 1981, *Phys. Rev. D*, 23, 347
- Haardt, F. & Madau, P. 1996, *ApJ*, 461, 20
- Haehnelt, M. G. 1995, *MNRAS*, 273, 249
- Haehnelt, M. G., Rauch, M., & Steinmetz, M. 1996, *MNRAS*, 283, 1055
- Haiman, Z., Abel, T., & Rees, M. J. 2000, *ApJ*, 534, 11
- Haiman, Z., Abel, T., & Madau, P. 2001, *ApJ*, 551, 599
- Haiman, Z., & Bryan, G. L. 2006, *ApJ*, 650, 7
- Haiman, Z., Thoul, A. A., & Loeb, A. 1996, *ApJ*, 464, 523
- Haiman, Z., Rees, M. J., & Loeb, A. 1997, *ApJ*, 476, 458
- Haiman, Z. & Loeb, A. 1997, *ApJ*, 483, 21
- Haiman, Z., Rees, M. J., & Loeb, A. 1997, *ApJ*, 476, 458
- Harrison, E. R. 1970, *Phys. Rev. D*, 1, 2726

- Heckman, T. M., Sembach, K. R., Meurer, G. R., Leitherer, C., Calzetti, D., & Martin, C. L. 2001, ApJ, 558, 56
- Heger, A. & Woosley, S. E. 2002, ApJ, 567, 532
- Heger, A. & Woosley, S. E. 2002, ApJ, 567, 532
- Heger, A., Fryer, C. L., Woosley, S. E., Langer, N., & Hartmann, D. H. 2003, ApJ, 591, 288
- Heger, A., Fryer, C. L., Woosley, S. E., Langer, N., & Hartmann, D. H. 2003, ApJ, 591, 288
- Heisenberg, W., & von Weizsäcker, C. F. 1948, Z. Phys., 125, 290
- Helmi, A., et al. 2006, ApJ, 651, L121
- Hernquist, L., & Springel, V. 2003, MNRAS, 341, 1253
- Hernquist, L. 1987, ApJS, 64, 715
- Hetznecker, H., & Burkert, A. 2006, MNRAS, 370, 1905
- Hillis, W. D., & Barnes, J. 1987, Nature, 326, 27
- Hockney, R. W., & Eastwood, J. W. 1988, *Computer simulation using particles*, (Hilger: Bristol)
- Hogan, C. J. & Rees, M. J. 1979, MNRAS, 188, 791
- Holmberg, E. 1941, ApJ, 94, 385
- Hoyle, F. 1949, in Problems of Cosmical Aerodynamics, ed. J. M. Burgers & H. C. van de Hulst (Dayton: Central Air Documents Office), 195.
- Hu, W. & Dodelson, S. 2002, ARA&A, 40, 171
- Hubble, E. P. 1925a, ApJ, 62, 409

- Hubble, E. P. 1925b, *Pub. Amer. Astron. Soc.*, 5, 261
- Hubble, E. P. 1925c, *Observatory*, 48, 139
- Hubble, E. P. 1926, *ApJ*, 63, 236
- Hubble, E. P. 1929, *ApJ*, 69, 103
- Hui, L. & Haiman, Z. 2003, *ApJ*, 596, 9
- Hurwitz, M., Jelinsky, P., & Dixon, W. V. D. 1997, *ApJ*, 481, L31
- Hutchings, R. M., Santoro, F., Thomas, P. A., & Couchman, H. M. P. 2002, *MNRAS*, 330, 927
- Iliev, I. T., & Shapiro, P. R. 2001, *MNRAS*, 325, 468
- Iliev, I. T., Scannapieco, E., Martel, H., & Shapiro, P. R. 2003, *MNRAS*, 341, 81
- Iliev, I. T., Mellema, G., Pen, U.-L., Merz, H., Shapiro, P. R., & Alvarez, M. A. 2006, *MNRAS*, 369, 1625
- Innanen, K. A. 1966, *ApJ*, 143, 150
- Iye, M., et al. 2006, *Nature*, 443, 186
- Jappsen, A.-K., Glover, S. C. O., Klessen, R. S., & Mac Low, M.-M. 2007, *ApJ*, *accepted*, ([astro-ph/0511400](#))
- Jeans, J. 1902, *Phil. Trans.*, 199A, 1
- Jeans, J. 1918, *Cosmogony and Stellar Dynamics* (Cambridge University, Cambridge)
- Jeans, J. 1928, *Astronomy and Cosmogony* (Cambridge University, Cambridge)
- Jenkins, A., Frenk, C. S., White, S. D. M., Colberg, J. M., Cole, S., Evrard, A. E., Couchman, H. M. P., & Yoshida, N. 2001, *MNRAS*, 321, 372
- Jessop, C., Duncan, M., & Chau, W. Y. 1994, *Journal of Computational Physics*, 115, 339

- Johnson, J. L., Greif, T. H., & Bromm, V. 2007, *ApJ*, *submitted*, (astro-ph/0612254)
- Jones, B. J. T. 1976, *Reviews of Modern Physics*, 48, 107
- Miralda-Escudé, J. & Rees, M. J. 1997, *ApJ*, 478, L57
- Kashikawa, N., et al. 2006, *ApJ*, 648, 7
- Kashlinsky, A., Arendt, R. G., Mather, J., & Moseley, S. H. 2007, *ArXiv Astrophysics e-prints*, arXiv:astro-ph/0612447
- Katz, N., Weinberg, D. H., & Hernquist, L. 1996, *ApJS*, 105, 19
- Kauffmann, G. et al. 2003, *MNRAS*, 341, 33
- Kauffmann, G., White, S. D. M., & Guiderdoni, B. 1993, *MNRAS*, 264, 201
- Kauffmann, G., Guiderdoni, B., & White, S. D. M. 1994, *MNRAS*, 267, 981
- Kauffmann, G., Charlot, S., & White, S. D. M. 1996, *MNRAS*, 283, L117
- Kazantzidis, S., Magorrian, J., & Moore, B. 2004, *ApJ*, 601, 37
- Keeler, J. E. 1900, *AJ*, 11, 346
- Kennicutt, R. C., Jr. 1998, *ARA&A*, 36, 189
- Kereš, D., Katz, N., Weinberg, D. H., & Davé, R. 2005, *MNRAS*, 363, 2
- Kim, W.-T., & Narayan, R. 2003, *ApJ*, 596, 889
- Kim, T., Hu, E. M., Cowie, L. L., & Songaila, A. 1997, *AJ*, 114, 1
- King, I. R. 1966, *ApJ*, 71, 64
- Kitayama, T., Yoshida, N., Susa, H., & Umemura, M. 2004, *ApJ*, 613, 631
- Kitayama, T., & Yoshida, N. 2005, *ApJ*, 630, 675

- Kogut, A., et al. 2003, ApJS, 148, 161
- Kohler, K., Gnedin, N. Y., & Hamilton, A. J. S. 2007, ApJ, 657, 15
- Kolmogorov, A. N. 1941, Dokl. Akad. Nauk SSSR 30, 301 [Proc. R. Soc. London, Ser. A 341, 9 (1991)]
- Kravtsov, A. V., Berlind, A. A., Wechsler, R. H., Klypin, A. A., Gottlöber, S., Allgood, B., & Primack, J. R. 2004, ApJ, 609, 35
- Kravtsov, A. V., Klypin, A. A., & Khokhlov, A. M. 1997, ApJS, 111, 73
- Krumholz, M. R., McKee, C. F., & Klein, R. I. 2004, ApJ, 611, 399
- Krumholz, M. R., McKee, C. F., & Klein, R. I. 2006, ApJ, 638, 369
- Kuhlen, M., & Madau, P. 2005, MNRAS, 363, 1069
- Lacey, C., & Silk, J. 1991, ApJ, 381, 14
- Lacey, C., & Cole, S. 1993, MNRAS, 262, 627
- Lacey, C., & Cole, S. 1994, MNRAS, 271, 676
- Lamb, D. Q. 1999, A&AS, 138, 607
- Laplace, P. S. 1799, *Traité de mécanique céleste*
- Larson, R. B. 2003, Reports of Progress in Physics, 66, 1651
- Larson, R. B. 1979, MNRAS, 186, 479
- Larson, R. B. 1981, MNRAS, 194, 809
- Lynden-Bell, D. 1967, MNRAS, 136, 101
- Lebovitz, N. R. 1967, ARA&A, 5, 465
- Lemaître, G. 1950, *The Primeval Atom* (van Nostrand, New York)

- Leitherer, C., Ferguson, H. C., Heckman, T. M., & Lowenthal, J. D. 1995, ApJ, 454, L19
- Leitherer, C. et al. 1999, ApJS, 123, 3
- LeVeque, R. J. 1992, *Numerical Methods for Conservation Laws* (Birkhauser: Boston)
- Liddle, A. R. & Lyth, D. H. 1992, Phys. Lett. B, 291, 391
- Liddle, A. R. & Lyth, D. H. 1993, Phys. Rep., 231, 1
- Lifschitz, E. M. 1946, J. Phys. USSR, 10, 116
- Lin, D. N. C. & Pringle, J. E. 1987, MNRAS, 225, 607
- Lodato, G., & Natarajan, P. 2006, MNRAS, 371, 1813
- Loeb, A. & Barkana, R. 2001, ARA&A, 39, 19
- Loeb, A. 2003, Proc. of IAU Colloquium 192 on “Supernovae”, April 2003, Valencia, Spain, eds. J. M. Marcaide and K. W. Weiler (astro-ph/0307231)
- Loeb, A., & Rasio, F. A. 1994, ApJ, 432, 52
- Lucy, L. B. 1977, AJ, 82, 1013
- Lynden-Bell, D., & Ostriker, J. P. 1967, MNRAS, 136, 293
- MacFadyen, A. I. & Woosley, S. E. 1999, ApJ, 524, 262
- Machacek, M. E., Bryan, G. L., & Abel, T. 2001, ApJ, 548, 509
- Mac Low, M.-M., & Ferrara, A. 1999, ApJ, 513, 142
- Madau, P., Ferrara, A., & Rees, M. J. 2001, ApJ, 555, 92
- Madau, P., & Rees, M. J. 2001, ApJ, 551, L27
- Madau, P. 1995, ApJ, 441, 18

- Madau, P., Ferguson, H. C., Dickinson, M. E., Giavalisco, M., Steidel, C. C., & Fruchter, A. 1996, *MNRAS*, 283, 1388
- Madau, P., Haardt, F., & Rees, M. J. 1999, *ApJ*, 514, 648
- Makino, J., & Hut, P. 1989, *Comp. Phys. Rep.*, 9, 199
- Maller, A. H., Dekel, A., & Somerville, R. 2002, *MNRAS*, 329, 423
- Marri, S., Ferrara, A., & Pozzetti, L. 2000, *MNRAS*, 317, 265
- Marri, S. & Ferrara, A. 1998, *ApJ*, 509, 43
- Mateo, M. L. 1998, *ARA&A*, 36, 435
- Matteucci, F. & Recchi, S. 2001, *ApJ*, 558, 351
- Matteucci, F. 2002, in *Proceedings of The Evolution of Galaxies III* (astro-ph/0210540)
- Mayer, L., Kazantzidis, S., Mastropietro, C., & Wadsley, J. 2007, *Nature*, 445, 738
- McDowell, M. R. C. 1961, *Observatory*, 81, 240
- Mellema, G., Iliev, I. T., Alvarez, M. A., & Shapiro, P. R. 2006, *New Astronomy*, 11, 374
- Mesinger, A., Bryan, G. L., & Haiman, Z. 2006, *ApJ*, 648, 835
- Mestel, L. 1963, *MNRAS*, 126, 553
- Mészáros, P. 2002, *ARA&A*, 40, 137
- Mo, H. J. & White, S. D. M. 2002, *MNRAS*, 336, 112
- Mo, H. J., Mao, S., & White, S. D. M. 1998, *MNRAS*, 295, 319
- Mobasher, B., et al. 2005, *ApJ*, 635, 832
- Moore, B., Frenk, C. S., & White, S. D. M. 1993, *MNRAS*, 261, 827

- Myers, P. C. 1999, in *The Physics and Chemistry of the Interstellar Medium*, eds. V. Ossenkopf, J. Stutzki, and G. Winnewisser, 3rd Cologne-Zermatt Symposium, p. 227
- Nagai, D., & Kravtsov, A. V. 2003a, *ApJ*, 587, 514
- Nagai, D., Kravtsov, A. V., & Kosowsky, A. 2003, *ApJ*, 587, 524
- Nagakura, T., & Omukai, K. 2005, *MNRAS*, 364, 1378
- Navarro, J. F., Frenk, C. S., & White, S. D. M. 1997, *ApJ*, 490, 493
- Norman, M. L., O'Shea, B. W., & Paschos, P. 2004, *ApJ*, 601, L115
- Norman, M. L., & Bryan, G. L. 1999, *LNP Vol. 530: The Radio Galaxy Messier 87*, 530, 106
- Oh, S. P., & Haiman, Z. 2002, *ApJ*, 569, 558
- Oh, S. P. & Haiman, Z. 2003, *MNRAS*, 346, 456
- Omukai, K., & Palla, F. 2003, *ApJ*, 589, 677
- Onken, C. A., & Miralda-Escudé, J. 2004, *ApJ*, 610, 1
- O'Shea, B. W., Bryan, G., Bordner, J., Norman, M. L., Abel, T., Harkness, R., & Kritsuk, A. 2004, *ArXiv Astrophysics e-prints*, arXiv:astro-ph/0403044
- O'Shea, B. W., Abel, T., Whalen, D., & Norman, M. L. 2005, *ApJ*, 628, L5
- O'Shea, B. W., & Norman, M. L. 2006, *ApJ*, 654, 66
- O'Shea, B. W., & Norman, M. L. 2007, *ApJ*, 654, 66
- Ostriker, J. P., & Tassoul, J. L. 1969, *ApJ*, 155, 987
- Ostriker, J. P., & Bodenheimer, P. 1973, *ApJ*, 180, 171
- Ostriker, J. P., & Peebles, P. J. E. 1973, *ApJ*, 186, 467

- Ostriker, J. P., & McKee, C. F. 1988, *Reviews of Modern Physics*, 60, 1
- Ostriker, J. P., & Gnedin, N. Y. 1996, *ApJ*, 472, L63
- Ozernoi, L. M. & Chernin, A. D. 1968a, *Sov. Astron.-AJ*, 11, 907
- Ozernoi, L. M. & Chernin, A. D. 1968b, *Sov. Astron.-AJ*, 12, 901
- Ozernoi, L. M. & Chibisov, G. V. 1971, *Sov. Astron.-AJ*, 14, 615
- Padmanabhan, T. 1993, *Structure Formation in the Universe*, (Cambridge University Press: Cambridge)
- Page, L., et al. 2006, *ApJ*, *submitted*, (astro-ph/0603450)
- Palla, F., Salpeter, E. E., & Stahler, S. W. 1983, *ApJ*, 271, 632
- Peebles, P. J. E. 1965, *ApJ*, 142, 1317
- Peebles, P. J. E., & Dicke, R. H. 1968, *ApJ*, 154, 891
- Peebles, P. J. E. 1968, *ApJ*, 153, 1
- Peebles, P. J. E., & Dicke, R. H. 1968, *ApJ*, 154, 891
- Peebles, P. J. E. 1969, *ApJ*, 155, 393
- Peebles, P. J. E., & Yu, J. T. 1970, *ApJ*, 162, 815
- Peebles, P. J. E. 1971, *A&A*, 11, 377
- Peebles, P. J. E. 1974, *ApJ*, 189, L51
- Peebles, P. J. E., & Groth, E. J. 1975, *ApJ*, 196, 1
- Peebles, P. J. E. 1982, *ApJ*, 263, L1
- Peebles, P. J. E. 1993, *Principles of Physical Cosmology* (Princeton: Princeton University Press)

- Peiris, H. V., et al. 2003, ApJS, 148, 213
- Pelló, R., Schaerer, D., Richard, J., Le Borgne, J.-F., & Kneib, J.-P. 2004, A&A, 416, L35
- Pen, U.-L. 1995, ApJS, 100, 269
- Penzias, A. A., & Wilson, R. W. 1965, ApJ, 142, 419
- Ponman, T. J., Cannon, D. B., & Navarro, J. F. 1999, Nature, 397, 135
- Popov, D. V. 1993, ApJ, 414, 712
- Pottasch, S. R. 1958, Reviews of Modern Physics, 30, 1053
- Press, W. H., & Teukolsky, S. A. 1973, ApJ, 181, 513
- Press, W. H. & Schechter, P. 1974, ApJ, 187, 425
- Press, W. H. & Schechter, P. 1974, ApJ, 187, 425
- Quinn, T., Katz, N., Stadel, J., & Lake, G. 1997, ArXiv Astrophysics e-prints, arXiv:astro-ph/9710043
- Rakavy, G., Shaviv, G., & Zinamon, Z. 1967, ApJ, 150, 131
- Rauch, M., Haehnelt, M. G., & Steinmetz, M. 1997, ApJ, 481, 601
- Lord Rayleigh. 1920, *Scientific Papers*, 6, 447
- Rees, M. J., & Ostriker, J. P. 1977, MNRAS, 179, 541
- Ricker, P. M., & Sarazin, C. L. 2001, ApJ, 561, 621
- Ricotti, M. & Shull, J. M. 2000, ApJ, 542, 548
- Ricotti, M., Gnedin, N. Y., & Shull, J. M. 2001, ApJ, 560, 580
- Ricotti, M., Gnedin, N. Y., & Shull, J. M. 2002a, ApJ, 575, 49

- Ricotti, M., Gnedin, N. Y., & Shull, J. M. 2002b, *ApJ*, 575, 33
- Ricotti, M. & Ostriker, J. P. 2004, *MNRAS*, 350, 539
- Ricotti, M. & Ostriker, J. P. 2004, *MNRAS*, 352, 547
- Ricotti, M., & Ostriker, J. P. 2004, *MNRAS*, 350, 539
- Ricotti, M., Ostriker, J. P., & Gnedin, N. Y. 2005, *MNRAS*, 357, 207
- Ritchmyer, R. D., & Morton, K. W. 1967, *Difference methods for initial-value problems*, (Interscience: New York)
- Roberts, I. 1889, *MNRAS*, 49, 362
- Rosse, Lord, 1850a, *MNRAS*, 10, 21
- Rosse, Lord 1850b, *Phil. Trans.*, 499
- Rottgering, H. J. A., et al. 2006, *ArXiv Astrophysics e-prints*, arXiv:astro-ph/0610596
- Rubin, V. C., & Ford, W. K. J. 1970, *ApJ*, 159, 379
- Ryu, D., Ostriker, J. P., Kang, H., & Cen, R. 1993, *ApJ*, 414, 1
- Salvatterra, R. & Ferrara, A. 2003, *MNRAS*, 339, 973
- Santos, M. R., Bromm, V., & Kamionkowski, M. 2002, *MNRAS*, 336, 1082
- Saslaw, W. C., & Zipoy, D. 1967, *Nature*, 216, 976
- Schaerer, D. 2000, *ASP Conf. Ser. 221: Stars, Gas and Dust in Galaxies: Exploring the Links*, 99
- Schaerer, D. 2002, *A&A*, 382, 28
- Schaerer, D. 2003, *A&A*, 397, 527
- Schaye, J., Theuns, T., Rauch, M., Efstathiou, G., & Sargent, W. L. W. 2000, *MNRAS*, 318, 817

- Schechter, P. 1976, *ApJ*, 203, 297
- Schilizzi, R. T. 2004, *Proc. SPIE*, 5489, 62
- Schneider, R., Omukai, K., Inoue, A. K., & Ferrara, A. 2006, *MNRAS*, 369, 1437
- Schuecker, P., Finoguenov, A., Miniati, F., Böhringer, H., & Briel, U. G. 2004, *A&A*, 426, 387
- Scott, D. & Rees, M. J. 1990, *MNRAS*, 247, 510
- Sedov, L. I. 1959, *Similarity and Dimensional Methods in Mechanics*, New York: Academic Press, 1959
- Shapiro, P. R. 1986, *PASP*, 98, 1014
- Shapiro, P. R., & Kang, H. 1987, *ApJ*, 318, 32
- Shapiro, P. R., Giroux, M. L., & Babul, A. 1994, *ApJ*, 427, 25
- Shapiro, P. R., Iliiev, I. T., & Raga, A. C. 1999, *MNRAS*, 307, 203
- Sharma, S., & Steinmetz, M. 2005, *ApJ*, 628, 21
- Shaw, L. D., Weller, J., Ostriker, J. P., & Bode, P. 2006, *ApJ*, 646, 815
- Sheth, R. K., Mo, H. J., & Tormen, G. 2001, *MNRAS*, 323, 1
- Sheth, R. K. & Tormen, G. 2002, *MNRAS*, 329, 61
- Sheth, R. K. & Tormen, G. 1999, *MNRAS*, 308, 119
- Shlosman, I., Frank, J., & Begelman, M. C. 1989, *Nature*, 338, 45
- Shlosman, I., Begelman, M. C., & Frank, J. 1990, *Nature*, 345, 679
- Shu, F. H., Lizano, S., Galli, D., Cantó, J., & Laughlin, G. 2002, *ApJ*, 580, 969
- Shu, F. H. 1992, *Physics of Astrophysics, Vol. II*, (Sausalito: University Science Books)

- Silk, J. 1974, *Confrontation of Cosmological Theories with Observational Data*, ed. M. S. Longair (Holland: Reidel), 175
- Silk, J. 1977, *ApJ*, 211, 638
- Smith, L. J., Norris, R. P. F., & Crowther, P. A. 2002, *MNRAS*, 337, 1309
- Smith, B. D., & Sigurdsson, S. 2007, ArXiv e-prints, 704, arXiv:0704.0477
- Sod, G. A. 1985, *Numerical Methods in Fluid Dynamics* (Cambridge Univ. Press: Cambridge)
- Sokasian, A., Abel, T., Hernquist, L., & Springel, V. 2003, *MNRAS*, 344, 607
- Sokasian, A., Yoshida, N., Abel, T., Hernquist, L., & Springel, V. 2004, *MNRAS*, 350, 47
- Somerville, R. S. & Livio, M. 2003, *ApJ*, 593, 611
- Somerville, R. S., & Primack, J. R. 1999, *MNRAS*, 310, 1087
- Songaila, A. 2001, *ApJ*, 561, L153
- Songaila, A. & Cowie, L. L. 1996, *AJ*, 112, 335
- Spaans, M., & Silk, J. 2006, *ApJ*, 652, 902
- Spergel, D. N., et al. 2003, *ApJS*, 148, 175
- Spergel, D. N., et al. 2007, *ApJ*, *submitted*, (astro-ph/0603449)
- Spitzer, L., Jr. 1978, *Physical Processes in the Interstellar Medium*, (John Wiley & Sons: New York)
- Splinter, R. J. 1996, *MNRAS*, 281, 281
- Springel, V., Di Matteo, T., & Hernquist, L. 2005, *MNRAS*, 361, 776
- Stanek, K. Z., et al. 2003, *ApJ*, 591, L17

- Stanway, E. R., Bunker, A. J., & McMahon, R. G. 2003, MNRAS, 342, 439
- Stark, D. P., et al. 2007, ApJ, *submitted*, ([astro-ph/0701279](#))
- Stetcher, T. P. & Williams, D. A. 1967, ApJ, 149, 29
- Steidel, C. C., Pettini, M., & Adelberger, K. L. 2001, ApJ, 546, 665
- Steinmetz, M., & Bartelmann, M. 1995, MNRAS, 272, 570
- Stone, J. M., Mihalas, D., & Norman, M. L. 1992, ApJS, 80, 819
- Strömgren, B. 1939, ApJ, 89, 526
- Susa, H., & Umemura, M. 2004, ApJ, 600, 1
- Susa, H., & Umemura, M. 2006, ApJ, 645, L93
- Sutherland, W. 1911, ApJ, 34, 251
- Sutherland, R. S., & Dopita, M. A. 1993, ApJS, 88, 253
- Swarup, G., Ananthakrishnan, S., Kapahi, V. K., Rao, A. P., Subrahmanya, C. R., & Kulkarni, V. K. 1991, Current Science, 60, 95
- Takizawa, M. 2005, ApJ, 629, 791
- Tan, J. C., & McKee, C. F. 2004, ApJ, 603, 383
- Tassis, K., Abel, T., Bryan, G. L., & Norman, M. L. 2003, ApJ, 587, 13
- Taylor, C. L., Hüttemeister, S., Klein, U., & Greve, A. 1999, A&A, 349, 424
- Tegmark, M., Silk, J., Rees, M. J., Blanchard, A., Abel, T., & Palla, F. 1997, ApJ, 474, 1
- Thompson, R. I., Eisenstein, D., Fan, X., Rieke, M., & Kennicutt, R. C. 2006, ArXiv Astrophysics e-prints, [arXiv:astro-ph/0612033](#)
- Thoul, A. A., & Weinberg, D. H. 1996, ApJ, 465, 608

- Tolstoy, E., Venn, K., Shetrone, M., Primas, F., Hill, V., Kaufer, A., & Szeifert, T. 2002, *Ap&SS*, 281, 217
- Tolstoy, E., Venn, K., Shetrone, M., Primas, F., Hill, V., Kaufer, A., & Szeifert, T. 2003, *AJ*, 125, 707
- Tolstoy, E., et al. 2004, *ApJ*, 617, L119
- Toomre, A. 1964, *ApJ*, 139, 1217
- Toomre, A., & Toomre, J. 1972, *ApJ*, 178, 623
- Totsuji, H., & Kihara, T. 1969, *PASJ*, 21, 221
- Truelove, J. K., Klein, R. I., McKee, C. F., Holliman, J. H., Howell, L. H., & Greenough, J. A. 1997, *ApJL*, 489, L179
- Tully, R. B., & Fisher, J. R. 1977, *A&A*, 54, 661
- Tumlinson, J. 2006, *ApJ*, 641, 1
- van den Bosch, F. C., Abel, T., Croft, R. A. C., Hernquist, L., & White, S. D. M. 2002, *ApJ*, 576, 21
- van den Bosch, F. C. 2002, *MNRAS*, 331, 98
- Venn, K., Tolstoy, E., Kaufer, A., & Kudritzki, R. P. 2003, *Carnegie Obs. Astrophysics Series*, Vol. 4, *Origin and Evolution of the Elements* (astro-ph/0305188)
- Venn, K. A., Irwin, M., Shetrone, M. D., Tout, C. A., Hill, V., & Tolstoy, E. 2004, *AJ*, 128, 1177
- Vitvitska, M., Klypin, A. A., Kravtsov, A. V., Wechsler, R. H., Primack, J. R., & Bullock, J. S. 2002, *ApJ*, 581, 799.
- Volonteri, M., & Rees, M. J. 2005, *ApJ*, 633, 624
- von Hoerner, S. 1960, *Z. Astrophys.*, 50, 184

- von Hoerner, S. 1963, *Z. Astrophys.*, 57, 47
- von Weizsäcker, C. F. 1943, *Z. Astrophys.*, 22, 319
- von Weizsäcker, C. F. 1948, *Naurewissenschaften*, 35, 188
- Vreeswijk, P. M., Møller, P., & Fynbo, J. P. U. 2003, *A&A*, 409, L5
- Wagoner, R. V., Fowler, W. A., & Hoyle, F. 1967, *ApJ*, 148, 3
- Wai, L., & GLAST LAT Collaboration 2007, *ArXiv Astrophysics e-prints*, arXiv:astro-ph/0701884
- Walter, F., Taylor, C. L., Hüttemeister, S., Scoville, N. & McIntyre, V. 2001, *AJ*, 121, 727
- Wang, P., & Abel, T. 2007, *ApJ*, *submitted*, (astro-ph/0701363)
- Wechsler, R. H., Somerville, R. S., Bullock, J. S., Kolatt, T. S., Primack, J. R., Blumenthal, G. R., & Dekel, A. 2001, *ApJ*, 554, 85
- Wechsler, R. H., Bullock, J. S., Primack, J. R., Kravtsov, A. V., & Dekel, A. 2002, *ApJ*, 568, 52
- Wechsler, R. H., Zentner, A. R., Bullock, J. S., Kravtsov, A. V., & Allgood, B. 2006, *ApJ*, 652, 71
- Weinberg, D. H., Davé, R., Katz, N., & Hernquist, L. 2004, *ApJ*, 601, 1
- Whalen, D., Abel, T. & Norman, M. L. 2004, *ApJ*, 610, 14
- White, S. D. M., & Rees, M. J. 1978, *MNRAS*, 183, 341
- White, S. D. M., & Frenk, C. S. 1991, *ApJ*, 379, 52
- Wilson, T. L., Beasley, A. J., & Wootten, H. A. 2005, *ASP Conf. Ser.* 344: *The Cool Universe: Observing Cosmic Dawn*, 344, 232
- Wise, J. H., & Abel, T. 2005, *ApJ*, 629, 615 (WA05)

- Wise, J. H., & Abel, T. 2007, *ApJ*, *accepted*
- Wise, J. H., & Abel, T. 2007a, *ApJ*, *accepted*
- Wise, J. H., & Abel, T. 2007b, *ApJ*, *in prep*
- Wise, J. H., & Abel, T. 2007c, *ApJ*, *submitted*
- Wood, K. & Loeb, A. 2000, *ApJ*, 545, 86
- Woodward, P. R. & Colella, P. 1984, *J. Comput. Phys.* 54, 115
- Woosley, S. E. & Weaver, T. A. 1986, *ARA&A*, 24, 205
- Woosley, S. E. 1993, *ApJ*, 405, 273
- Xu, G. 1995, *ApJS*, 98, 355
- Yoneyama, T. 1972, *PASJ*, 24, 87
- York, D. G. et al. 2000, *AJ*, 120, 1579
- Yorke, H. W. 1986, *ARA&A*, 24, 49
- Yoshida, N., Abel, T., Hernquist, L., & Sugiyama, N. 2003, *ApJ*, 592, 645
- Yoshida, N., Oh, S. P., Kitayama, T., & Hernquist, L. 2006a, *MNRAS*, *submitted*,
(astro-ph/0610819)
- Yoshida, N., Omukai, K., Hernquist, L., & Abel, T. 2006b, *ApJ*, 652, 6
- Zahn, O., Lidz, A., McQuinn, M., Dutta, S., Hernquist, L., Zaldarriaga, M., &
Furlanetto, S. R. 2007, *ApJ*, 654, 12
- Zaldarriaga, M., Hui, L., & Tegmark, M. 2001, *ApJ*, 557, 519
- Zel'dovich, Ya. B. 1972, *MNRAS*, 160, 1
- Zhang, Y., Anninos, P., & Norman, M. L. 1995, *ApJ*, 453, L57

Zhang, Y., Anninos, P., Norman, M. L., & Meiksin, A. 1997, *ApJ*, 485, 496

Zheng, W., et al. 2003, *Proc. SPIE*, 4850, 1132

Zwicky, F. 1933, *Helvetica Physica Acta*, 6, 110